

AD-A263 497



WL-TR-92-2098

PULSE MITIGATION AND HEAT TRANSFER
ENHANCEMENT TECHNIQUES

VOL 4 - TRANSIENT BEHAVIOR OF HEAT PIPE WITH
THERMAL ENERGY STORAGE UNDER PULSE HEAT LOADS



L.C. Chow
M.J. Chang

University of Kentucky
Department of Mechanical Engineering
Lexington, KY 40506-0046

AUG 1992

FINAL REPORT FOR 07/01/87 - 07/31/92

APPROVED FOR PUBLIC RELEASE; DISTRIBUTION IS UNLIMITED.

DTIC
ELECTE
MAY 03 1993
S B D

D8 4 80 02 4

93-09321



201P8
0000

AERO PROPULSION AND POWER DIRECTORATE
WRIGHT LABORATORY
AIR FORCE MATERIEL COMMAND
WRIGHT-PATTERSON AFB OH 45433-6563


NOTICE


When Government drawings, specifications, or other data are used for any purpose other than in connection with a definitely Government-related procurement, the United States Government incurs no responsibility or any obligation whatsoever. The fact that the government may have formulated or in any way supplied the said drawings, specifications, or other data, is not to be regarded by implication, or otherwise in any manner construed, as licensing the holder, or any other person or corporation; or as conveying any rights or permission to manufacture, use, or sell any patented invention that may in any way be related thereto.

This report is releasable to the National Technical Information Service (NTIS). At NTIS, it will be available to the general public, including foreign nations.

This technical report has been reviewed and is approved for publication.


MICHAEL J. MORGAN
Project Engineer


JERRY E. BEAM, Chief
Thermal Technology Section


MICHAEL D. BRAYDICH, Lt Col, USAF
Deputy Chief
Aerospace Power Division
Aero Propulsion & Power Directorate

If your address has changed, if you wish to be removed from our mailing list, or if the addressee is no longer employed by your organization please notify WL/POOS, WPAFB, OH 45433-6563 to help us maintain a current mailing list.

Copies of this report should not be returned unless return is required by security considerations, contractual obligations, or notice on a specific document.

REPORT DOCUMENTATION PAGE			Form Approved OMB No 0704 0188	
<small>Public reporting burden for this collection of information is estimated to average 1 hour per response, including the time for reviewing instructions, searching existing data sources, gathering and maintaining the data needed, and completing and reviewing the collection of information. Send comments regarding this burden estimate or any other aspect of this collection of information, including suggestions for reducing this burden, to Washington Headquarters Services, Directorate for Information Operations and Reports, 1215 Jefferson Davis Highway, Suite 1204, Arlington, VA 22202-4302, and to the Office of Management and Budget, Paperwork Reduction Project (0704-0188), Washington, DC 20503.</small>				
1. AGENCY USE ONLY (Leave blank)		2. REPORT DATE AUG 1992		3. REPORT TYPE AND DATES COVERED FINAL 07/01/87--07/31/92
4. TITLE AND SUBTITLE PULSE MITIGATION AND HEAT TRANSFER ENHANCEMENT TECHNIQUES VOL 4 - TRANSIENT BEHAVIOR OF HEAT PIPE WITH THERMAL ENERGY STORAGE UNDER PULSE HEAT LOADS			5. FUNDING NUMBERS C F33615-87-C-2777 PE 63218 PR D812 TA 00 WU 08	
6. AUTHOR(s) J. C. Chow M. J. Chang				
7. PERFORMING ORGANIZATION NAME(S) AND ADDRESS(ES) University of Kentucky Department of Mechanical Engineering Lexington, KY 40506-0046			8. PERFORMING ORGANIZATION REPORT NUMBER UK-ME-92-04	
9. SPONSORING / MONITORING AGENCY NAME(S) AND ADDRESS(ES) AERO PROPULSION AND POWER DIRECTORATE WRIGHT LABORATORY AIR FORCE MATERIEL COMMAND WRIGHT PATTERSON AFB OH 45433-6563 WL/POOS, Attn: MORGAN 513-2552922			10. SPONSORING / MONITORING AGENCY REPORT NUMBER WL-TR-92-2098	
11. SUPPLEMENTARY NOTES				
12a. DISTRIBUTION / AVAILABILITY STATEMENT APPROVED FOR PUBLIC RELEASE; DISTRIBUTION IS UNLIMITED.			12b. DISTRIBUTION CODE	
13. ABSTRACT (Maximum 200 words) A novel design of a high-temperature axially grooved heat pipe (HP) which incorporates with thermal energy storage (TES) to mitigate pulse heat loads was presented. Phase-change material (PCM) encapsulated in cylindrical containers was used for thermal energy storage. The transient responses of the HP/TES system under two types of pulse heat loads were studied numerically. The first type is pulse heat loads applied at the heat pipe evaporator; the second type is reversed-pulse heat loads applied at the condenser. The transient response of three different HP/TES configurations were compared: (1) a heat pipe with a large empty cylinder installed in the vapor core, (2) a heat pipe with a large PCM cylinder, and (3) a heat pipe with six small PCM cylinders. It was found that the PCM is very effective in mitigating the adverse effect of pulse heat loads. The six small PCM cylinders are more efficient than the large PCM cylinder in relaxing the heat pipe temperature increase under pulse heat loads.				
14. SUBJECT TERMS HEAT PIPE, THERMAL ENERGY STORAGE, PHASE-CHANGE MATERIAL, PULSE HEAT LOAD			15. NUMBER OF PAGES 201	
			16. PRICE CODE	
17. SECURITY CLASSIFICATION OF REPORT UNCLASSIFIED	18. SECURITY CLASSIFICATION OF THIS PAGE UNCLASSIFIED	19. SECURITY CLASSIFICATION OF ABSTRACT UNCLASSIFIED	20. LIMITATION OF ABSTRACT UL	

TABLE OF CONTENTS

CHAPTER		PAGE
1	INTRODUCTION	1
	1.1 Statement of The Problem	1
	1.2 Description of The Heat Pipe	3
	1.3 Literature Review	6
2	AN IMPROVED ALTERNATING-DIRECTION-IMPLICIT METHOD	13
	2.1 Introduction	13
	2.2 Mathematical Formulation	15
	2.3 Results and Discussions	26
	2.4 Concluding Remark	36
3	NUMERICAL MODEL	38
	3.1 Heat Conduction Through Pipe Wall and Wick	41
	3.2 Melting and Solidification of PCM	47
	3.3 One-Dimensional Vapor Flow Model	55
	3.4 Coupling of Vapor Flow With Evaporation and Condensation	60
	3.5 Liquid Pressure Drop	63
4	TRANSIENT BEHAVIOR OF HP/TES SYSTEM UNDER PULSE HEAT LOADS APPLIED AT EVAPORATOR	64
	4.1 Limitations of the Heat Pipe	64
	4.2 Operation Under Normal Conditions	68
	4.3 Operation Near HP/TES Limitation	84
5	TRANSIENT BEHAVIOR OF HP/TES SYSTEM UNDER REVERSED PULSED HEAT LOADS APPLIED AT CONDENSER	93
	5.1 Description of The Problem	93
	5.2 Analytical Model	95

5.3	Results for Heat Pipes With Adiabatic Section	97
5.4	Results for Heat Pipes Without Adiabatic Section	119
6	CONCLUSIONS	133
	APPENDIX Listing of The Computer Program	137
	REFERENCES	

DTIC QUALITY INSPECTED 3

Accession For	
NTIS GRA&I	<input checked="checked" type="checkbox"/>
DTIC TAB	<input type="checkbox"/>
Unannounced	<input type="checkbox"/>
Justification	
By _____	
Distribution/	
Availability Codes	
Dist	Avail and/or Special
A-1	

LIST OF FIGURES

FIGURE	PAGE
1.1 Three different HP/TES configurations	2
1.2 Details of a conventional heat pipe	4
2.1 The f-factor modified ADI Method	22
2.2 Coordinate system: parallelepiped	27
2.3 Average temperature error for a cube with constant wall heat flux, $\tau = 2$	30
2.4 Average temperature error for a cube with constant wall heat flux, $\tau = 10$	32
2.5 Variation of average temperature error with f factor for a cube with constant wall heat flux, $\tau = 10$	33
2.6 Average temperature error for a cube with constant wall temperature, $\tau = 0.2$	35
2.7 Average temperature error for a cube with constant wall temperature, $\tau = 1.0$	37
3.1a Nodal map of the heat pipe - side view	39
3.1b Nodal map of the heat pipe - end view	40
3.2 Combined specific heat including latent heat effect across the melting temperature for a phase-change material	48
3.3 Enthalpy over a $2\Delta T$ interval across the melting temperature for a phase-change material	50
3.4 A typical location of the fusion front on the nodal map	51
3.5 Temperature distribution during melting of a one-dimensional half-space ($Ste = 1$)	56
3.6 Location of the fusion front during melting of a one-dimensional half-space ($Ste = 1$)	57
3.7 Coupling of vapor flow with evaporation and condensation	62
4.1 Operation limits for a grooved heat pipe without anything installed in the vapor core	66
4.2 Operation limits for a grooved heat pipe with an empty cylinder mounted in the vapor core	67

4.3	Transient response of heat pipes with a sudden increase in heat input from $q = 4.3$ to 10 W/cm^2	70
4.4	Definition of \dot{Q}_{in} and \dot{Q}_t	72
4.5	The ratio between \dot{Q}_t and \dot{Q}_{in} for the same operating conditions depicted in Fig 4.3	74
4.6a	Axial variation of vapor pressure at $t = 100 \text{ s}$ for the same operating conditions depicted in Fig 4.3	75
4.6b	Axial variation of vapor temperature at $t = 100 \text{ s}$ for the same operating conditions depicted in Fig 4.3	76
4.7	Comparison of results from Fig 4.3 and those obtained using a larger time step and wider grid spacings	78
4.8	Transient response of heat pipes with pulsed heat loads $q = 10 \text{ W/cm}^2$	79
4.9	Portion of PCM melted versus time for pulsed heat loads $q = 10 \text{ W/cm}^2$	80
4.10	Transient response of heat pipes with periodic pulsed heat loads $q = 10 \text{ W/cm}^2$	82
4.11	Portion of PCM melted versus time for periodic pulsed heat loads $q = 10 \text{ W/cm}^2$	83
4.12	Transient response of heat pipes with a sudden increase in heat inputs from $q = 4.3$ to 20 W/cm^2	85
4.13	Axial variation of liquid and vapor pressure at $t = 12 \text{ s}$ for the same operating conditions depicted in Fig 4.12	87
4.14	Variation of \dot{Q}_{in} for the same operating conditions depicted in Fig 4.12	88
4.15	The ratio between \dot{Q}_t and \dot{Q}_{in} for the same operating conditions depicted in Fig 4.12	90
5.1	Schematic diagram of the cooling system for a power generator	94

5.2	Transient response of heat pipe with $C_{loop} = 1000$ J/K under a reversed heat load	98
5.3	Variations of heat input and heat output of heat pipes with $C_{loop} = 1000$ J/K under a reversed heat load	100
5.4	Transient response of heat pipe with $C_{loop} = 10000$ J/K under a reversed heat load	103
5.5	Variations of heat input and heat output of heat pipes with $C_{loop} = 10000$ J/K under a reversed heat load	104
5.6	Comparison of the transient response of heat pipe without PCM predicted by lumped model and finite-difference method	106
5.7	Vapor mass flow rate of heat pipes under the same operating conditions depicted in Fig 5.2	107
5.8a	Axial variation of vapor pressure for the same operating conditions depicted in Fig 5.2	109
5.8b	Axial variation of vapor temperature for the same operating conditions depicted in Fig 5.2	110
5.9	Transient response of heat pipes under a reversed-pulse heat load	112
5.10	Portion of PCM melted versus time for heat pipes under a reversed-pulse heat load	113
5.11	Transient response of heat pipes under a periodic reversed-pulse heat load with time period of 2000 s	115
5.12	Portion of PCM melted versus time for heat pipes under a periodic reversed-pulse heat load with time period of 2000 s	116
5.13	Transient response of heat pipes under a periodic reversed-pulse heat load with time period of 600 s	117
5.14	Portion of PCM melted versus time for heat pipes under a periodic reversed-pulse heat load with time period of 600 s	118
5.15	A heat pipe without an adiabatic section operates under a partially reversed heat load	120
5.16	Transient response of heat pipes under a reversed heat load which covers 75% of condenser	121
5.17	Variations of heat input and heat output of heat pipes under a reversed heat load which covers 75% of condenser	123
5.18	Transient response of heat pipes under a reversed heat	

	load which covers 50% of condenser	124
5.19	Variations of heat input and heat output of heat pipes under a reversed heat load which covers 50% of condenser	125
5.20	Transient response of heat pipes under a reversed heat load which covers 25% of condenser	127
5.21	Variations of heat input and heat output of heat pipes under a reversed heat load which covers 25% of condenser	128
5.22	Vapor mass flow rate of heat pipes under a reversed heat load which covers 25% of condenser	129
5.23	Transient response of heat pipes under a reversed-pulse heat load which covers 25% of condenser	131
5.24	Portion of PCM melted versus time for heat pipes under a reversed-pulse heat load which covers 25% of condenser	132

NOMENCLATURE

c	specific heat
C	heat capacitance
D_h	hydraulic diameter of vapor flow
E	truncation error function, defined in Eq. (27)
f	vapor friction coefficient or f-factor
h	average convection heat transfer coefficient
H	enthalpy
I, J, K	number of nodal points in x, y and z directions
k	thermal conductivity
l_c	length of condensation region
L	half-length of parallelepiped
L'	dimensionless half-length of parallelepiped
L_c	characteristic length
\dot{m}	axial local vapor mass flow rate
Ma	Mach number
P	vapor pressure
q	surface heat flux
\bar{q}	dimensionless surface heat flux
\dot{Q}	total heat rate
r, θ, z	space coordinates
Re	axial Reynolds number of vapor flow
Re_w	radial Reynolds number of vapor flow
Ste	Stefan number of phase change material

t	time
T	temperature
U, V	temperature at intermediate time steps
U	mean axial vapor velocity
v	radial vapor velocity
x, y, z	space coordinates
X, Y, Z	dimensionless space coordinates
α	thermal diffusivity
δ^2	central difference operator
ϵ	average temperature error
γ	ratio of specific heats
λ	stability parameter, defined in Eq. (8)
ρ	density
σ	Stefan-Boltzmann constant
τ	dimensionless time or Fourier number
θ	dimensionless temperature
ξ	amplification factor of truncation error function

Superscript

n	time index
-----	------------

Subscripts

a	analytical solution
c	condenser
e	evaporator
g	power generator
hp	heat pipe
i, j, k	mesh point indices in x , y and z directions

or in r , θ and z directions

l liquid state

loop liquid sodium loop

rev reverse

s solid state

w wall surface of parallelepiped

x,y,z indicate x, y and z directions

0 initial

1,2,3 indicate x, y and z directions

CHAPTER 1

INTRODUCTION

1.1 Statement of The Problem

Future space missions will require thermal transport devices with the ability to handle transient pulse heat loads [1], especially evaporator loads with high peak-to-average power ratios and reversed-pulse heat loads at the condenser. Utilization of systems which are designed to handle pulse heat loads is impractical because of the large masses required. Incorporation of thermal energy storage (TES) into heat pipe rejection systems can be a promising method to mitigate such pulse heat loads.

Tilton et al. [2] and El-Genk et al. [3] have examined the transient response of a heat pipe under external thermal loading at the condenser. However, they did not offer any suggestion for dealing with these pulse heat loads. Some configurations to reduce the dangers of pulse heat loads have been proposed by Beam [4] and Sheffield [5], but a detailed analysis of HP/TES mitigation techniques has not been attempted. These concepts must be tested and understood so that they may be integrated successfully into an overall thermal control system design.

The surface-area-to volume ratio of the TES elements is an important parameter in the melting and solidification process of the PCM. In this research, the transient responses of three different HP/TES configurations, as shown in Fig 1.1, were tested and compared under a variety of heat load conditions.

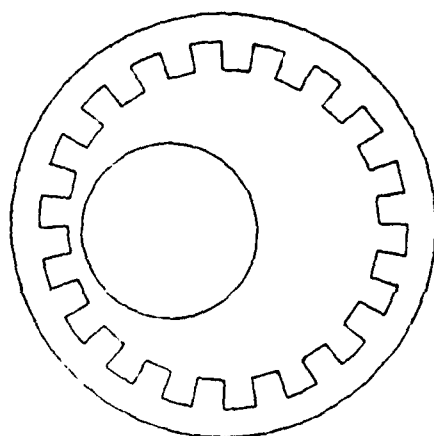
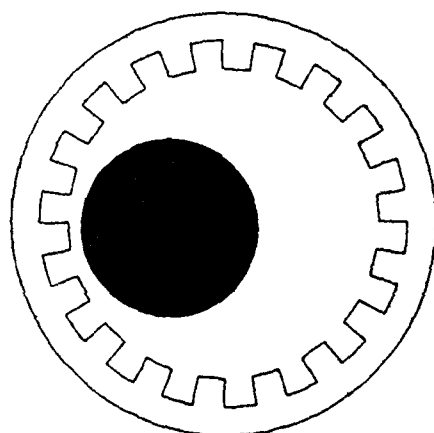
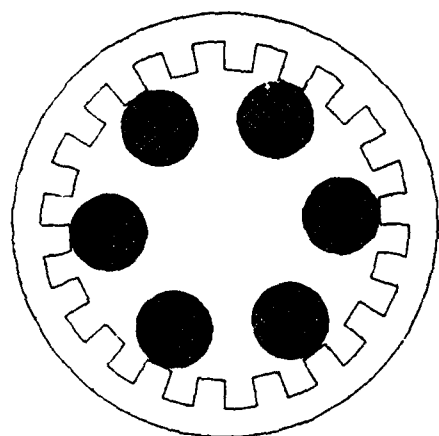
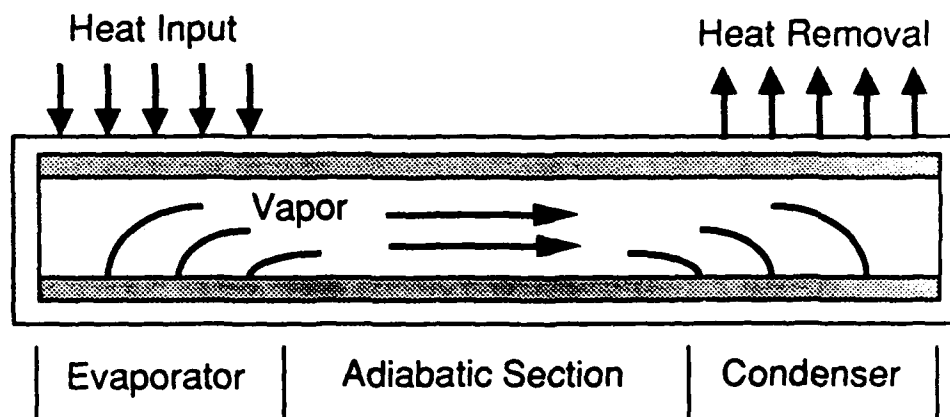


Figure 1.1 Three different HP/TES configurations

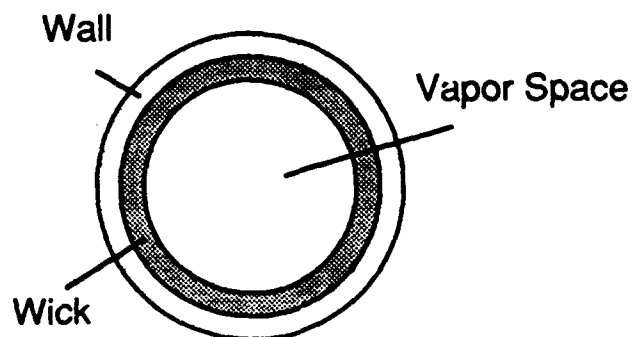
1.2 Description of The Heat Pipe

The heat pipe is an innovative device capable of transferring large quantities of heat through relatively small cross-sectional areas with very small temperature differences. Moreover, a heat pipe requires no external power input to sustain its operation. The concept behind the heat pipe was first suggested by Gauler [6] in 1942. However, it was not widely publicized until 1964 when Grover [7,8] and his colleagues at the Los Alamos Scientific Laboratory independently reinvented the concept. Grover also demonstrated the device effectiveness as a high-performance heat transmission mechanism, coined the name "heat pipe," and developed several applications for such systems. Since then, the remarkable properties of the heat pipe have become appreciated, and serious developmental work is still taking place.

A heat pipe consists of a closed tube or chamber with various shapes whose inner surface is lined with a porous capillary wick as shown in Fig 1.2. Wire screen, fiber glass, porous metal, and woven cloth have all been used as the capillary wick. Narrow grooves, cut lengthwise in the interior pipe wall, can also serve as a capillary wick structure. The wick is saturated with the liquid phase of a working fluid and the remaining volume of the tube contains the working fluid vapor phase. Heat applied at the evaporator by an external source vaporizes the working fluid in that section. The resulting difference in pressure drives vapor from the evaporator to the condenser, where it condenses releasing the latent heat of vaporization to a heat sink in that section of the pipe. Depletion of liquid by evaporation causes the liquid-vapor interface in the evaporator to enter into the wick surface



Side View



End View

Figure 1.2 Details of a conventional heat pipe

and a capillary pressure is developed there. This capillary pressure pumps the condensed liquid back to the evaporator for reevaporation. Thus, the heat pipe can continuously transport the latent heat of vaporization from the evaporator section to the condenser section without drying out the wick. This process will continue as long as the flow passage for the working fluid is not blocked and a sufficient capillary pressure is maintained. Heat pipes may be operated over a broad range of temperatures by choosing an appropriate working fluid.

The amount of heat that can be transported by the latent heat of vaporization is usually several orders of magnitude larger than that which can be transported as sensible heat in a conventional convective system. The heat pipe can, therefore, transport a large amount of heat with only a small unit size. Because only a very small temperature drop occurs in the vapor flow, heat pipes have thermal characteristics orders of magnitude better than any known solid.

However, unlike solid conductors, the heat pipe characteristics are dependent not only upon size, shape, and material but also upon construction, working fluid, and heat transfer rate. Moreover, heat pipes operate under heat transfer limitations such as the sonic limit, capillary limit, entrainment limit, and boiling limit. When any of these limitations is encountered, the capillary wick structure may dry out, leading to failure of the heat pipe.

In this research, a stainless steel grooved heat pipe using sodium as the working fluid was studied. Grooved heat pipes, which use narrow grooves as the capillary wick structure, have been used quite successfully in practice. The advantages of a grooved heat pipe are its low capillary liquid flow resistance, high reliability, and ease of

fabrication. However, the rather large nominal diameter of the grooves makes both the capillary limit and entrainment limit quite low. Vinz and Busse [9] and Barantsevich et al. [10] showed experimentally that if the grooves in the evaporator section are wrapped with layers of fine wick mesh, the capillary limit and entrainment limit can be improved significantly while maintaining low capillary liquid flow resistance.

1.3 Literature Review

Analysis of transient heat pipe behavior has been the subject of many recent studies [11-16]. Chang and Colwell's [11] model for low temperature heat pipes neglects the hydrodynamics of the vapor flow and, therefore, cannot predict the vapor pressure and temperature variations along the heat pipe. Kuramae [12] and Tilton et al. [13] did not include vapor flow in their models. Bowman et al. [14] and Jang et al. [15] applied too complicated vapor flow models which lead to lengthy computation time and only represent the earliest stages of heat pipe transient behavior effectively. The model developed by Seo et al. [16] is impressive. However, this two-dimensional (axial and radial) model cannot predict the transient behavior of a heat pipe with angularly nonsymmetric boundary conditions. It would be desirable to assimilate all of the current works by incorporating the strongest features of each previous approach into a state-of-the-art model.

A transient three-dimensional numerical method is desired to model the heat conduction through the heat pipe wall and wicks, including the liquid in the grooves. Thibault [17] gave a comparison of nine

numerical schemes for the solution of the transient three-dimensional heat diffusion equation. The major drawback of the pure explicit scheme is that the stability criterion $\Delta\tau/(\Delta X)^2$ is very small and should not exceed 0.5. The computations may become prohibitively expensive because of the need to employ very small time steps. On the other hand, the pure implicit scheme cannot be used efficiently for the solution of multidimensional problems. In three dimensions it necessitates the solution of large sparse matrices, which requires extremely long computation time. After considering the relative accuracy, computation time, and the computer core storage requirement, Thibault concluded that alternating-direction-implicit (ADI) finite-difference methods offered the best compromise. The ADI methods only require solving tridiagonal matrices, so they have a tremendous advantage in computation time compared to the pure implicit method. Chang and Colwell [11] and Jang et al. [15] used two-dimensional ADI methods to model heat pipe transients with great success. The conventional, two-dimensional ADI method is unconditionally stable. However, when extended to three dimensions, the conventional ADI method is conditionally stable, and very small time steps are required to ensure convergence and stability. In heat pipe modeling, a small Δr is needed due to the slender geometry of the heat pipe, and only a very small time step Δt (about 0.001s) can be used with the conventional three-dimensional ADI method. Chang et al. [18] developed a new three-dimensional ADI method by modifying the conventional ADI method with an f-factor ($0 < f < 1$). This modification allows the time step to be increased by about 2 orders of magnitude without significantly compromising the accuracy of the numerical solution. They also showed that this new ADI method yields much higher

accuracy than the well-known Douglas' [19] and Brian's [20] ADI methods. Details of this new ADI method, which was used to model the heat conduction through the heat pipe wall and wicks, will be introduced in Chapter 2.

In the numerical solution of heat conduction problems with phase change (Stefan's problem) by finite differences, enthalpy methods [21-25] or heat capacity methods [26-30] can be used. The former methods require either an explicit procedure which may lead to convergence problems, or iteration at each time step if an implicit procedure is used. The latter methods are subject to the problem of jumping the latent heat peak, necessitating the use of very small time steps to avoid underprediction of the phase change time. Recently, Hsiao [31,32] proposed a new finite-difference method for Stefan's problem. In his scheme, the equivalent heat capacity at a node is a function of the temperature at that node and all the surrounding nodes. Hsiao concluded that his method can avoid the problem of jumping the latent heat peak and allows the use of a relatively large time step. Hsiao's method was tested, but a large energy balance error was found. Pham [33,34,35] suggested a simple method which includes features from both the enthalpy and heat capacity methods. Comparing this method with other existing methods for test problems with exact solutions, Pham pointed out that most of the methods agree to within 0.2% with the analytical result, except for Hsiao's method which yielded results with up to 22% error. The low accuracy of Hsiao's method could be due to its ambiguous theoretical basis. Pham also concluded that his method is much faster than other methods. However, Pham's method has a singularity problem in finding the equivalent specific heat. In this

research, we adopted the best features of Pham's method and made some modifications to improve on its weak points. Compared with analytical solutions, the present method for melting and solidification was found to have very good accuracy without the singularity problem of Pham's method.

The vapor flow in the evaporator of a heat pipe is dynamically similar to pipe flow with blowing through a porous wall, while the condenser section is analogous to flow with suction. The axial vapor mass flow increases along the length of the evaporator region to a maximum value at the end of the evaporator; it will then decrease along the condenser region. The behavior of the vapor flow in a heat pipe is also similar to that of a gas flowing through a converging-diverging nozzle. In the heat pipe the area remains constant but the mass flow varies. In a nozzle, the mass flow is constant but the cross-sectional area is changed. There are many theoretical investigations of heat pipe vapor dynamics [36-45]. Most of this research work focuses on the vapor flow itself instead of studying the vapor flow phenomena coupled with heat pipe transients. The majority of these vapor flow models are very complicated and impractical because their calculations require prohibitively large amount of computer time. Bowman [46] reached a very important conclusion that since the response time of the vapor dynamics is very short compared to the heat transfer response time of the heat pipe wall and wicks, the vapor flow can be modeled as a quasi-steady process. He also studied the compressible vapor dynamics in a heat pipe experimentally using air flowing in a porous tube with blowing and suction along the wall. He modeled the vapor flow using a numerical solution to the axisymmetric, unsteady Navier-Stokes equations and a

steady one-dimensional solution technique. Bowman concluded that it is adequate to treat the vapor flow as steady and one-dimensional, and he also provided suitable vapor pressure drop correlations. In our research, this steady, one-dimensional vapor flow model was used and coupled with the evaporation and condensation in the heat pipe.

The transient response of a heat pipe under normal operating conditions is mainly controlled by its thermal capacity, conductance, and vapor temperature drop, and is only slightly influenced by the liquid dynamics. However, liquid dynamics become very significant when dryout and rewetting occur in the wick. The dryout phenomena can cause a dramatic temperature increase at the evaporator section and may affect the overall heat transport device. To predict dryout of the wick, a detailed liquid flow model in the wick is needed. Beam [47] and Ambrose [48] et al. investigated the transient behavior of the liquid flow in a heat pipe wick using a one-dimensional flat-front model. Their models for the liquid flow utilized a simplified, lumped-parameter solution to the energy equation to predict the temperature response and determine the mass flux of vapor out of the evaporator region. Both Beam [47] and Chang and Colwell [11] concluded that the transient response of the working fluid in screen wicks is so fast that acceleration terms in the momentum equation for the liquid are negligible. However, dryout depends on the heated zone and the instantaneous local saturation. Thus, if dryout is to be accurately predicted, the temporal dependence of the saturation distribution must be taken into account. Ambrose [49] developed a technique utilizing X-ray radiography to measure liquid distribution in the porous wick structures of a heat pipe with beryllium walls. He also presented a new transient liquid flow model to predict

the continuous saturation distribution in the wick structure. The measured saturation distributions compared favorably with those predicted by the liquid model. However, solution of this new transient liquid flow model requires knowledge of the saturation dependence of the capillary flow properties, which can only be determined by experiment. Kamotani [50] and Hwangbo et al. [51] developed two very similar liquid flow models for a grooved heat pipe. Their models can predict the variations of liquid meniscus contact angle and liquid pressure variation along the heat pipe. However, they assumed the liquid meniscus is always attached to the top of the groove side walls. According to the experimental verifications given by Ogushi et al. [52], this assumption is not correct. They also ignored the effect of vapor pressure variation on the liquid meniscus contact angle. This is not a good simplification for high temperature heat pipes where the vapor pressure drop is always the dominant one. A complete capillary liquid flow model for a screen covered groove like the one we recommended in this research is urgently needed in the near future to predict the dryout and rewetting behaviors of a heat pipe with this type of wick. A good capillary liquid flow model should include the effect of vapor pressure changes on the liquid meniscus contact angle and also be able to predict the saturation distribution analytically.

Kamotani [53] analyzed the thermal behavior of the condenser section of a heat pipe with axial rectangular grooves. Some of the vapor condensation occurs on the land areas between grooves. The liquid forms a thin film on the land surface, and heat is removed from the vapor through the liquid film. When the heat pipe is operating, the liquid in each land area is drawn continuously into the grooves by

capillary force and then transported to the evaporator section along the grooves. Because of viscous drag, liquid flow in the grooves suffers a pressure drop, and consequently the curvature of the liquid free surface varies along the path. This meniscus variation will influence the motion of the liquid film on the land and thus the condensation rate. Kamotani claimed that the thickness of the liquid film on the land surface is only on the order of several microns. In this research, we neglected the thermal resistance of the condensed thin liquid film because it is miniscule when compared with the resistance of the heat pipe wall.

CHAPTER 2

AN IMPROVED ALTERNATING-DIRECTION-IMPLICIT METHOD

The conventional three-dimensional alternating-direction implicit (ADI) method is modified by introducing an f -factor ($0 < f < 1$). This modification allows the time-step limit be increased by a factor of $1/f$ with the solutions remaining stable and retaining high accuracy. This new method is tested for two different boundary conditions: a constant heat flux and a sudden heating of the surface to a constant temperature. In addition, it is compared with the popular Brian and Douglas ADI methods. Results show that the new ADI method has higher accuracy and requires less computer storage than the Brian and Douglas ADI methods.

2.1 Introduction

The diffusion of heat in solids has numerous applications in various branches of science and engineering. Generally, there are two different approaches to deal with this type of problems: analytical and numerical approaches. The analytical methods are usually only applicable to linear problems with simple geometries. On the contrary, the numerical methods are useful for handling practical problems involving nonlinearities, complex geometries and/or complicated boundary conditions.

Thibault [17] gave a comparison of nine numerical schemes for the solution of the transient three-dimensional heat diffusion equation.

Considering the relative accuracy, the computation time, and the computer core storage requirement, he recommended that alternating-direction implicit (ADI) finite-difference methods are among the most preferred methods. The conventional two-dimensional ADI method was introduced by Peaceman and Rachford [54] in 1955. The advantage of the ADI method is that only tridiagonal matrices need to be solved. However, when extended to three dimensions, the conventional ADI method is conditionally stable and very small time steps are required to ensure convergence and stability. Other forms of the ADI method include the Douglas method [19] and the Brian method [20]. Douglas and Brian ADI methods are unconditionally stable; they possess the advantages of the implicit scheme with no limitation on the size of the time step. However, Thibault [17] pointed out that these two unconditionally stable ADI methods cannot retain good accuracy if the time step is more than 2 times larger than the time-step limit required for the conventional ADI method.

In this research, the conventional three-dimensional ADI method is modified by an f -factor ($0 < f < 1$). A very important characteristic of this modification is that it is consistent with physical considerations, and is not just based on mathematical manipulations. This modification allows the time-step limit to be increased by approximately a factor of $1/f$ without compromising significantly on the accuracy of the numerical solution. This new ADI method is presented and compared with the Brian and Douglas ADI methods for two cases where analytical solutions are available. Compared with the Brian and Douglas methods, this new ADI method has higher accuracy when large time steps are used. Also, the present method requires less computer storage.

2.2 Mathematical Formulation

First, we will look at of the formulations of the existing three-dimensional ADI methods: conventional, Brian and Douglas methods. Then, the proposed new ADI method designed to overcome the shortcomings of these existing ADI methods will be introduced.

The differential equations for the three-dimensional heat diffusion equation can be written as

$$\frac{1}{a} \frac{\partial T}{\partial t} = \frac{\partial^2 T}{\partial x^2} + \frac{\partial^2 T}{\partial y^2} + \frac{\partial^2 T}{\partial z^2} \quad (1)$$

Introducing dimensionless parameters:

$$X = \frac{x}{L_c}, \quad Y = \frac{y}{L_c}, \quad Z = \frac{z}{L_c}$$
$$\theta = \frac{T}{T_0}, \quad \tau = \frac{at}{L_c^2}$$

Eq. (1) becomes

$$\frac{\partial \theta}{\partial \tau} = \frac{\partial^2 \theta}{\partial X^2} + \frac{\partial^2 \theta}{\partial Y^2} + \frac{\partial^2 \theta}{\partial Z^2} \quad (2)$$

Conventional ADI Method

In the conventional ADI method, the heat diffusion equation is solved implicitly in turn in the three coordinate directions for one-third of the time increment each [55]. The basic finite-difference

equations for each of the three one-third time steps can be expressed as:

$$\frac{U_{i,j,k} - \theta_{i,j,k}^n}{\Delta\tau/3} = \delta_x^2 U_{i,j,k} + \delta_y^2 \theta_{i,j,k}^n + \delta_z^2 \theta_{i,j,k}^n \quad (3)$$

$$\frac{V_{i,j,k} - U_{i,j,k}}{\Delta\tau/3} = \delta_x^2 U_{i,j,k} + \delta_y^2 V_{i,j,k} + \delta_z^2 U_{i,j,k} \quad (4)$$

$$\frac{\theta_{i,j,k}^{n+1} - V_{i,j,k}}{\Delta\tau/3} = \delta_x^2 V_{i,j,k} + \delta_y^2 V_{i,j,k} + \delta_z^2 \theta_{i,j,k}^{n+1} \quad (5)$$

For convenience of analysis, we let $\Delta X = \Delta Y = \Delta Z$. After rearranging Eq. (3), it becomes:

$$\begin{aligned} & -U_{i-1,j,k} + \left[\frac{3(\Delta X)^2}{\Delta\tau} + 2 \right] U_{i,j,k} - U_{i+1,j,k} \\ & = \left[\frac{3(\Delta X)^2}{\Delta\tau} - 4 \right] \theta_{i,j,k}^n + \theta_{i,j-1,k}^n + \theta_{i,j+1,k}^n + \theta_{i,j,k-1}^n + \theta_{i,j,k+1}^n \quad (6) \end{aligned}$$

Similar equations can be easily derived from Eqs. (4) and (5) for the y- and z- directions. Physically, an increase in the central nodal temperature or an increase in any one of the neighboring nodal temperatures at the old time step should, with other conditions remaining unchanged, lead to an increase in the central nodal temperature at the next 1/3 time step. This implies that all the coefficients on the right-hand side of Eq. (6) must have the same sign (positive) as the coefficient of $U_{i,j,k}$. In other words, negative coefficients on the right-hand side of Eq. (6) make the equations physically unrealistic and may lead to low accuracy [56]. Same

statements can be made regarding to the equations for the y- and z- directions.

On the right-hand side of Eq. (6), only the coefficient for $\theta_{i,j,k}^n$ could be negative if the time step $\Delta\tau$ is large. In order to have positive coefficient for $\theta_{i,j,k}^n$, it is required that:

$$\frac{\Delta\tau}{(\Delta X)^2} < 0.75 \quad (7)$$

Since $\Delta X = \Delta Y = \Delta Z$, the equations for the y- and z- directions require the same condition in Eq. (7) to hold. The other important thing we need to consider is the stability problem. We define the stability parameter λ as follows:

$$\lambda = \frac{\Delta\tau}{(\Delta X)^2} \quad (8)$$

The stability criterion for the conventional three-dimensional ADI method is [55]:

$$\lambda \leq 1.5 \quad (9)$$

Equation (7) is the condition for the solution of the conventional three-dimensional ADI method to be physically realistic and have good accuracy. Equation (9) is the criterion for the solution to be stable. The main disadvantage of the conventional ADI method is that it is conditionally stable and very small time step is required.

Brian's ADI Method

The method proposed by Brian [20] is similar to the conventional ADI method. However, the successive approximations of the temperature are calculated at the half-time step. The basic equations of Brian's ADI method are given as follow:

$$\frac{U_{i,j,k} - \theta_{i,j,k}^n}{\Delta\tau/2} = \delta_x^2 U_{i,j,k} + \delta_y^2 \theta_{i,j,k}^n + \delta_z^2 \theta_{i,j,k}^n \quad (10)$$

$$\frac{V_{i,j,k} - \theta_{i,j,k}^n}{\Delta\tau/2} = \delta_x^2 U_{i,j,k} + \delta_y^2 V_{i,j,k} + \delta_z^2 \theta_{i,j,k}^n \quad (11)$$

$$\frac{\theta_{i,j,k}^{n+1} - V_{i,j,k}}{\Delta\tau/2} = \delta_x^2 U_{i,j,k} + \delta_y^2 V_{i,j,k} + \delta_z^2 \theta_{i,j,k}^{n+1} \quad (12)$$

Subtracting Eq. (10) from Eq. (11), we have:

$$\frac{V_{i,j,k} - U_{i,j,k}}{\Delta\tau/2} = \delta_y^2 V_{i,j,k} - \delta_y^2 \theta_{i,j,k}^n \quad (11a)$$

Subtracting Eq. (11) from Eq. (12), we have:

$$\frac{\theta_{i,j,k}^{n+1} - \theta_{i,j,k}^n - 2V_{i,j,k}}{\Delta\tau/2} = \delta_z^2 \theta_{i,j,k}^{n+1} - \delta_z^2 \theta_{i,j,k}^n \quad (12a)$$

Eqs. (10), (11a) and (12a) are the simplified equations suggested by Brian. After rearranging these equations, the following equations can be obtained:

$$\begin{aligned}
& - U_{i-1,j,k} + \left[\frac{2(\Delta X)^2}{\Delta \tau} + 2 \right] U_{i,j,k} - U_{i+1,j,k} \\
& = \left[\frac{2(\Delta X)^2}{\Delta \tau} - 4 \right] \theta_{i,j,k}^n + \theta_{i,j-1,k}^n + \theta_{i,j+1,k}^n + \theta_{i,j,k-1}^n + \theta_{i,j,k+1}^n \quad (13)
\end{aligned}$$

$$\begin{aligned}
& - V_{i,j-1,k} + \left[\frac{2(\Delta Y)^2}{\Delta \tau} + 2 \right] V_{i,j,k} - V_{i,j+1,k} \\
& = \left[\frac{2(\Delta Y)^2}{\Delta \tau} \right] U_{i,j,k} + 2\theta_{i,j,k}^n - \theta_{i,j-1,k}^n - \theta_{i,j+1,k}^n \quad (14)
\end{aligned}$$

$$\begin{aligned}
& - \theta_{i,j,k-1}^{n+1} + \left[\frac{2(\Delta Z)^2}{\Delta \tau} + 2 \right] \theta_{i,j,k}^{n+1} - \theta_{i,j,k+1}^{n+1} \\
& = \left[\frac{4(\Delta Z)^2}{\Delta \tau} \right] V_{i,j,k} + \left[-\frac{2(\Delta Z)^2}{\Delta \tau} + 2 \right] \theta_{i,j,k}^n - \theta_{i,j,k-1}^n - \theta_{i,j,k+1}^n \quad (15)
\end{aligned}$$

Brian showed that his scheme is unconditionally stable. However, there also exist negative coefficients on the right-hand sides of the discretization equations (13)-(15). As we mentioned earlier, these negative coefficients are physically unrealistic.

Douglas ADI method

Another unconditionally stable three-dimensional ADI method was presented by Douglas [19]. The algorithm is given by the following three equations:

$$\frac{U_{i,j,k} - \theta_{i,j,k}^n}{\Delta \tau} = \frac{1}{2} \delta_x^2 [U_{i,j,k} + \theta_{i,j,k}^n] + \delta_y^2 \theta_{i,j,k}^n + \delta_z^2 \theta_{i,j,k}^n \quad (16)$$

$$\begin{aligned}
\frac{V_{i,j,k} - \theta_{i,j,k}^n}{\Delta \tau} &= \frac{1}{2} \delta_x^2 [U_{i,j,k} + \theta_{i,j,k}^n] + \frac{1}{2} \delta_y^2 [V_{i,j,k} + \theta_{i,j,k}^n] \\
&\quad + \delta_z^2 \theta_{i,j,k}^n \quad (17)
\end{aligned}$$

$$\frac{\theta_{i,j,k}^{n+1} - \theta_{i,j,k}^n}{\Delta\tau} = \frac{1}{2} \delta_x^2 [U_{i,j,k} + \theta_{i,j,k}^n] + \frac{1}{2} \delta_y^2 [V_{i,j,k} + \theta_{i,j,k}^n] + \frac{1}{2} \delta_z^2 [\theta_{i,j,k}^{n+1} + \theta_{i,j,k}^n] \quad (18)$$

Subtracting Eq. (16) from Eq. (17), we have:

$$\frac{V_{i,j,k} - U_{i,j,k}}{\Delta\tau} = \frac{1}{2} \delta_y^2 [V_{i,j,k} - \theta_{i,j,k}^n] \quad (17a)$$

Subtracting Eq. (17) from Eq. (18), we have:

$$\frac{\theta_{i,j,k}^{n+1} - V_{i,j,k}}{\Delta\tau} = \frac{1}{2} \delta_z^2 [\theta_{i,j,k}^{n+1} - \theta_{i,j,k}^n] \quad (18a)$$

Equations (16), (17a) and (18a) are the simplified equations and they can be rearranged as:

$$\begin{aligned} & -0.5 U_{i-1,j,k} + \left[\frac{(\Delta X)^2}{\Delta\tau} + 1 \right] U_{i,j,k} - 0.5 U_{i+1,j,k} \\ & = \left[\frac{(\Delta X)^2}{\Delta\tau} - 5 \right] \theta_{i,j,k}^n + 0.5 \theta_{i-1,j,k}^n + 0.5 \theta_{i+1,j,k}^n \\ & + \theta_{i,j-1,k}^n + \theta_{i,j+1,k}^n + \theta_{i,j,k-1}^n + \theta_{i,j,k+1}^n \end{aligned} \quad (19)$$

$$\begin{aligned} & -0.5 V_{i,j-1,k} + \left[\frac{(\Delta Y)^2}{\Delta\tau} + 1 \right] V_{i,j,k} - 0.5 V_{i,j+1,k} \\ & = \left[\frac{(\Delta Y)^2}{\Delta\tau} \right] U_{i,j,k} + \theta_{i,j,k}^n - 0.5 \theta_{i,j-1,k}^n - 0.5 \theta_{i,j+1,k}^n \end{aligned} \quad (20)$$

$$\begin{aligned} & -0.5 \theta_{i,j,k-1}^{n+1} + \left[\frac{(\Delta Z)^2}{\Delta\tau} + 1 \right] \theta_{i,j,k}^{n+1} - 0.5 \theta_{i,j,k+1}^{n+1} \\ & = \left[\frac{(\Delta Z)^2}{\Delta\tau} \right] V_{i,j,k} + \theta_{i,j,k}^n - 0.5 \theta_{i,j,k-1}^n - 0.5 \theta_{i,j,k+1}^n \end{aligned} \quad (21)$$

The unconditional stability of this algorithm was proved by Douglas [19]. However, as in the Brian ADI method, the Douglas ADI method has negative coefficients on the right-hand sides of the discretization equations (19)-(21).

New ADI Method

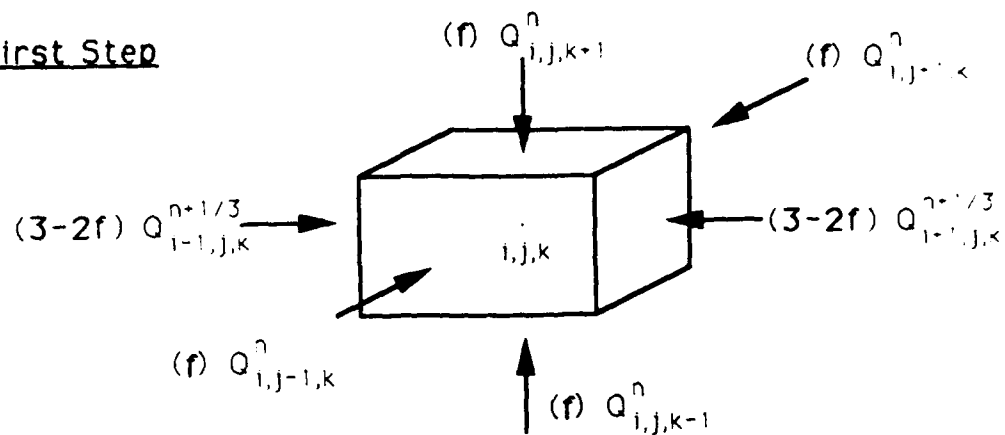
As we have seen above, the three existing ADI methods all have shortcomings. The conventional ADI method is conditionally stable and very small time steps are required to satisfy the stability criterion. All three ADI methods have a common problem: negative coefficients in their discretization equations which are physically unrealistic.

In light of the above observation, an improved ADI method is proposed. The conventional three-dimensional ADI method is modified by introducing an f -factor ($0 < f < 1$). Consider a control volume as shown in Fig 2.1, the heat fluxes from the directions in which the equation is implicit are multiplied by a factor $(3-2f)$ and the heat fluxes from the remaining four directions are multiplied by a factor f . As we can see, the total heat flux counted in each direction through a full time step remains unchanged. The finite-difference Eqs. (3)-(5) of the conventional ADI method are modified by a f -factor and become the following equations:

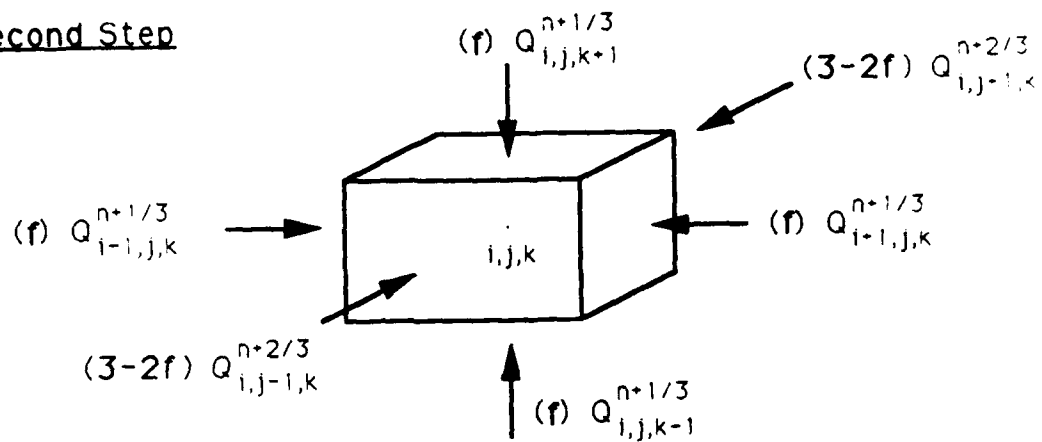
$$\frac{U_{i,j,k} - \theta_{i,j,k}^n}{\Delta\tau/3} = (3-2f) \delta_x^2 U_{i,j,k} + f \delta_y^2 \theta_{i,j,k}^n + f \delta_z^2 \theta_{i,j,k}^n \quad (22)$$

$$\frac{V_{i,j,k} - U_{i,j,k}}{\Delta\tau/3} = f \delta_x^2 U_{i,j,k} + (3-2f) \delta_y^2 V_{i,j,k} + f \delta_z^2 U_{i,j,k} \quad (23)$$

First Step



Second Step



Third Step

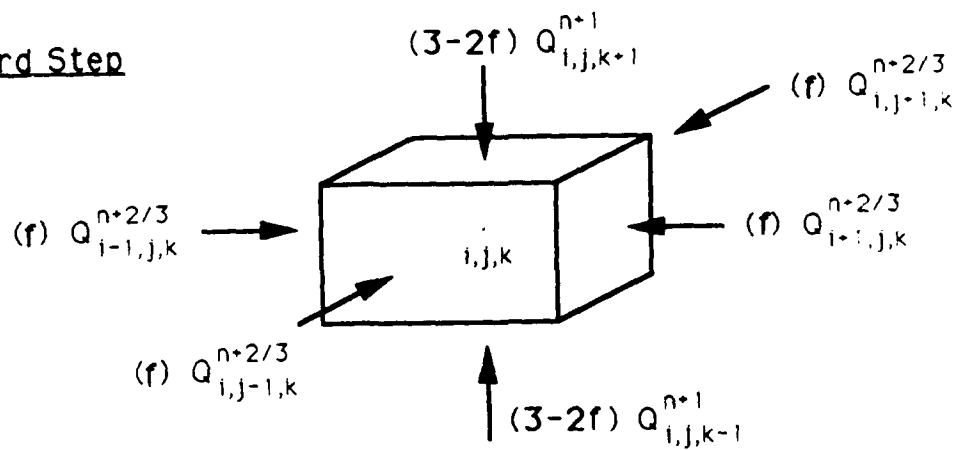


Figure 2.1 The f-factor modified ADI Method

$$\frac{\theta_{i,j,k}^{n+1} - \theta_{i,j,k}^n}{\Delta\tau/3} = f \delta_x^2 \theta_{i,j,k}^n + f \delta_y^2 \theta_{i,j,k}^n + (3-2f) \delta_z^2 \theta_{i,j,k}^{n+1} \quad (24)$$

After rearranging Eq. (22), the following discretization equation can be obtained:

$$\begin{aligned} & - (3-2f) \theta_{i-1,j,k}^n + \left[\frac{3(\Delta X)^2}{\Delta\tau} + 2(3-2f) \right] \theta_{i,j,k}^n - (3-2f) \theta_{i+1,j,k}^n \\ & = \left[\frac{3(\Delta X)^2}{\Delta\tau} - 4f \right] \theta_{i,j,k}^n \\ & + f \theta_{i,j-1,k}^n + f \theta_{i,j+1,k}^n + f \theta_{i,j,k-1}^n + f \theta_{i,j,k+1}^n \end{aligned} \quad (25)$$

Similar equations can be easily derived from Eqs. (23) and (24) for the y- and z- directions. On the right-hand side of Eq. (25), only the coefficient for central nodal temperatures at previous time step could be negative. To avoid it from becoming negative, we require:

$$\frac{\Delta\tau}{(\Delta X)^2} < \frac{0.75}{f} \quad (26)$$

The stability criterion can be determined by the Von Neumann method. Assuming that there exists an error function $E_{p,q,r,n}$ at each nodal point in the following form [57]:

$$E_{p,q,r,n} = \exp(i\beta_1 p \Delta X) \exp(i\beta_2 q \Delta Y) \exp(i\beta_3 r \Delta Z) \xi^n \quad (27)$$

where the parameter ξ is the amplification factor and $n = \tau/\Delta\tau$, the error will be bounded provided that:

$$|\xi| \leq 1$$

This is the condition for the solution to be stable. It can be shown for these linear problems with constant coefficients that the error function $E_{p,q,r,n}$ also satisfies the finite-difference equation (25) and two similar equations for y- and z- directions. With $\Delta X = \Delta Y = \Delta Z$, substitution of $E_{p,q,r,n}$ from Eq. (27) into these equations gives:

$$\xi_1 = \frac{3/\lambda - 4(f)\sin^2(\beta_2\Delta X/2) - 4(f)\sin^2(\beta_3\Delta X/2)}{3/\lambda + 4(g)\sin^2(\beta_1\Delta X/2)} \quad (28)$$

$$\xi_2 = \frac{3/\lambda - 4(f)\sin^2(\beta_1\Delta X/2) - 4(f)\sin^2(\beta_3\Delta X/2)}{3/\lambda + 4(g)\sin^2(\beta_2\Delta X/2)} \quad (29)$$

$$\xi_3 = \frac{3/\lambda - 4(f)\sin^2(\beta_1\Delta X/2) - 4(f)\sin^2(\beta_2\Delta X/2)}{3/\lambda + 4(g)\sin^2(\beta_3\Delta X/2)} \quad (30)$$

where $g = 3 - 2f$.

These ξ_1 , ξ_2 and ξ_3 are the amplification factors for the finite-difference equations for the x-, y- and z- directions, respectively. Since these equations are used alternately, the stability condition should be:

$$|\xi_1\xi_2\xi_3| \leq 1$$

Rearranging $\xi_1\xi_2\xi_3$ as follows:,

$$\begin{aligned}
\xi_1 \xi_2 \xi_3 &= \left[\frac{3/\lambda - 4(f) \sin^2(\beta_2 \Delta X/2) - 4(f) \sin^2(\beta_3 \Delta X/2)}{3/\lambda + 4(g) \sin^2(\beta_2 \Delta X/2)} \right] \\
&\times \left[\frac{3/\lambda - 4(f) \sin^2(\beta_1 \Delta X/2) - 4(f) \sin^2(\beta_3 \Delta X/2)}{3/\lambda + 4(g) \sin^2(\beta_3 \Delta X/2)} \right] \\
&\times \left[\frac{3/\lambda - 4(f) \sin^2(\beta_1 \Delta X/2) - 4(f) \sin^2(\beta_2 \Delta X/2)}{3/\lambda + 4(g) \sin^2(\beta_1 \Delta X/2)} \right] \\
&= [a] \times [b] \times [c]
\end{aligned}$$

the stability condition can be written as:

$$|a| |b| |c| \leq 1$$

The stability criterion can be obtained from either one of the following three conditions:

$$|a| \leq 1, |b| \leq 1 \text{ or } |c| \leq 1$$

For the condition $|a| \leq 1$, since the value of a is always less than unity, we need only to consider the condition $a \geq -1$. This leads to:

$$\lambda \leq \frac{1.5}{(f) \sin^2(\beta_3 \Delta X/2) - (g-f) \sin^2(\beta_2 \Delta X/2)}$$

It should be mentioned here that the parameter λ defined in Eq. (8) is always positive. The right-hand side of the above equation has a minimum value when $\sin^2(\beta_3 \Delta X/2) = 1$ and $\sin^2(\beta_2 \Delta X/2) = 0$. So, the stability criterion becomes:

$$\lambda \leq \frac{1.5}{f} \quad (31)$$

Comparing Eqs. (26) and (31) with Eqs. (7) and (9), the time-step limit for the conventional ADI method can now be increased by a factor $1/f$ by using this new ADI method. The computational results which will be discussed later show that this modification allows the time-step limit to be increased by 2 orders of magnitude with $f=0.01$ and the solutions still remain stable with high accuracy.

Also, it should be mentioned, this new ADI method only requires two-thirds of the computer storage compared to the Brian or Douglas method. This is because only the temperatures at one intermediate time step need to be stored.

2.3 Results and Discussions

To validate the present new ADI method, the finite-difference solutions obtained are tested for a simple geometry with two different boundary conditions: a constant surface heat flux and a sudden heating of the surface to a constant temperature. In addition, it is compared with the Brian and Douglas methods.

Consider a parallelepiped ($-L_1 \leq x \leq L_1$, $-L_2 \leq y \leq L_2$, $-L_3 \leq z \leq L_3$), shown in Fig 2.2, having constant thermophysical properties and initially at a uniform temperature $\theta_0=1.0$. At time $\tau>0$, the parallelepiped is allowed to have heat flow through its boundaries. To obtain the temperature distribution within the parallelepiped, equation (2) must be solved with the following initial conditions:

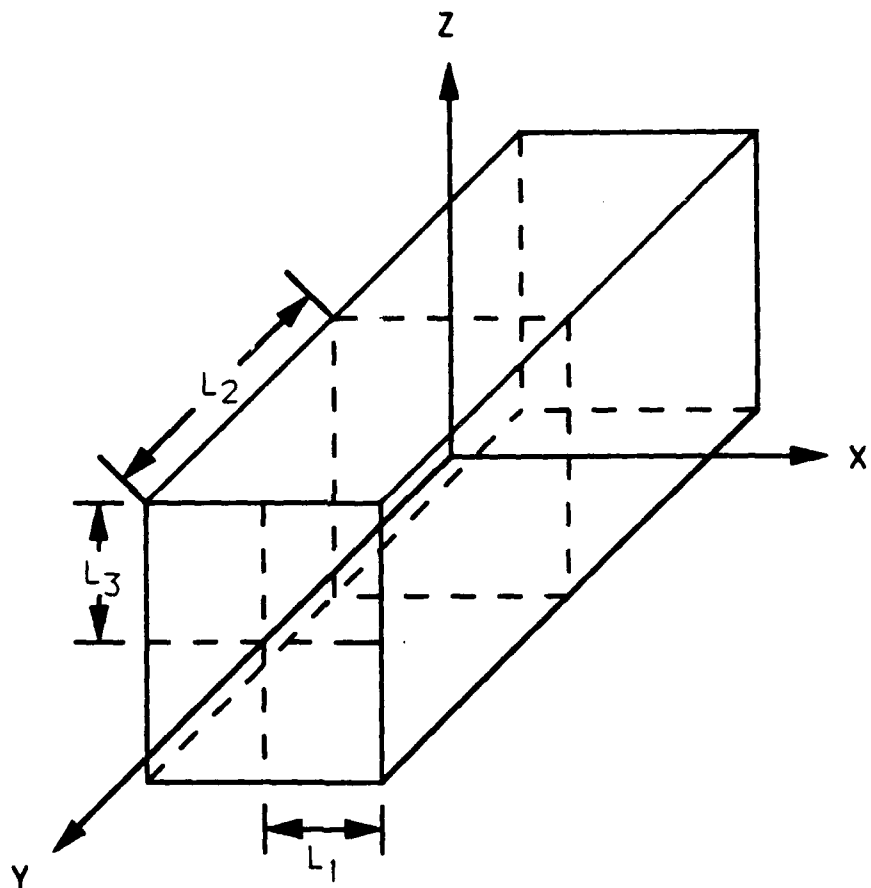


Figure 2.2 Coordinate system: parallelepiped

$$\text{at } \tau = 0, \quad \theta = 1 \quad \text{for} \quad \begin{array}{l} -1 \leq X \leq 1 \\ -L'_2 \leq Y \leq L'_2 \\ -L'_3 \leq Z \leq L'_3 \end{array} \quad (32)$$

where L_1 is chosen as the characteristic length L_c , $L'_2 = L_2/L_1$, and $L'_3 = L_3/L_1$.

Because of symmetry, only the region $0 \leq X \leq 1$, $0 \leq Y \leq L'_2$, and $0 \leq Z \leq L'_3$ need to be solved. The boundary conditions are:

$$\tau > 0 \quad \frac{\partial \theta}{\partial X} \Big|_{X=0} = \frac{\partial \theta}{\partial Y} \Big|_{Y=0} = \frac{\partial \theta}{\partial Z} \Big|_{Z=0} = 0 \quad (33a)$$

$$\frac{\partial \theta}{\partial X} \Big|_{X=1} = \frac{\partial \theta}{\partial Y} \Big|_{Y=L'_2} = \frac{\partial \theta}{\partial Z} \Big|_{Z=L'_3} = \bar{q}_w \quad (33b)$$

$$\text{or} \quad \theta \Big|_{X=1} = \theta \Big|_{Y=L'_2} = \theta \Big|_{Z=L'_3} = \theta_w \quad (33c)$$

where $\bar{q}_w = \frac{q_w}{kT_0/L_1}$ = dimensionless surface heat flux.

In this report, each numerical method will be used to solve the three-dimensional heat diffusion equation for the two different boundary conditions. To evaluate the accuracy of the various methods, an average temperature error is used. It is defined as the square root of the average of the squares of the error between the predicted temperature and the analytical temperature. It is given by:

$$\epsilon = \sqrt{\frac{\sum_{i=1}^I \sum_{j=1}^J \sum_{k=1}^K [\theta_{i,j,k} - \theta_a]^2}{IJK}} \quad (34)$$

where θ_a is the analytical dimensionless temperature.

Case I - Constant Surface Heat Flux

Consider a parallelepiped, initially at a uniform temperature $\theta_0=1.0$. At time $\tau=0$, all faces of the parallelepiped are exposed to a constant surface heat flux $\bar{q}_w = 0.5$. For a parallelepiped exposed to a constant surface heat flux, the temperature distribution as a function of time can be represented by the summation of three one-dimensional solutions [17]:

$$\begin{aligned} \theta(X,Y,Z,\tau) = & \theta_0 \\ & + 2\bar{q}_w\sqrt{\tau} \left\{ \sum_{m=0}^{\infty} \left[\text{ierfc}\left(\frac{(2m+1)+X}{2\sqrt{\tau}}\right) + \text{ierfc}\left(\frac{(2m+1)-X}{2\sqrt{\tau}}\right) \right] \right. \\ & + \sum_{m=0}^{\infty} \left[\text{ierfc}\left(\frac{(2m+1)L_2'+Y}{2\sqrt{\tau}}\right) + \text{ierfc}\left(\frac{(2m+1)L_2'-Y}{2\sqrt{\tau}}\right) \right] \\ & \left. + \sum_{m=0}^{\infty} \left[\text{ierfc}\left(\frac{(2m+1)L_3'+Z}{2\sqrt{\tau}}\right) + \text{ierfc}\left(\frac{(2m+1)L_3'-Z}{2\sqrt{\tau}}\right) \right] \right\} \quad (35) \end{aligned}$$

Presented in Fig 2.3 are the results obtained for a cube exposed to a constant surface heat flux $\bar{q}_w = 0.5$ at time $\tau = 2.0$. Twenty nodal points are used in each direction for this calculation. According to Eq. (7), the time-step limit required for the conventional ADI method ($f=1.0$) is 0.001875. In Fig 2.3, the solutions from the conventional ADI method have very good accuracy with time step 0.002, but they become unstable as time step is increased further. The Brian and Douglas methods are unconditionally stable, but the negative coefficients in the discretization equations cause their solutions to be physically unrealistic. The results show that their solutions have good accuracy

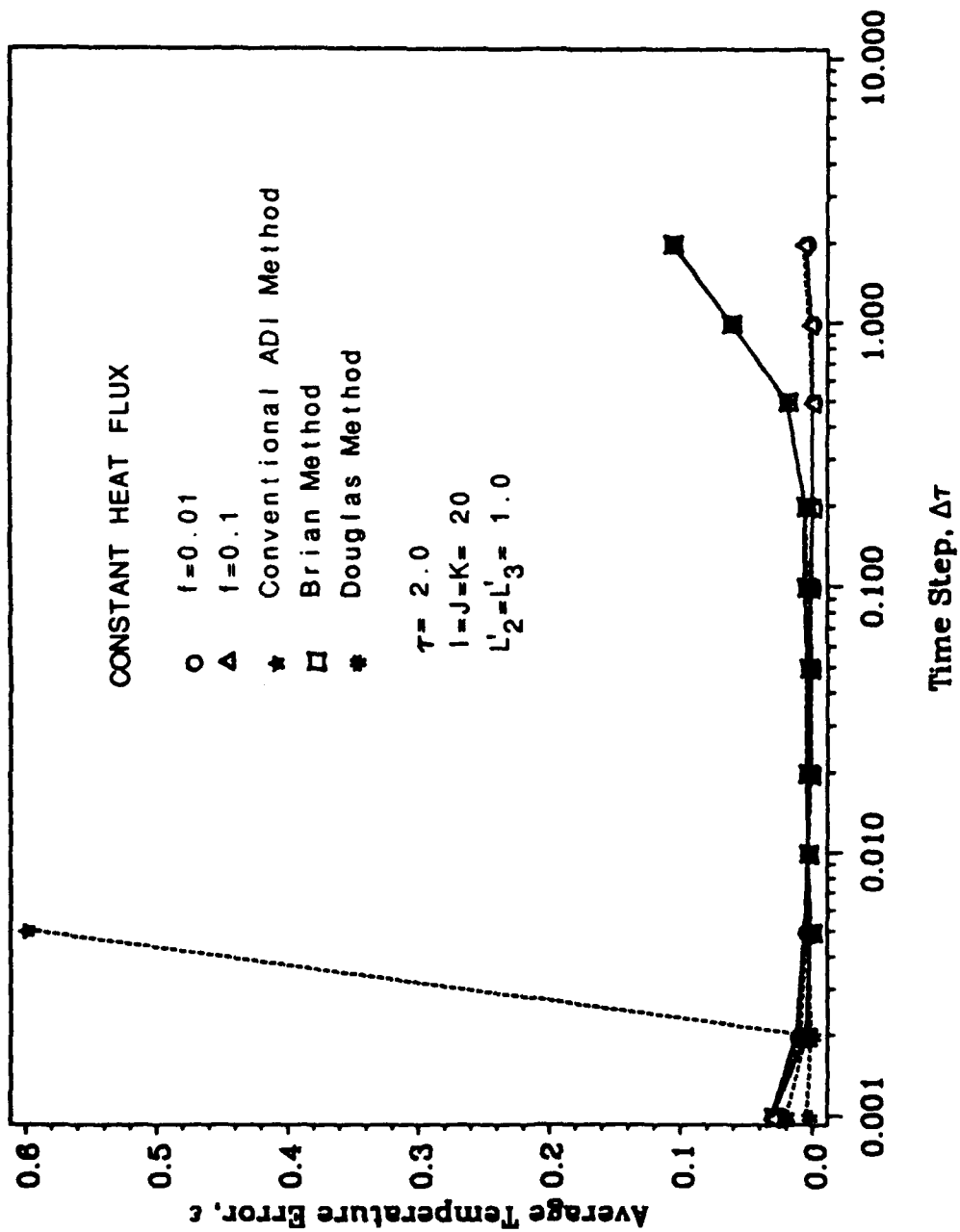


Figure 2.3 Average temperature error for a cube with constant wall heat flux, $\tau = 2$

if time step is smaller than 0.5 but become more and more inaccurate if the time step is increased further. On the contrary, the proposed new ADI method with $f = 0.1$ and $f = 0.01$ is very accurate even when a time step of 2.0 is used. The average temperature error is less than 0.007. It can be seen from Eqs. (26) and (31) that this f-factor ADI method has a much higher time-step limit than the conventional ADI method.

Shown in Fig 2.4 are the results at time $\tau = 10.0$ for a cube with the same boundary condition of a constant surface heat flux $\bar{q}_w = 0.5$. For very small time steps, every method yields poor accuracy. This is due to the large amount of calculations involved and the accumulation of round-off errors. For time steps greater than 0.01, the Brian and Douglas methods are always stable but they yield poor accuracy with average temperature errors up to about 0.15. The new ADI method with $f = 0.01$ predicts the results exceptionally well, the average temperature errors are always less than 0.02 for time steps larger than 0.01. However, the new ADI method with $f = 0.1$ only predicts well up to a time step of 0.5. This is because the new ADI method with $f=0.1$ has a lower time-step limit compared to that with $f=0.01$.

Figure 2.5 shows the variation of the average temperature error with the f-factor at $\tau = 10.0$ for a cube with the same boundary condition of a constant surface heat flux $\bar{q}_w = 0.5$. It can be seen, as long as the solutions do not diverge, the temperature errors remain almost the same with different values of the f-factor. In other words, the value of f we chose does not influence the numerical results as long as the solutions remain stable. The results for very small time step $\Delta\tau=0.001$ always have larger errors. This is due to the accumulation of round-off errors we have mentioned earlier. Also, we can see that the

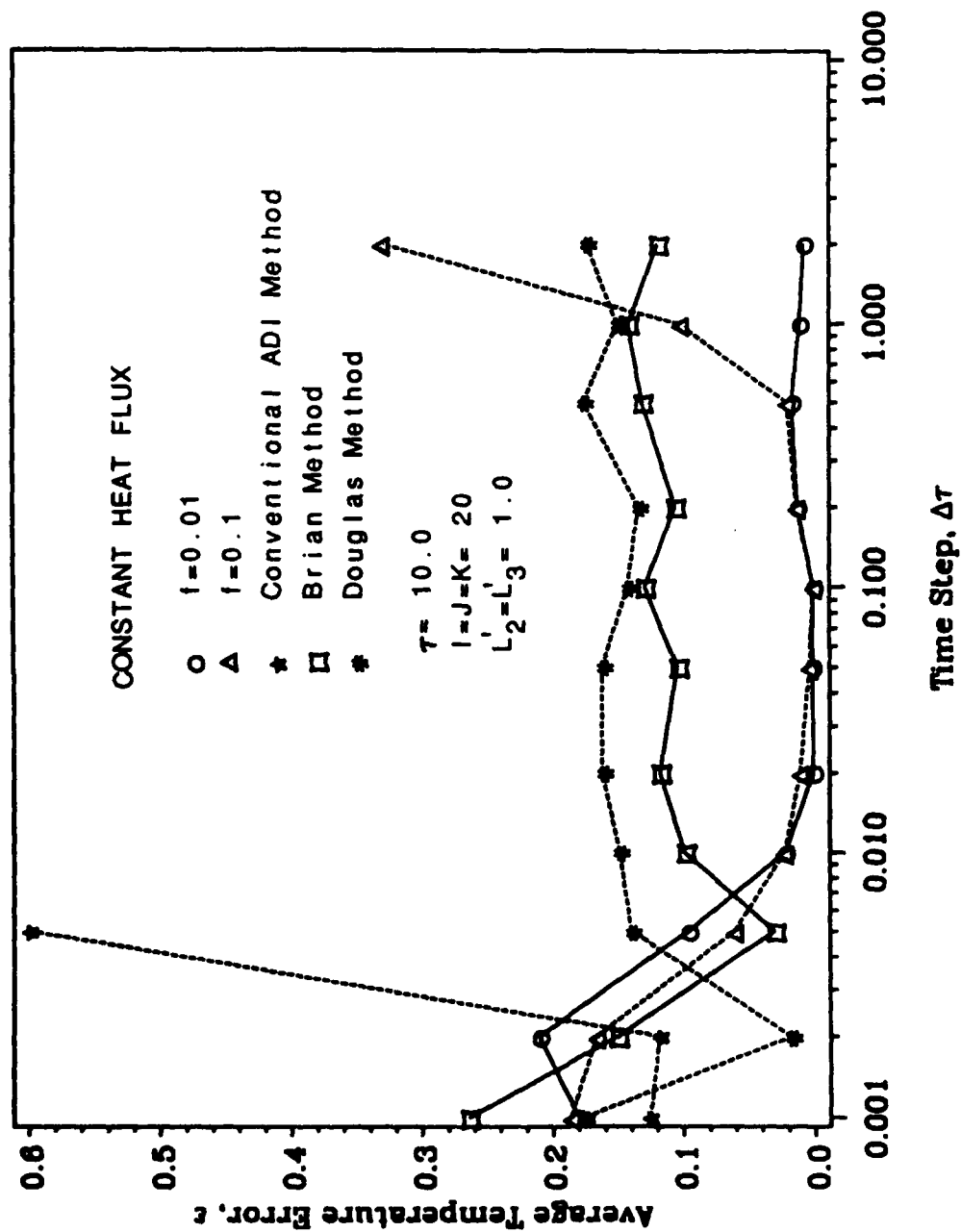


Figure 2.4 Average temperature error for a cube with constant wall heat flux, $\tau = 10$

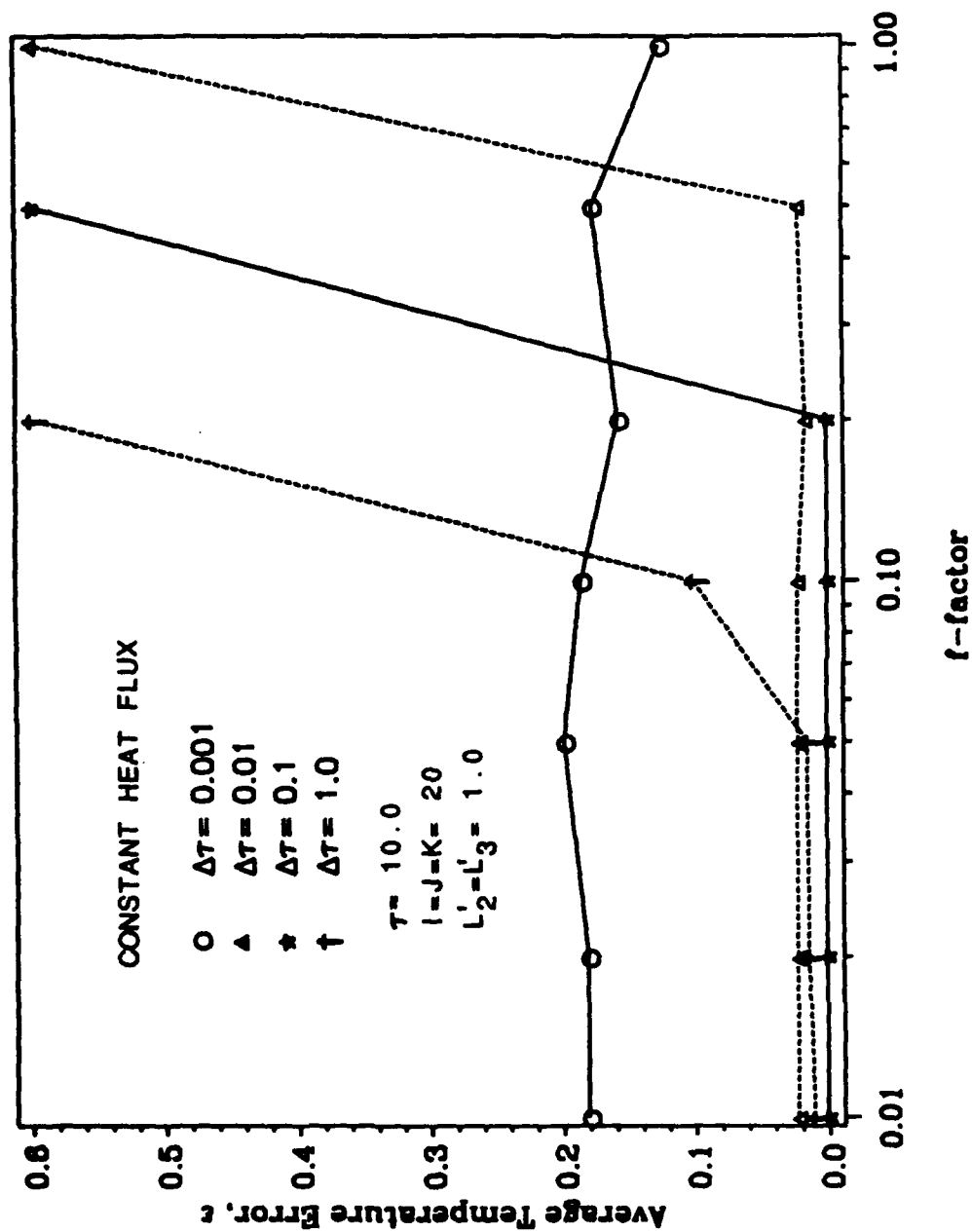


Figure 2.5 Variation of average temperature error with f factor for a cube with constant wall heat flux, $\tau = 10$

solutions are more stable with smaller values of the f-factor in the sense that much larger $\Delta\tau$ can be used.

Case II - Constant Wall Temperature

In this case, the parallelepiped, initially at a uniform temperature $\theta_0=1.0$, has its surfaces suddenly increased and maintained at a constant temperature $\theta_w = 2.0$. The analytical temperature can be easily obtained by using the method of separation of variables [58]:

$$\theta(X,Y,Z,\tau) = \theta_w + \sum_{m=1}^{\infty} \sum_{n=1}^{\infty} \sum_{l=1}^{\infty} a_{mnl} \exp[-\kappa_{mnl}^2 \tau] \cos\left[\frac{(2m-1)\pi X}{2}\right] \cos\left[\frac{(2n-1)\pi Y}{2L_2}\right] \cos\left[\frac{(2l-1)\pi Z}{2L_3}\right] \quad (36)$$

$$\text{where } a_{mnl} = \frac{64(\theta_0 - \theta_w)}{\pi^3 (2m-1)(2n-1)(2l-1)} \sin\frac{(2m-1)\pi}{2} \sin\frac{(2n-1)\pi}{2} \sin\frac{(2l-1)\pi}{2}$$

$$\kappa_{mnl}^2 = \left[\frac{(2m-1)\pi}{2}\right]^2 + \left[\frac{(2n-1)\pi}{2L_2}\right]^2 + \left[\frac{(2l-1)\pi}{2L_3}\right]^2$$

Presented in Fig 2.6 are the results obtained for a cube at time $\tau = 0.2$. At this time, the temperature field is still undergoing transient development. Similar to Case I with constant surface heat flux, the conventional ADI method becomes unstable if the time step is greater than 0.002. The Brian and Douglas methods predict the temperature field accurately only with a time step less than 0.02. Their methods become inaccurate if the time step is increased beyond 0.02. The new ADI method with both $f=0.1$ and $f=0.01$ always yields better accuracy than the other methods, the average temperature error increases only slightly with the time step and is about 0.03 with a time

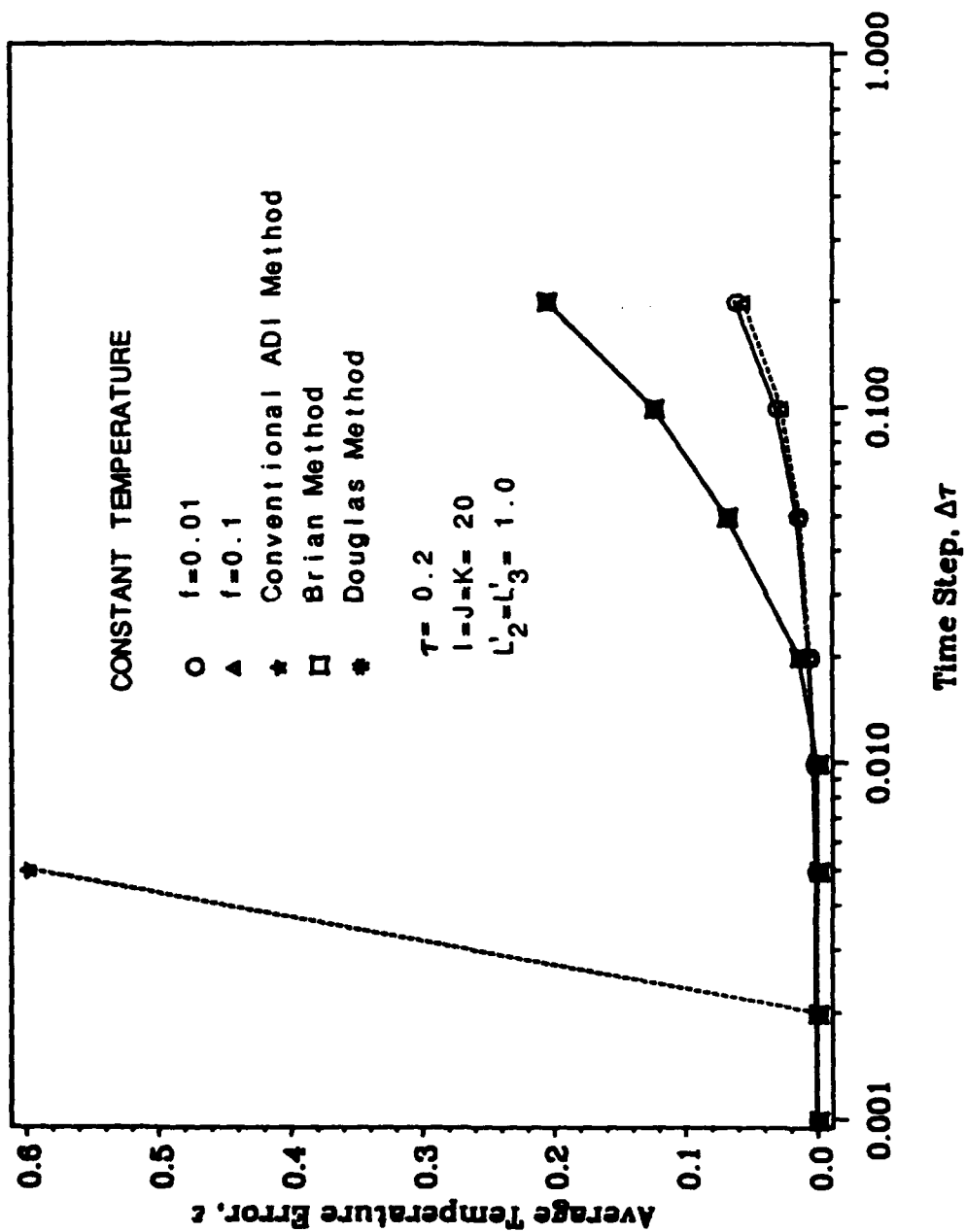


Figure 2.6 Average temperature error for a cube with constant wall temperature, $\tau = 0.2$

step of 0.1.

Shown in Fig 2.7 are the results for a cube at time $\tau = 1.0$. At this time, the temperature field has already reached steady-state. The Brian and Douglas methods predict the steady-state temperature field rather poorly if the time step is greater than 0.1. The average temperature error is about 0.5 with a time step of 1.0. On the contrary, the new ADI method predicts the steady-state results very well. With a time step of 1.0, the new ADI method yields solutions with an average temperature error about 0.024 for $f=0.1$ and about 0.016 for $f=0.01$.

2.4 Concluding Remark

In this chapter, an f -factor ADI method for solving transient three-dimensional heat diffusion problems is introduced. An important characteristic of this new ADI method is that the resulting finite-difference equations are consistent with physical considerations. Compared to the conventional ADI method, this modification allows the time step to be increased by about a factor of $1/f$ without compromising the accuracy of the numerical solution. Compared with the conventional ADI method and the Brian and Douglas ADI methods, this new ADI method yields higher accuracy and requires less computer storage.

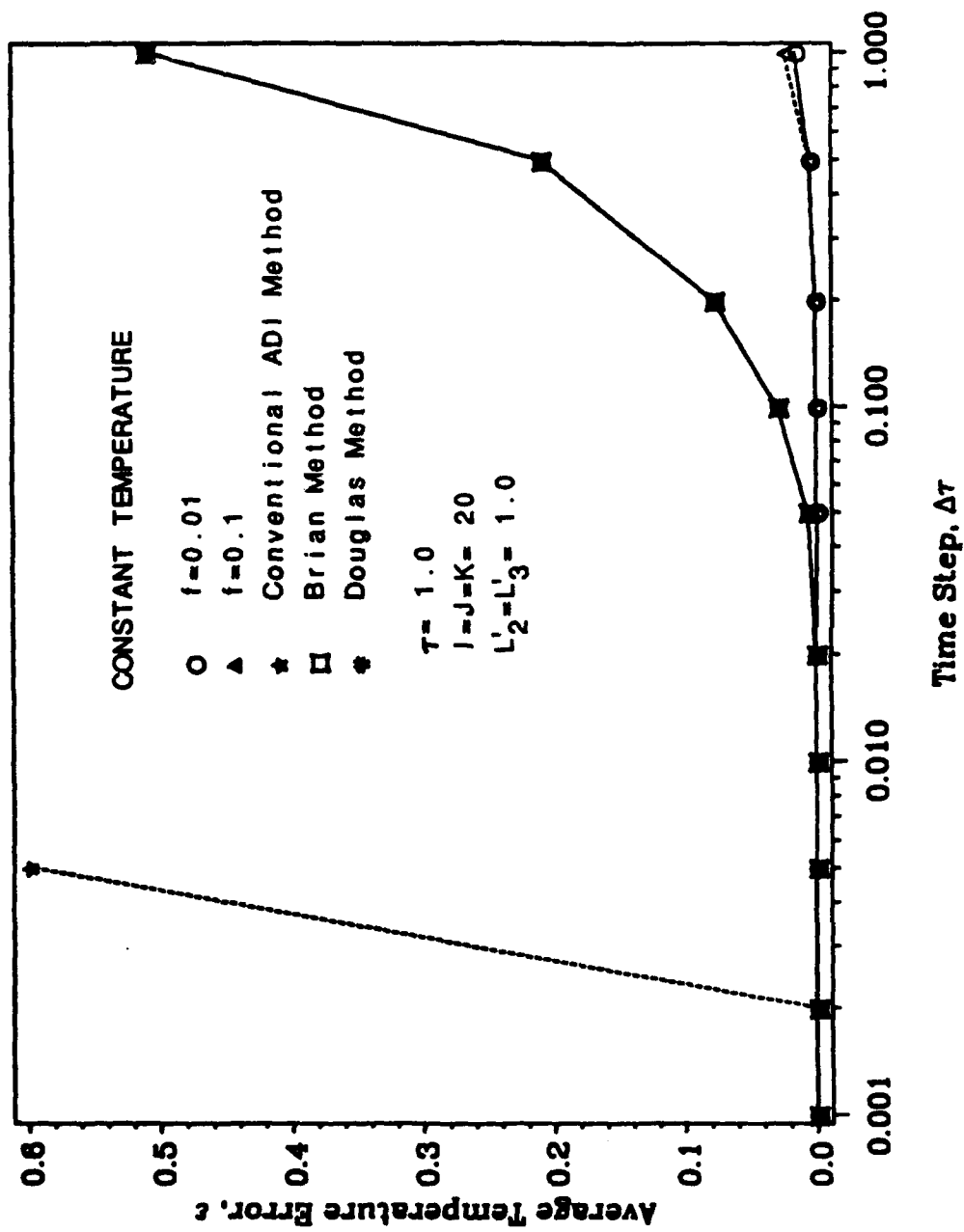


Figure 2.7 Average temperature error for a cube with constant wall temperature, $\tau = 1.0$

CHAPTER 3

NUMERICAL MODEL

A numerical model and solution techniques have been developed to predict the transient behavior of a high-temperature axially grooved heat pipe with thermal energy storage. The heat transfer through the pipe wall and wick, including the liquid in the grooves, was modeled as three-dimensional in the radial, angular and axial directions. The liquid and vapor flow dynamics were modeled using quasi-steady, one-dimensional methods. The heat transfer within the phase-change material, which was encapsulated in a cylindrical container, was modeled as two-dimensional in the radial and axial directions. A nodal system used to develop finite-difference approximations was depicted in Figs 3.1a and 3.1b. Finite-difference equations have been derived for three-dimensional heat transfer under the following assumptions:

- (1) The heat transferred through the wick and working fluid is by conduction only, since liquid flow velocity is very low and the liquid thermal conductivity is very high.
- (2) The grooves are nearly filled with liquid. This is a good assumption for high temperature heat pipes under normal operation without burnout, because the thermal resistance of liquid metal is much smaller than that of the heat pipe wall.
- (3) The top lands of the groove structure in the evaporator section are adiabatic because no evaporation occurs.
- (4) The thermal resistance of the condensed liquid on the top lands of the groove structure in the condenser section is very small compared to the thermal resistance of the solid wall and

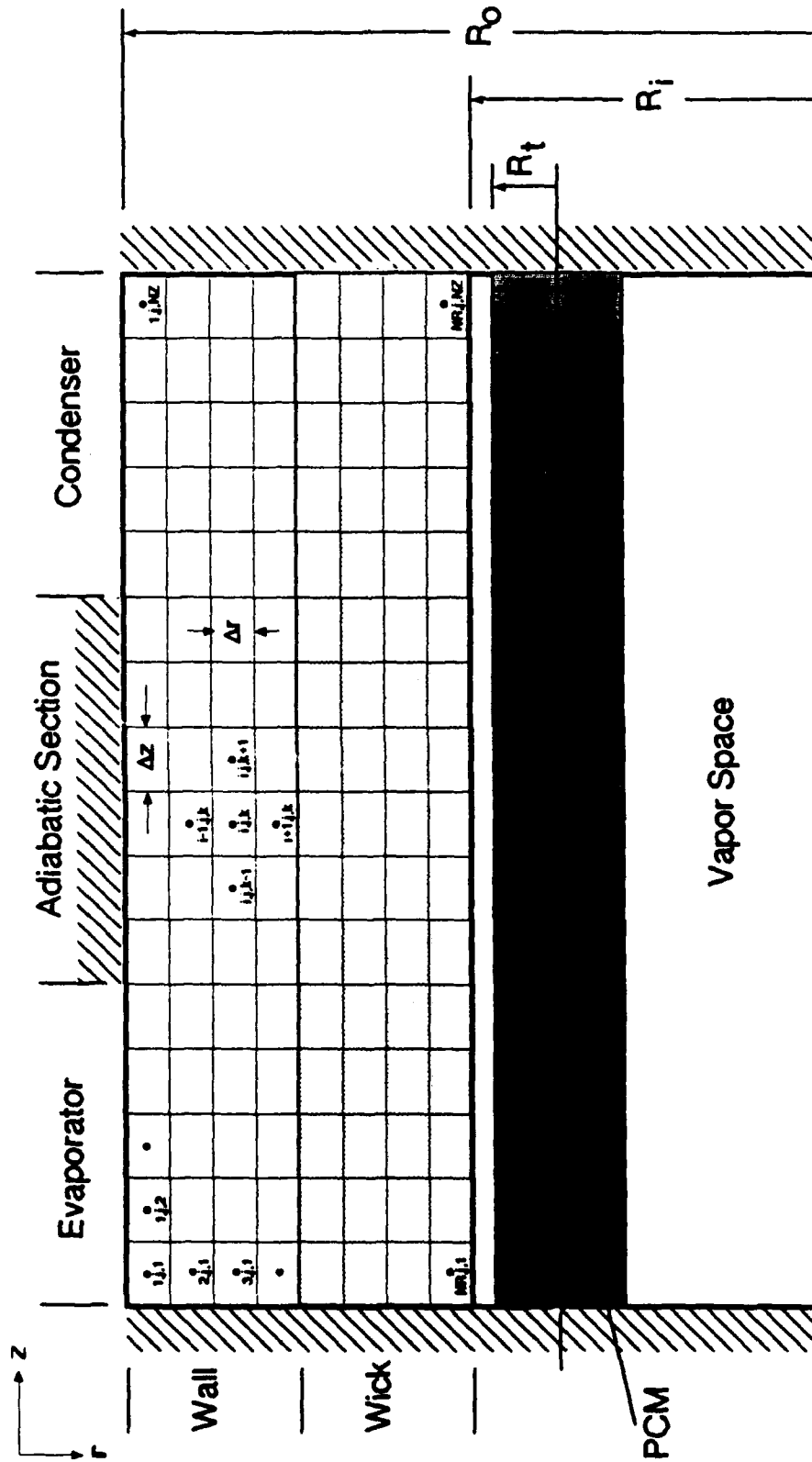


Figure 3.1a Modal map of the heat pipe - side view

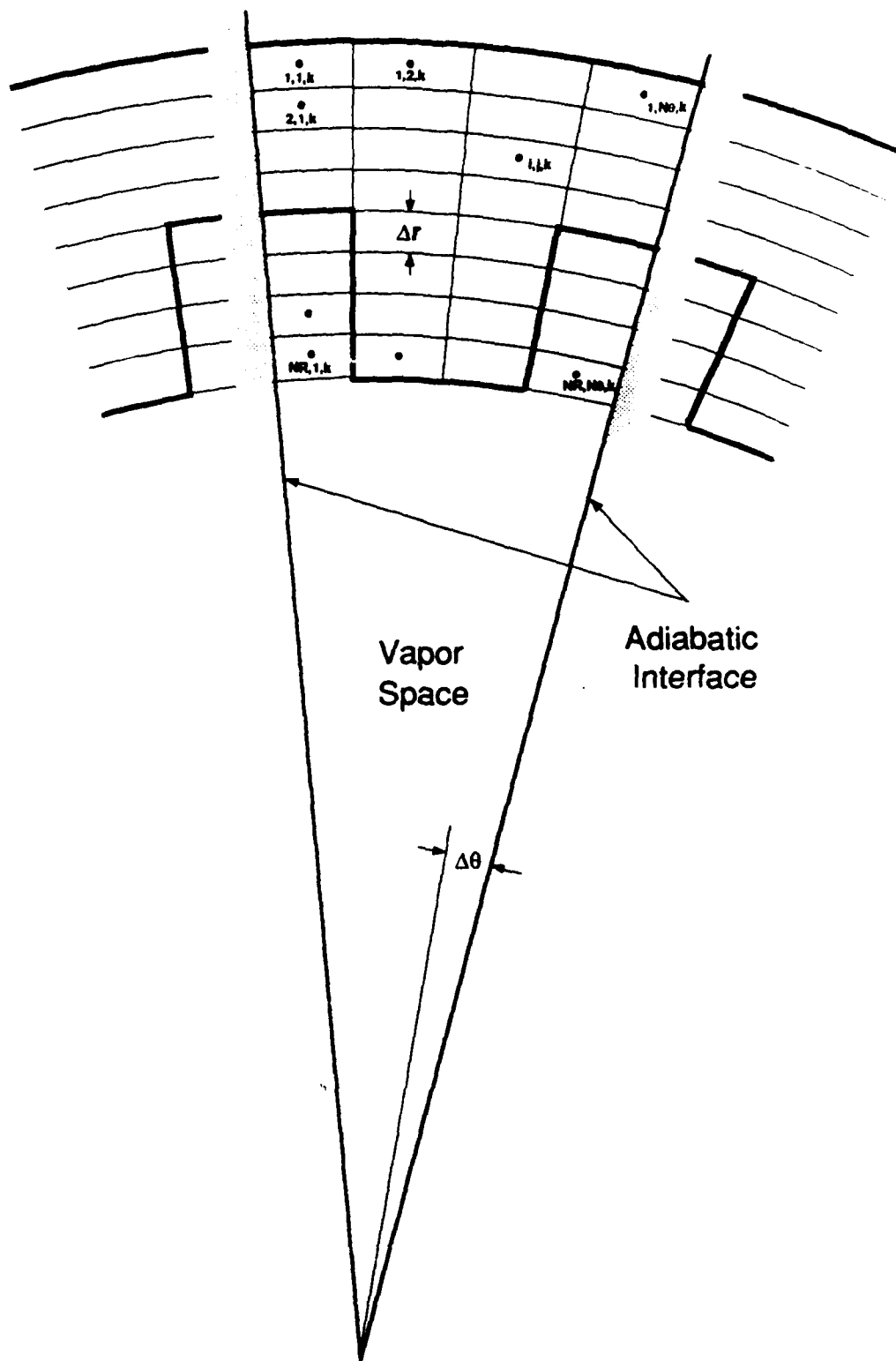


Figure 3.1b Nodal map of the heat pipe - end view

can be neglected.

- (5) The liquid-vapor interface temperature is equal to the local vapor temperature, because the thermal resistances due to evaporation and condensation are very small.
- (6) The thermal resistance of the condensed liquid on the PCM cylinder is much smaller than that of the phase-change material, the surface temperature of the PCM cylinder is assumed to be equal to the vapor temperature at the same axial location. Hence, only a two-dimensional analysis is needed to calculate the temperature and heat transfer within the PCM cylinder because of angular symmetry.

A variety of boundary conditions for the thermal coupling between the heat pipe and its heat source and sink have been included in the numerical model:

Evaporator surface

- (1) variable uniform heat flux, and
- (2) variable uniform temperature.

Condenser surface

- (1) radiation,
- (2) radiation and variable uniform heat flux, and
- (3) radiation and partially-covered variable uniform heat flux.

3.1 Heat Conduction Through Pipe Wall and Wick

The improved three-dimensional ADI finite-difference method [18] was used to model the heat conduction through the wall and wick,

including the liquid in the grooves. The advantage of the ADI method is that only tridiagonal matrices need to be solved. However, the conventional three-dimensional ADI method is conditionally stable and very small time steps are required to ensure convergence and stability. Since small Δr is needed due to the slender geometry of the heat pipe, only very small Δt (about 0.001s) can be used with the conventional ADI method. Other forms of the ADI method include the well-known Douglas [19] and Brian ADI methods [20]. Douglas and Brian ADI methods are unconditionally stable, they possess the advantages of the implicit scheme with no limitation on the size of time step. However, Thibault [17] pointed out that these two unconditionally stable ADI methods cannot retain good accuracy if the time step is more than 2 times larger than the time-step limit required for the conventional ADI method. The conventional ADI method was modified with an f -factor ($0 < f < 1$) as introduced in Chapter 2. This modification allows the time step to be increased by about two orders of magnitude without compromising significantly on the accuracy of the numerical solution. It also was shown that this new ADI method yields much higher accuracy than the Brian and Douglas ADI methods.

The conventional Douglas and Brian ADI methods have a common problem: negative coefficients in their discretization equations which are physically unrealistic [56]. After the three-dimensional finite-difference equations of conventional ADI method with cylindrical coordinates are modified by an f -factor, they become the following equations:

$$\frac{1}{a} \frac{T_{i,j,k}^{n+1/3} - T_{i,j,k}^n}{\Delta t/3} = (3-2f) \delta_r^2 T_{i,j,k}^{n+1/3} + f \delta_\theta^2 T_{i,j,k}^n + f \delta_z^2 T_{i,j,k}^n \quad (38)$$

$$\frac{1}{a} \frac{T_{i,j,k}^{n+2/3} - T_{i,j,k}^{n+1/3}}{\Delta t/3} = f \delta_r^2 T_{i,j,k}^{n+1/3} + (3-2f) \delta_\theta^2 T_{i,j,k}^{n+2/3} + f \delta_z^2 T_{i,j,k}^{n+1/3} \quad (39)$$

$$\frac{1}{a} \frac{T_{i,j,k}^{n+1} - T_{i,j,k}^{n+2/3}}{\Delta t/3} = f \delta_r^2 T_{i,j,k}^{n+2/3} + f \delta_\theta^2 T_{i,j,k}^{n+2/3} + (3-2f) \delta_z^2 T_{i,j,k}^{n+1} \quad (40)$$

In the above equations the superscripts n , $n+1/3$, $n+2/3$, and $n+1$ denote times $n\Delta t$, $(n+1/3)\Delta t$, $(n+2/3)\Delta t$, and $(n+1)t$, respectively. After rearranging Eqs. (38)-(40), the following discretization equations can be obtained:

$$\begin{aligned} & \left[\frac{3\rho c r_i (\Delta r)^2}{\Delta t} + (3-2f) k_{i-} (r_i + \frac{\Delta r}{2}) + (3-2f) k_{i+} (r_i - \frac{\Delta r}{2}) \right] T_{i,j,k}^{n+1/3} \\ & - (3-2f) k_{i-} (r_i + \frac{\Delta r}{2}) T_{i-1,j,k}^{n+1/3} - (3-2f) k_{i+} (r_i - \frac{\Delta r}{2}) T_{i+1,j,k}^{n+1/3} \\ & = \left[\frac{3\rho c r_i (\Delta r)^2}{\Delta t} - f (k_{j-} + k_{j+}) \frac{(\Delta r)^2}{r_i (\Delta \theta)^2} - f (k_{k-} + k_{k+}) \frac{r_i (\Delta r)^2}{(\Delta z)^2} \right] T_{i,j,k}^n \\ & + \left[f k_{j-} \frac{(\Delta r)^2}{r_i (\Delta \theta)^2} \right] T_{i,j-1,k}^n + \left[f k_{j+} \frac{(\Delta r)^2}{r_i (\Delta \theta)^2} \right] T_{i,j+1,k}^n \\ & + \left[f k_{k-} \frac{r_i (\Delta r)^2}{(\Delta z)^2} \right] T_{i,j,k-1}^n + \left[f k_{k+} \frac{r_i (\Delta r)^2}{(\Delta z)^2} \right] T_{i,j,k+1}^n \end{aligned} \quad (41)$$

$$\begin{aligned} & \left[\frac{3\rho c (r_i \Delta \theta)^2}{\Delta t} + (3-2f) k_{j-} + (3-2f) k_{j+} \right] T_{i,j,k}^{n+2/3} \\ & - (3-2f) k_{j-} T_{i,j-1,k}^{n+2/3} - (3-2f) k_{j+} T_{i,j+1,k}^{n+2/3} \\ & = \left[\frac{3\rho c (r_i \Delta \theta)^2}{\Delta t} - f k_{i-} (r_i + \frac{\Delta r}{2}) \frac{r_i (\Delta \theta)^2}{(\Delta r)^2} - f k_{i+} (r_i - \frac{\Delta r}{2}) \frac{r_i (\Delta \theta)^2}{(\Delta r)^2} \right] T_{i,j,k}^n \end{aligned}$$

$$\begin{aligned}
& - f (k_{k-} + k_{k+}) \frac{(r_i \Delta \theta)^2}{(\Delta z)^2}] T_{i,j,k}^{n+1/3} \\
& + [f k_{i-} (r_i + \frac{\Delta r}{2}) \frac{r_i (\Delta \theta)^2}{(\Delta r)^2}] T_{i-1,j,k}^{n+1/3} + [f k_{i+} (r_i - \frac{\Delta r}{2}) \frac{r_i (\Delta \theta)^2}{(\Delta r)^2}] T_{i+1,j,k}^{n+1/3} \\
& + [f k_{k-} \frac{(r_i \Delta \theta)^2}{(\Delta z)^2}] T_{i,j,k-1}^{n+1/3} + [f k_{k+} \frac{(r_i \Delta \theta)^2}{(\Delta z)^2}] T_{i,j,k+1}^{n+1/3} \quad (42)
\end{aligned}$$

$$\begin{aligned}
& [\frac{3\rho c (\Delta z)^2}{\Delta t} + (3-2f) (k_{k-} + k_{k+})] T_{i,j,k}^{n+1} \\
& - (3-2f) k_{k-} T_{i,j,k-1}^{n+1} - (3-2f) k_{k+} T_{i,j,k+1}^{n+1} \\
& = [\frac{3\rho c (\Delta z)^2}{\Delta t} - f k_{i-} (r_i + \frac{\Delta r}{2}) \frac{(\Delta z)^2}{r_i (\Delta r)^2} - f k_{i+} (r_i - \frac{\Delta r}{2}) \frac{(\Delta z)^2}{r_i (\Delta r)^2} \\
& - f (k_{j-} + k_{j+}) \frac{(\Delta z)^2}{(r_i \Delta \theta)^2}] T_{i,j,k}^{n+2/3} \\
& + [f k_{i-} (r_i + \frac{\Delta r}{2}) \frac{(\Delta z)^2}{r_i (\Delta r)^2}] T_{i-1,j,k}^{n+2/3} + [f k_{i+} (r_i - \frac{\Delta r}{2}) \frac{(\Delta z)^2}{r_i (\Delta r)^2}] \\
& T_{i+1,j,k}^{n+2/3} \\
& + [f k_{j-} \frac{(\Delta z)^2}{(r_i \Delta \theta)^2}] T_{i,j-1,k}^{n+2/3} + [f k_{j+} \frac{(\Delta z)^2}{(r_i \Delta \theta)^2}] T_{i,j+1,k}^{n+2/3} \quad (43)
\end{aligned}$$

Where ρ 's and c 's are the nodal density and specific heat based on local properties and k 's are the thermal conductivities based on the harmonic mean of two relevant nodal conductivities.

On the right-hand sides of Eqs. (41)-(43), only the coefficients for central nodal temperatures at previous time step could be negative. It was shown [18] that the time-step limit to avoid the coefficients

from becoming negative can now be increased by a factor of $1/f$. It was also shown [18] that the stability criterion can be increased by the same factor. So, it is clear that the time-step limit for the conventional ADI method can now be increased by a factor of $1/f$ by using this new ADI method. The computational results showed that this modification allows the time-step limit to be increased by 2 orders of magnitude with $f=0.01$ and the solutions still remain stable with very high accuracy.

The resulting finite-difference approximations for all nodes form a nonhomogeneous set of linear algebraic equations for each one-third time-step:

For the first one-third time-step,:

$$\begin{bmatrix}
 B_1 & C_1 & 0 & 0 & & 0 & 0 & 0 \\
 A_2 & B_2 & C_2 & 0 & 0 & 0 & 0 & 0 \\
 0 & A_3 & B_3 & C_3 & 0 & 0 & 0 & 0 \\
 & & & A_i & B_i & C_i & & \\
 0 & 0 & 0 & & & & & \\
 0 & 0 & 0 & & & 0 & A_{NR} & B_{NR}
 \end{bmatrix}
 \begin{bmatrix}
 T_{1,j,k}^{n+1/3} \\
 T_{2,j,k}^{n+1/3} \\
 T_{3,j,k}^{n+1/3} \\
 T_{i,j,k}^{n+1/3} \\
 T_{NR,j,k}^{n+1/3}
 \end{bmatrix}
 =
 \begin{bmatrix}
 D_1 \\
 D_2 \\
 D_3 \\
 D_i \\
 D_{NR}
 \end{bmatrix}
 \quad (44)$$

for the second one-third time-step,:

$$\begin{bmatrix}
 B'_1 & C'_1 & 0 & 0 & 0 & 0 & 0 \\
 A'_2 & B'_2 & C'_2 & 0 & 0 & 0 & 0 \\
 0 & A'_3 & B'_3 & C'_3 & 0 & 0 & 0 \\
 & & & A'_j & B'_j & C'_j & \\
 & & & & & & \\
 0 & 0 & 0 & & & & \\
 0 & 0 & 0 & & 0 & A'_{N\theta} & B'_{N\theta}
 \end{bmatrix}
 \begin{bmatrix}
 T^{n+2/3}_{i,1,k} \\
 T^{n+2/3}_{i,2,k} \\
 T^{n+2/3}_{i,3,k} \\
 \\
 T^{n+2/3}_{i,j,k} \\
 \\
 T^{n+2/3}_{i,N\theta,k}
 \end{bmatrix}
 =
 \begin{bmatrix}
 D'_1 \\
 D'_2 \\
 D'_3 \\
 \\
 D'_j \\
 \\
 D'_{N\theta}
 \end{bmatrix}
 \quad (45)$$

and for the third one-third time-step:

$$\begin{bmatrix}
 B''_1 & C''_1 & 0 & 0 & 0 & 0 & 0 \\
 A''_2 & B''_2 & C''_2 & 0 & 0 & 0 & 0 \\
 0 & A''_3 & B''_3 & C''_3 & 0 & 0 & 0 \\
 & & & A''_k & B''_k & C''_k & \\
 & & & & & & \\
 0 & 0 & 0 & & & & \\
 0 & 0 & 0 & & 0 & A''_{NZ} & B''_{NZ}
 \end{bmatrix}
 \begin{bmatrix}
 T^{n+1}_{i,j,1} \\
 T^{n+1}_{i,j,2} \\
 T^{n+1}_{i,j,3} \\
 \\
 T^{n+1}_{i,j,k} \\
 \\
 T^{n+1}_{i,j,NZ}
 \end{bmatrix}
 =
 \begin{bmatrix}
 D''_1 \\
 D''_2 \\
 D''_3 \\
 \\
 D''_k \\
 \\
 D''_{NZ}
 \end{bmatrix}
 \quad (46)$$

Since each coefficient matrix in Equations (44-46) is tridiagonal, the sets of equations can be easily solved by using the tridiagonal matrix algorithm (TDMA) with known initial and boundary conditions.

This algorithm is very efficient for digital computation.

3.2 Melting and Solidification of PCM

Since the thermal resistance of the condensed liquid on the TES is much smaller than that of the phase-change material, the surface temperature of the TES is assumed to be equal to the vapor temperature at the same axial location. Hence, if the PCM is encapsulated in a cylindrical container, only a two-dimensional analysis is needed to calculate the temperature and heat transfer within the PCM because of angular symmetry.

In the numerical solution of heat conduction problems with phase change, the heat diffusion equation can be formulated in either of the following two ways:

$$C(T) \frac{\partial T}{\partial t} = \text{div} [k(T)\text{grad}(T)] \quad (47)$$

$$\text{or} \quad \frac{\partial H}{\partial t} = \text{div} [k(H)\text{grad}(T(H))] \quad (48)$$

Equation (47) is the basis of heat capacity methods, while Eq. (48) is the basis of enthalpy methods.

In heat capacity methods, the latent heat is represented by a peak of small but finite width in the $C(T)$ curve as shown in Fig 3.2. Since $C(T)$ is not a continuous function of Temperature, if a large time step is used in the computation, a nodal temperature may jump past the melting/freezing temperature range in one time step, resulting in the

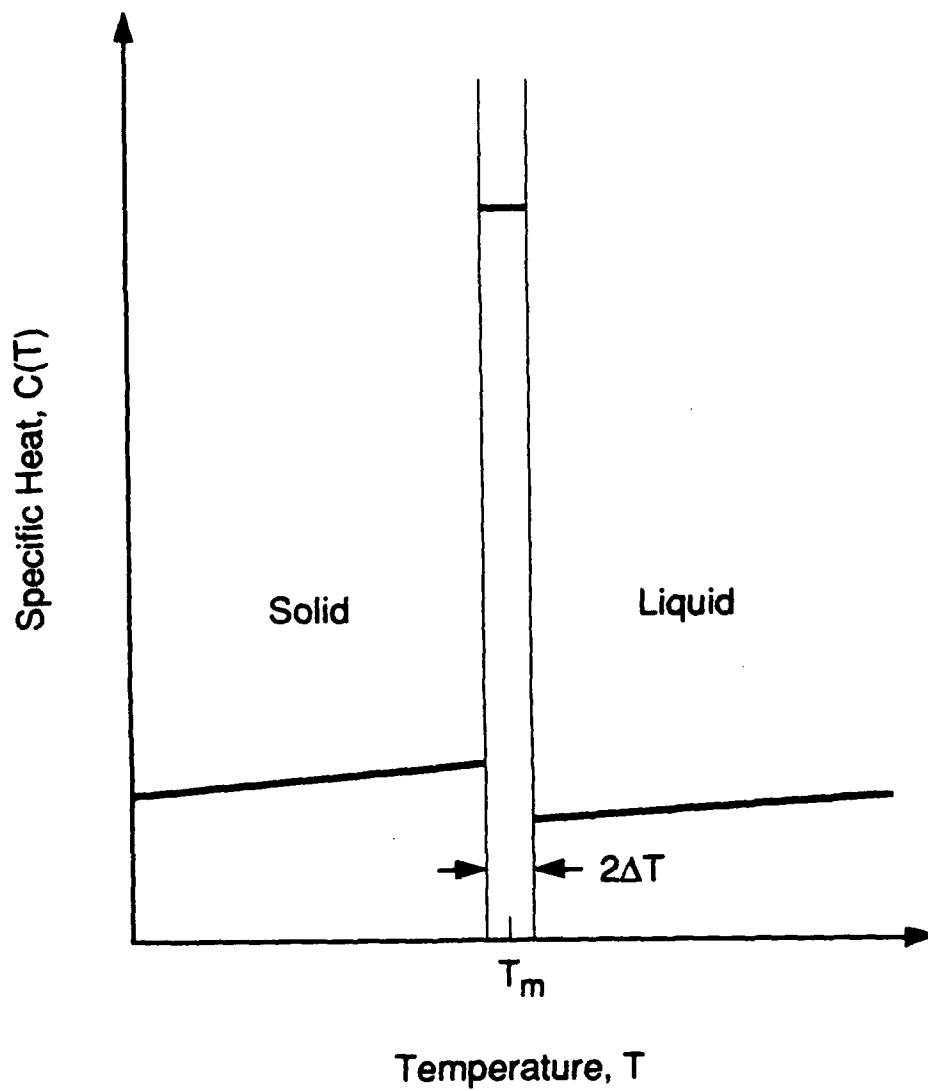


Figure 3.2 Combined specific heat including latent heat effect across the melting temperature for a phase-change material

latent heat being ignored. This is termed "jumping of the latent heat peak" and can be a major problem. To avoid it, very small time steps have to be used.

Enthalpy methods do not suffer from the problem of jumping the latent heat peak mentioned above because the enthalpy is a continuous function of temperature as shown in Fig 3.3. However, the major disadvantage of enthalpy methods is that because a high non linear function, $T(H)$, is involved, an explicit scheme must usually be employed, with consequent stability problems. Implicit schemes have been proposed by Longworth [59] and Furzeland [60], but they require iteration at each time step and are less efficient in terms of computer time [33,61].

To overcome the problem of jumping the latent heat peak which heat capacity methods suffer, Hsiao [31,32] suggested that $C(T)$ should be linearly interpolated between the temperatures of adjacent nodes. Hsiao considered a typical situation during a phase change process (see Fig 3.4). In this case only three nodes (inside the shaded region) have temperatures within the range of $T_m - \Delta T$ and $T_m + \Delta T$, and are able to include the latent heat effect if heat capacity method is applied. All other nodes next to the fusion front will employ the specific heat of either the solid or liquid phase, depending on whether the nodal temperature is less than $T_m - \Delta T$ or greater than $T_m + \Delta T$, respectively. Clearly, the latent heat effect is not properly included, and as a result numerical error always arise. In light of the above observation, Hsiao proposed a new scheme to improve the heat capacity model. The nodal temperature is not used directly to yield the corresponding specific heat of the node. Instead, the following averaged specific

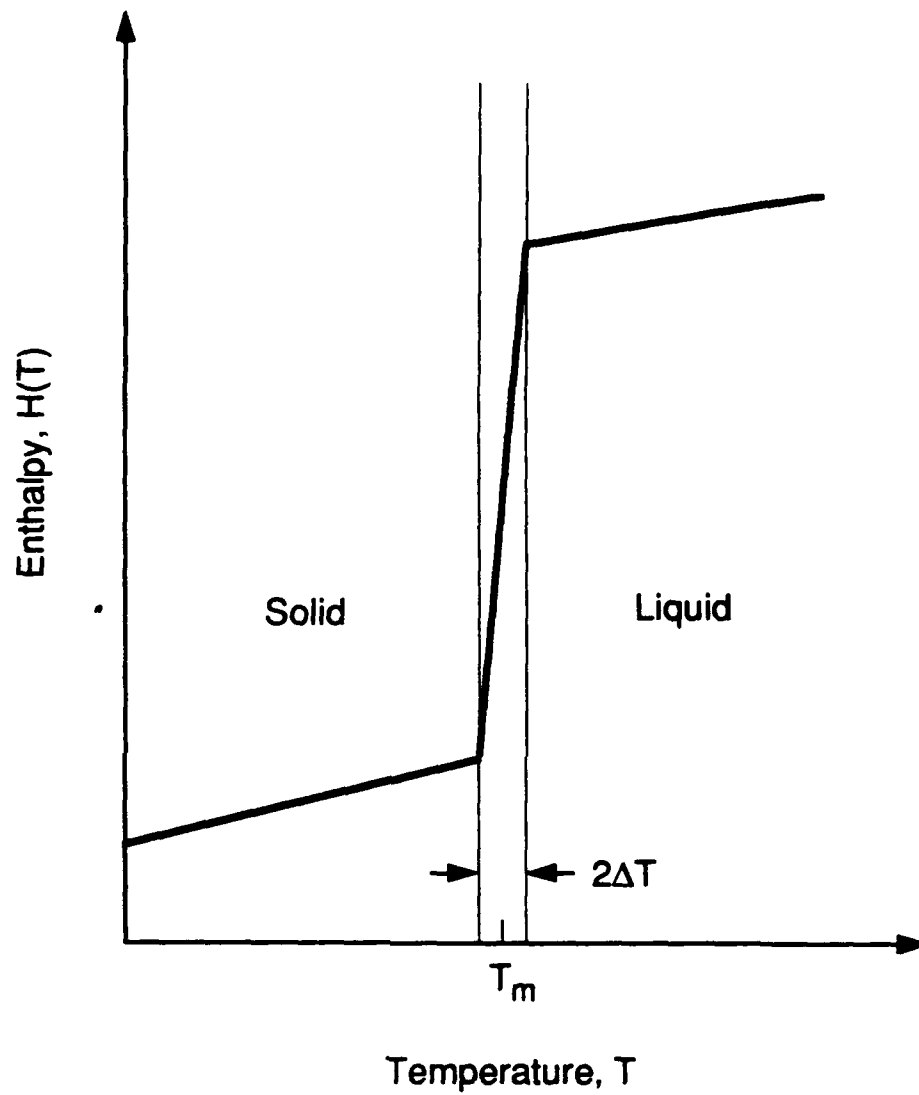


Figure 3.3 Enthalpy over a $2\Delta T$ interval across the melting temperature for a phase-change material

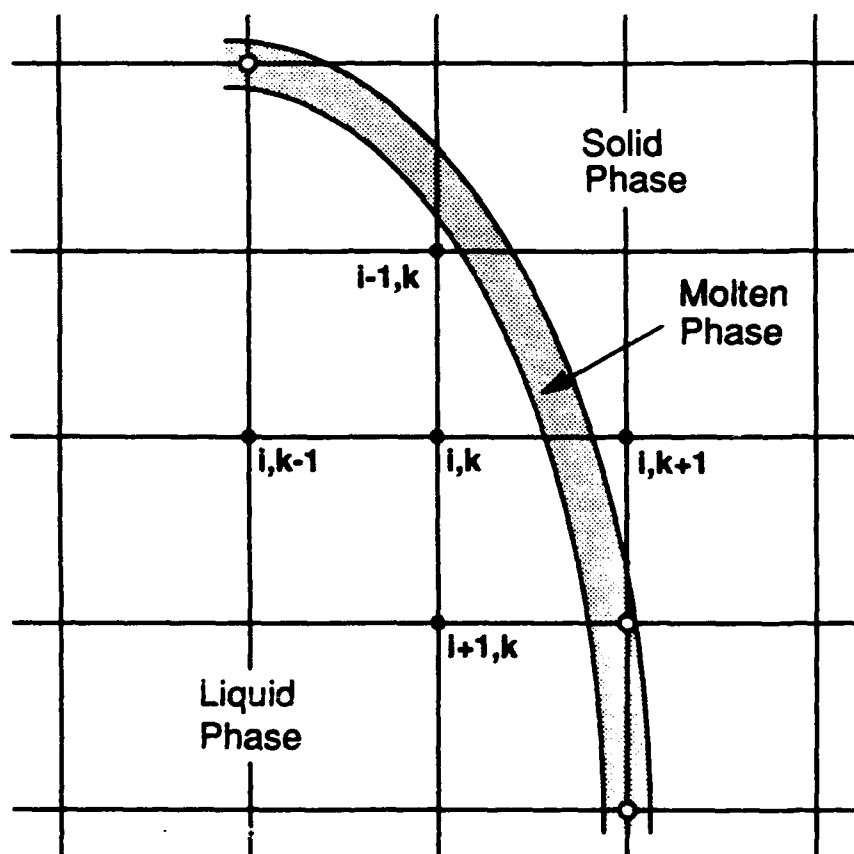


Figure 3.4 A typical location of the fusion front on the nodal map

heat, which is derived from the node (i,k) and its surrounding nodes, is employed:

$$C(T_{i,k}) = \frac{1}{4} [C(T_{i,k}, T_{i-1,k}) + C(T_{i,k}, T_{i+1,k}) + C(T_{i,k}, T_{i,k-1}) + C(T_{i,k}, T_{i,k+1})] \quad (49)$$

where $C(T_{i,k}, T_{i-1,k})$, for example, represents an adjusted specific heat, which is determined by the physical status of the material with temperature within the range of $T_{i,k}$ and $T_{i-1,k}$.

In Hsiao's new heat capacity method, the latent heat effect is accounted for by using a linear interpolation between the temperatures of adjacent nodes. As shown in Fig 3.4, the latent heat effect is included in $C(T_{i,k}, T_{i,k+1})$ since the melting/freezing temperature interval falls in between $T_{i,k}$ and $T_{i,k+1}$. Hsiao concluded that this new method can avoid the problem of jumping the latent heat peak and allows the use of a relatively large time step. However, we have tested Hsiao's new method but a large energy balance error was found. Pham [35] also pointed out that Hsiao's new method yielded results with up to 22% error compared with the analytical result. The low accuracy of Hsiao's new method could be due to its ambiguous theoretical basis.

Pham [33-35] presented a simple and accurate method which combines the good features of enthalpy methods and heat capacity methods. Pham's method can be used in conjunction with the two-dimensional ADI scheme using the following procedure:

1. At the start of each time step, the enthalpy change ΔH^* at each node is estimated from the known temperature $T_{i,k}^n$ of that node and

those of its immediate neighbors at previous time step.

2. Since the enthalpy is a continuous function of the temperature for the phase change material, we can determine an estimated new temperature $T_{i,k}^*$ from the following equation:

$$T_{i,k}^* = f_T[f_H(T_{i,k}^n) + \Delta H_{i,k}^*] \quad (50)$$

where $T_{i,k}^n$ is the nodal temperature at previous time step.
 f_T and f_H are the temperature and enthalpy functions, respectively.

3. When the estimated new temperature $T_{i,k}^*$ is known, the equivalent specific heat of each node can be obtained:

$$c_{i,k}^* = \frac{\Delta H^*}{T_{i,k}^* - T_{i,k}^n} \quad (51)$$

4. With the equivalent specific heat $c_{i,k}^*$ known, we can use the two dimensional ADI method to find the new nodal temperature $T_{i,k}^{n+1}$.

One of the good features of Pham's method is that it estimates the new temperature from the estimated enthalpy change to avoid the problem of jumping the latent heat peak. The other good feature of Pham's method is that its theoretical basis is clear. However, Pham's method has a singularity problem in finding the equivalent specific heat in step 2. If there is no enthalpy change in a particular node, the estimated new temperature $T_{i,k}^*$ will be equal to the previous temperature

$T_{i,k}^n$. Then, we are not able to find the equivalent specific heat from Eq. (51) due to the singularity problem. Fortunately, we have found a way around this problem. If the melting temperature is T_m and the latent heat effect is over a $2\Delta T$ interval, let $H_1 = f_H(T_m - \Delta T)$, $H_2 = f_H(T_m + \Delta T)$ and $H_{i,k}^{n+1} = H_{i,k}^n + \Delta H^*$. We redefine the equivalent specific heat in Eq. (13) as follows:

$$c_{i,k}^* = \left[\begin{array}{ll} c_s & \text{if } H_{i,k}^n, H_{i,k}^{n+1} < H_1 \\ (H_2 - H_1)/(2\Delta T) & \text{if } H_1 < H_{i,k}^n, H_{i,k}^{n+1} < H_2 \\ c_l & \text{if } H_{i,k}^n, H_{i,k}^{n+1} > H_2 \\ \frac{\Delta H^*}{T_{i,k}^* - T_{i,k}^n} & \text{if } H_{i,k}^n < H_1 < H_{i,k}^{n+1} \\ & \text{or } H_{i,k}^n < H_2 < H_{i,k}^{n+1} \\ & \text{or } H_{i,k}^n > H_1 > H_{i,k}^{n+1} \\ & \text{or } H_{i,k}^n > H_2 > H_{i,k}^{n+1} \end{array} \right. \quad (52)$$

where c_s and c_l are the specific heats for solid state and liquid state.

After the modification, Eq. (51) is now used when only one of $H_{i,k}^n$ or $H_{i,k}^{n+1}$ falls in between H_1 and H_2 . In other words, Eq. (51) can only be used when ΔH^* is not equal to zero. Compared with analytical solutions, this modified method for melting and solidification was found to have very good accuracy and does not have the singularity problem Pham's method has.

Consider a one-dimensional melting problem with a solid in a half-space initially at the melting temperature $T_i = T_m = 950$ K. At time

zero, the temperature at the front surface of the solid is suddenly heated to a constant Temperature $T_0=1300$ K and melting takes place immediately. Figs 3.5 and 3.6 show the comparisons of temperature and melting front between the exact solution and the present finite-difference solution during the melting process. The physical variables chosen in the numerical experiment are $k_s=4.2$ W/m-K, $k_l=2.1$ W/m-K; $c_s=6280$ J/K-kg, $c_l=7370$ J/K-kg; PCM latent heat is 2.58×10^6 J/kg. The finite-difference solution is obtained by using 100 equally spaced elements along a length $l=0.01$ m. Time step $\Delta t=0.01$ s and a phase transition temperature interval $2\Delta T= 2.0$ K are used for this example. The dimensionless time is defined as $\tau=t/(l^2/a_l)$. The Stefan number is defined as $Ste=c_l(T_0-T_i)/L$ and is equal to unity in this problem. As it can be seen in Figs 3.5 and 3.6, the present solution agrees very well with the exact solution.

3.3 One-Dimensional Vapor Flow Model

The vapor flow was modeled by using a quasi-steady, one-dimensional friction coefficient developed by Bowman [46]. In the evaporation region, mass blowing causes a slight steepening in the velocity gradients at the pipe wall, leading to an increase in the friction coefficient. Bowman pointed out that the favorable pressure gradient in the mass blowing region influences the flow to remain laminar, even for very large axial Reynolds numbers up to 10^6 . In the condenser region, where there is mass removal and an adverse pressure gradient, the flow was found to stay laminar at axial Reynolds numbers around 12000. In

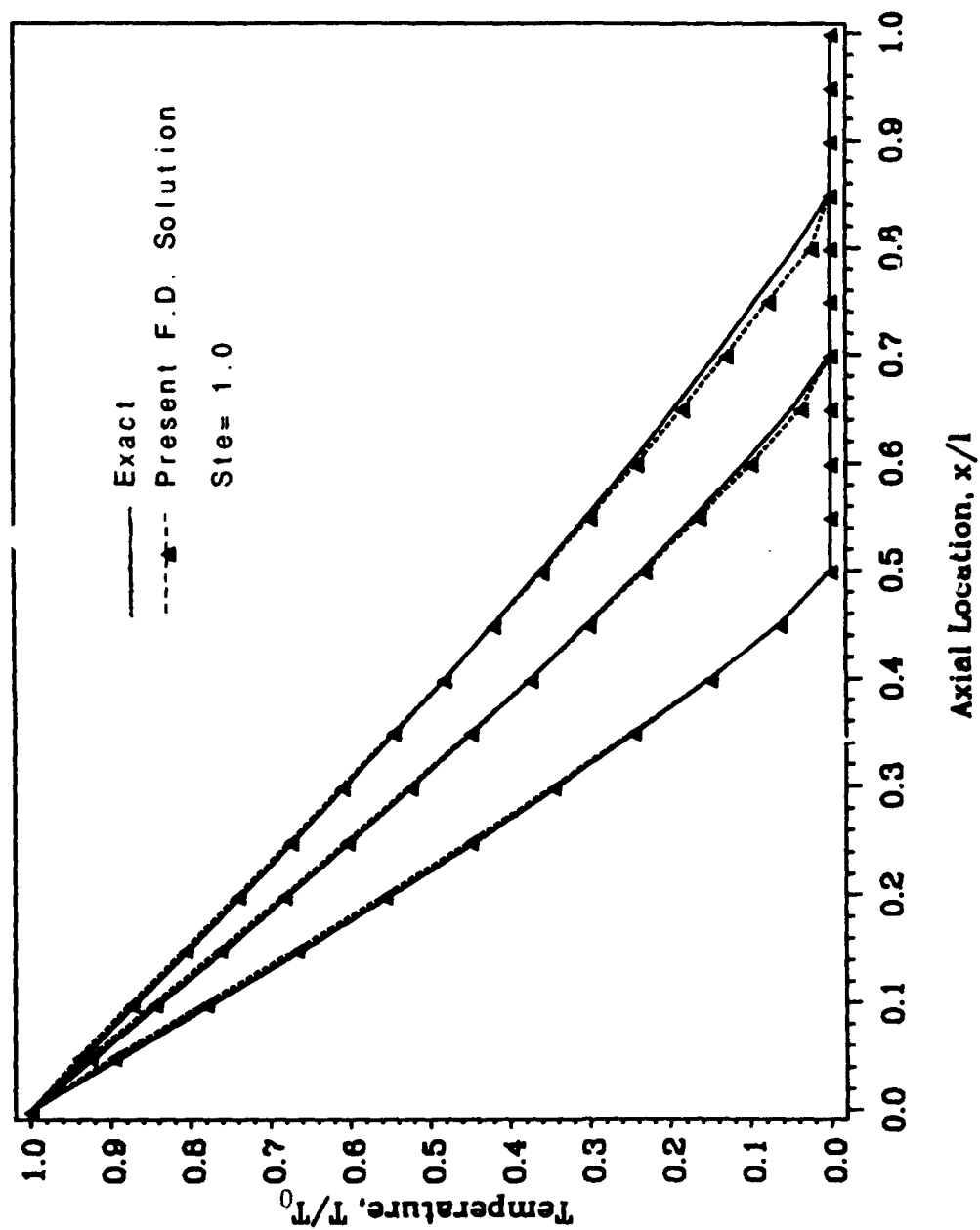


Figure 3.5 Temperature distribution during melting of a one-dimensional half-space (Ste= 1)

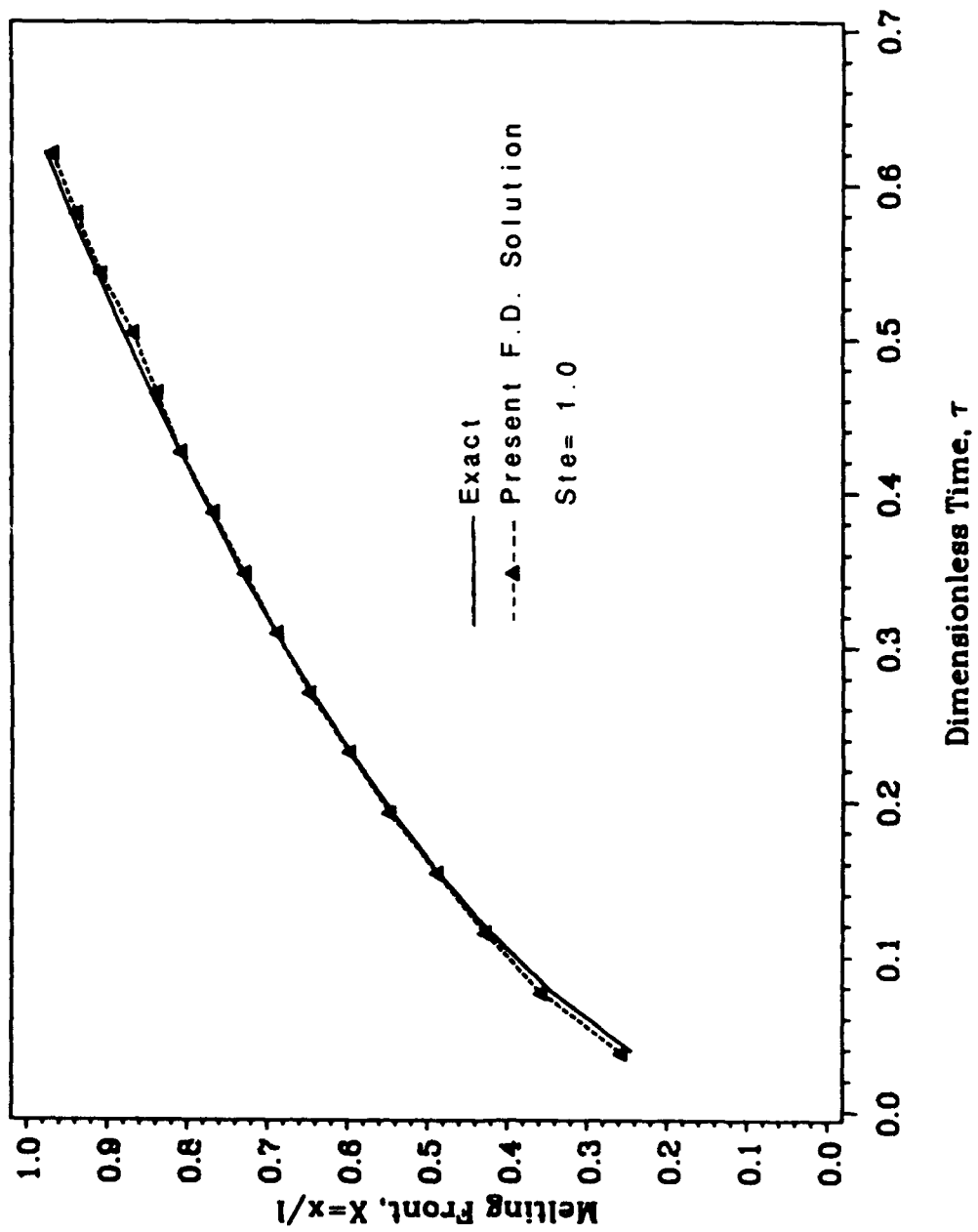


Figure 3.6 Location of the fusion front during melting of a one-dimensional half-space (Ste= 1)

this research, the vapor flow was always assumed to be laminar because the maximum axial Reynolds numbers are always much less than 12000. The correlation of the vapor friction coefficient for laminar flow given by Bowman can be expressed as:

$$f = \frac{16}{Re} (1.2337 - 0.2337 e^{0.0363 Re_w}) e^{6Ma^2/5} \quad (53)$$

where Ma is the Mach number based on the local mean axial velocity U , Re_w is the radial Reynolds number, and Re is the axial Reynolds number defined as:

$$Re_w = \frac{\rho v D_h}{\mu}, \quad Re = \frac{\rho U D_h}{\mu}$$

In these expression, ρ is the vapor flow density, μ is vapor dynamic viscosity, v is the radial velocity at the wall and D_h is the hydraulic diameter of the vapor core.

The vapor flow was assumed to be compressible, one-dimensional and quasi-steady. The governing equations for such a flow can be expressed in terms of influence coefficients as presented by Shapiro [62]:

$$\frac{dMa^2}{Ma^2} = F_{f,a} 4f \frac{dz}{D_h} + F_{\dot{m},a} \frac{d\dot{m}}{\dot{m}} \quad (54)$$

with the two influence coefficients given by:

$$F_{f,a} = \frac{4Ma^2 [1 + \frac{\gamma-1}{2} Ma^2]}{1 - Ma^2} \quad (55)$$

$$F_{\dot{m},a} = \frac{2[1+\gamma Ma^2] \left[1 + \frac{\gamma-1}{2} Ma^2\right]}{1 - Ma^2} \quad (56)$$

where f is the friction coefficient defined earlier by Eq. (53), γ is the ratio of specific heats, z is the axial coordinate, and \dot{m} is the mass flow rate.

For the friction solution, a second expression is needed to relate the change in total pressure (P_0) to the change in mass flow rate and to the friction coefficient. From Shapiro [62]:

$$\frac{dP_0}{P_0} = F_{f,b} 4f \frac{dz}{D_h} + F_{\dot{m},b} \frac{d\dot{m}}{\dot{m}} \quad (57)$$

where

$$F_{f,b} = \frac{-\gamma Ma^2}{2} \quad (58)$$

$$F_{\dot{m},b} = -\gamma Ma^2 \quad (59)$$

Other useful relations are:

$$\frac{T_a}{T_b} = \frac{1 + \frac{\gamma-1}{2} Ma_b^2}{1 + \frac{\gamma-1}{2} Ma_a^2} \quad (60)$$

$$\frac{P_b}{P_a} = \frac{(P_0)_b}{(P_0)_a} \left[\frac{T_a}{T_b}\right]^{\gamma/\gamma-1} \quad (61)$$

$$\frac{\rho_a}{\rho_b} = \frac{P_a T_b}{P_b T_a} \quad (62)$$

These relate properties between two different axial locations, a and b, in the vapor flow field.

3.4 Coupling of Vapor Flow With Evaporation and Condensation

To calculate the pressure and temperature variations in the vapor flow, we need to know the evaporation and condensation rates. However, these rates depend on the vapor temperature and liquid-vapor interface temperature distributions. This means that the vapor pressure and temperature variations are coupled to evaporation and condensation rates simultaneously. In the present model, the evaporation and condensation rates are coupled to the vapor temperature and pressure in an explicit manner so that no iterations are required. However, we still have to guess the vapor temperature at the evaporator end to calculate the vapor temperature distribution. The vapor temperature at the evaporator end can be estimated based on an assumption. Since the vapor density is very small, we can assume that the heat absorbed by the vapor itself is negligible compared to the total evaporation and condensation rates. In other words, at every time step, the total evaporation rate and the total condensation rate are equal. So, the following equation should be always satisfied:

$$\dot{Q}_{in} = \dot{Q}_{out} \quad (63)$$

where \dot{Q}_{in} is the total evaporation rate and \dot{Q}_{out} is the total

condensation rate (see Fig 3.7).

In this research, the one-dimensional vapor flow was coupled with the local evaporation and condensation rates, as shown in Fig 3.7, using the following procedure:

- (1) The local evaporation rate or condensation rate $\dot{Q}_v^n(k)$ at previous time step, can be evaluated from previous local temperatures $T_{NR,j,k}^n$ and $T_v^n(k)$.
- (2) Guess the new vapor temperature at the evaporator end $T_v^{n+1}(1)$, and then use the evaporation and condensation rates to predict the vapor pressure and temperature variations at new time step ($P_v^{n+1}(k)$ and $T_v^{n+1}(k)$).
- (3) As $T_v^{n+1}(k)$ is obtained, we can calculate the new temperature distribution in the heat pipe wall and wick $T_{i,j,k}^{n+1}$.
- (4) The local evaporation or condensation rate $\dot{Q}_v^{n+1}(k)$ at new time step can be evaluated from $T_v^{n+1}(k)$ and $T_{NR,j,k}^{n+1}$.
- (5) The total evaporation rate $\Sigma \dot{Q}_{in}^{n+1}$ and condensation rate $\Sigma \dot{Q}_{out}^{n+1}$ can be evaluated from $\dot{Q}_v^{n+1}(k)$.
- (6) If $\Delta = \Sigma \dot{Q}_{in}^{n+1} - \Sigma \dot{Q}_{out}^{n+1} > \epsilon$, go back to step (2) and iterate until $\Delta < \epsilon$.
- (7) After it converges, $\dot{Q}_v^{n+1}(k)$, $T_v^{n+1}(k)$, $P_v^{n+1}(k)$, and $T_{i,j,k}^{n+1}$ at new time step can finally be obtained.

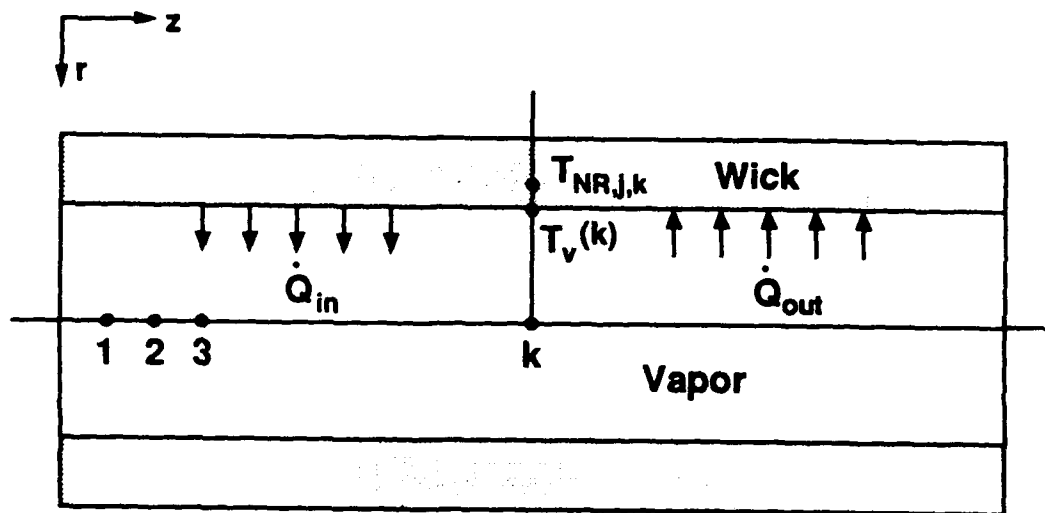


Figure 3.7 Coupling of vapor flow with evaporation and condensation

3.5 Liquid Pressure Drop

In calculating the liquid pressure drop, we assumed that the groove structures are fully wetted with working fluid and the liquid flow is always laminar owing to the generally low liquid velocity. The liquid pressure drop can be obtained by using the following expression [63]:

$$\frac{dP_1}{dz} = -F_1 Q \quad (64)$$

Here, Q is the local axial heat rate along a groove, and F_1 is a frictional coefficient for the liquid flow and is defined as:

$$F_1 = \frac{\mu_1}{KA_g \lambda \rho_1} \quad (65)$$

Here, μ_1 is the liquid viscosity, A_g is the groove cross-sectional area, λ is the latent heat of evaporation, ρ_1 is the liquid density, and K is the permeability of the groove structure and is calculated from the equation:

$$K = \frac{2\epsilon r_{h,1}^2}{(f_1 Re_1)} \quad (66)$$

where ϵ is the groove porosity, $r_{h,1}$ is the hydraulic radius of the groove structure defined as twice the cross-sectional area divided by the wetted perimeter, and $(f_1 Re_1)$ is a constant for laminar flow whose magnitude depends only on the geometry of the groove structure and can be obtained from Ref. 63.

CHAPTER 4
TRANSIENT BEHAVIOR OF HP/TES SYSTEM
UNDER PULSE HEAT LOADS APPLIED AT THE EVAPORATOR

In this chapter, we will examine two important points. First, how effectively can a PCM mitigate the adverse effects of pulse heat loads applied at the evaporator? Second, is there any disadvantage associated with installing phase-change material (PCM) in the vapor core? Also, if there are significant difficulties associated with such a system, will they be offset by the capabilities of the PCM itself?

It is clear that the main disadvantage of installing phase change material in the vapor core of a heat pipe is the accompanying reduction in the vapor flow area. This reduction in vapor flow area could cause vapor pressure drop and vapor velocity to increase, and thus decrease the heat pipe capability. Fortunately, the PCM itself can absorb a large portion of the heat loads during the melting process after pulse heat loads are applied. Some vapor will condense on the surface of PCM cylinders and reduce the vapor velocity and pressure drop. The net increase (or decrease) in vapor velocity and pressure drop due to the installation of PCM is strongly dependent on how efficiently the PCM can absorb the heat loads.

4.1 Limitations of the Heat Pipe

Circulation of working fluid is an important heat pipe design

factor. The greatest possible circulation is required to obtain a maximum heat transport capability from the heat pipe. Limitations on the heat transport capability include capillary pumping ability (capillary limit), choking of vapor flow (sonic limit), tearing of liquid off the liquid-vapor interface by vapor flowing at high velocity (entrainment limit), and disruption of the liquid flow by nucleate boiling in the wick (boiling limit).

Figure 4.1 shows how transport capability varies with the operating temperature for a screen-wrapped grooved heat pipe without anything installed in the vapor core. These data are based on a total heat pipe length of 1.0 m with evaporator, condenser and adiabatic sections of 0.3m, 0.3m and 0.4m, respectively. The heat pipe outside diameter is assumed to be 1.9 cm (3/4 in) with an inside diameter of 1.4 cm. Liquid sodium is used as the working fluid, and the screen wick has 200 meshes per inch. As one can see, within the operating temperature range between 900 and 1300 K, the entrainment limit places the greatest restrictions on heat transport capability. At 950 K, the entrainment limit is about 5.4 kW, which is equivalent to a uniform heat flux 30 W/cm^2 applied at the evaporator. If an empty cylinder was installed in the vapor core, the heat pipe capacity would be degraded due to the reduction in vapor flow area. Fig 4.2 shows the operation limits for the heat pipe with an empty cylinder with a radius of 0.4 cm mounted in the vapor core. The entrainment, capillary, and sonic limits are decreased due to installation of the empty cylinder. At an operating temperature of 950 K, the entrainment limit is decreased by about 33% to 3.6 kW, which is equivalent to a uniform heat flux 20 W/cm^2 applied at the heat pipe evaporator. Fortunately, filling the cylinder with PCM

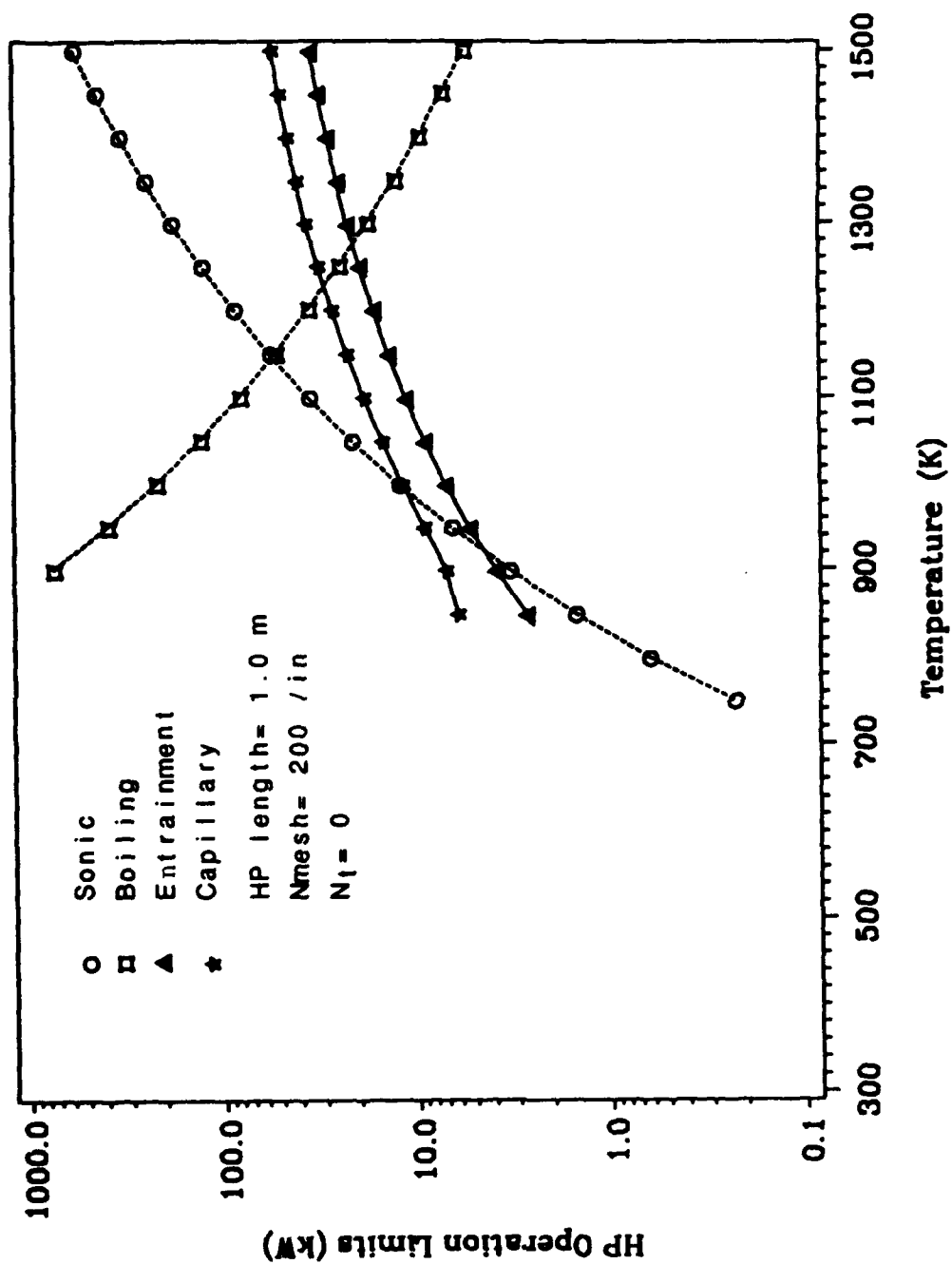


Figure 4.1 Operation limits for a grooved heat pipe without anything installed in the vapor core

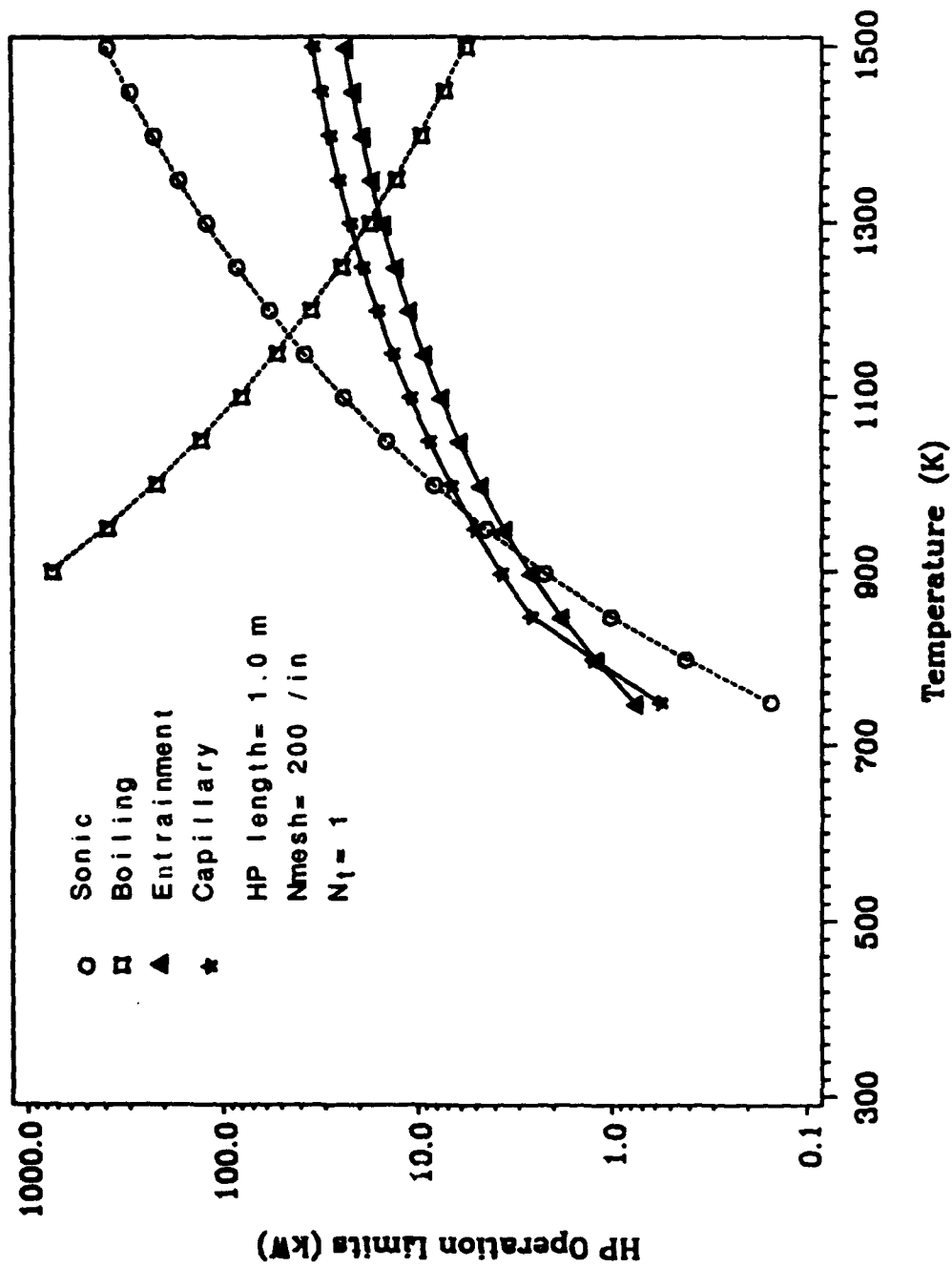


Figure 4.2 Operation limits for a grooved heat pipe with an empty cylinder mounted in the vapor core

can offset this disadvantage by absorbing a large portion of the heat loads during the melting process. Such a mechanism will be discussed in the last section of this chapter.

4.2 Operation Under Normal Conditions

In this section, we will see how the HP/TES system responds under the pulse heat loads which are less than the heat pipe operation limit. We have applied the numerical model, introduced in Chapter 3, to a heat pipe with 18 grooves using sodium as the working fluid. The material for the heat pipe container is assumed to be type 316 stainless steel. All axial and radial dimensions of the heat pipe are the same as those just discussed in connection with Fig 4.1. A uniform heat flux is applied to the evaporator, and heat is removed at the condenser by radiative heat transfer to the surroundings which are maintained at 0 K. The emissivity of the condenser wall surface is assumed equal to unity. Lithium hydride, which has a latent heat of 2.58×10^6 J/Kg and a melting temperature of 956 K, is used as the phase-change material.

For numerical modeling of the heat pipe wall and wicks, 8 and 40 nodes were chosen in radial and axial directions, respectively. Since the heat pipe could be divided into 18 identical land-and-groove subunits, only 4 nodes were needed in the angular direction for each unit once symmetry was invoked. The transient responses of three different HP/TES configurations were compared: (1) a heat pipe with one large empty cylinder installed in the vapor core, (2) a heat pipe with one large PCM cylinder, and (3) a heat pipe with six small PCM

cylinders. The radius of the single large cylinders is 0.4 cm while each of the small cylinders has a radius of 0.163 cm. These radii were chosen so that the large cylinder holds the same amount of PCM as the six small cylinders combined. The hydraulic diameter for vapor flow is about 0.82 cm for the heat pipe with a single large cylinder and about 0.75 cm for the one with six small PCM cylinders. For the numerical modeling of the PCM, 40 nodes in the radial direction were chosen for the large PCM cylinder and 16 nodes were used with the small one. A phase transition temperature interval of $2\Delta T_m = 10.0$ K was assumed and the time step $\Delta t = 0.1$ s has been used for all the examples in this report.

Figure 4.3 illustrates the transient response of four different HP/TES configurations when a higher heat load is suddenly applied to the evaporator. Before $t = 10$ s, all four different heat pipes are operating at steady-state under a uniform evaporator heat load $q = 4.3$ W/cm². The average heat pipe temperature is about 940 K. After $t = 10$ s, a higher heat load of $q = 10$ W/cm² is suddenly applied to the evaporator. As shown in the figure, the temperature of both heat pipes without PCM increases quite sharply. It should also be noted that the temperature of the heat pipe without anything installed in the vapor core shows no difference with that of the one mounted with an empty cylinder through the whole test period. The temperature of both heat pipes fitted with PCM also increases rapidly immediately right after the heat load is applied, but this steep temperature increase is arrested when the PCM reaches its fusion temperature where melting begins. One should also note that the temperature increase of the heat pipe with six small PCM cylinders is much slower than for the one with a single large PCM

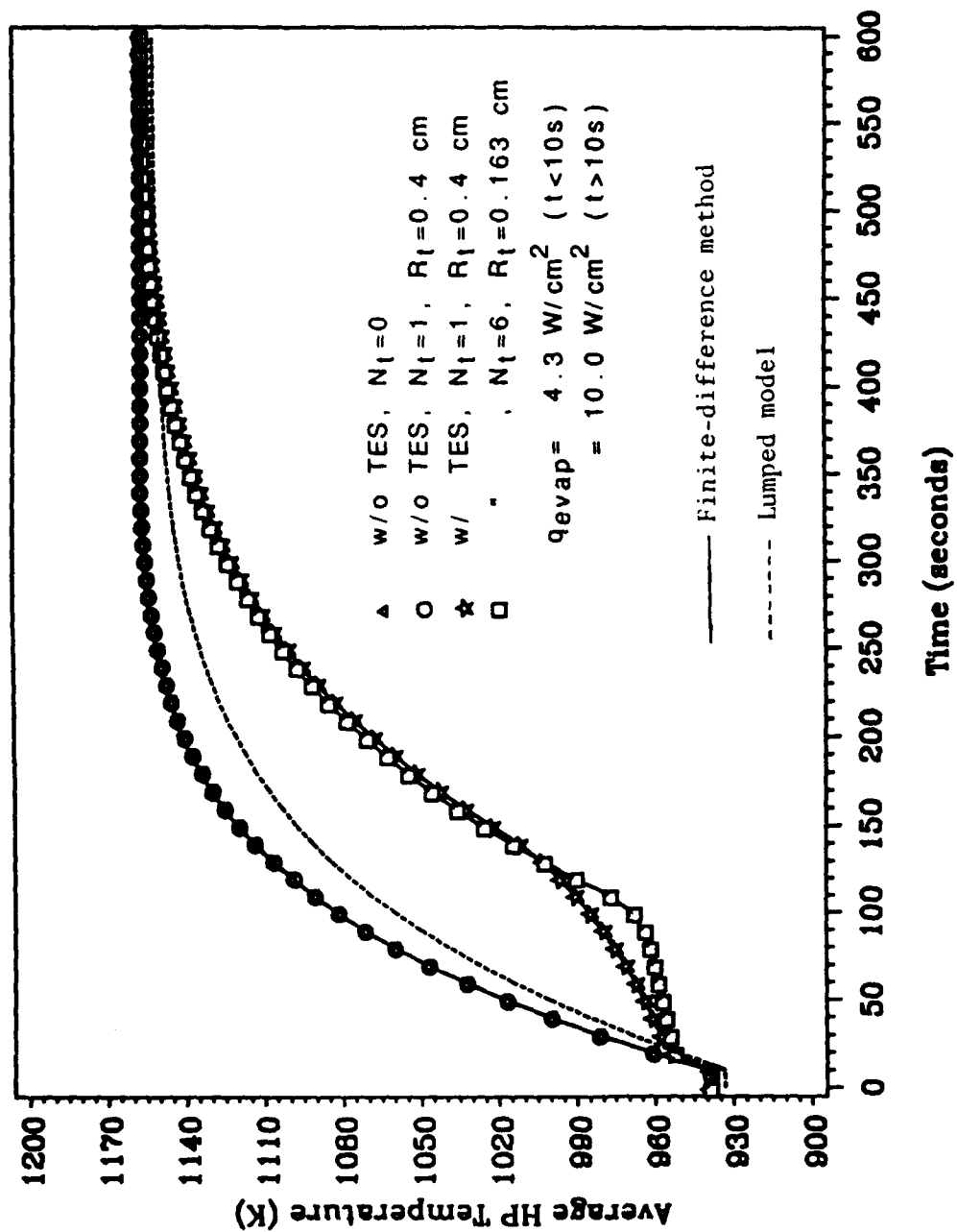


Figure 4.3 Transient response of heat pipes with a sudden increase in heat input from $q = 4.3$ to 10 W/cm^2

cylinder during the melting process. The smaller PCM cylinders have an advantage because their total heat transfer surface area is greater and their heat conduction path is shorter compared to the configuration with a single large PCM cylinder. However, the six small PCM cylinders will be completely melted earlier than a single large PCM cylinder. The six small PCM cylinders are completely melted at about $t = 100$ s, and the larger PCM cylinder does not completely melt until about $t = 130$ s. After the PCM has completely melted, the temperature of both heat pipes with PCM starts to increase rapidly until the heat pipes reach a new steady-state condition with $q = 10 \text{ W/cm}^2$. Both heat pipes without PCM reaches their new steady-state conditions at about $t = 350$ s. Due to the additional heat capacity of the phase-change materials, the other two heat pipes with PCM reach the steady-state condition somewhat later at about $t = 580$ s. We also applied a lumped model to predict the heat pipe transient behavior. As one can see, the results from the lumped model for the heat pipe without a PCM are in good agreement with those from the finite-difference method. The heat pipe temperature predicted by the lumped model averages about 10 K average lower than that obtained using the finite-difference method. This discrepancy arises because the heat removed from the condenser by radiation is overestimated by the lumped model, which uses the average heat pipe temperature as the condenser wall surface temperature.

An interesting output from the finite-difference solution is the fraction of the heat conducted through the heat pipe wall at the evaporator which is absorbed by the PCM during the melting process. In other words, one would like to know what percentage of the heat conducted into the vapor core significantly contributes to the vapor

flow. As shown in Fig 4.4, we define \dot{Q}_{in} as the total heat rate transferred through the heat pipe wall at the evaporator and \dot{Q}_t as the total heat rate absorbed by the PCM. Both \dot{Q}_{in} and \dot{Q}_t are estimated from the temperature distributions near the heat pipe inner wall and the outside surfaces of the PCM cylinders.

Figure 4.5 plots the ratio between \dot{Q}_t and \dot{Q}_{in} for the same operating conditions depicted in Fig 4.3. For the heat pipe with a single large PCM cylinder, this ratio reaches 46% and then declines to 27% before the PCM is fully melted. If the heat pipe is equipped with six small PCM cylinders, the ratio of \dot{Q}_t to \dot{Q}_{in} reaches 52% and then decreases to 40% before the PCM is fully melted. Apparently if the heat pipe contains a single large PCM cylinder, no more than 73% maximum of the heat conducted through the heat pipe wall contributes to the vapor flow during the PCM melting process. For the TES configuration using six small PCM cylinders, the maximum fraction influencing vapor flow is only 60%. These results imply that the increases in vapor pressure drop and vapor velocity due to installation of the PCM can be significantly offset by the capabilities of the PCM itself during the melting process.

Figures 4.6a and 4.6b show the axial variation of vapor pressure and temperature for four different HP/TES configurations at $t = 100$ s. The heat pipes without PCM have vapor temperature of 1082 K, which is much higher than that of the other two heat pipe designs which incorporate PCM. The heat pipe with a single large cylinder of phase-change material has a vapor temperature of 985 K, and distributing the PCM among six small cylinders lowers the vapor temperature to only

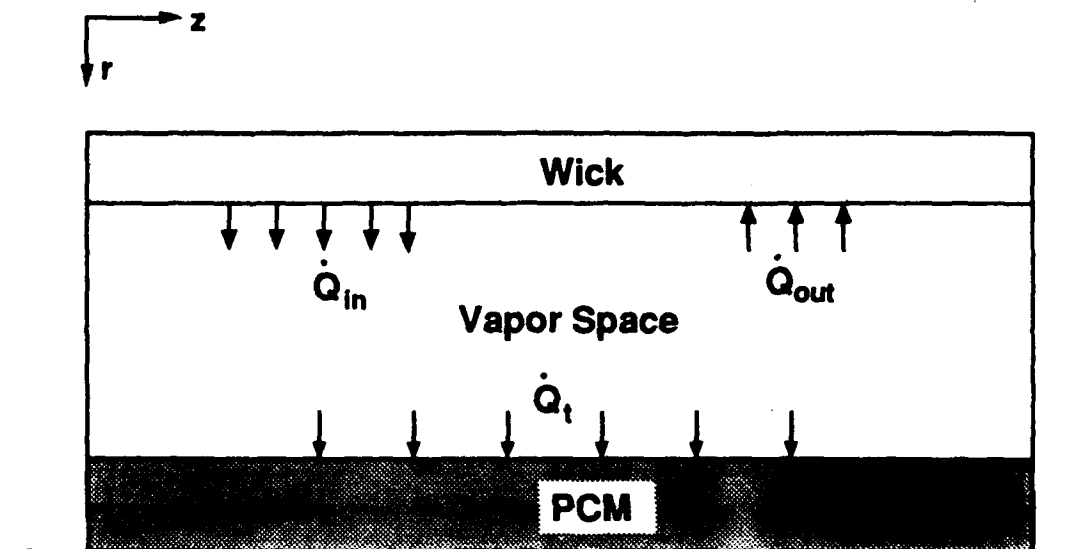


Figure 4.4 Definition of \dot{Q}_{in} and \dot{Q}_t

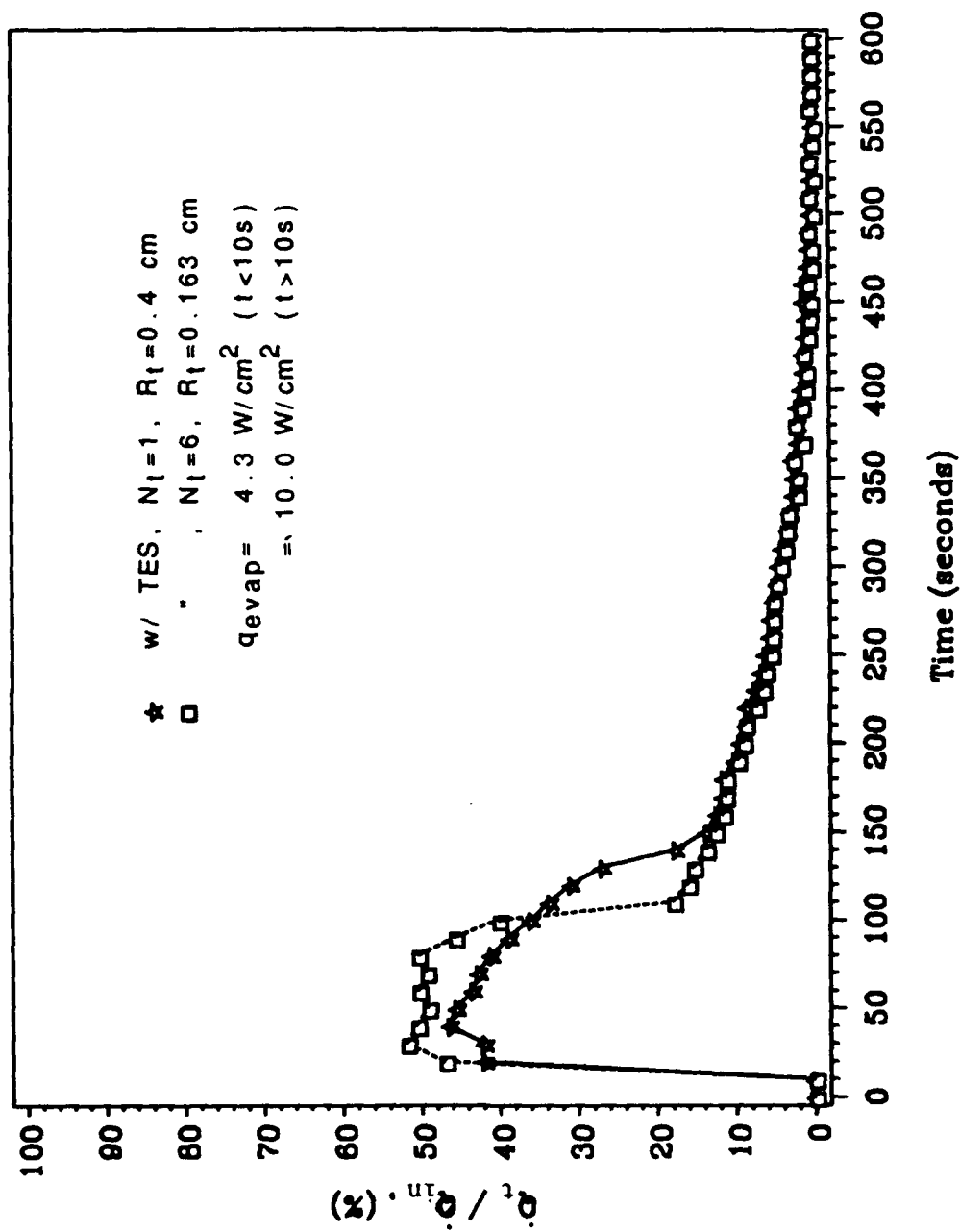


Figure 4.5 The ratio between \dot{Q}_t and \dot{Q}_{in} for the same operating conditions depicted in Fig. (4.3)

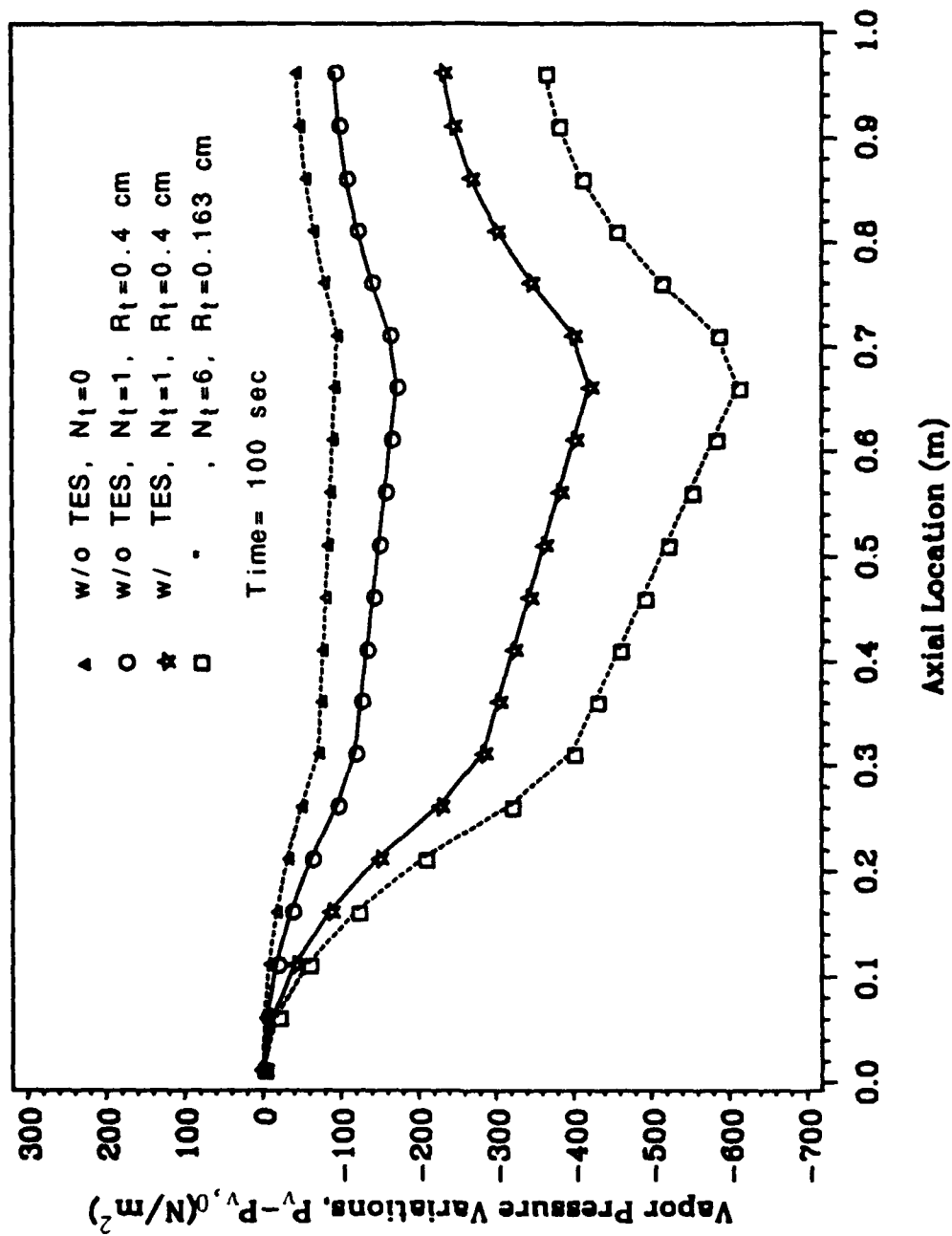


Figure 4.6a Axial variation of vapor pressure at $t = 100$ s for the same operating conditions depicted in Fig. 4.3

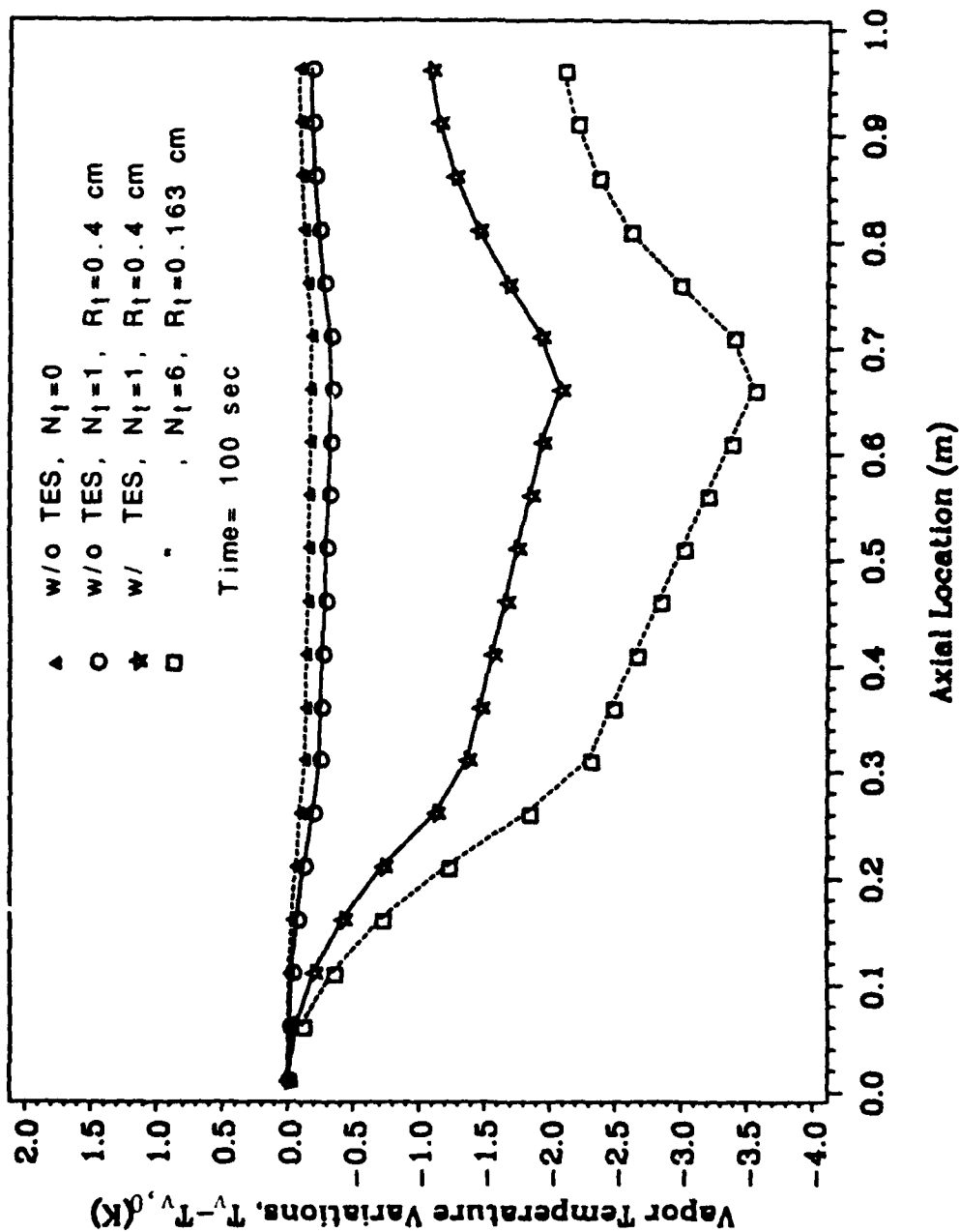


Figure 4.6b Axial variation of vapor temperature at $t=100$ s for the same operating conditions depicted in Fig. 4.3

968 K. The results in Figs 4.6a and 4.6b indicate that the vapor pressure and temperature drops are strongly dependent on the operating vapor temperature. A lower vapor temperature will result in a lower speed of sound in the vapor and a higher Mach number for the flow. From Eq. (53) in Chapter 3, one can see that higher Mach numbers will lead to higher friction coefficients, resulting in larger total pressure drops. Higher Mach numbers also cause the static pressure to drop even more. In the adiabatic section, much less mass blowing or suction will take place. Thus, the pressure decreases there are mainly due to friction and will be smaller than those occurring in the evaporator. As expected, these pressure and temperature losses are partially recovered in the condenser section. Fig 4.6a also shows the vapor pressure drop of the heat pipe without anything installed in the vapor core is smaller than that of the one mounted with an empty cylinder due to larger vapor flow area.

In Fig 4.7, the results from Fig 4.3 are compared with those obtained using a larger time step and wider grid spacings. The time step was increased from 0.1 second to 0.5 second and the grid spacings Δr , Δr_t and Δz have been doubled. As shown in the figure, the longer time step and coarser grid mesh have little effect on the solution. For all practical purposes, the numerical results presented in Fig 4.3 are essentially independent of the time step and grid spacing.

The transient responses of the heat pipes with a pulse heat load applied to the evaporator from $t = 10$ s to $t = 100$ s are shown in Figs 4.8 and 4.9. As can be observed from Fig 4.8, the heat pipe responds very quickly, and the temperature starts to decrease as soon as the pulse heat load is removed at $t = 100$ s. The temperature of the heat

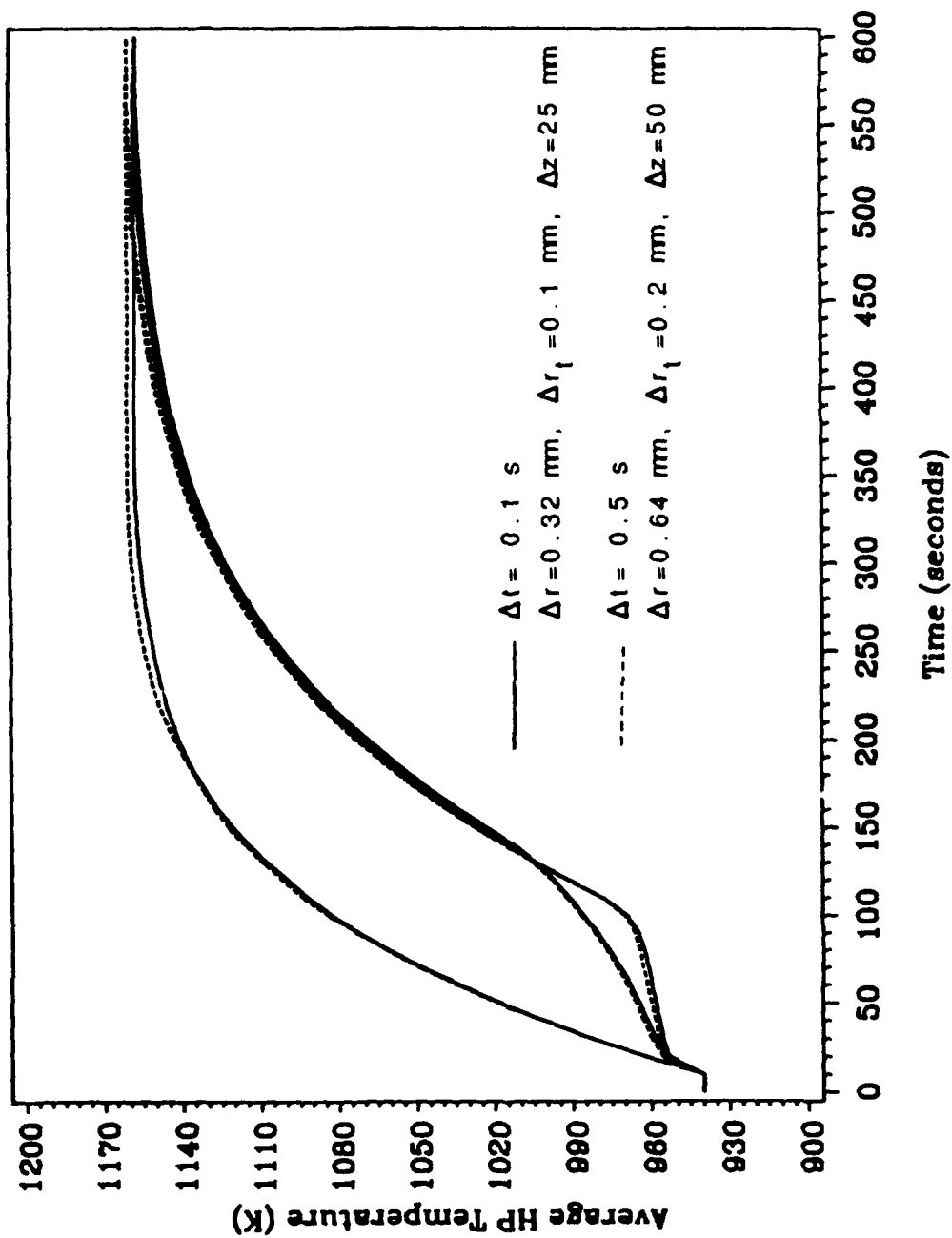


Figure (4.7) Comparison of results from Fig. 4.3 and those obtained using a larger time step and wider grid spacings

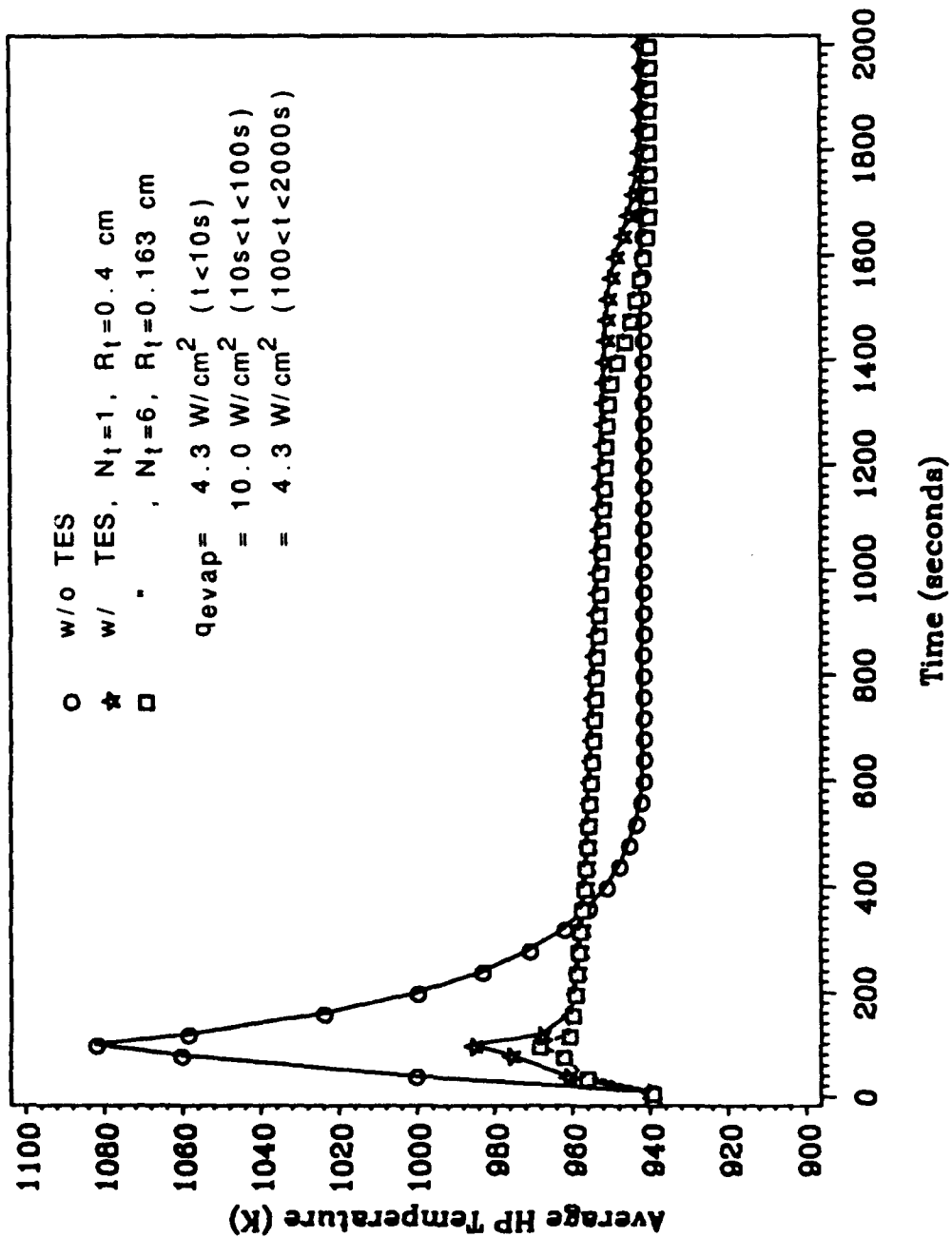


Figure 4.8 Transient response of heat pipes with pulsed heat loads $q = 10 \text{ W/cm}^2$

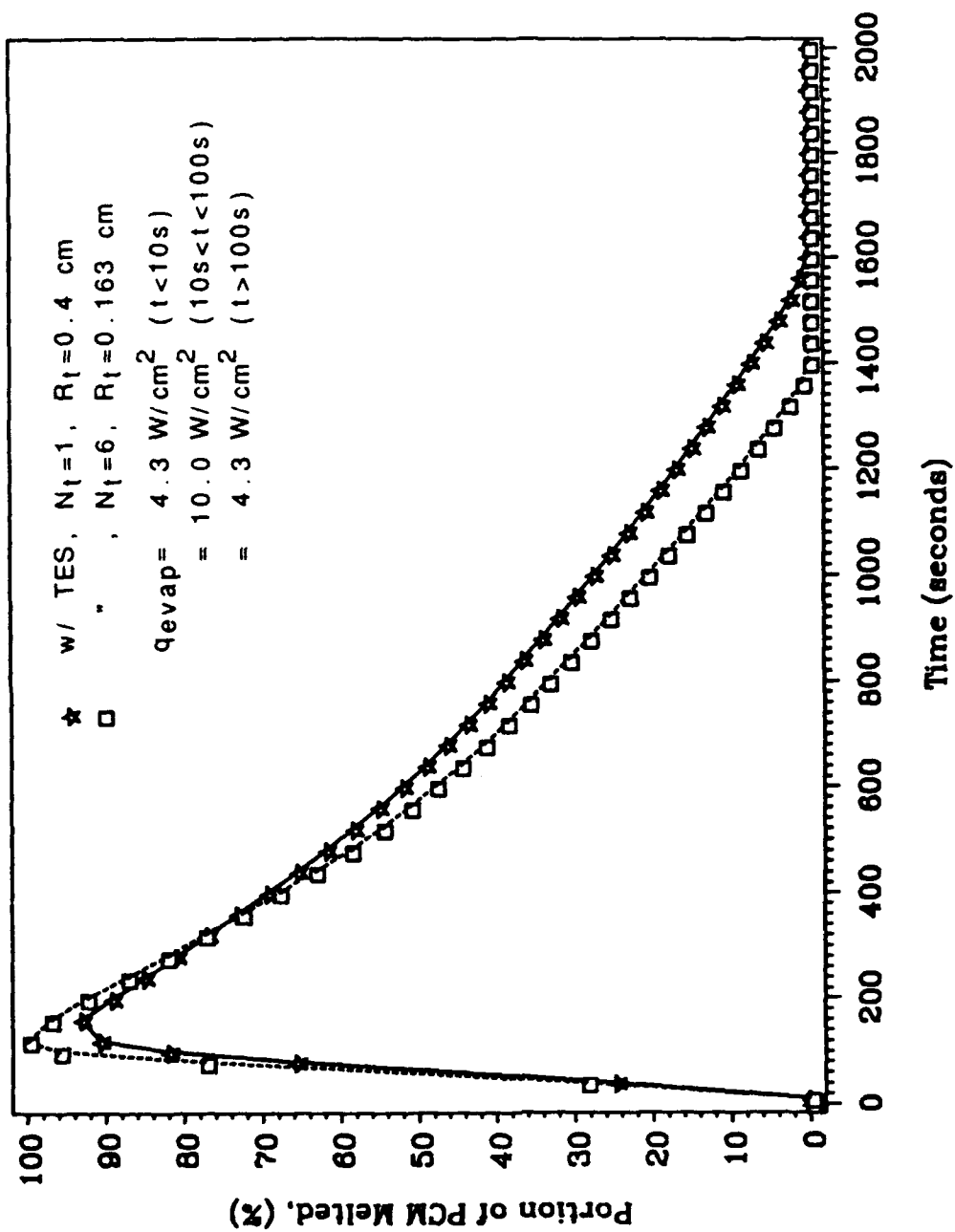


Figure 4.5 Portion of PCM melted versus time for pulsed heat loads $q = 10 \text{ W/cm}^2$

pipe without a PCM decreases quite rapidly after the pulse heat load is removed. The temperature of the other two designs with PCM also decreases immediately after the pulse heat load is removed, but the decrease becomes very slow when the PCM reaches its melting point and starts to solidify. The six small PCM cylinders will become completely solidified sooner than a single large PCM cylinder. After the PCM cylinders have completely solidified, the temperature of both heat pipes incorporating a PCM begins decreasing again and the heat pipes return to their initial steady-state condition with $q = 4.3 \text{ W/cm}^2$. For the heat pipe with six PCM cylinders and the design with one large PCM cylinder to return to the initial steady-state conditions after the pulse heat load is removed requires about 1,620 seconds and 1,740 seconds, respectively. Fig 4.9 shows the percentage of PCM melted versus time for the same cases covered in Fig 4.9. One can see that the phase-change material does not respond as fast as the heat pipe temperature does. In fact, after the pulse heat load is removed at $t = 100 \text{ s}$, 2% more of the six small PCM cylinders and 10% more of the single large PCM cylinder will still be melted by residual heat. It should also be noted that the small PCM cylinders solidify more quickly than the larger one can.

Figures 4.10 and 4.11 illustrate the results for the transient response of the heat pipes with periodic pulse heat loads. The time period of the pulses is 200 s and each pulse heat load lasts for 20 s. These periodic pulse heat loads are applied before the heat pipes have enough time to return to their initial steady-state operating condition. The temperature response on each cycle is similar to the results shown in Fig 4.8. On the other hand, temperature of the heat pipe without

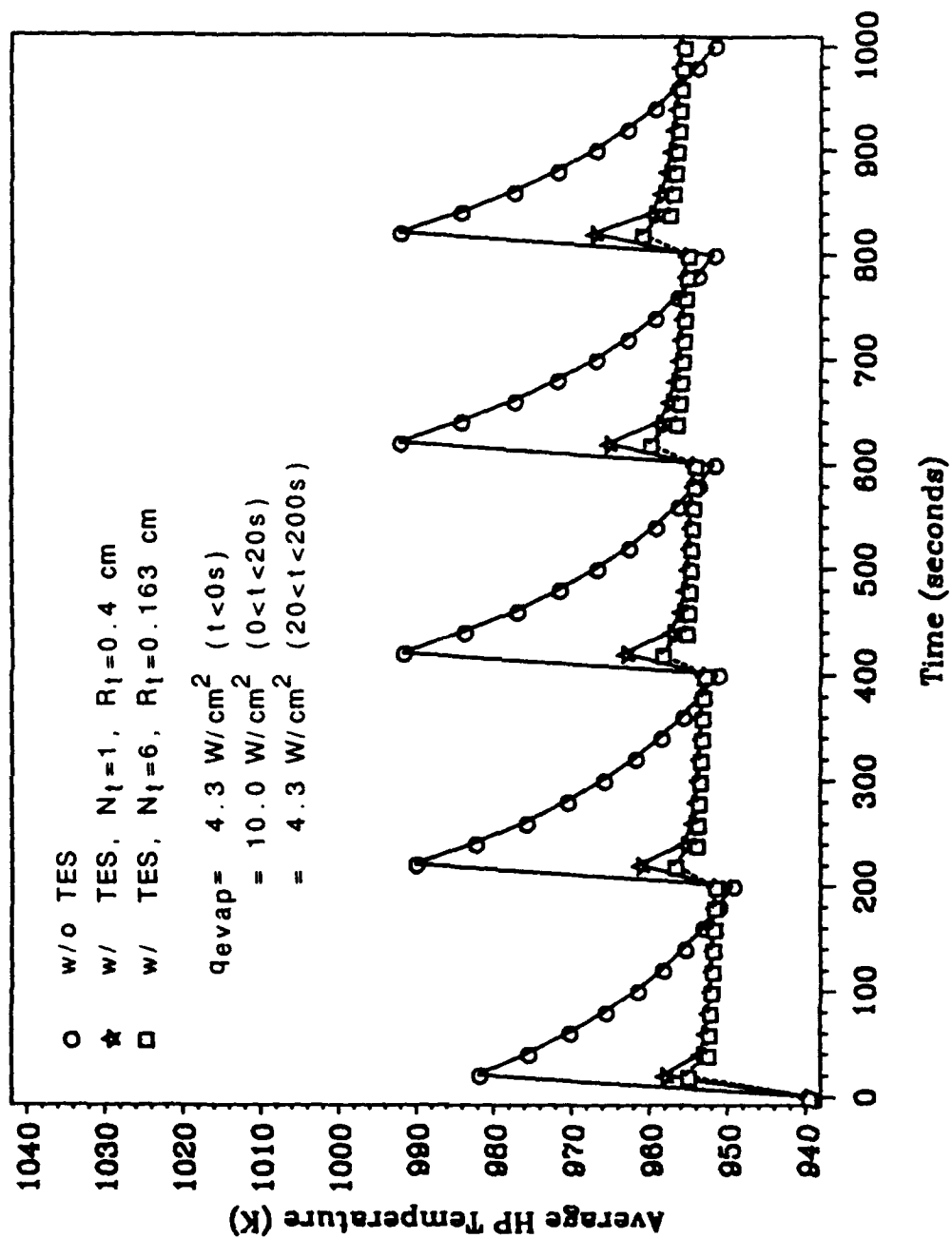


Figure 4.1(i) Transient response of heat pipes with periodic pulsed heat loads
 $q = 10 \text{ W/cm}^2$

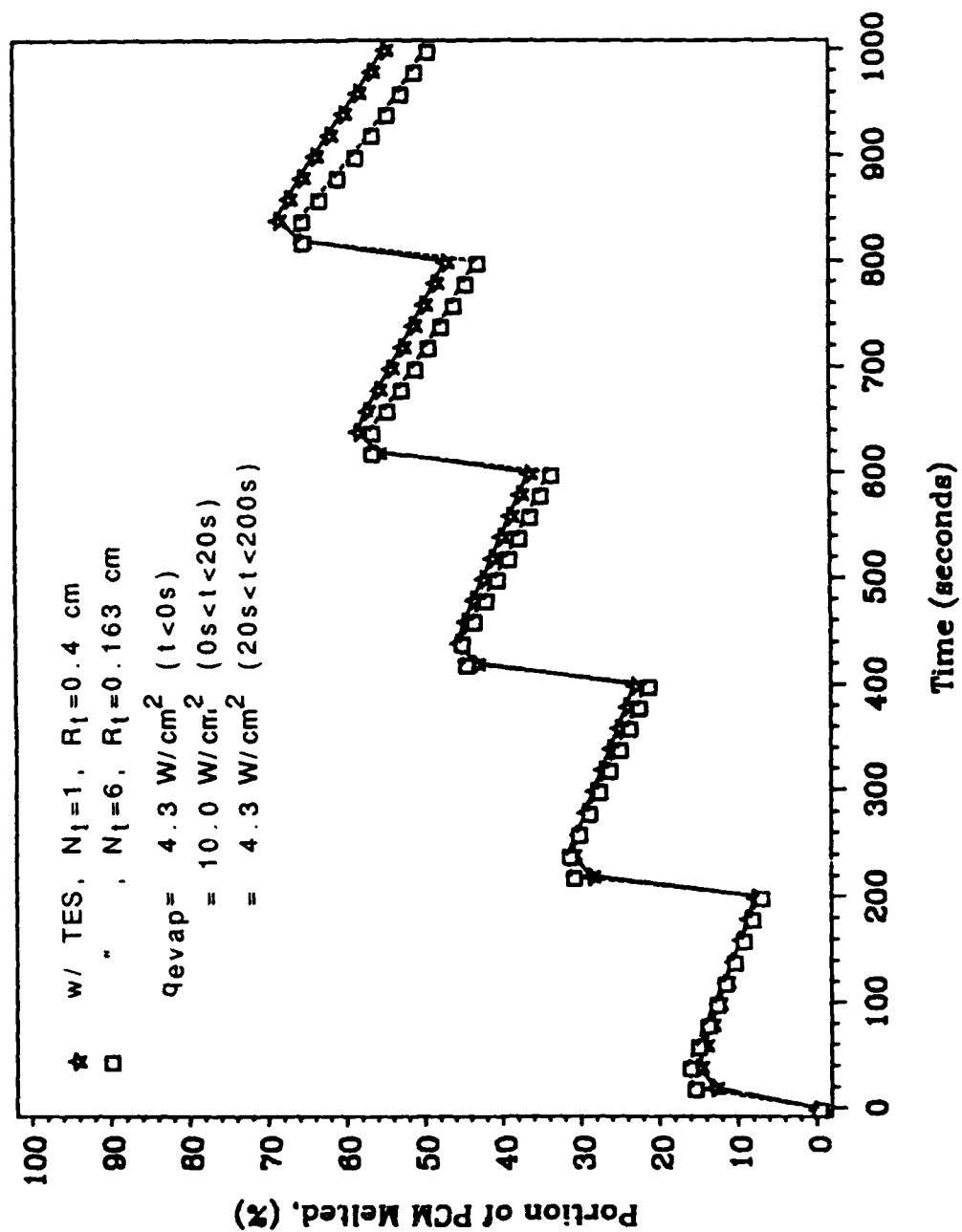


Figure 4.11 Portion of PCM melted versus time for periodic pulsed heat loads
 $q = 10 \text{ W/cm}^2$

a PCM temperature regulation system goes up and down periodically. The temperature of the heat pipe with six small PCM cylinders remains almost constant over several cycles due to very efficient melting and solidification. It is clear from Fig 4.11 that the percentage of molten PCM for both heat pipes containing PCM cylinders continues to increase as the cycles persist. This increase in the melted PCM fraction over time takes place because the PCM does not have enough time during the low-power periods to solidify completely before the next pulse cycle begins.

4.3 Operation Near HP/TES Limitation

As was mentioned earlier, the main drawback to installing PCM in the vapor core of a heat pipe, neglecting the PCM ability to absorb a portion of the heat load during melting, is that the heat pipe capability is degraded due to a reduction in the vapor flow area. From Fig. 4.2, the heat transport limitation for a heat pipe with a large empty cylinder at temperature 950 K is equivalent to a uniform heat flux of 20 W/cm^2 applied to the evaporator. In this section, we will examine the transient response of the HP/TES system under pulse heat loads near this heat pipe limitation to see if the decrease in heat pipe capability from the reduction in vapor flow area can be recovered.

Figure 4.12 shows the transient response of three different HP/TES configurations when a pulse heat load near the heat pipe limitation is suddenly applied to the evaporator. Before $t = 10 \text{ s}$, all three different heat pipes are operating at steady-state under a uniform

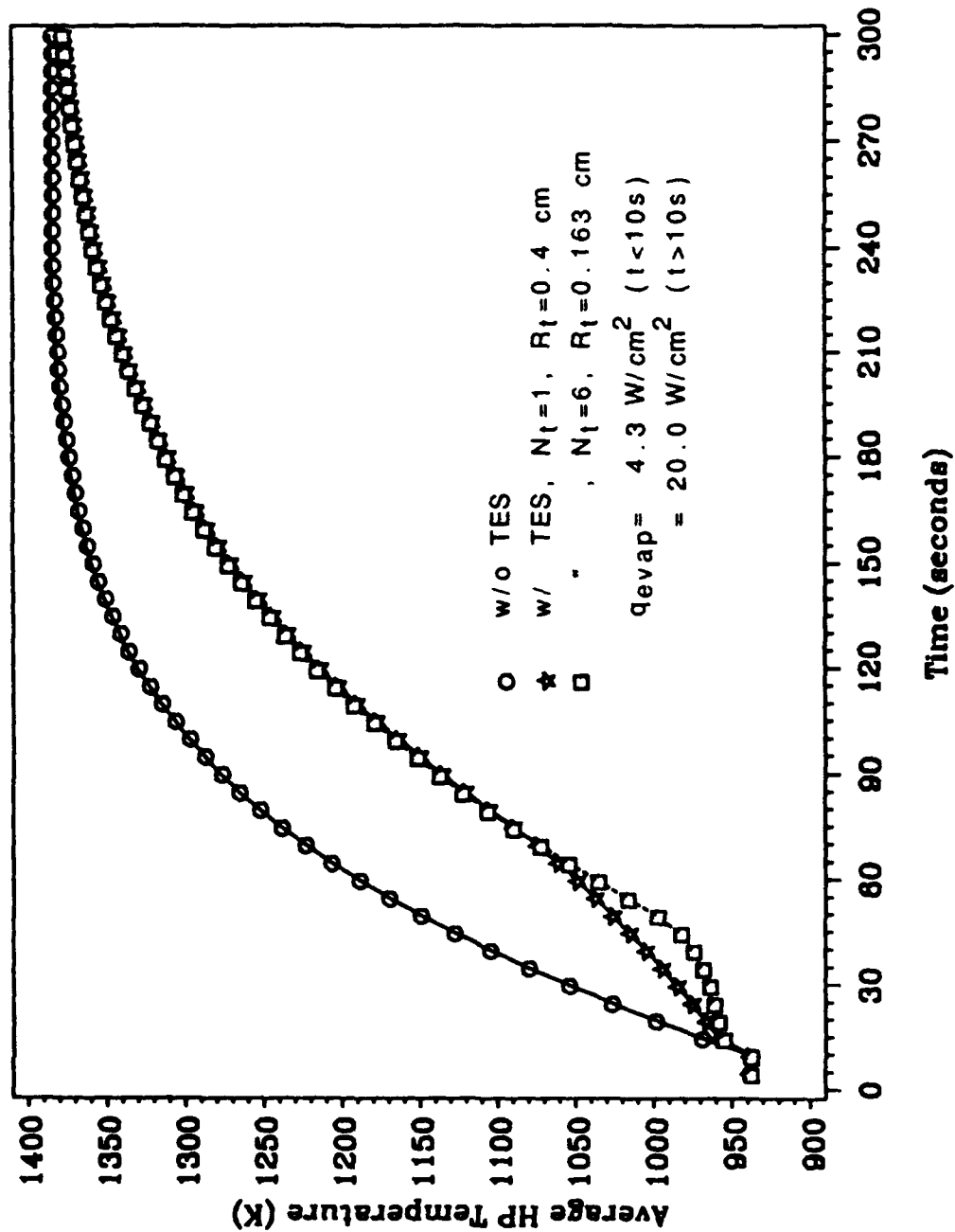


Figure 4.12 Transient response of heat pipes with a sudden increase in heat inputs from $q = 4.3$ to 20 W/cm^2

heat load $q = 4.3 \text{ W/cm}^2$ in the evaporator. The average heat pipe temperature is about 940 K. After $t = 10 \text{ s}$, a higher heat load of $q = 20 \text{ W/cm}^2$ will be applied to the evaporator. As shown in the figure, the trend of the temperature increases for all three heat pipes is similar to the results seen in Fig 4.3 with lower pulse heat loads. However, the PCM will be fully melted much earlier under the higher pulse heat load. The six small PCM cylinders will finish melting at about $t = 50 \text{ s}$ while the single larger PCM cylinder does not completely melt until about $t = 70 \text{ s}$.

Figure 4.13 depicts the axial variation of liquid and vapor pressure for the heat pipe without a PCM at $t = 12 \text{ s}$. At this moment, the heat pipe has the greatest liquid and vapor pressure drops due to the high liquid and vapor mass flow rates and low heat pipe temperature. Apparently, the vapor pressure drop dominates the liquid pressure drop for this type of heat pipe. As one knows, the heat pipe capillary limit is strongly dependent on the overall liquid and vapor pressure drops. Thus, for this type of heat pipe, the effect of the liquid pressure drop on the heat pipe capillary limit can be neglected.

The total heat rates transferred through the heat pipe wall at the evaporator for three different heat pipes are plotted in Fig 4.14. The total pulse heat load applied at evaporator is $\dot{Q}_e = 3.64 \text{ kW}$ (which is equivalent to a uniform heat flux $q = 20 \text{ W/cm}^2$) after $t = 10 \text{ s}$. For the heat pipe without a PCM, only $\dot{Q}_{in} = 2.8 \text{ kW}$ is transferred through the heat pipe wall into the vapor core at $t = 20 \text{ s}$. This reduction in the heat transfer rate arises because a large portion of the heat load is absorbed by the heat pipe wall due to the rapid temperature increases

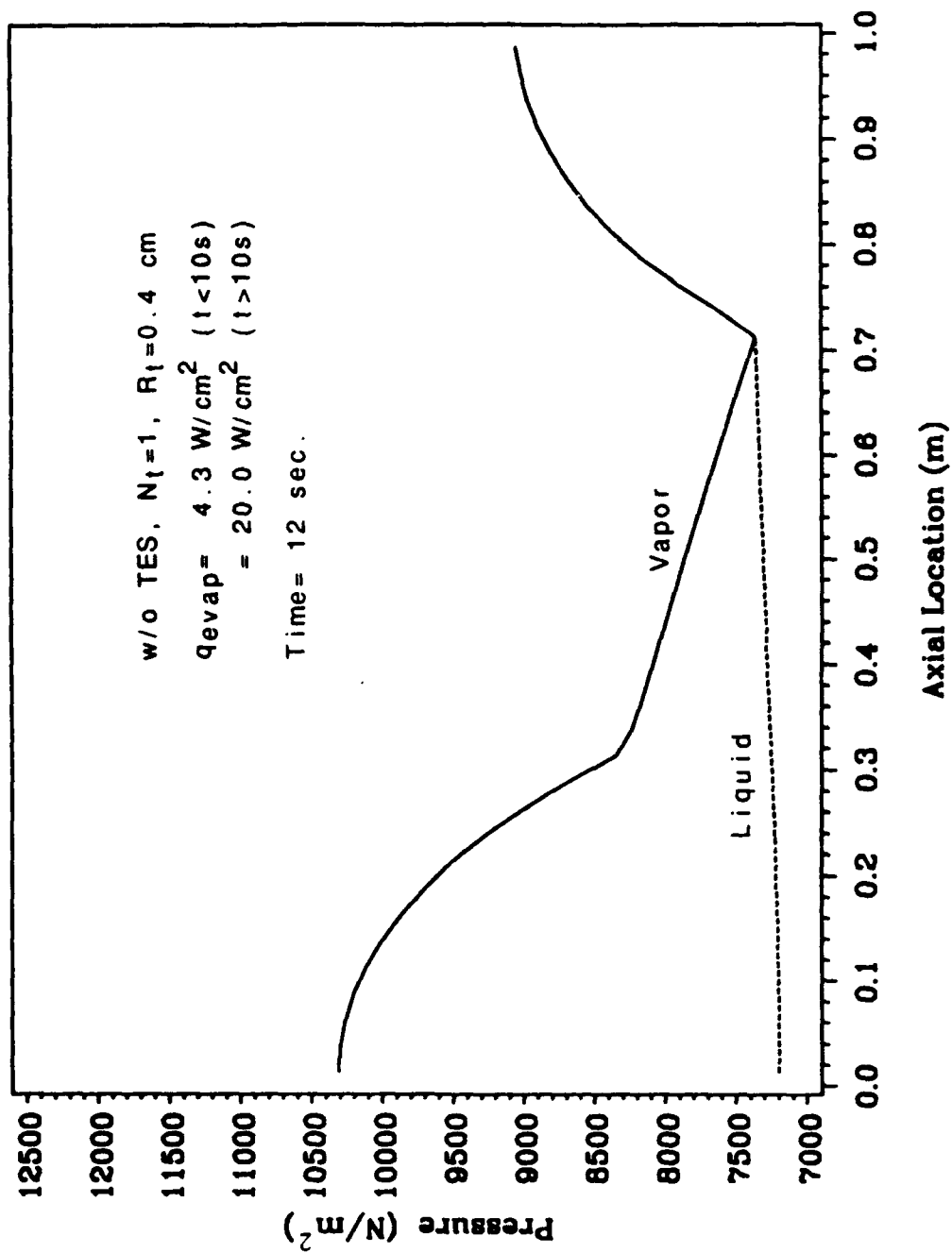


Figure 4.13 Axial variation of liquid and vapor pressure at $t = 12$ s for the same operating conditions depicted in Fig. 4.12

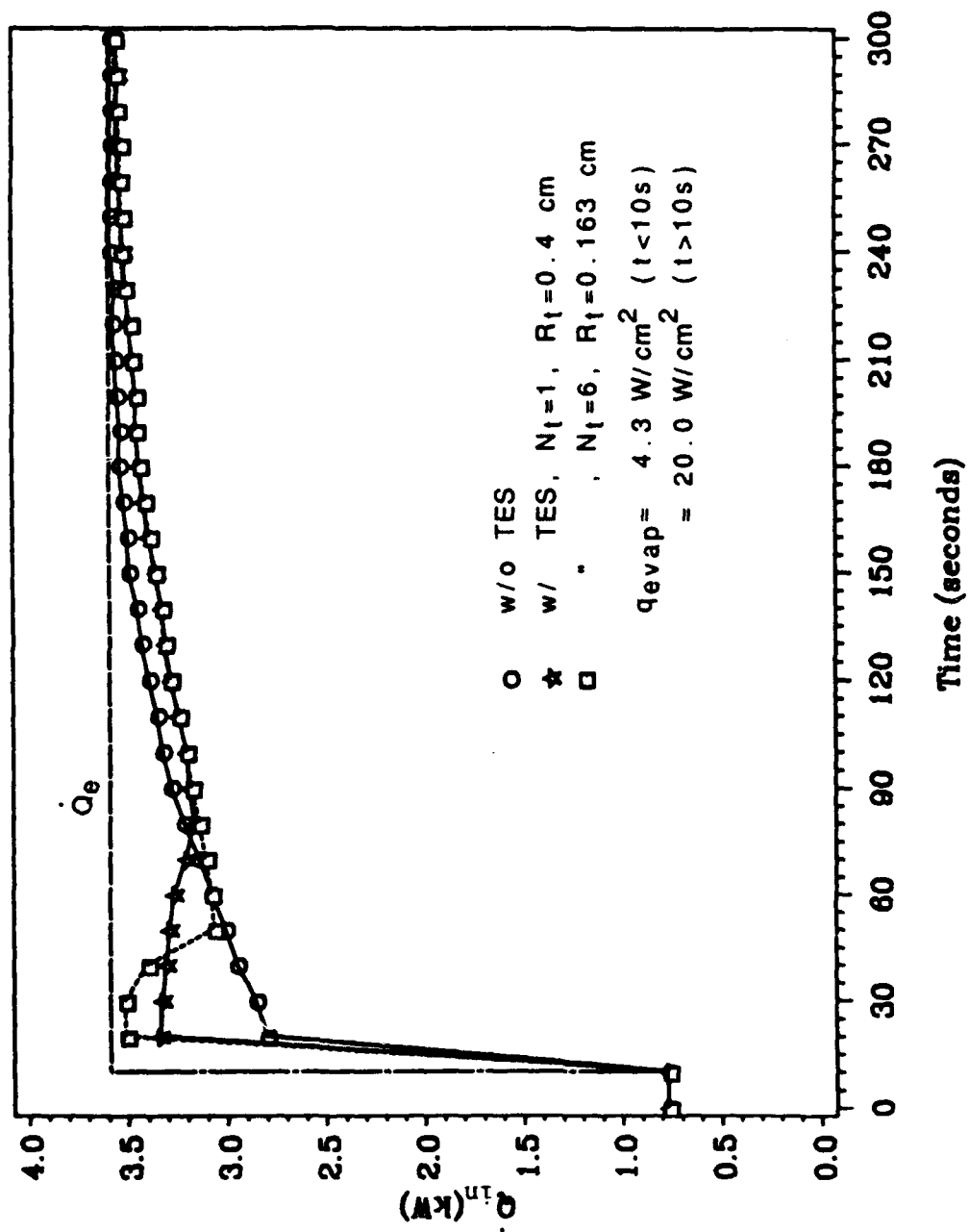


Figure 4.14 Variation of \dot{Q}_{in} for the same operating conditions depicted in Fig. 4.12

taking place at this moment. The \dot{Q}_{in} value rises gradually once the heat pipe temperature increase slows down, and finally approaches \dot{Q}_e upon reaching another steady-state. On the other hand, for both heat pipes with PCM most of the heat loads are transferred through the heat pipe wall into the vapor core at $t = 20$ s. Heat transfer to the vapor core is more efficient for the PCM designs because the heat pipe temperature increases are being slowed by the PCM melting process. The \dot{Q}_{in} value for both heat pipes with PCM remains almost constant throughout the melting process. It then drops suddenly as soon as the PCM is completely melted, and the heat pipe temperature starts to increase rapidly.

Figure 4.15 shows the ratio \dot{Q}_t/\dot{Q}_{in} for both heat pipes equipped with PCM and operating under pulse heat loads near the heat pipe limitation. It is quite apparent that the PCM responds very quickly to pulse loading. The PCM starts to melt and absorbs a large portion of the heat immediately after the pulse heat loads are applied. For the heat pipe with one large PCM cylinder, this ratio reaches a maximum of 58% and then decreases to 38% before the PCM is completely melted. For the one with six small PCM cylinders, the ratio \dot{Q}_t/\dot{Q}_{in} peaks at 71% and then declines to 53% when the PCM is totally melted. In effect, the heat pipe with one large PCM cylinder has at most 62% of the heat which is conducted through the heat pipe wall contributing to the vapor flow during the PCM melting process. In the design with six small PCM cylinders, the maximum fraction adding to the vapor flow is only 47%. As we mentioned earlier, the decrease in the vapor flow area due to the

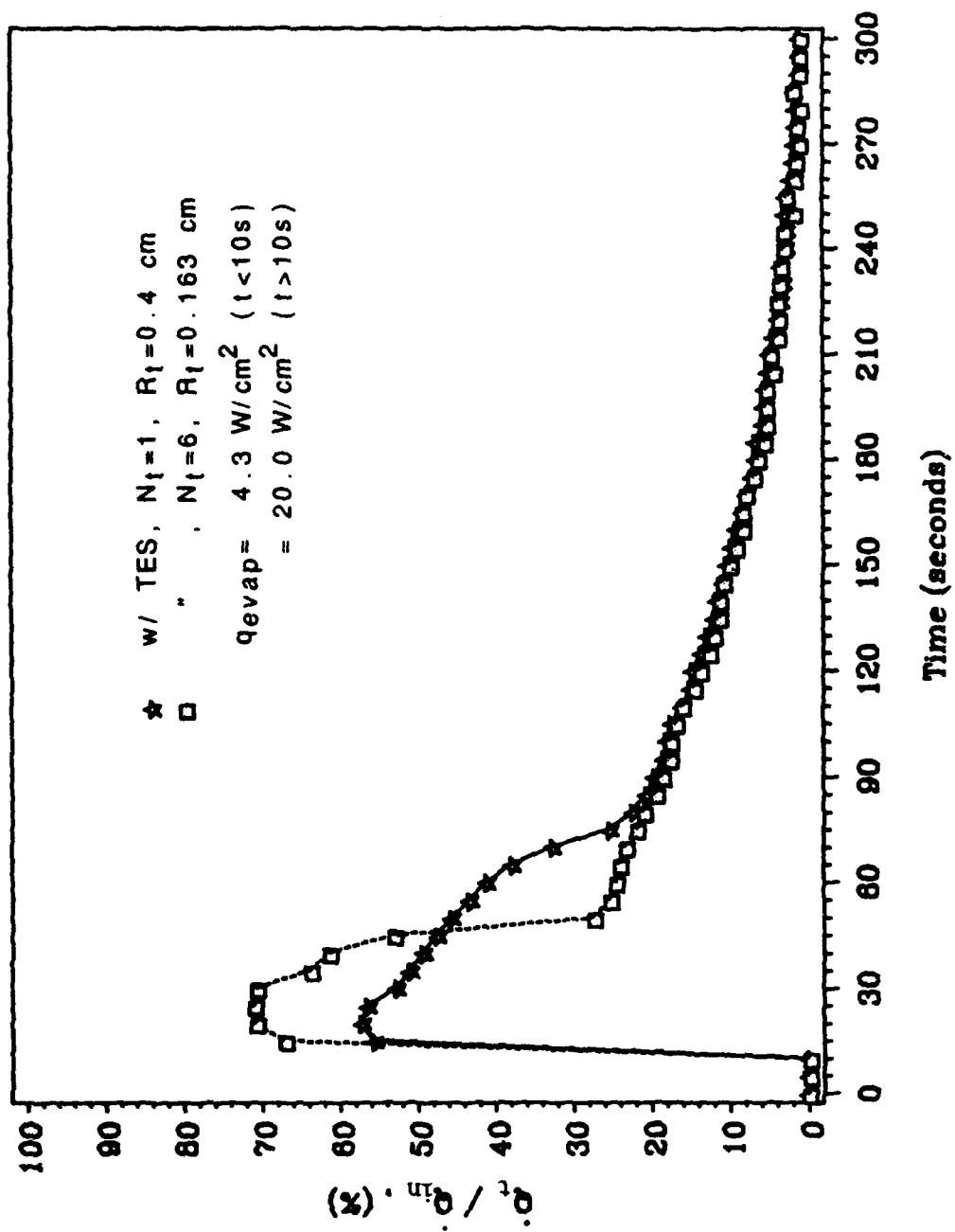


Figure 4.15 The ratio between \dot{Q}_t and \dot{Q}_{in} for the same operating conditions depicted in Fig. 4.12

installation of PCM causes the heat pipe capability to decrease by about 33%. From the results shown in Fig 4.15, it is clear that this decrease in heat pipe capability can be completely offset by the capabilities of the PCM itself during the melting process.

Comparing the results between Fig 4.5 and Fig 4.15, one finds that the ratio \dot{Q}_t/\dot{Q}_{in} is larger with higher pulse heat loads during the PCM melting process. Since the heat pipe temperature remains about the same during the PCM melting process for both pulse heat loads, the heat removed from the condenser by radiation will also be similar. Thus, the percentage of the heat loads directly contributing to the vapor flow during the PCM melting process will be lower under higher pulse heat loads. We can, therefore, predict that the HP/TES system can operate without burnout under uniform heat fluxes even greater than $q = 30 \text{ W/cm}^2$, the heat pipe limitation present without anything installed in the vapor core. Not only can the PCM recover the decrease in heat pipe performance due to the reduction in vapor flow area, but it can actually increase heat pipe transport capability.

In the design of a HP/TES system, one should choose a PCM with a melting point slightly higher than the normal operating temperature. Then if a pulse heat load higher than the heat pipe limitation is applied, the PCM can respond fast enough to begin melting and absorb some of the heat before the heat pipe reaches its operating limit and burns out. To reduce the chance of completely melting during the pulse period, the latent heat of fusion of the chosen PCM should also be as large as possible.

The concept of incorporating phase-change material inside a

low-temperature heat pipe (such as a water heat pipe) is also sound if the goal is to limit the temperature extremes encountered when the heat load is time-dependent. For most low temperature heat pipes, the vapor pressure drop is small, and vapor flow usually does not play an important role in determining the heat pipe capability. Thus the increases in the vapor pressure drop and vapor velocity caused by the reduction in flow area would not have a significant effect on heat pipe capability.

CHAPTER 5

TRANSIENT BEHAVIOR OF HP/TES SYSTEM

UNDER REVERSED-PULSE HEAT LOADS APPLIED AT THE CONDENSER

The transient behavior of a high-temperature axially grooved heat pipe (HP) which incorporates thermal energy storage (TES), under reversed-pulse heat loads applied at the condenser is presented in this chapter. Liquid sodium, which is used to remove the heat released by a power generator, circulates through a HP/TES cooling device from which the heat is rejected into space. The transient response of three different HP/TES configurations under reversed-pulse heat loads are compared: (1) a heat pipe with a large empty cylinder installed in the vapor core, (2) a heat pipe with a single large PCM cylinder, and (3) a heat pipe with six small PCM cylinders. The results for a heat pipe with and without an adiabatic section will be presented, respectively.

5.1 Description of The Problem

Future space missions will involve thermal transport devices with the ability to handle reversed-pulse heat loads. Figure 5.1 shows a schematic diagram of the cooling system for a power generator. A certain amount of heat is continuously being released by the power generator and removed by the liquid sodium loop. The sodium loop circulates through the HP/TES cooling device, where the heat is rejected into space. Under normal conditions, the system is operating at steady-

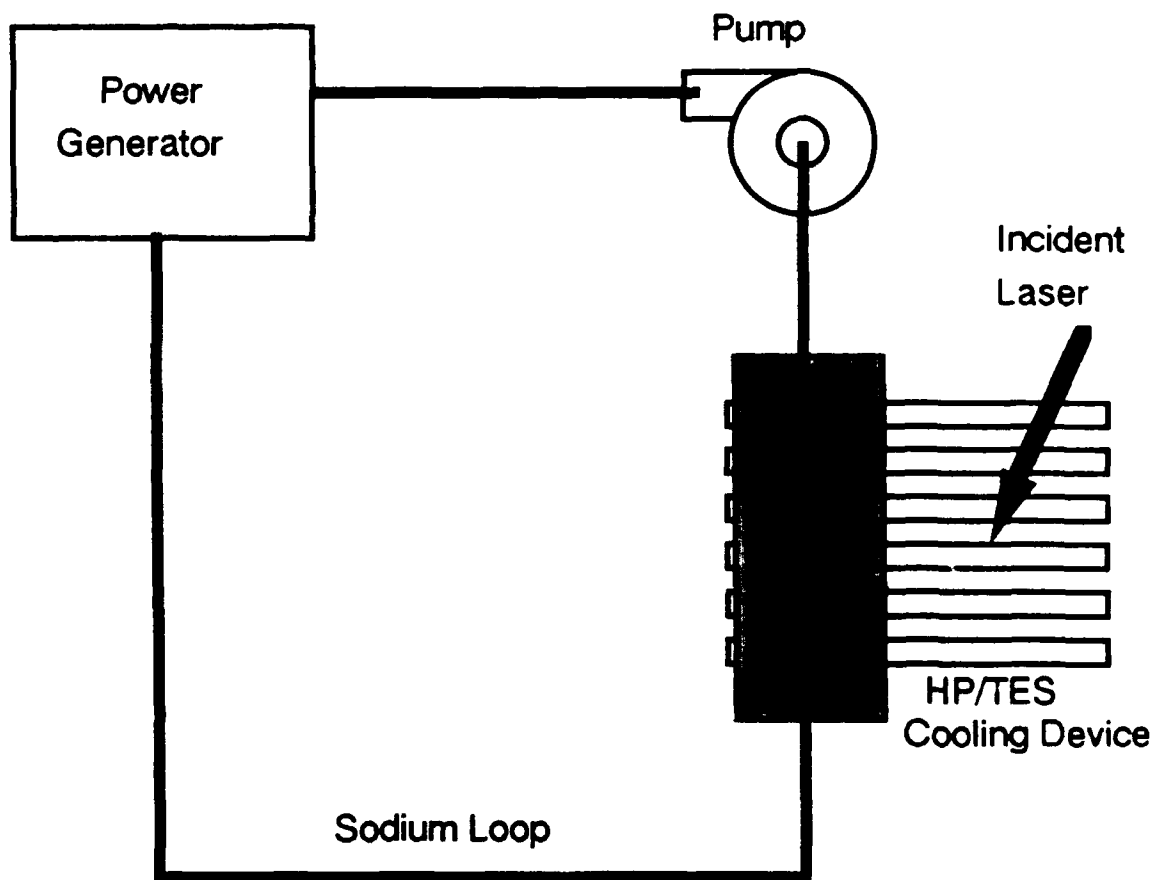


Figure 5.1 Schematic diagram of the cooling system for a power generator

state. Suddenly, an incident laser strikes the condenser section of the HP/TES cooling device. Under such severe operating conditions, the heat released by the power generator can no longer be removed by the HP/TES cooling device, and the reversed-pulse heat load caused by the incident laser will be reversely transferred back into the liquid sodium loop. Incorporation of thermal energy storage (TES) into heat pipe rejection systems can be a promising method to mitigate damage from reversed-pulse heat loads. The transient response of different heat pipes (with or without phase-change material) under reversed-pulse heat loads will be studied in this chapter.

5.2 Analytical Model

The numerical model used in this chapter to predict the transient response of the HP/TES cooling system has already been described in Chapters 3 and 4. In the numerical solution, the heat pipe evaporator wall surface temperature was assumed equal to the sodium loop temperature because the surface heat transfer coefficient is very high. The liquid sodium loop temperature can be predicted by the following equation:

$$C_{\text{loop}} \frac{\Delta T_{\text{loop}}}{\Delta t} = \dot{Q}_g - \dot{Q}_e \quad (67)$$

Since this study focused only on a heat pipe unit, it should be noticed that C_{loop} and \dot{Q}_g in Eq. (67) are the total sodium loop heat

capacitance and the heat rate released from the power generator, respectively, divided by the total number of heat pipes in the system. The heat rate released from the power generator \dot{Q}_g is always positive and remains constant. \dot{Q}_e is defined as the heat rate transferred from the sodium loop to the heat pipe, and is evaluated from the temperature gradient in the heat pipe wall. It can become negative when a reversed heat load is applied. If liquid sodium with velocity 1 m/s is circulating through the heat pipe, a very high surface heat transfer coefficient (about $5 \cdot 10^4 \text{ W/m}^2\text{K}$) can be obtained. Since the heat transfer coefficient is so high, we will assume that the heat pipe evaporator wall surface temperature is equal to the sodium loop temperature.

We also applied a simple lumped-heat-capacity model to predict the transient behavior of the heat pipe without a PCM. The average heat pipe temperature was predicted by the following equation:

$$C_{hp} \frac{\Delta T_{hp}}{\Delta t} = \dot{Q}_e - \dot{Q}_c \quad (68)$$

where $\dot{Q}_e = hA_e(T_{loop} - T_{hp})$

$$\dot{Q}_c = A_c(\sigma T_{hp}^4 - q_{rev})$$

Eq.(68) is coupled with Eq.(67) to calculate the sodium loop and heat pipe temperatures. For the lumped-heat-capacity model, an average surface heat transfer coefficient between the liquid sodium loop and the heat pipe evaporator of $h = 5 \cdot 10^4 \text{ W/m}^2\text{K}$ was assumed. The heat

capacitance of the heat pipe C_{hp} is about 540 J/K.

5.3 Results for Heat Pipes With Adiabatic Section

We applied the numerical model to a grooved heat pipe for which the specifications were given in Chapter 4. The total length of the heat pipe was 1.0 m with an adiabatic section having length of 0.4 m. Under normal condition, heat was transferred from the sodium loop to the heat pipe evaporator section by forced convection and was removed at the condenser by radiation.

Figure 5.2 shows the transient response of three HP/TES configurations with $C_{loop} = 1000$ J/K when a reversed heat load is suddenly applied at the condenser. Prior to $t = 10$ s, the three heat pipes all are operating at steady-state conditions with the temperature of the sodium loop maintained at 950 K. Under this steady-state condition, the total heat rate transferred from the sodium loop, \dot{Q}_e , is about 0.78 kW (for an average surface heat flux of about 4.3 W/cm^2) and is equal to the total heat rate removed at the condenser by radiation heat transfer, \dot{Q}_c . The average heat pipe temperature is about 945 K. A heat transfer rate of 0.78 kW is continuously released from the power generator to the sodium loop throughout the entire operating period. After $t = 10$ s, a reversed heat load of $q_{rev} = 10 \text{ W/cm}^2$ is suddenly applied to the condenser. As one can see, the temperature of the heat pipe without PCM increases rapidly. On the other hand, the temperatures of the other two heat pipes with PCM also increase rapidly immediately

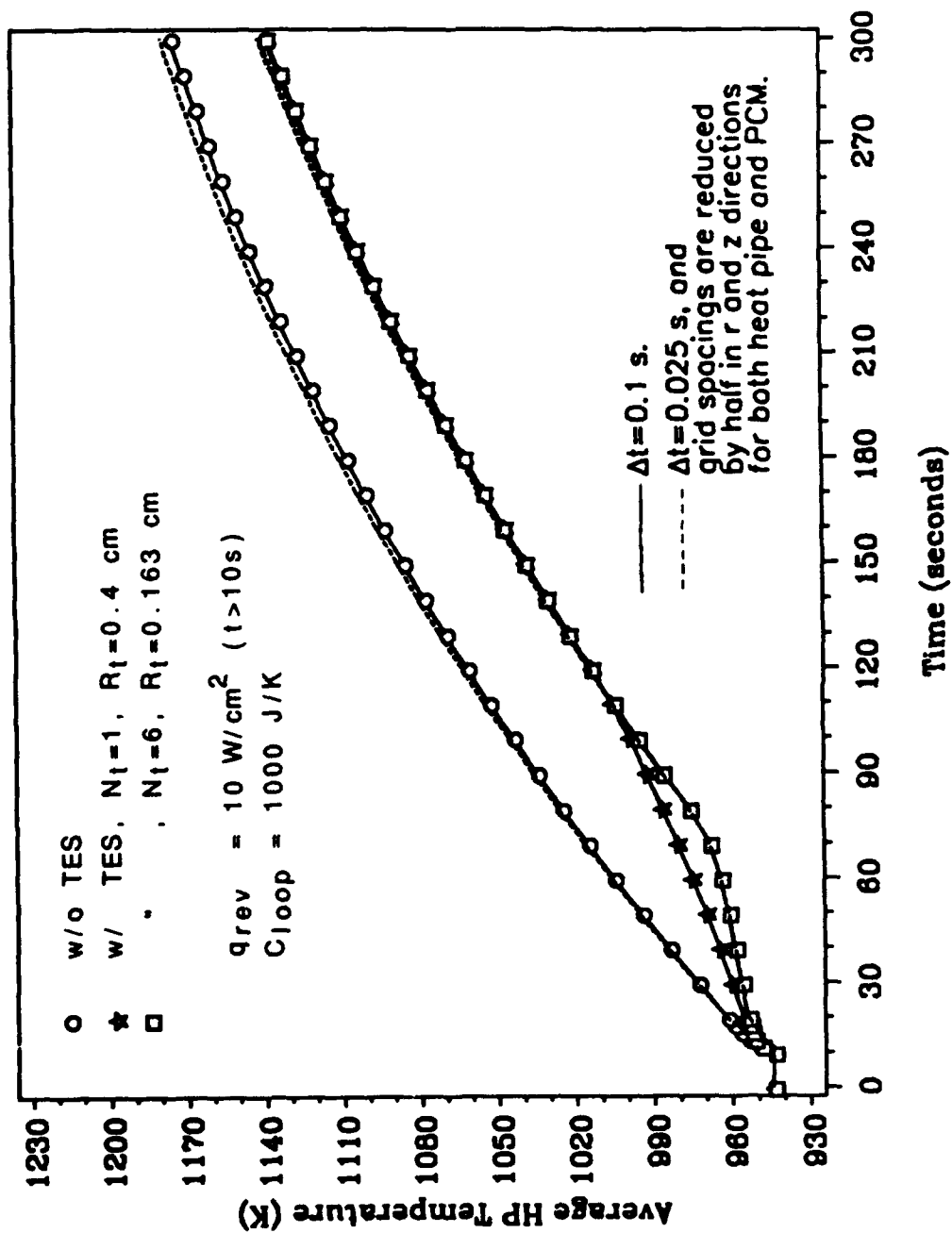


Figure 5.2 Transient response of heat pipe with $C_{loop} = 1000 \text{ J/K}$ under a reversed heat load

after the reversed heat load is applied. But the rapid temperature increase is arrested after the PCM reaches its melting temperature and starts to melt. It can also be seen that the temperature increase during the melting process with six small PCM cylinders is slower than with one large PCM cylinder. This slower temperature rise occurs because the total surface area of the six small PCM cylinders available for heat transfer is larger and the heat conduction path is shorter compared to the case with one large PCM cylinder. However, the six small PCM cylinders will be completely melted earlier, at about $t = 80$ s, compared to $t = 110$ s for the one large PCM cylinder. After the PCM is completely melted, both PCM equipped heat pipes undergo rapid temperature increases until they reach a new steady-state condition.

Due to the complexity of the present heat pipe problem, we are not able to predict the error of the numerical solutions accurately because no analytical solution is available. However, in order to retain high accuracy, the time step and grid spacings used in this research were chosen to satisfy the stability and accuracy conditions in Ref. [18]. Under these conditions, the error of the present numerical solutions should be only a few percent. To further validate the numerical solutions, we applied the numerical model to the same problem depicted in Fig 5.2 by using a smaller time step $\Delta t = 0.025$ s and reducing the grid spacings in the r and z directions by half for both the heat pipe and PCM. As we can see from Fig 5.2, the solutions remain almost the same with smaller values of the time step and grid spacings.

Figure 5.3 shows the variations of heat input, \dot{Q}_e , and heat output, \dot{Q}_c , for three different HP/TES configurations with $C_{loop} = 1000$

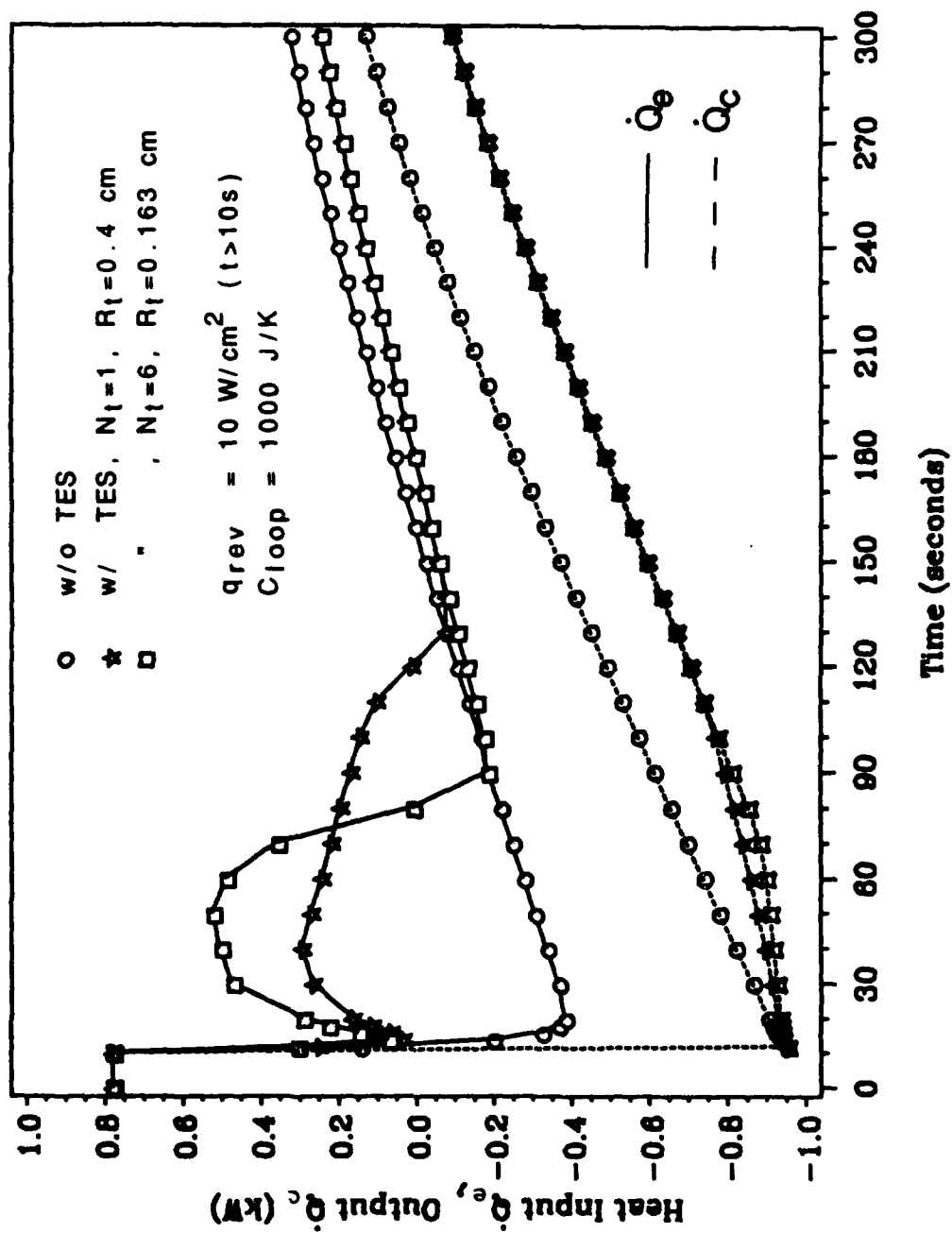


Figure 5.3 Variations of heat input and heat output of heat pipes with $C_{loop} = 1000 \text{ J/K}$ under a reversed heat load

J/K under a reversed heat load applied at the condenser. The total heat rate transferred from the sodium loop to the heat pipe evaporator, \dot{Q}_e , can be determined by knowing the temperature gradient inside the wall along the evaporator. The total heat rate removed from the condenser, \dot{Q}_c , is the summation of the heat removed by radiation and the reversed heat load. Prior to $t = 10$ s, all three heat pipes are operating at steady-state with a heat input of $\dot{Q}_e = 0.78$ kW equal to the heat output of $\dot{Q}_c = 0.78$ kW. After a reversed heat load $q_{rev} = 10$ W/cm² is applied at $t = 10$ s, the heat outputs at the condensers of the three heat pipes all become negative, indicating that there are external heat loads being added at the condensers. However, these heat outputs all begin to increase due to greater heat removal by radiation at the higher condenser wall temperatures. The variation of heat output is similar to that of the heat pipe temperature because the heat output depends strongly on the condenser wall surface temperature.

The heat input variation is a strong function of the sodium loop heat capacitance C_{loop} . After the reversed heat load is applied, the heat input of the heat pipe without PCM decreases very rapidly in the first 10 seconds and is reversed to negative. After $t = 20$ s, the heat input begins to increase because the heat output increases, and the reversed heat flow effect becomes less and less. The heat inputs of the other two heat pipes fitted with PCM also decrease rapidly immediately after the reversed heat loads are applied. After the PCM starts to melt at about $t = 15$ s, the heat inputs increase very rapidly. This is because most of the reversed heat load is absorbed by the PCM so that the heat pipe temperature increase becomes very slow. However, the heat

inputs decrease slightly during later stages of the melting process because the PCM capability to absorb the reversed heat load is declining. The heat inputs for the two heat pipes equipped with PCM drop again and reverse to negative after the PCM is completely melted because the heat pipe temperature starts to increase rapidly. It can also be seen that the heat input of the heat pipe with six small PCM cylinders is higher than that of the one with a single large PCM cylinder during the melting process. The greater heat input occurs because the temperature of the heat pipe with six small PCM cylinders is lower. The three different HP/TES configurations all tend to reach a new steady-state temperature with same original heat input and heat output equal to 0.78 kW.

Figure 5.4 shows the transient response of three different HP/TES configurations with $C_{loop} = 10000 \text{ J/K}$ under a reversed heat load suddenly applied at the condenser. Before $t = 10 \text{ s}$, all three heat pipes are operating at steady-state conditions as we mentioned in the earlier case. After $t = 10 \text{ s}$, a reversed heat load of $q_{rev} = 10 \text{ W/cm}^2$ is applied at the condenser. As can be seen from the figure, the temperature increase of all three HP/TES configurations is very slow. Because of its high heat capacitance, the sodium loop acts like a huge heat sink which can absorb most of the reversed heat loads and arrest the heat pipe temperature increase. It is clear that with such a high sodium loop heat capacitance, installation of PCM to mitigate the reversed heat loads is unnecessary.

Figure 5.5 shows the variations of heat input and heat output of three different HP/TES configurations with $C_{loop} = 10000 \text{ J/K}$ under a reversed heat load applied at the condenser. Compared with the results

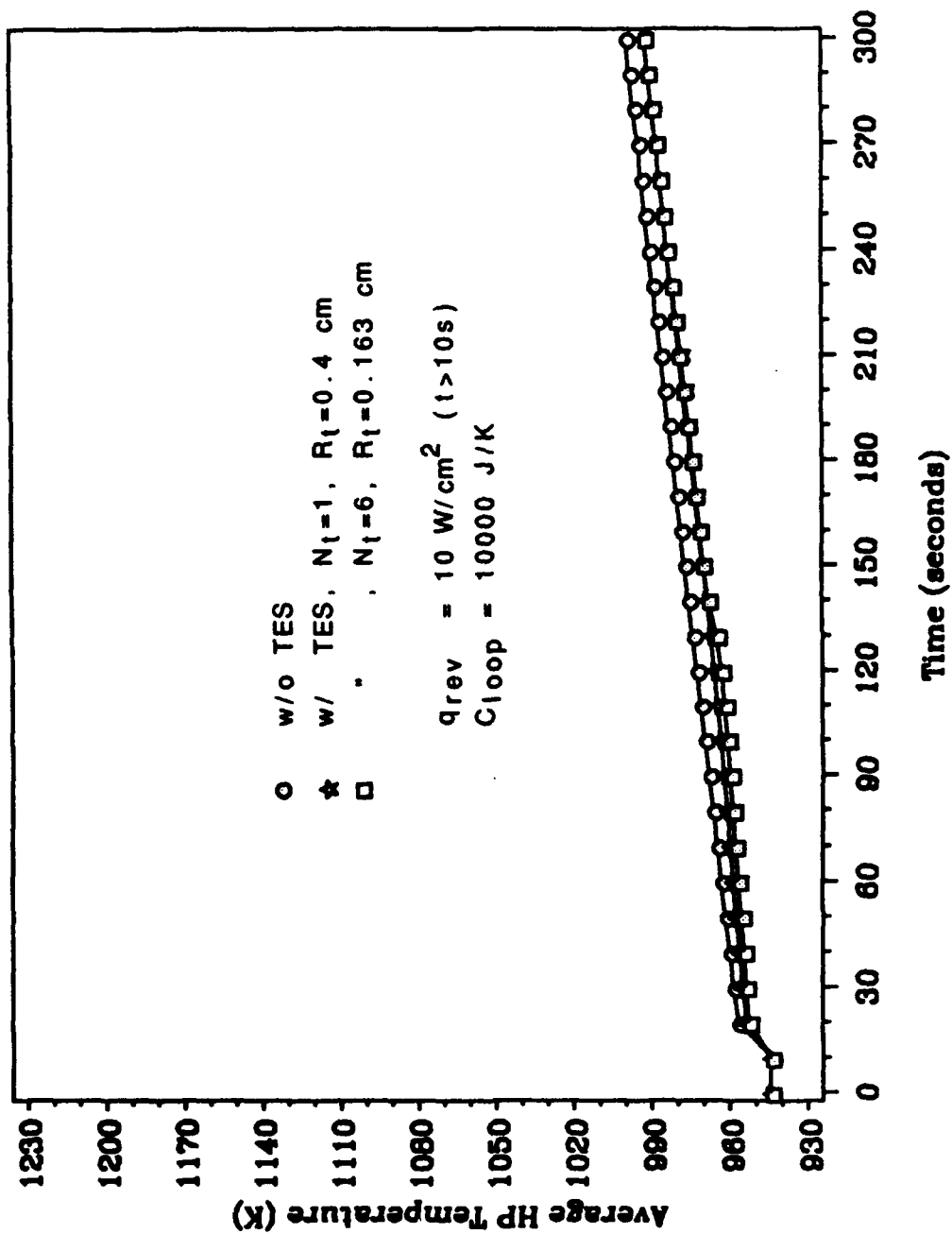


Figure 5.4 Transient response of heat pipe with $C_{loop} = 10000 \text{ J/K}$ under a reversed heat load

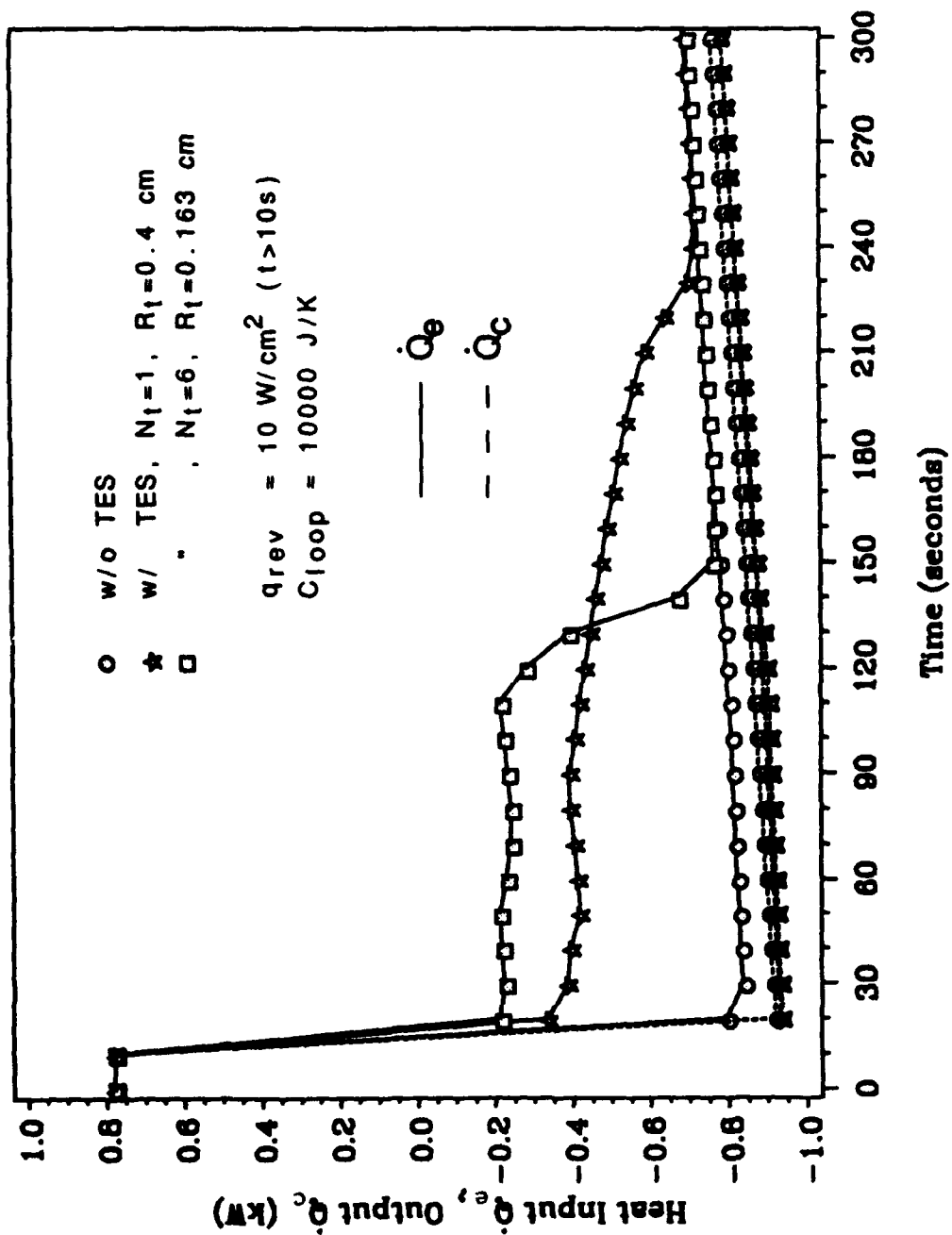


Figure 5.5, variations of heat input and heat output of heat pipes with $C_{loop} = 10000 \text{ J/K}$ under a reversed heat load

shown in Fig 5.3 for the case with $C_{\text{loop}} = 1000 \text{ J/K}$, the heat inputs of all three heat pipes decrease very rapidly and all are reversed to negative after the reversed heat load is applied. With such a high sodium loop heat capacitance, the sodium loop itself behaves like a massive heat sink and can absorb the reversed heat loads easily. The heat inputs of the two heat pipes with PCM are reversed less than the one without PCM after the condenser heat loads are applied. However, they immediately drop again after the PCM is completely melted.

Figure 5.6 presents the transient response of the heat pipe without PCM under reversed heat loads as predicted by the lumped-heat-capacity model. It can be seen that the results from the lumped model have very good agreement with those from the finite-difference method. The lumped model can predict the average heat pipe temperature and the heat flow input/output at the evaporator and condenser very well for the heat pipe without PCM. The heat pipe temperature predicted by the lumped model is about 10 K lower than that obtained from the finite-difference method throughout the time period of interest. This discrepancy arises because the heat removed from the condenser by radiation is overestimated by using the average heat pipe temperature as the condenser wall surface temperature.

Figure 5.7 shows the axial variation of vapor mass flow rate for two different HP/TES configurations with $C_{\text{loop}} = 1000 \text{ J/K}$. At $t = 10 \text{ s}$, both heat pipes are operating at steady-state conditions with forward heat loads applied at the evaporators. All the vapor mass flow rates are positive along the two units. The vapor mass flow rates increase in the evaporator section, remain almost constant in the adiabatic section, and then decrease in the condenser section. As can be seen from Fig

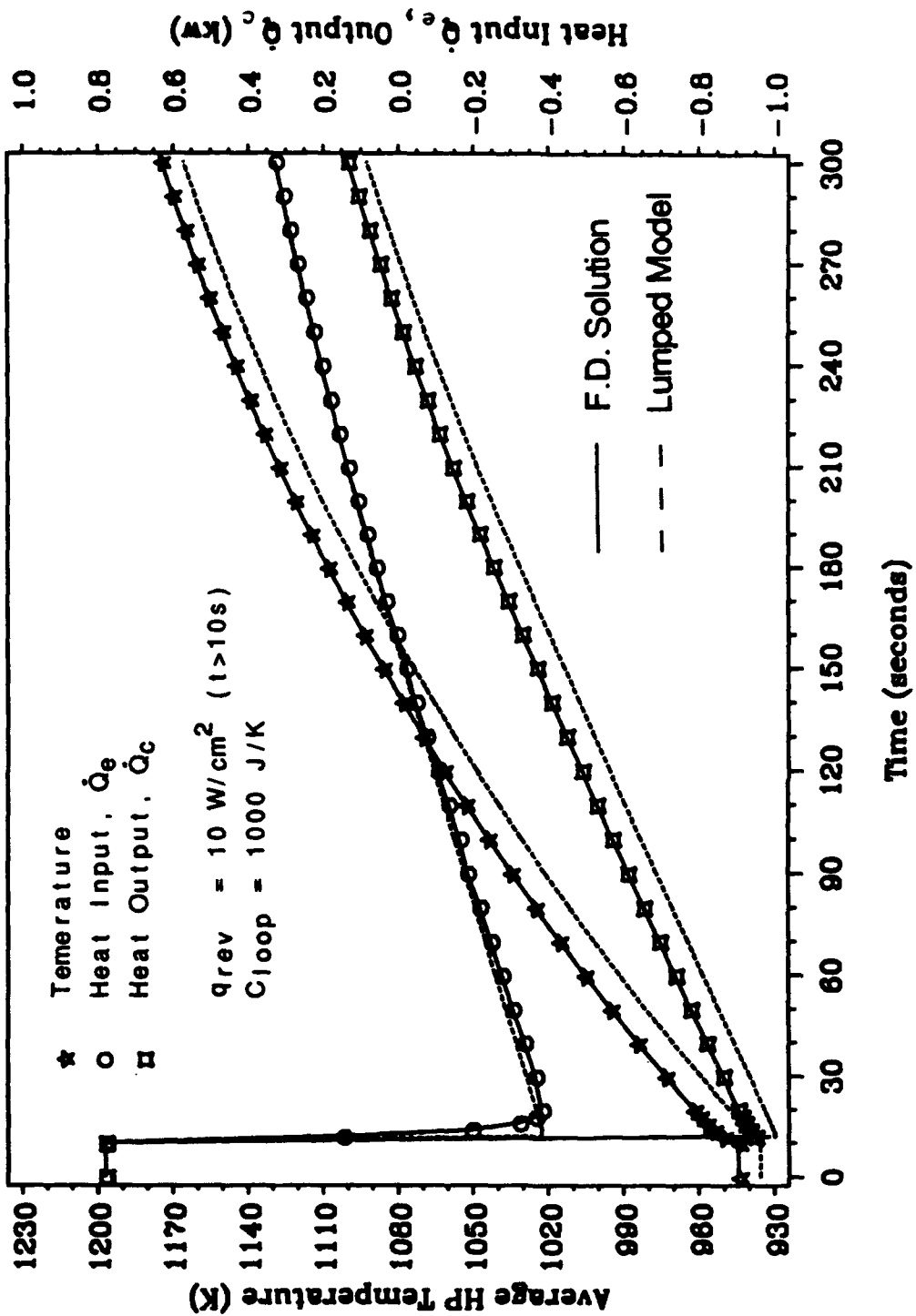


Figure 5.6 Comparison of the transient response of heat pipe without PCM predicted by lumped model and finite-difference method

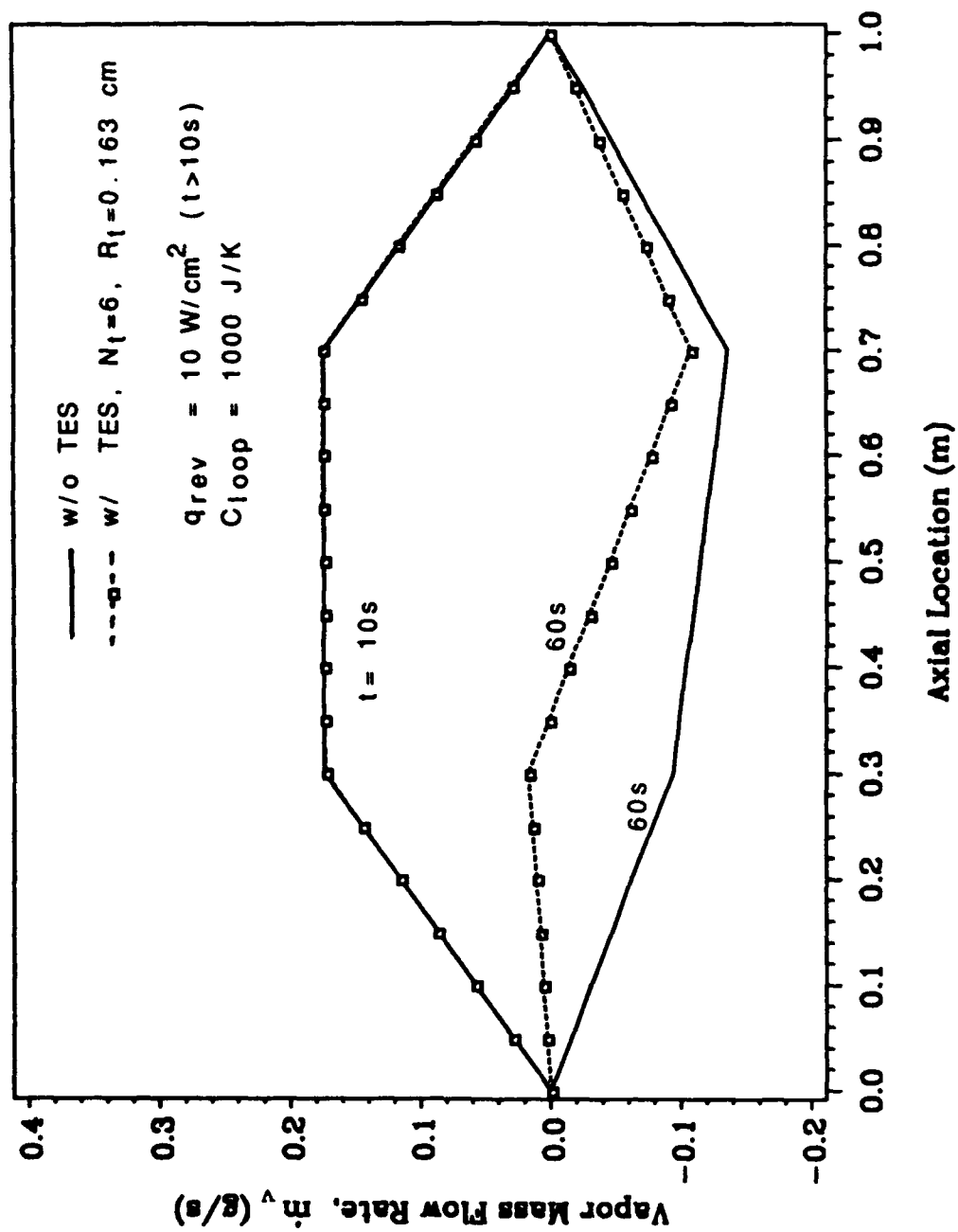


Figure 5.7 Vapor mass flow rate of heat pipes under the same operating conditions depicted in Fig. 5.2

5.5, the vapor flow of the heat pipe without a PCM is totally reversed at $t = 60$ s since both heat input and heat output are negative. For the heat pipe with six small PCM cylinders, the vapor flow becomes two separate flows with opposite directions because the heat input is positive while the heat output will be negative. Evaporation occurs at both evaporator and condenser sections, while the vapor condenses in the adiabatic section and on the outside surfaces of the PCM containers. As shown in Fig 5.7, the vapor mass flow rate is positive only in the evaporator section and part of the adiabatic section. It is negative over the remainder of the heat pipe. One should also note that the vapor mass flow rate at the adiabatic section of the heat pipe with six small PCM cylinders changes more rapidly than it does when no PCM is present. This difference occurs because a considerable amount of vapor condenses on the outside surfaces of the PCM containers during the melting process.

Figures 5.8a,b show the axial variation of vapor pressure and temperature for two different HP/TES configurations with $C_{loop} = 1000$ J/K. At $t = 10$ s, both heat pipes are operating at steady-state conditions. The variation of the vapor pressure for both heat pipes is almost identical since there is little difference between the heat pipe temperatures and vapor mass flow rates. At $t = 60$ s, both heat pipes have a higher vapor pressure at the condenser end because the vapor flows are reversed. The vapor pressure drop along each heat pipe at $t = 60$ s is much less than at $t = 10$ s. For the heat pipe without a PCM, the smaller pressure drop is mainly due to its higher temperature, which strongly influences vapor pressure variation as discussed in Chapter 4. For the heat pipe with six small PCM cylinders, the lower pressure drop

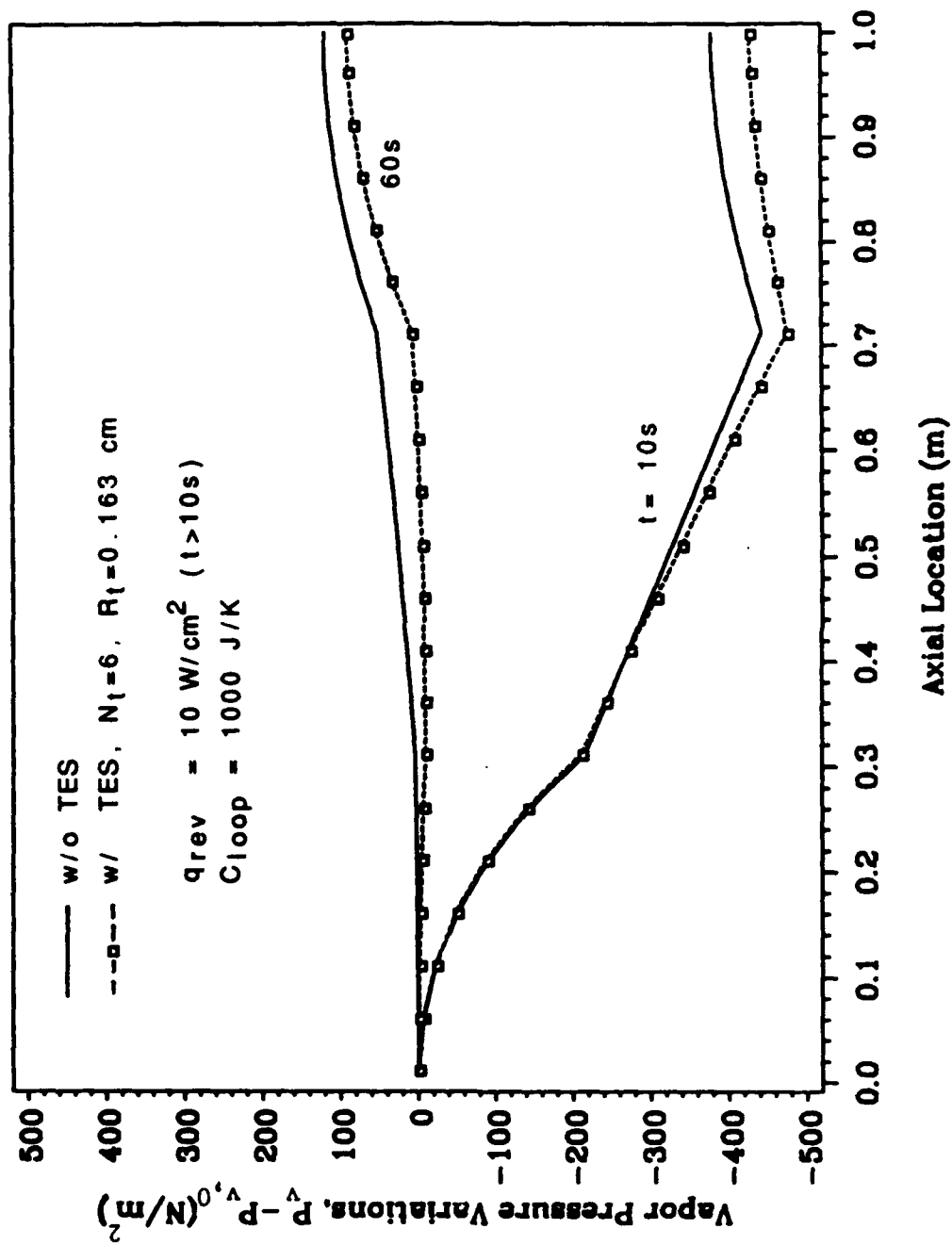


Figure 5.8a Axial variation of vapor pressure for the same operating conditions depicted in Fig. 5.7

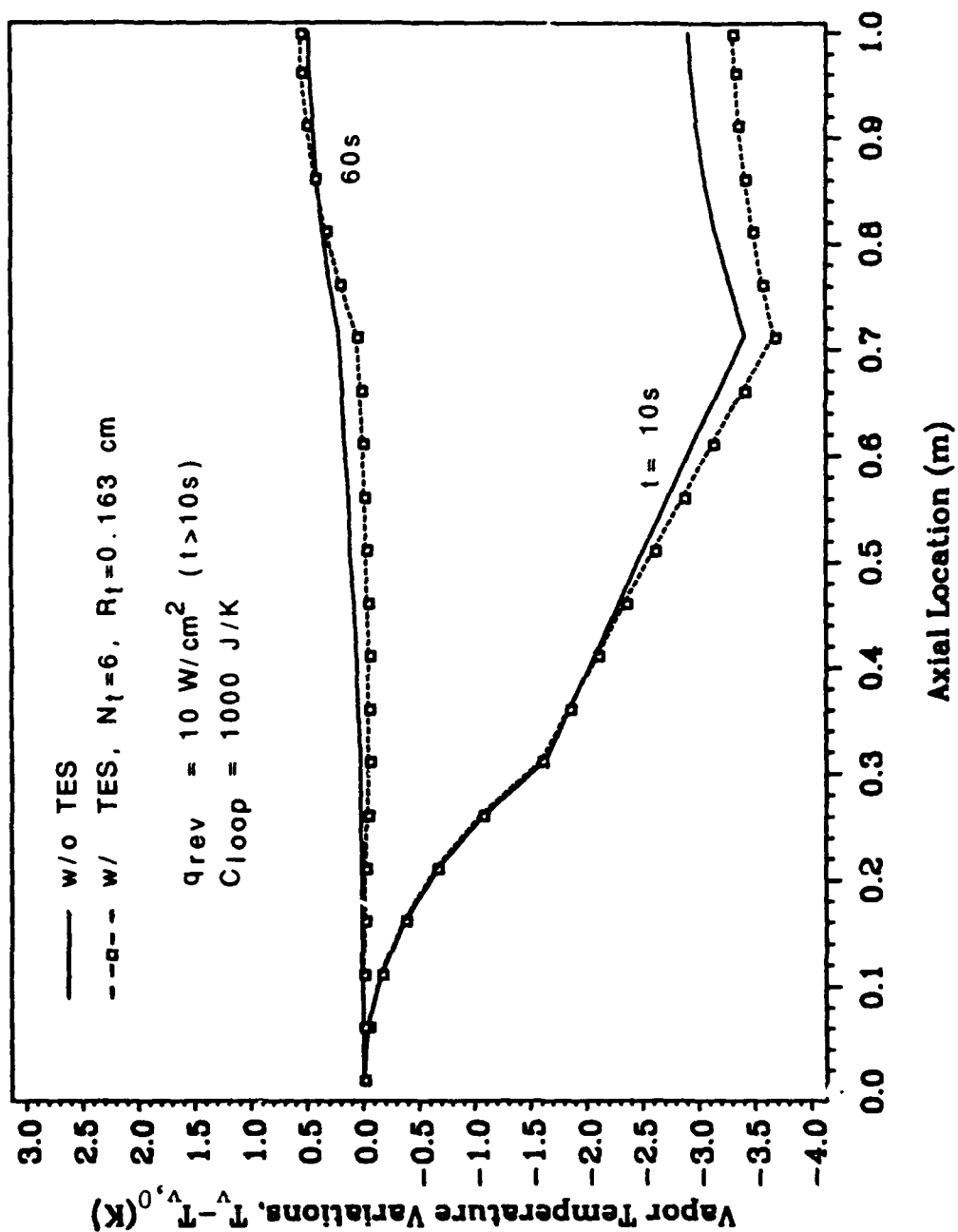


Figure 5.8b Axial variation of vapor temperature for the same operating conditions depicted in Fig. 5.2

is a result of higher heat pipe operating temperature, smaller vapor mass flow rate and the shorter vapor flow path resulting from the two separate vapor flows. One should also note that the axial variation of vapor temperature is very similar to that of vapor pressure.

The transient responses of the heat pipes under a reversed-pulse heat load applied to the condenser from $t = 20$ s to $t = 80$ s are shown in Figs 5.9 and 5.10. As is apparent from Fig 5.9, the temperature of all three heat pipes responds very rapidly and starts to decrease as soon as the reversed-pulse heat load is removed at $t = 80$ s. The temperature of the heat pipe without PCM decreases very rapidly after the reversed-pulse heat load is removed. The temperature of each unit with PCM also decreases rapidly immediately after this time, but the decrease becomes very slow when the PCM reaches the melting point and starts to solidify. The six small PCM cylinders will completely solidify earlier than a single large PCM cylinder. After the PCM has completely solidified, the temperature of both heat pipes with PCM resumes its decrease, and the heat pipes gradually return to their initial steady-state operating conditions. Approximately 1,660 seconds are required for the heat pipe with six small PCM cylinders to return to the initial steady-state condition after the reversed-pulse heat load is removed, while the configuration with a single large cylinder needs 2,260 seconds. Fig 5.10 shows the percentage of PCM melted versus time for the same case depicted in Fig 5.9. One can readily see that the PCM does not respond as rapidly as the heat pipe temperature does. In fact, after the reversed-pulse heat load is removed at $t = 80$ s, 14% more of the six small PCM cylinders and 25% more of the one large PCM cylinder will still be melted before the phase change ceases. It is also clear

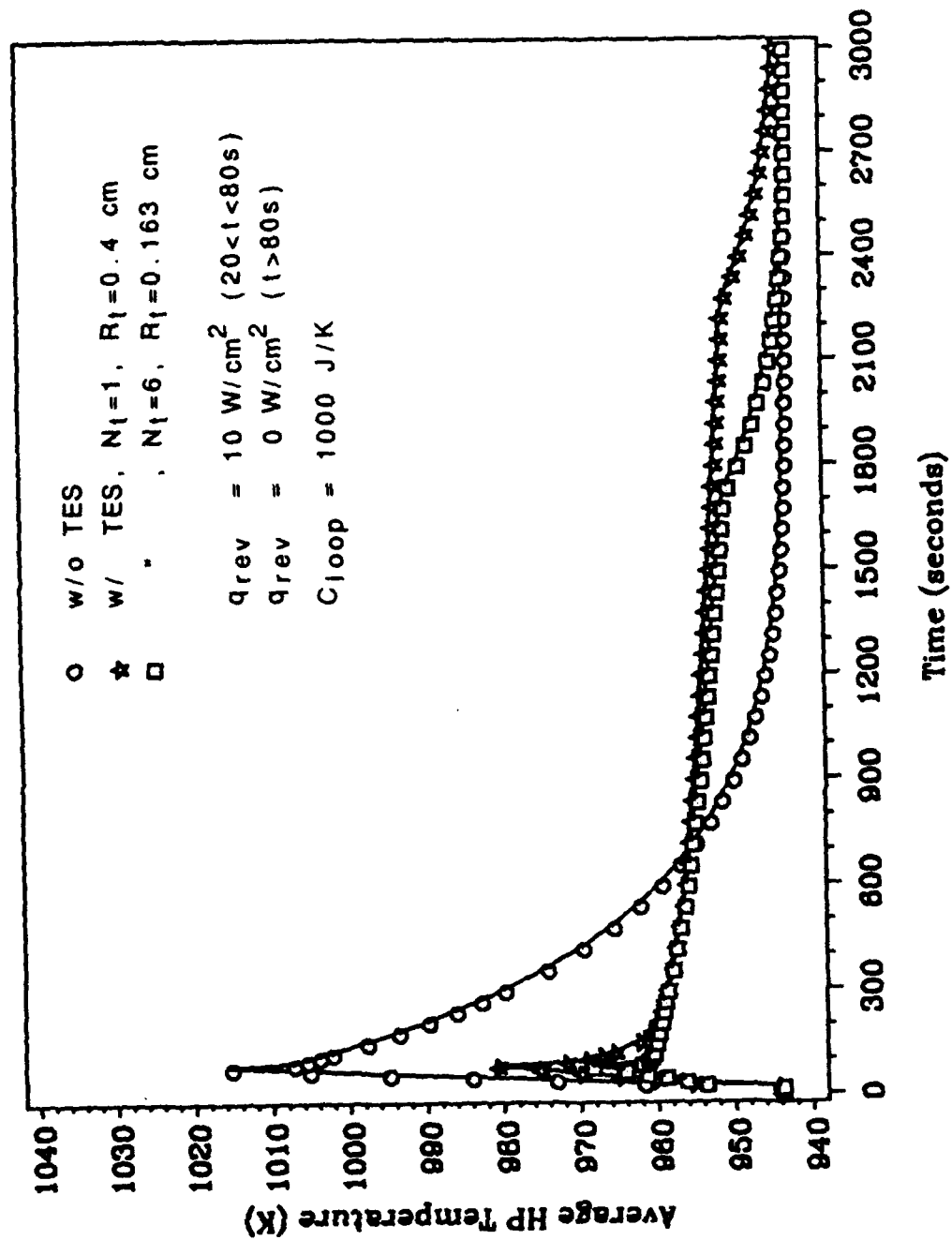


Figure 5.9 Transient response of heat pipes under a reversed-pulse heat load

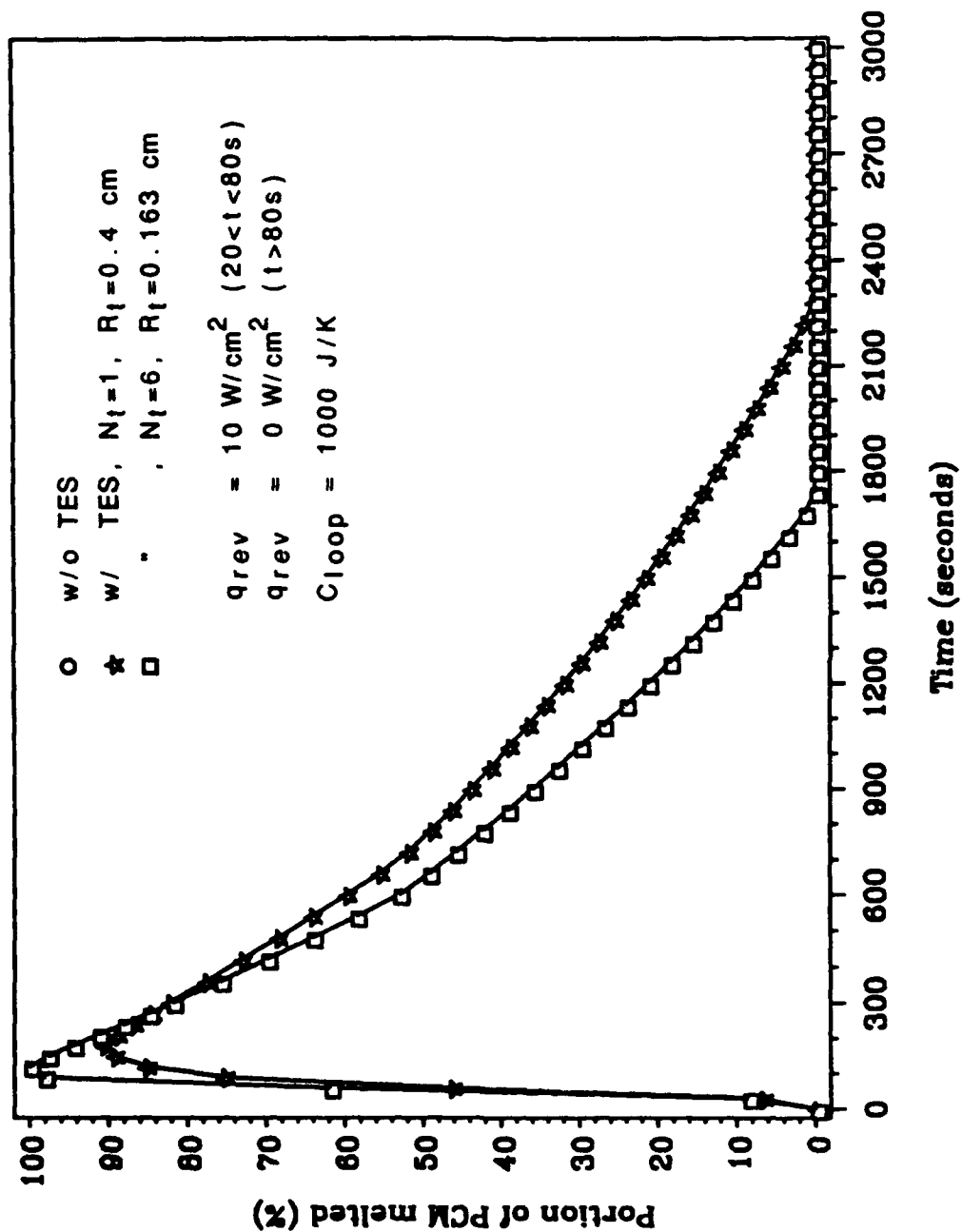


Figure 5.16 Portion of PCM melted versus time for heat pipes under a reversed-pulse heat load

that the small PCM cylinders solidify faster than the larger one does.

Figures 5.11 and 5.12 illustrate the results for the transient response of the heat pipes with periodic, reversed-pulse heat loads. The time period is 2000 s and each of the reversed-pulse heat loads lasts 60 s. The temperature response in each time period is similar to the results shown in Fig 5.9. The temperature of the heat pipe without a PCM simply oscillates up and down periodically. The temperature of the heat pipe with six small PCM cylinders remains almost constant throughout the whole period due to the very efficient melting and solidification of this PCM configuration. As shown in Fig 5.12, the molten fraction of the PCM for the heat pipe with six small PCM cylinders does not differ from one cycle to the next. This is because the six small PCM cylinders solidify completely at the end of each cycle. The percentage of PCM melted for the heat pipe with one large PCM cylinder continues to increase as the pulse cycles continue. This occurs because the one large PCM cylinder does not have sufficient time to solidify completely at the end of each time period for this cyclic rate.

Figures 5.13 and 5.14 present the results for the heat pipes under periodic, reversed-pulse heat loads with a shorter time period of 600 s. Each of the reversed-pulse heat loads also lasts 60 s. It is clear from these figures that the temperature of both heat pipes with PCM is under control during the first cycle. However, the temperatures become very high during the next two cycles. This failure of the PCM temperature regulation mechanism occurs because the time period is too short for the PCM to solidify completely at the end of each cycle. At the end of the first cycle, only about 50% of the PCM is solidified for

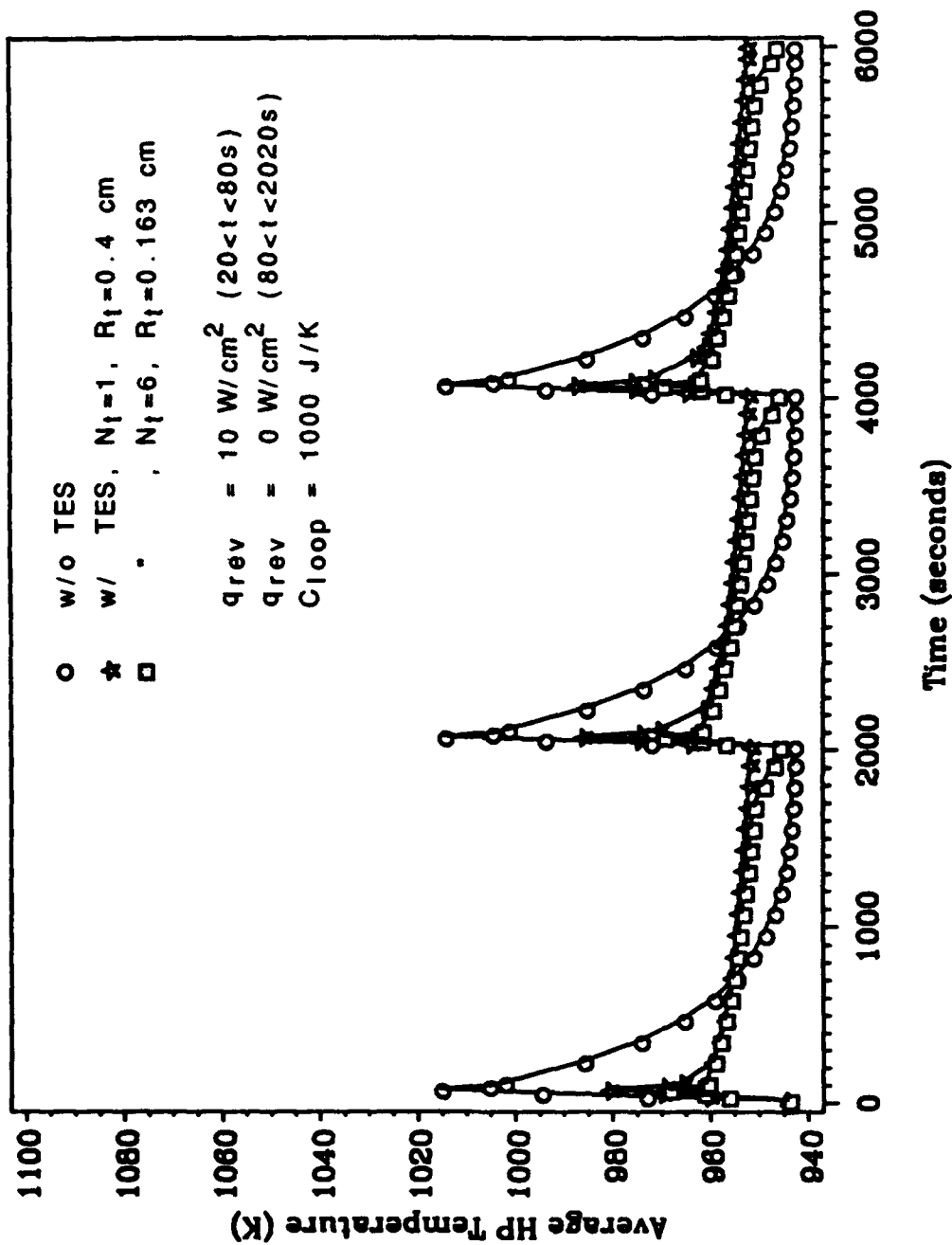


Figure 5.11 Transient response of heat pipes under a periodic reversed-pulse heat load with time period of 2000 s

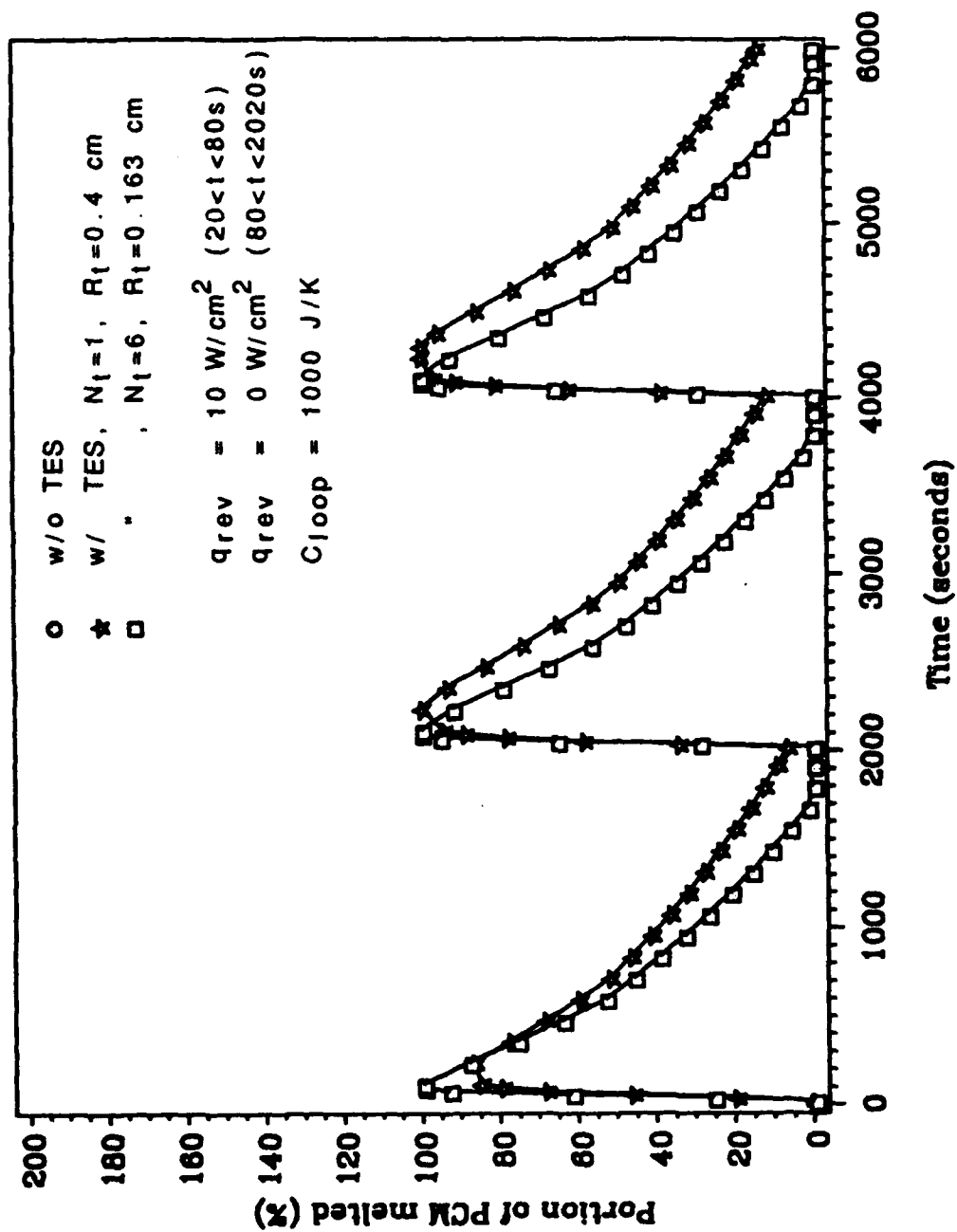


Figure 5.12 Portion of PCM melted versus time for heat pipes under a periodic reversed-pulse heat load with time period of 2000 s

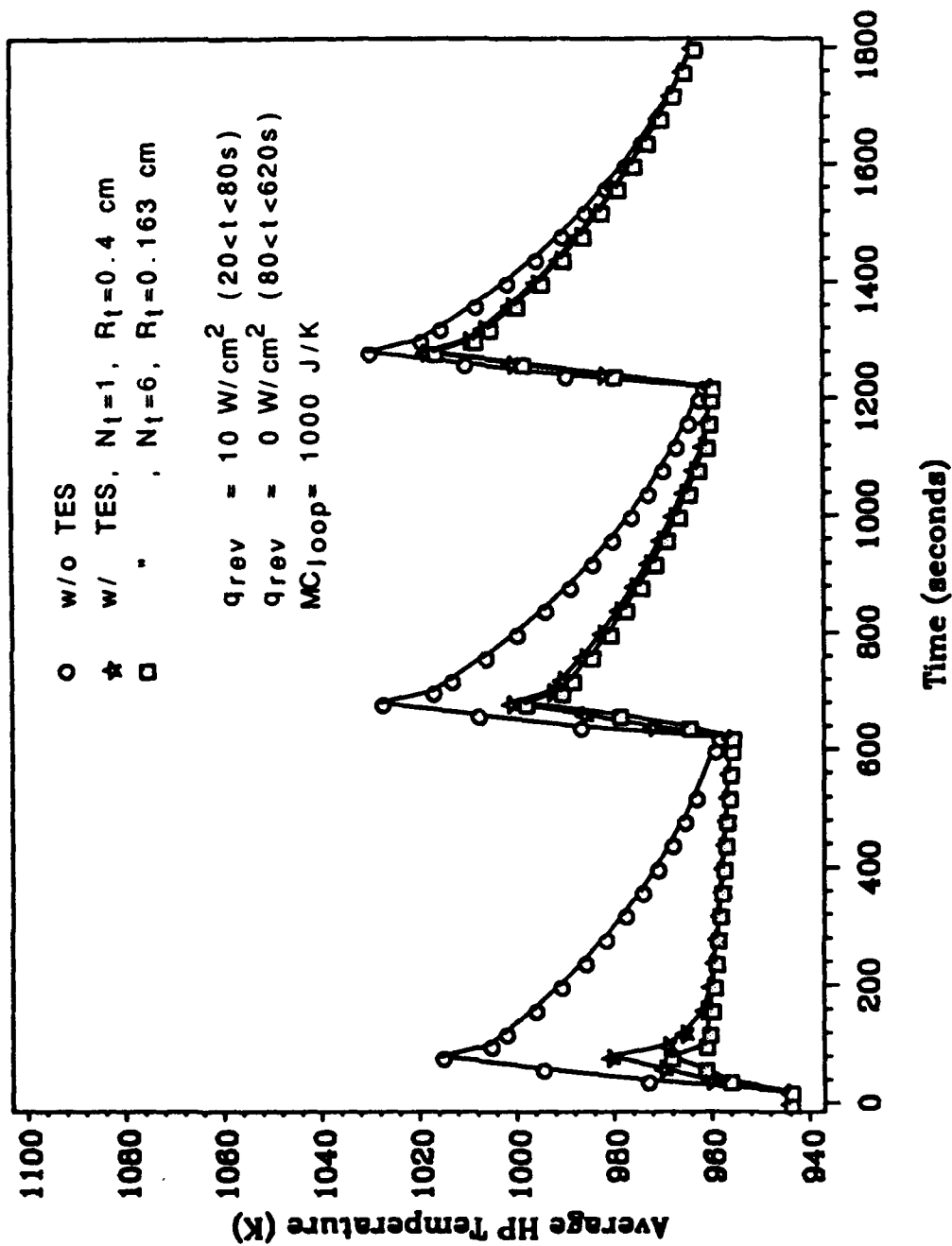


Figure 5.13 Transient response of heat pipes under a periodic reversed-pulse heat load with time period of 600 s

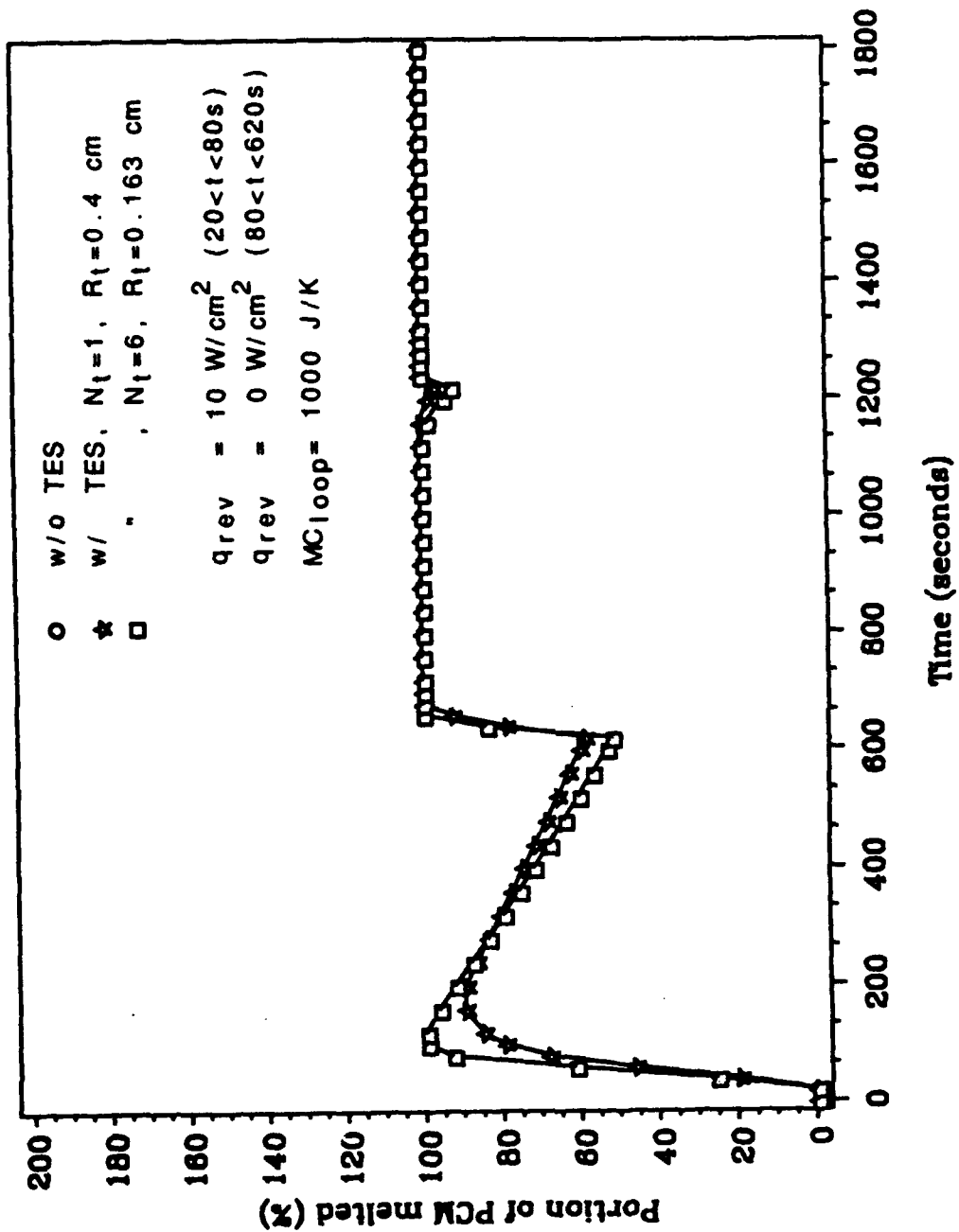


Figure 5.14 Portion of PCM melted versus time for heat pipes under a periodic reversed-pulse heat load with time period of 600 s

either heat pipe. After the second reversed-pulse heat load is applied, the PCM soon becomes completely melted, and the heat pipe temperature increases rapidly. The PCM will never again have time to solidify and thus becomes useless for thermal regulation purposes after the second cycle. Obviously, cycle time is a vital consideration in the design of a HP/TES cooling system to handle periodic, reversed-pulse heat loads.

5.4 Results for Heat Pipes Without Adiabatic Section

In this section, the numerical model will be applied to a grooved heat pipe without an adiabatic section under partially reversed heat loads applied at the condenser. The specifications of the heat pipe are the same as those given in Chapter 4, except there is no adiabatic section. The total length of the heat pipe is 1.0 m with the evaporator and condenser sections having lengths of 0.3 m and 0.7 m, respectively. The numerical model predicted the transient response of the HP/TES cooling system under a variety of partially reversed heat loads as shown in Fig 5.15.

Figure 5.16 shows the transient response of three HP/TES configurations with $C_{\text{loop}} = 1000 \text{ J/K}$ when a reversed heat load is suddenly applied to 75% of the condenser surface. Prior to $t = 10 \text{ s}$, the three heat pipes all are operating at steady-state conditions with the temperature of the sodium loop maintained at 950 K. Under this steady-state condition, the total heat rate transferred from the sodium loop, \dot{Q}_e , is about 1.78 kW (for an average surface heat flux of about

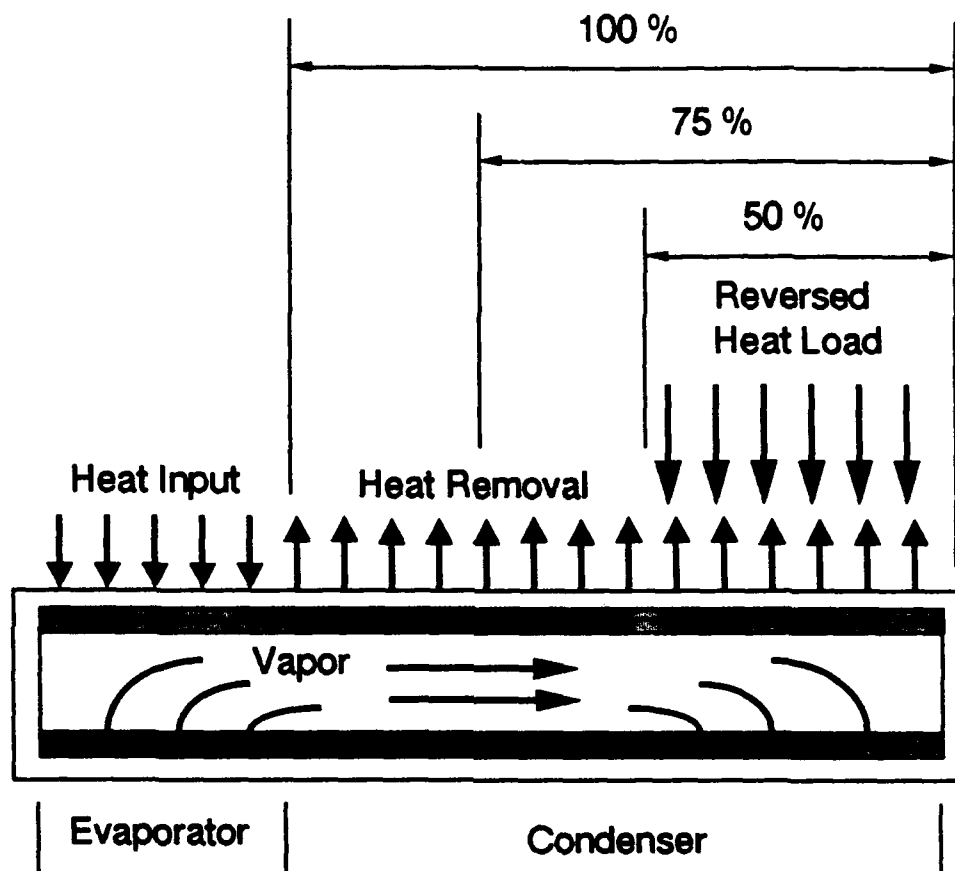


Figure 5.15 A heat pipe without an adiabatic section operates under a partially reversed heat load

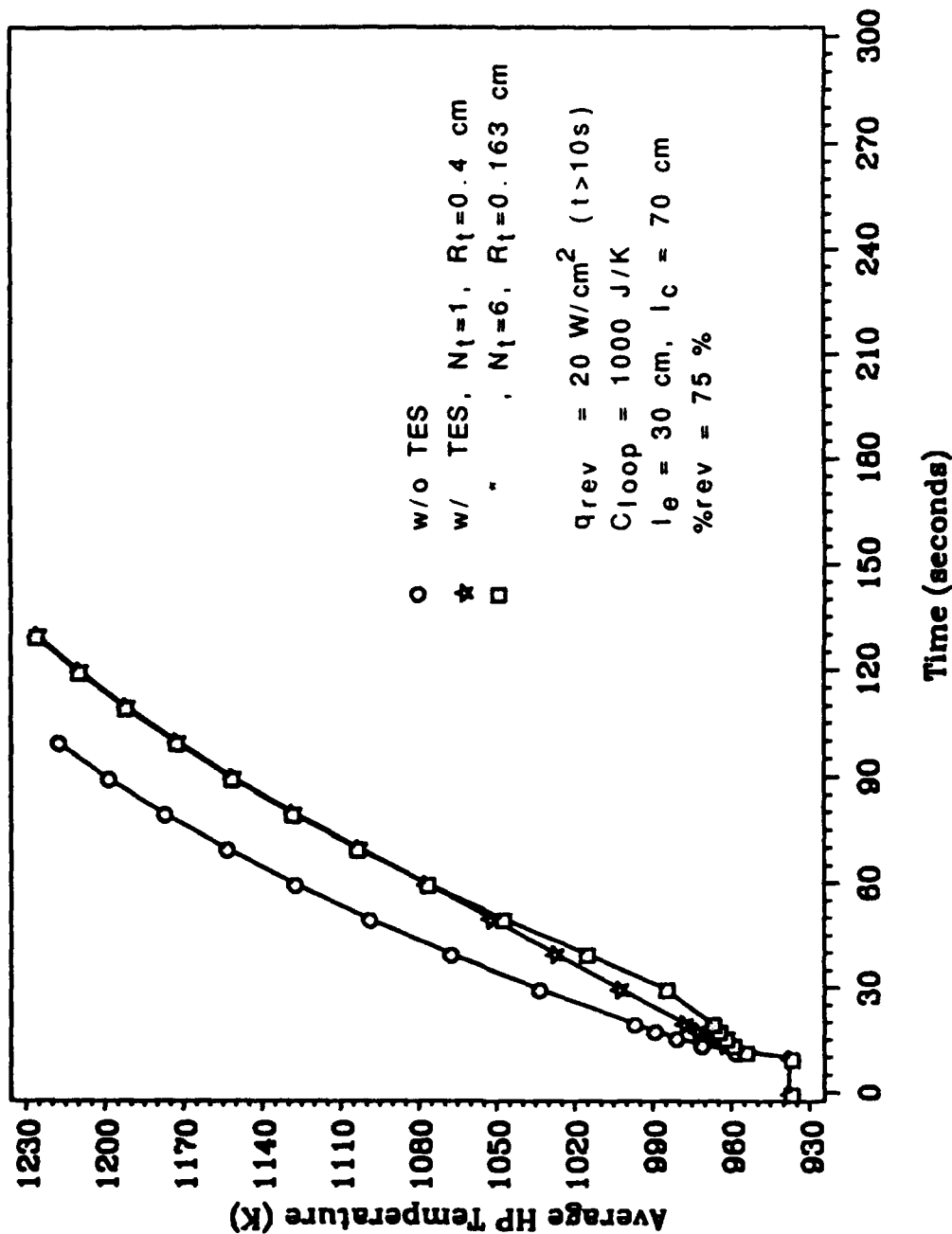


Figure 5.16 Transient response of heat pipes under a reversed heat load which covers 75% of condenser

9.8 W/cm^2) and is equal to the total heat rate removed at the condenser by radiation heat transfer \dot{Q}_c . The average heat pipe temperature is about 938 K. A heat transfer rate of 1.78 kW is continuously released from the power generator to the sodium loop throughout the entire operating period. After $t = 10 \text{ s}$, a reversed heat load of $q_{\text{rev}} = 20 \text{ W/cm}^2$ is suddenly applied to 75% of the condenser surface. Compared with the results shown in Fig 5.2, the PCM is completely melted earlier due to the higher heat loads applied at the evaporator and condenser. The six small PCM cylinders will be completely melted at about $t = 40 \text{ s}$ and the single large PCM cylinder at $t = 60 \text{ s}$. As one can see from the figure, the temperature of both heat pipes fitted with PCM also increases very swiftly during the PCM melting process. This rapid temperature rise happens because that the radial temperature gradient inside the PCM is very large under such high heat loads. The surface temperature of a single large PCM cylinder is about 90 K higher than the PCM melting point at $t = 50 \text{ s}$. In designing an HP/TES cooling system to handle such high total reversed heat loads, one must install more PCM cylinders in a heat pipe with a larger vapor flow area. Thus the heat load to each PCM cylinder can be reduced, the radial temperature gradient inside the PCM can be decreased, and the PCM melting process will last longer. The variations of the heat input, \dot{Q}_e , and heat output, \dot{Q}_c , as shown in Fig 5.17 are similar to the results already given in Fig 5.3.

Figures 5.18 and 5.19 present the transient response of three HP/TES configurations with $C_{\text{loop}} = 1000 \text{ J/K}$ when a reversed heat load is suddenly applied to 50% of the condenser surface. The six small PCM

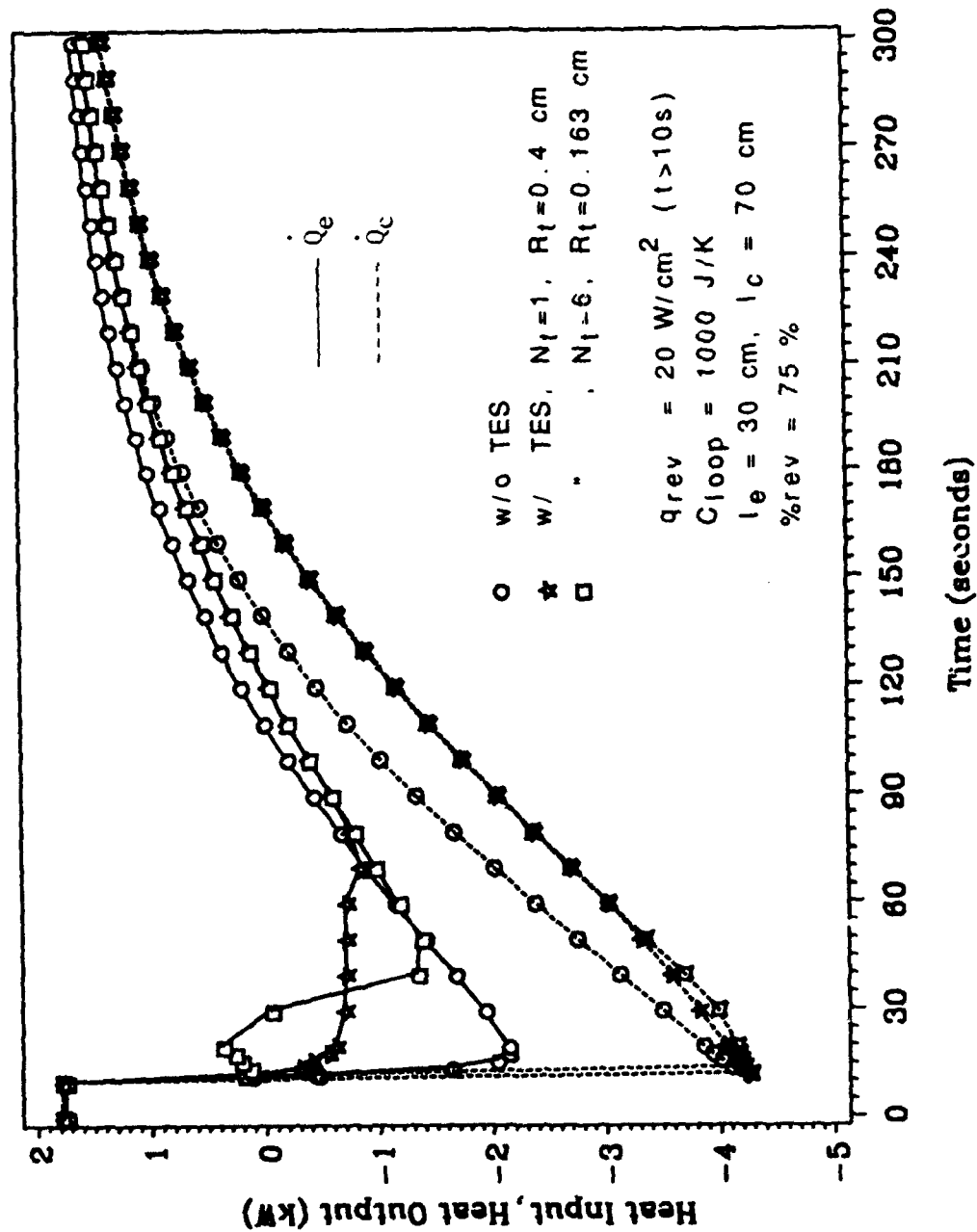


Figure 5.17 Variations of heat input and heat output of heat pipes under a reversed heat load which covers 75% of condenser

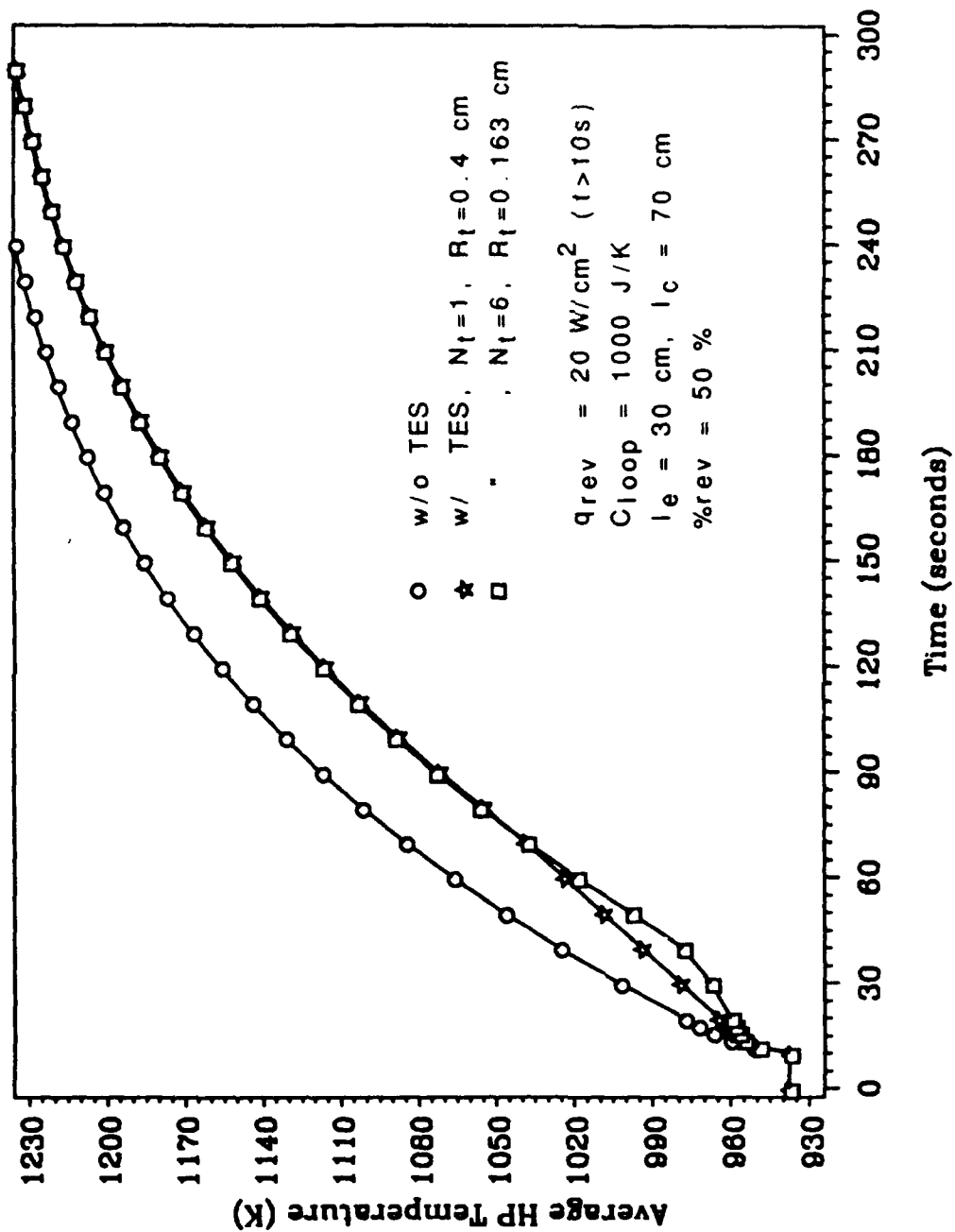


Figure 5.18 Transient response of heat pipes under a reversed heat load which covers 50% of condenser

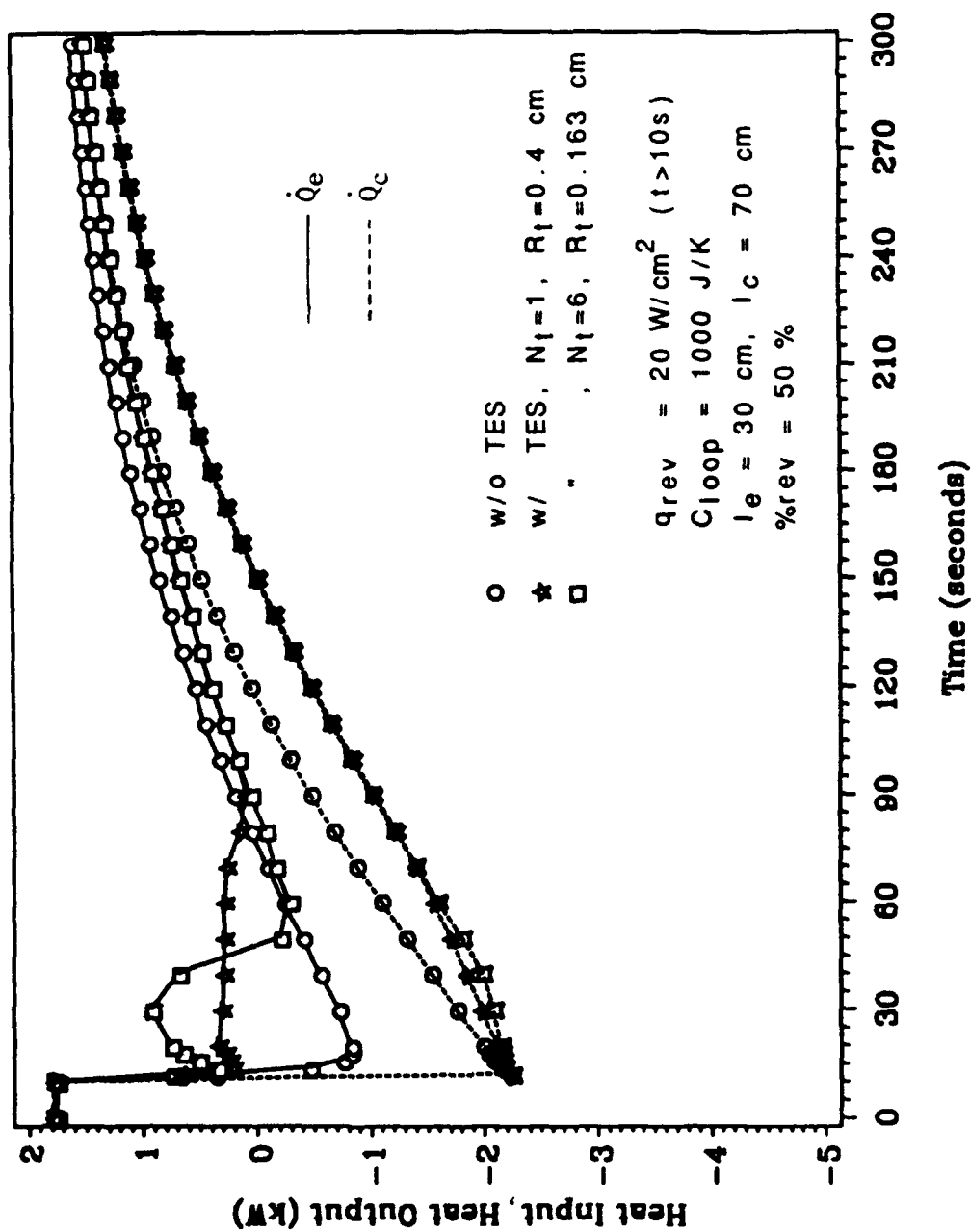


Figure 5.19 Variations of heat input and heat output of heat pipes under a reversed heat load which covers 50% of condenser

cylinders and the one larger PCM cylinder will be completely melted at $t = 50$ s and 80 s, respectively. Although both the fraction of the condenser surface directly exposed to the reversed heat loads and the total load itself are reduced from the previous case, the temperature of both heat pipes still increases rapidly during the PCM melting process. The surface temperature of the single large PCM cylinder is about 80 K higher than the PCM melting point at $t = 70$ s.

Figures 5.20 and 5.21 show the transient response of three HP/TES configurations with $C_{loop} = 1000$ J/K when a reversed heat load is suddenly applied to 25% of the condenser surface. The six small PCM cylinders and the single large PCM cylinder will now be completely melted at $t = 80$ s and 120 s, respectively. As one can see, the temperature of the heat pipe with six small PCM cylinders only increases about 10 K during the PCM melting process. The surface temperature of the single large PCM cylinder is about 40 K higher than the PCM melting point at $t = 110$ s; however, the surface temperature excess is only about 12 K for the small PCM cylinders at $t = 70$ s.

Figure 5.22 shows the axial variation of vapor mass flow rate for the same case as shown in Fig 21. At $t = 10$ s, both heat pipes are operating at steady-state conditions with forward heat loads applied at the evaporators. All the vapor mass flow rates are positive along the two units. The vapor mass flow rate increases at the evaporator section and then decreases at the condenser section. At $t = 60$ s, each vapor flow in both heat pipes becomes two separate flows moving in opposite directions. Evaporation occurs at both the evaporator and the portion of the condenser section where the reversed heat load is applied, while the vapor condenses in the remaining portion of the condenser section

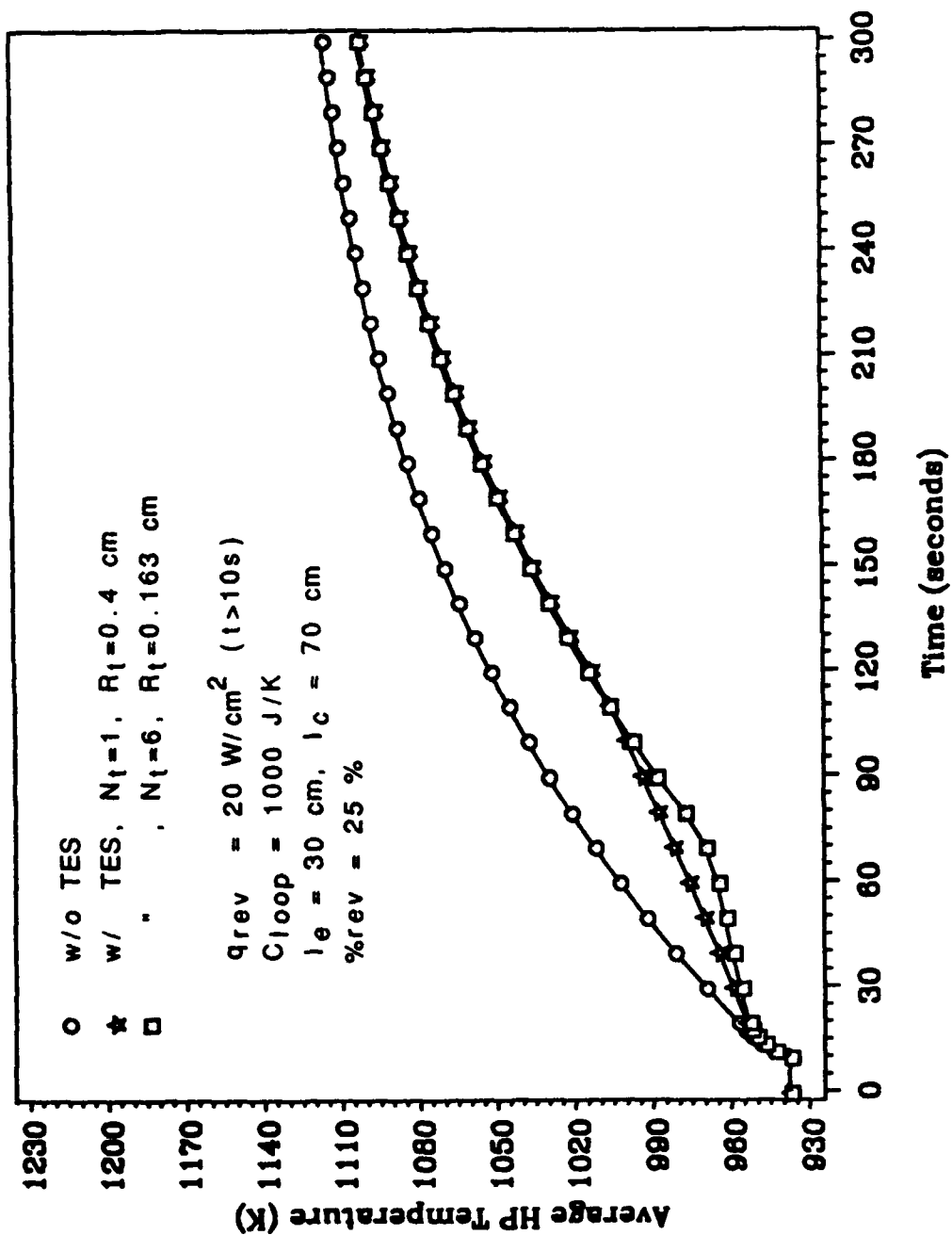


Figure 5.2c Transient response of heat pipes under a reversed heat load which covers 25% of condenser

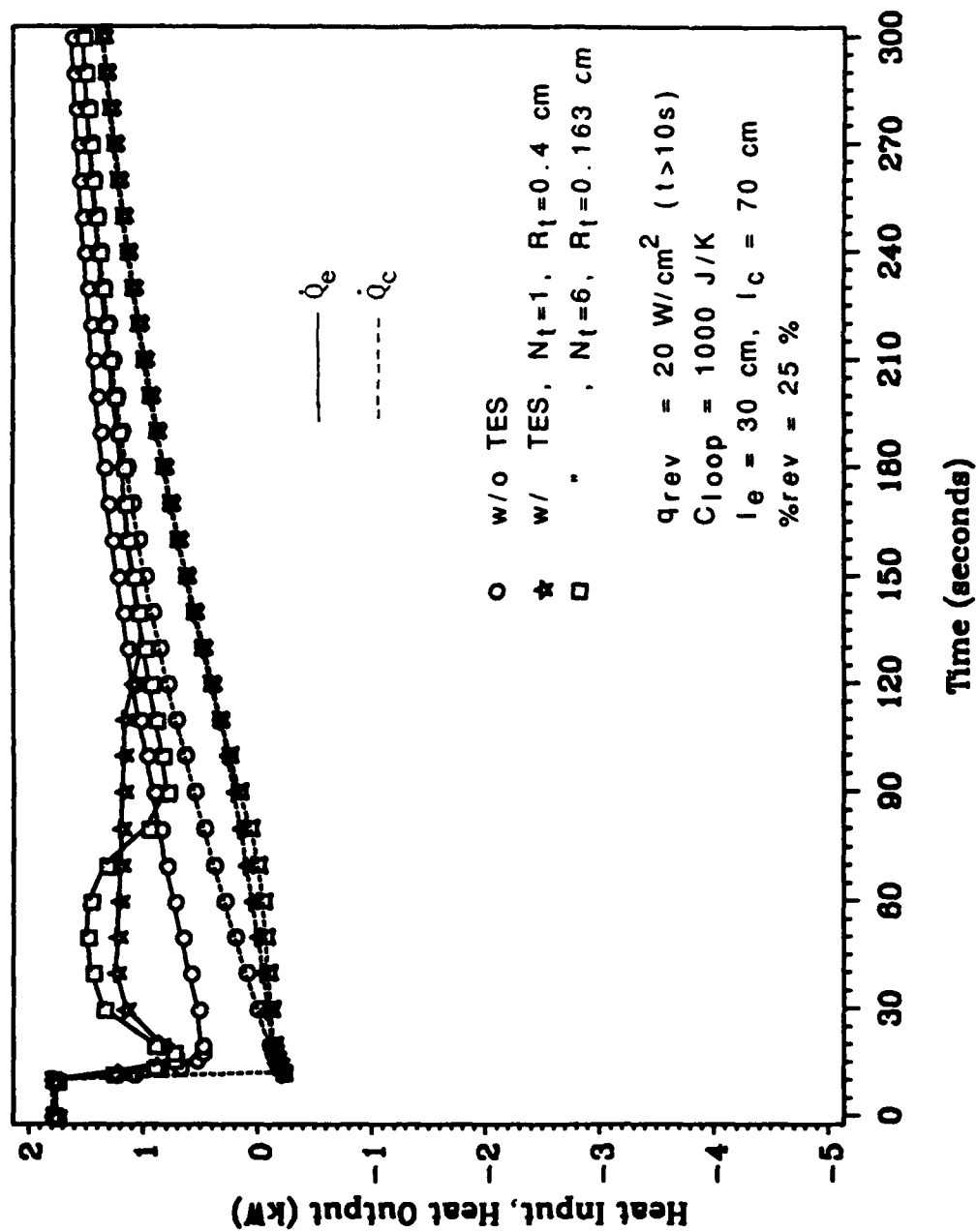


Figure 5.21 Variations of heat input and heat output of heat pipes under a reversed heat load which covers 25% of condenser

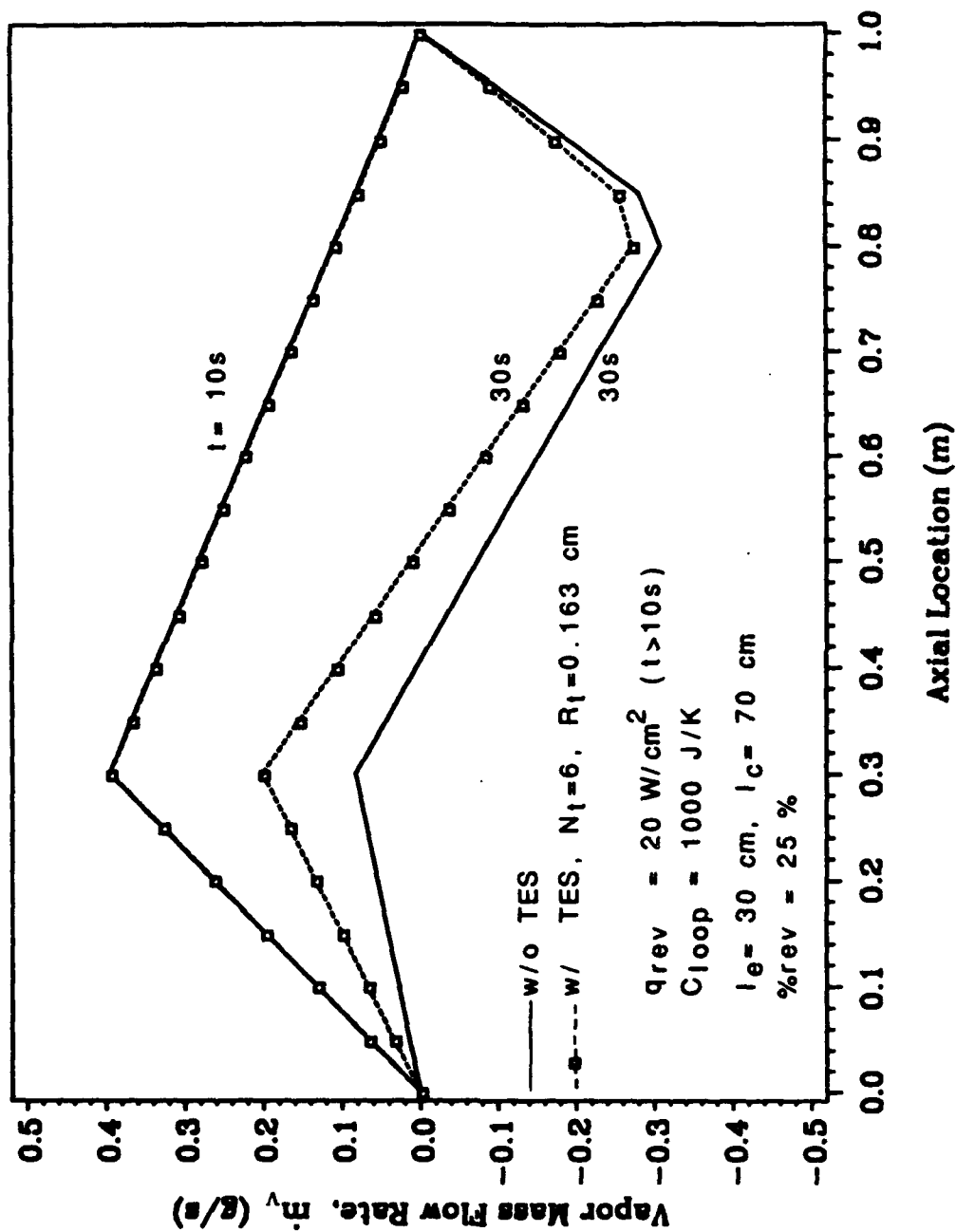


Figure 5.22 Vapor mass flow rate of heat pipes under a reversed heat load which covers 25% of condenser

and on the outside surfaces of the PCM containers.

The transient responses of the heat pipes under a reversed-pulse heat load applied to 25% of the condenser surface from $t = 20$ s to $t = 80$ s are shown in Figs 5.23 and 5.24. The trends depicted by the transient responses are similar to the results shown in Figs 5.9 and 5.10. However, compared to the results in Figs 5.9 and 5.10, the PCM cylinders are completely solidified much more quickly after the reversed-pulse heat loads are removed. Only about 1,000 seconds are required for the heat pipe with six PCM cylinders to return to its initial steady-state condition after the reversed-pulse heat load is removed, and the configuration with one large cylinder can accomplish this in about 1,270 seconds. This shorter adjustment time can be achieved because the heat will be removed more quickly from a heat pipe with a larger condenser area.

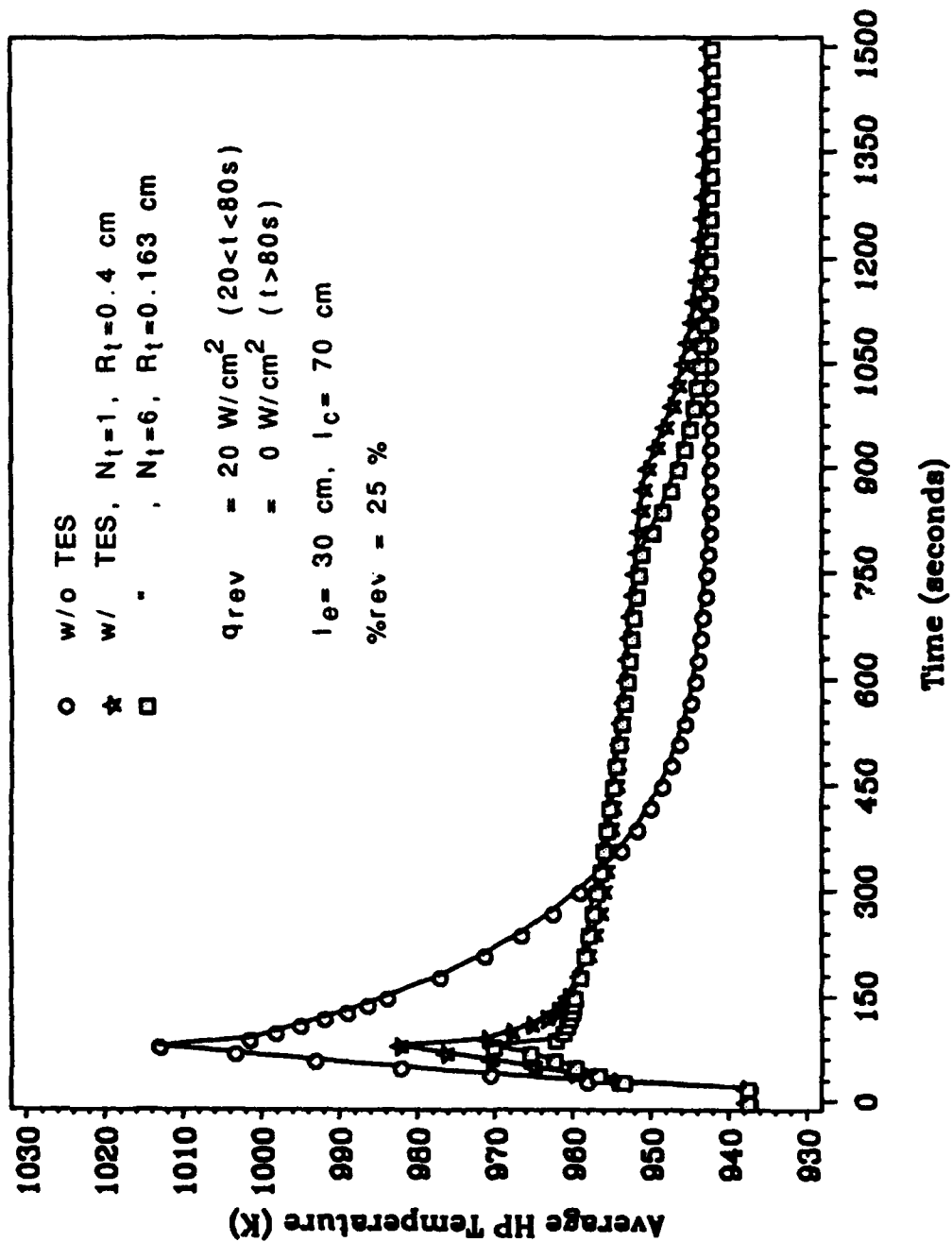


Figure 5.23 Transient response of heat pipes under a reversed-pulse heat load which covers 25% of condenser

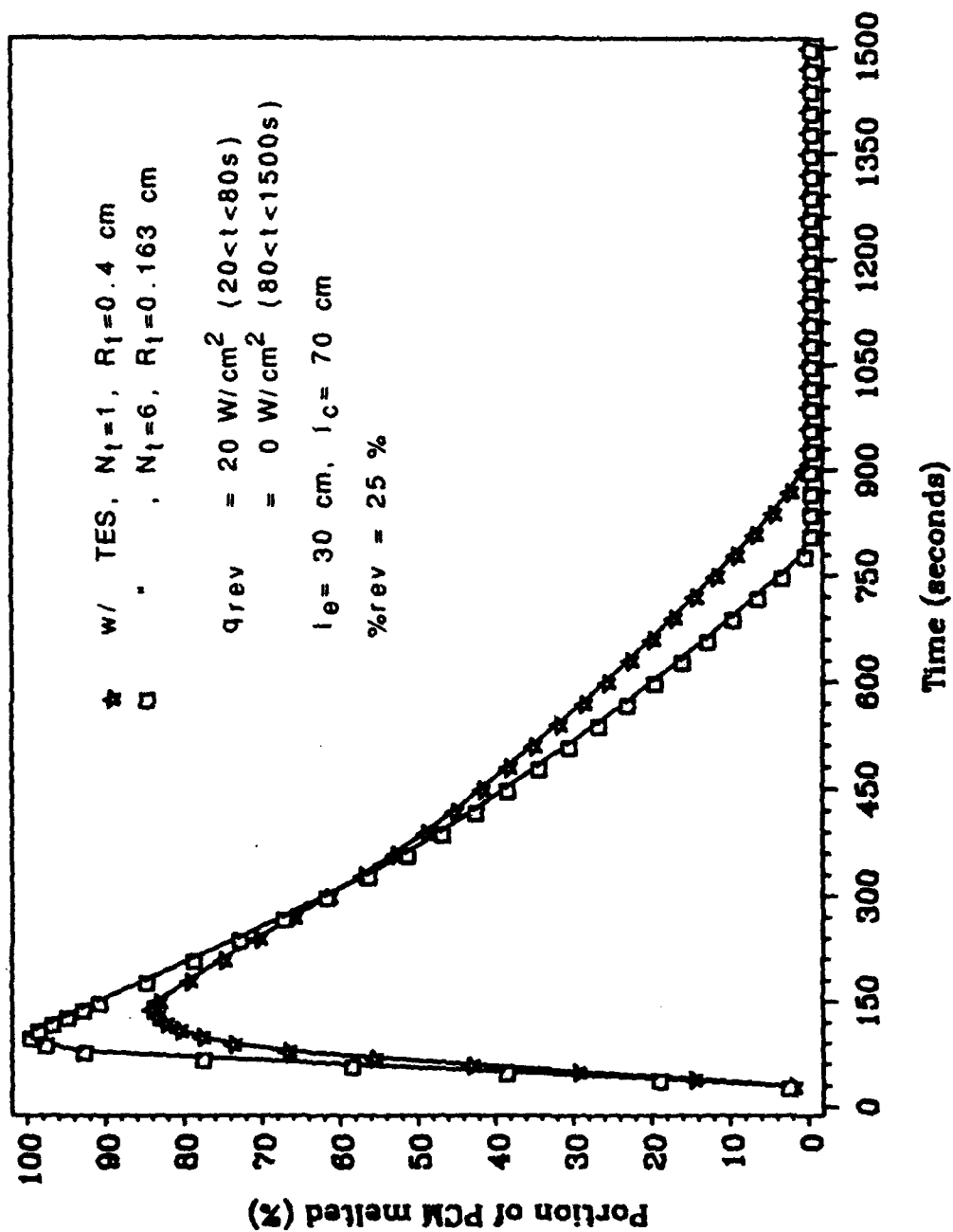


Figure 5.24 Portion of PCM melted versus time for heat pipes under a reversed-pulse heat load which covers 25% of condenser

CHAPTER 6

CONCLUSIONS

In this research, the transient behavior of a high-temperature grooved heat pipe with thermal energy storage (TES) under pulse heat loads was modeled using a three-dimensional ADI finite-difference method. A phase-change material (PCM) encapsulated in cylindrical containers was used as the TES. Two different types of pulse heat loads applied to the heat pipe were studied. One was high-pulse heat loads applied at the heat pipe evaporator. The other one was reversed-pulse heat loads applied at the condenser. It was found that the PCM is very effective in mitigating the adverse effects of both types of pulse heat loads. The six small PCM cylinders are more efficient than the single large PCM cylinder in reducing the rapid increase in heat pipe temperature under pulse heat loads, and they can also handle periodic, pulse heat loads better since they solidify faster.

Since the heat pipe capillary limit is dependent on the overall liquid and vapor pressure drops and the vapor pressure drop dominates the liquid pressure drop for this type of heat pipe, the effect of the liquid pressure drop on the heat pipe capillary limit can be neglected. The vapor pressure and temperature drops of the heat pipe were found to be strongly dependent on the operating vapor temperature. The vapor flow can be reversed or become two opposing flows under reversed heat loads. The numerical results also indicated that the heat inputs and outputs of the heat pipes in the cooling system under reversed-pulse heat loads are strongly dependent on the sodium loop heat capacitance.

The main disadvantage of installing phase-change material in the

vapor core of a heat pipe is the accompanying reduction in the vapor flow area. This reduction in vapor flow area could cause the vapor pressure drop and vapor velocity to increase significantly, and thus decrease the heat pipe capability. Fortunately, the PCM itself can absorb a large portion of the heat loads during the melting process after pulse heat loads are applied. Some vapor will condense on the surface of PCM cylinders and reduce the vapor velocity and pressure drop. From the numerical results, one can find that not only can the PCM compensate for the decrease in heat pipe transport capability due to the reduction in vapor flow area, it can also actually handle the pulse heat loads very effectively.

In the design of an HP/TES system, one should choose a PCM with a melting point slightly higher than the normal operating temperature. Then if a pulse heat load higher than the heat pipe transport limitation is applied, the PCM can respond fast enough to begin melting and absorb some of the heat before the heat pipe reaches its operating limit and burns out. To reduce the chance of complete melting during the pulse period, the latent heat of fusion of the PCM should be as large as possible. Also, the cycle time is a vital consideration in the design of an HP/TES cooling system to handle periodic, pulse heat loads.

The concept of incorporating phase-change material inside a low-temperature heat pipe (such as a water heat pipe) is also sound if the goal is to limit the temperature extremes encountered when the heat load is time dependent. For most low-temperature heat pipes, the vapor pressure drop is small, and vapor flow usually does not play an important role in determining the heat pipe transport capability. Thus the increase in the vapor pressure drop and vapor velocity caused by the

reduction in flow area would not have a significant effect on heat pipe capability.

An improved three-dimensional ADI finite-difference method used to model the heat conduction through the heat pipe wall and wick was developed in this research. An important characteristic of this new ADI method is that the resulting finite-difference equations are consistent with physical considerations. Compared to the conventional ADI method, this modification allows the time step to be increased by about 2 orders of magnitude without compromising significantly on the accuracy of the numerical solution. Compared with the well-known Brian and Douglas ADI methods, this new ADI method yields higher accuracy and requires less computer storage.

The equivalent heat capacity method proposed by Hsiao for the Stefan problem was tested in this research, but a large energy balance error was found. Similar conclusion was also given by Pham. Comparing with exact solutions, Pham pointed out that the Hsiao method yields results with up to 22% error. The low accuracy of the Hsiao's method could be due to its ambiguous theoretical basis. Pham suggested a simple and accurate method which includes the good features of the enthalpy and heat capacity methods. One of the good features in the Pham method is that it estimates the new temperature from the estimated enthalpy change to avoid the problem of jumping the latent heat peak. However, the Pham method has a singularity problem.

In this report, we adopted the best features of the Pham method for the Stefan problem and made some modifications to improve on its weak points. This modified Pham method was used in conjunction with a two-dimensional ADI scheme. Compared with analytical solutions, the

present method for melting and solidification was found to have very good accuracy without the singularity problem of the Pham method.

Liquid dynamics in a heat pipe become very significant when dryout and rewetting occur in the heat pipe wick. However, dryout depends on the heated zone and the instantaneous local saturation. Thus, if dryout is to be accurately predicted, the temporal dependence of the saturation distribution must be taken account. A complete capillary liquid flow model is needed to predict the dryout and rewetting behaviors of a heat pipe. A good capillary liquid flow model should include the effect of vapor pressure changes on the liquid meniscus contact angle and also be able to predict the saturation distribution.

It was found that the lumped-heat-capacity model can predict the average heat pipe temperature and the heat flow input/output at the evaporator and condenser very well for the heat pipe without PCM. We have also checked the total energy balance and found the error is less than 1% at each time step. To further validate the numerical solutions, we applied the numerical model to some problems by using different time steps and grid spacings. The results reported here were obtained with a sufficiently fine grid spacing and time step so that numerical results are essentially independent of the time step and grid spacing.

APPENDIX

Listing of The Computer Program

```

C 3-D COMPUTER PROGRAM FOR TRANSIENT BEHAVIOR OF AXIALLY GROOVED HEAT
C PIPE UNDER PULSE HEAT LOADS
C
C
C CKL -THERMAL CONDUCTIVITY OF LIQUID (W/M-K)
C CKLHL -THERMAL CONDUCTIVITY OF LIQUID LIH (W/M-K)
C CKLHS -THERMAL CONDUCTIVITY OF SOLID LIH (W/M-K)
C CKSS -THERMAL CONDUCTIVITY OF SOLID (W/M-K)
C CKP -NODAL THERMAL CONDUCTIVITY (W/M-K)
C CL -LIQUID HEAT CAPACITY (J/K-KG)
C CLHL -HEAT CAPACITY OF LIQUID LIH (J/K-KG)
C CLHS -HEAT CAPACITY OF SOLID LIH (J/K-KG)
C CP -NODAL HEAT CAPACITY (J/K-KG)
C CS -SOLID HEAT CAPACITY (J/K-KG)
C DENL -DENSITY OF LIQUID (KG/M3)
C DENLHL -DENSITY OF LIQUID LIH (KG/M3)
C DENLHS -DENSITY OF SOLID LIH (KG/M3)
C DENP -NODAL DENSITY (KG/M3)
C DENS -DENSITY OF SOLID (KG/M3)
C DQVDA(K) -LOCAL INWARD HEAT FLUX ON THE VAPOR INTERFACE (W/M2)
C DRS -SPACE INCREMENT IN RADIAL DIRECTION IN SOLID (M)
C DRW -SPACE INCREMENT IN RADIAL DIRECTION IN WICK (M)
C DT -TIME STEP (SEC)
C DTHETA -ANGULAR INCREMENT (RADIAN)
C DTV1 -HALF TEMPERATURE INTERVAL OF VAPOR FOR SEARCHING TV(1) (K)
C DZ -SPACE INCREMENT IN AXIAL DIRECTION (M)
C EMISS -EMISSIVITY
C HFUSLH -FUSION HEAT OF LIH (J/KG)
C HTCAMB -AMBIENT HEAT TRANSFER COEFFICIENT FOR THE CONDENSER (W/M2K)
C NG -NUMBER OF GROOVES
C PV(K) -VAPOR THERMODYNAMIC PRESSURE (N/M2)
C QEVP -HEAT FLUX ON THE WALL OF THE EVAPORATOR (W/M2)
C QVIN -NODAL HEAT TRANSFER FROM HEAT PIPE WALL TO VAPOR FLOW (W)
C QV(K) -LOCAL HEAT TRANSFER FROM HEAT PIPE WALL TO VAPOR FLOW (W)
C R -NODAL RADIUS (M)
C RI -INSIDE RADIUS OF HEAT PIPE WALL (M)
C RMENIS -MENISCUS RADIUS (M)
C RO -OUTSIDE RADIUS OF HEAT PIPE WALL(M)
C RW -VAPOR CORE RADIUS (M)
C SIGMA -STEFAN-BOLTZMAN CONSTANT (W/M2K4)
C SUMQVI -TOTAL EVAPORATION RATE (W)
C SUMQVO -TOTAL CONDENSATION RATE (W)
C TAMB -AMBIENT TEMPERATURE TO THE CONDENSER (K)
C TMELLH -MELT TEMPERATURE OF LIH (K)
C T(I,J,K) -NODAL TEMPERATURE (K)
C TV(K) -VAPOR TEMPERATURE (K)
C XL -HEAT PIPE LENGTH (M)
C*****
      REAL *8 TVOLD(100),TV(100),TE(40,100),TTE(40,100),DTV(100)
      REAL *8 T(8,5,100),TW(5,100),TT(8,5,100),TOLD(8,5,100)
      REAL *8 TV0(100),TVNEW(100),DPV(100),DPL(100)

```

```

        DIMENSION P(100),Q(100),CKNR(5,100)
        DIMENSION QWALL(5,100),DQVDAN(100),DQDATN(100)
        DIMENSION THPAVG(20000),TVAVG(20000),CTIME(20000)
        DIMENSION QV0(100),QVNEW(100),QVOLD(100)

C
C
        COMMON /HPIPE/ TV,DQDATE(100),ZL,DZ,NZ,NDT,QVTES(100),
        $NTESTU,TIME,KBURN,NWRITE,XWRITE,NGROV,RW,NADIA,PV(100)
        COMMON /VCORE/ DQVDA(100),DQDABAR(100),IPCM,PVTTL(100)
        $ ,TVREAL(100),PLM,DTES,DVAPOR,DWICK,DHYDRO,XMMAX,KPLM
        $ ,NEVAP,XTI,DENV(100)
        COMMON /PCM/ TVOLD,TE,TTE,DTV,DT,NADI,NRTES,DTHETA,RTES,
        $ TSTART,NTHETA,QPCM,QMELT,QPCMTTL
        COMMON /LIQ/ QV(100),PL(100),SUMQVI,KPVMIN,PCMAX,DPVPLMAX,
        $ CL,NZP1,WIDBAR,DEPTHG,DENL,VISLIQ,TENLIQ,LAMBDA

C  CHOOSE RUNNING CASE:      IPCM=1 (WITHOUT PCM);      IPCM=2 (WITH PCM)
C                           METHOD=1 (EXPLICIT);        METHOD=2 (IMPLICIT)

        IPCM=1
        METHOD=1

        FRELAX=0.02

        IF(METHOD.EQ.1) FRELAX=0.0

C  CHOOSE TIME STEP (SEC)
        DT=0.1
        NDTEND= 6000

C  SPECIFY THERMAL ENERGY STORAGE
        NTESTU= 0
        RTES=0.004
        NRTES= 40

CC  NTESTU= 6
CC  RTES=0.001633001
CC  NRTES= 10

        NWINCH=200

C  CHOOSE TIME TO WRITE
        NWRITE= 100
        XWRITE=1.0*NWRITE
C

```

C
 C CONVERGENCE CRITERIA FOR THE EVAPORATOR END VAPOR TEMPERATURE
 EPSQVK=0.01
 C
 C
 C SPECIFIED TRUNCATION ERROR FOR THE VAPOR FLOW
 EPSV=0.01
 C SPECIFIED BOUNDARY CONDITIONS OF HEAT TRANSFER ON THE HEAT PIPE WALL
 QEVP= 4.3*10000.0
 CC TF=941.0
 CC HTCF=37043.0

 EMISS=1.0
 SIGMA=5.669E-8
 TAMB= 0.0

 KBURN=0

 C
 C
 C HEAT PIPE GEOMETRY
 NGROV=18
 NTHETA=4
 NTHEPG=4
 NRS=4
 NRW=4
 NR=NRS+NRW

 NZ= 40
 NEVAP=12
 NADIA= 28
 ZL= 1.0
 NZP1=NZ+1

 PLM=NEVAP*DZ
 KPLM=NEVAP

 RO=0.009525
 RI=0.008262
 RW=0.007000

 NWIRE=NWINCH/0.0254
 RC=1.0/(2.0*NWIRE)

 WIDBAR=2.0*3.1416*(RI+RW)/2.0/2.0/NGROV/2.0
 DEPTHG=RI-RW
 DWICK=2.0*RW
 DTES=2.0*RTES

 DRS=(RO-RI)/NRS

DRW=(RI-RW)/NRW
 DTHETA=2*3.14/NTHETA/NGROV
 DZ=ZL/NZ

XTI=NEVAP*DZ

C GROOVE GEOMETRY
 JING2=2
 JING3=3
 C THERMAL CONDUCTIVITY, HEAT CAPACITY AND DENSITY
 C SOLID:STAINLESS STEEL, LIQUID:SODIUM
 CKSS=18.4
 CKL=75.7
 CS=530.0
 CL=1305.0
 DENS=7744.0
 DENL=882.0
 NTHEP1=NTHETA

WRITE(6,*) 'NTESTU=', NTESTU
 WRITE(6,*) 'RO=', RO, 'PL=', ZL
 WRITE(6,*) 'NZ=', NZ, 'NR=', NR, 'NRS=', NRS, 'NRW=', NRW
 WRITE(6,*) 'QEVAP=', QEVAP, 'SIGMA=', SIGMA, 'TAMB=', TAMB

C HEAT PIPE STARTING TEMPERATURE
 TSTART= 940.0
 DO 30 K=1,NZ
 DO 33 J=1,NTHEP1
 DO 36 I=1,NR
 T(I,J,K)=TSTART
 TOLD(I,J,K)=TSTART
 TW(J,K)=TSTART
 36 CONTINUE
 33 CONTINUE
 TV(K)=TSTART
 TVOLD(K)=TSTART
 QV(K)=0.0
 DQVDA(K)=0.0
 QVTES(K)=0.0
 DQDATE(K)=0.0
 DTV(K)=0.0
 30 CONTINUE

 QETTTL=0.0
 QCTTL=0.0
 QTES=0.0

SUMQVI=0.0

TIME=0.0

DO 60 NDT= 1,NDTEND

C PULSE HEAT FLUX SPECIFICATION

IF (NDT.LE.100) PULSE=1.0

IF (NDT.GT.100) PULSE=10.0/4.3

CC IF (NDT.LE.100) PULSE=1.0

CC IF (NDT.GT.100.AND.NDT.LE.1000) PULSE=10.0/4.3

CC IF (NDT.GT.1000) PULSE=1.0

CC IF (NDT.LE.200) PULSE=1.0

CC IF (NDT.GT.200.AND.NDT.LE.400) PULSE=10.0/4.3

CC IF (NDT.GT.400.AND.NDT.LE.2200) PULSE=1.0

CC IF (NDT.GT.2200.AND.NDT.LE.2400) PULSE=10.0/4.3

CC IF (NDT.GT.2400.AND.NDT.LE.4200) PULSE=1.0

CC IF (NDT.GT.4200.AND.NDT.LE.4400) PULSE=10.0/4.3

CC IF (NDT.GT.4400.AND.NDT.LE.6200) PULSE=1.0

CC IF (NDT.GT.6200.AND.NDT.LE.6400) PULSE=10.0/4.3

CC IF (NDT.GT.6400.AND.NDT.LE.8200) PULSE=1.0

CC IF (NDT.GT.8200.AND.NDT.LE.8400) PULSE=10.0/4.3

CC IF (NDT.GT.8400.AND.NDT.LE.10200) PULSE=1.0

IF (NTESTU.EQ.0) DHYDRO=0.014

IF (NTESTU.EQ.1) DHYDRO=0.0082

IF (NTESTU.EQ.6) DHYDRO=0.0075

DVAPOR=(DWICK**2.0-NTESTU*DTES**2.0)**0.5

IF (NDT.LE.20) EPSV=0.01

IF (NDT.GT.20) EPSV=0.01

F=0.01

F1=3.0-2.0*F

C DDTV1=1.0

C DTV1=(TV(1)-TVOLD(1))+DDTV1

DTV1=3.0

DO 10 K=1,NZ

TVOLD(K)=TV(K)

10 CONTINUE

IF ((NDT/XWRITE).EQ.(NDT/NWRITE)) THEN

```

TIME=NDT*DT
C  LIQUID PROPERTIES
  VISLIQ=0.0011-1.45E-6*TV(1)+5.32E-10*TV(1)**2.0
  TENLIQ=0.22-9.1E-5*TV(1)
  LAMBDA=4636437.0-180.8*TV(1)

  PCMAX=2.0*TENLIQ/RC

  DO 20 K=1,NZ
    QV0(K)=QV(K)+QVTES(K)
    TV0(K)=TV(K)
20  CONTINUE

  DO 25 K=1,NZ
    IF(K.LE.NEVAP) DQDABAR(K)=(SUMQVI/NEVAP)/(2.0*3.1416*RW*DZ
$                                     +NTESTU*2.0*3.1416*RTES*DZ)
    IF(K.GT.NEVAP.AND.K.LE.NADIA) DQDABAR(K)=0.0
    IF(K.GT.NADIA) DQDABAR(K)=- (SUMQVI/(NZ-NADIA))/(2.0*3.1416*RW*DZ
$                                     +NTESTU*2.0*3.1416*RTES*DZ)
25  CONTINUE
C
C*****
C ***** COMPUTATION FOR THE FIRST ONE-THIRD TIME STEP *****

  NADI=123

  QHP=0.0

  DO 180 J=1,NTHEP1
    NGORD=(J-1)/NTHEPG+1
    JING=J-(NGORD-1)*NTHEPG
  DO 160 I=1,NR
  DO 100 K=1,NZ

    IF(NDT.EQ.1) QV(K)=0.0

    IF(K.LE.KBURN) THEN
      CKL=0.0000001
    ELSE
      CKL=75.7
    ENDIF

    IF(K.LE.NEVAP) QWALL(J,K)=PULSE*QEVAP

```

```

CC      IF (K.LE.NEVAP) QWALL(J,K)=HTCF*(TF-TW(J,K))
      IF (K.GT.NEVAP.AND.K.LE.NADIA) QWALL(J,K)=0.0
      IF (K.GT.NADIA) QWALL(J,K)=EMISS*SIGMA*(TAMB**4.0-TW(J,K)**4.0)

```

```

      IF (I.LE.NRS) THEN
        R=RO-(I-0.5)*DRS
        DR=DRS
        CKP=CKSS
        CKN=CKSS
        CKS=CKSS
        CKE=CKSS
        CKW=CKSS
        CKF=CKSS
        CKB=CKSS
        DENP=DENS
        CP=CS
        IF (I.EQ.NRS.AND.JING.GE.JING2.AND.JING.LE.JING3) CKS=
$          CKSS*CKL*(DRS+DRW)/(CKSS*DRW+CKL*DRS)
      ENDIF

```

```

      IF (I.EQ.1) THEN
        R1M=R
        DR1=DR
        CK1M=CKN
      ENDIF

```

```

      IF (I.GT.NRS) THEN
        R=RI-(I-NRS-0.5)*DRW
        DR=DRW
        IF (JING.LT.JING2.OR.JING.GT.JING3) THEN
          CKP=CKSS
          CKN=CKSS
          CKS=CKSS
          CKE=CKSS
          CKW=CKSS
          CKF=CKSS
          CKB=CKSS
          DENP=DENS
          CP=CS
          IF (JING.EQ.(JING2-1)) CKF=2.0*CKSS*CKL/(CKSS+CKL)
          IF (JING.EQ.(JING3+1)) CKB=2.0*CKSS*CKL/(CKSS+CKL)
        ENDIF

```

```

      IF (JING.GE.JING2.AND.JING.LE.JING3) THEN
        CKP=CKL
        CKN=CKL
        CKS=CKL
        CKE=CKL
        CKW=CKL
        CKF=CKL
        CKB=CKL

```

```

DENP=DENL
CP=CL
IF (I.EQ.(NRS+1)) CKN=CKSS*CKL*(DRS+DRW)/(CKSS*DRW+CKL*DRS)
IF (JING.EQ.JING2) CKB=2.0*CKSS*CKL/(CKSS+CKL)
IF (JING.EQ.JING3) CKF=2.0*CKSS*CKL/(CKSS+CKL)
ENDIF
ENDIF

VOLP=((R+DR/2)**2.0-(R-DR/2)**2.0)*(DTHETA/2)*DZ
QHP=QHP+DENP*VOLP*CP*(T(I,J,K)-TSTART)*NGROV

IF (I.EQ.NR.AND.JING.NE.JING2.AND.JING.NE.JING3.AND.
$   DQDABAR(K).GT.0.0) CKS=0.0

C=-CKW*F1
A=3.0*DENP*CP*DZ**2.0/DT+(CKW+CKE)*F1
B=-CKE*F1
D2=(DZ**2.0*CKN*(R+DR/2.0)/R/DR**2.0)*F
D3=(DZ**2.0*CKS*(R-DR/2.0)/R/DR**2.0)*F
D4=(DZ**2.0*CKB/(R*DTHETA)**2.0)*F
D5=(DZ**2.0*CKF/(R*DTHETA)**2.0)*F

IF (J.EQ.1) D4=0.0
IF (J.EQ.NTHETA) D5=0.0

D1=3.0*DENP*CP*DZ**2.0/DT-D2-D3-D4-D5

IF (I.EQ.1.OR.I.EQ.NR.OR.J.EQ.1.OR.J.EQ.NTHEP1) THEN

    D7=(2.0*DZ**2.0*CKS*(R-DR/4.0)/R/DR**2.0)*F

    IF (I.EQ.1.OR.I.EQ.NR) THEN
        IF (J.EQ.1.OR.J.EQ.NTHEP1) THEN
            IF (I.EQ.1.AND.J.EQ.1) D=(D1+D2)*T(I,J,K)+D3*T(I+1,J,K)
$                                     +D5*T(I,J+1,K)
$                                     + (QWALL(J,K)*RO*DZ**2.0/R/DR)*F
            IF (I.EQ.1.AND.J.EQ.NTHEP1) D=(D1+D2)*T(I,J,K)+D3*T(I+1,J,K)
$                                     +D4*T(I,J-1,K)
$                                     + (QWALL(J,K)*RO*DZ**2.0/R/DR)*F
            IF (I.EQ.NR.AND.J.EQ.1) D=(D1+D3)*T(I,J,K)+D2*T(I-1,J,K)
$                                     +D7*TVOLD(K) +D5*T(I,J+1,K) -D7*TOLD(I,J,K)
            IF (I.EQ.NR.AND.J.EQ.NTHEP1) D=(D1+D3)*T(I,J,K)
$                                     +D2*T(I-1,J,K) +D7*TVOLD(K) +D4*T(I,J-1,K) -D7*TOLD(I,J,K)
        ELSE
            IF (I.EQ.1) D=(D1+D2)*T(I,J,K)+D3*T(I+1,J,K)+D4*T(I,J-1,K)
$                                     +D5*T(I,J+1,K) + (QWALL(J,K)*RO*DZ**2.0/R/DR)*F
            IF (I.EQ.NR) D=(D1+D3)*T(I,J,K)+D2*T(I-1,J,K)
$                                     +D7*TVOLD(K) +D4*T(I,J-1,K) +D5*T(I,J+1,K) -D7*TOLD(I,J,K)
        ENDIF
    ENDIF

```

```

ELSE
  IF (J.EQ.1) D=D1*T(I,J,K)+D2*T(I-1,J,K)+D3*T(I+1,J,K)
$      +D5*T(I,J+1,K)
  IF (J.EQ.NTHEP1) D=D1*T(I,J,K)+D2*T(I-1,J,K)+D3*T(I+1,J,K)
$      +D4*T(I,J-1,K)
ENDIF

ELSE
  D=D1*T(I,J,K)+D2*T(I-1,J,K)+D3*T(I+1,J,K)+D4*T(I,J-1,K)
$  +D5*T(I,J+1,K)
ENDIF
IF (D1.LT.0.0) WRITE(6,128) I,J,K
128 FORMAT(1X,'D1=(-) IN ROOP3 I,J,K=',3(2X,I3))
IF (D1.LT.0.0) GO TO 1000
IF (K.EQ.1) THEN
  C=0.0
  A=A-CKW*F1
  B=B
  D=D
ENDIF
IF (K.EQ.NZ) THEN
  C=C
  A=A-CKE*F1
  B=0.0
  D=D
ENDIF
C
C TDMA ALGORITHM
C
  P(K)=-B/(A+C*P(K-1))
  Q(K)=(D-C*Q(K-1))/(A+C*P(K-1))

  IF (I.EQ.NR) CKNR(J,K)=CKS
  IF (K.LE.KBURN) CKNR(J,K)=0.0

  IF (NDT.EQ.1.AND.I.EQ.NR) THEN
    QVIN=CKNR(J,K)*(DTHETA*(RW+DRW/4.0)*DZ)*NGROV
$    *(T(NR,J,K)-TVOLD(K))/(DRW/2.0)
    QV(K)=QV(K)+QVIN
    DQVDA(K)=QV(K)/(2.0*3.1416*RW*DZ)
  ENDIF

100 CONTINUE

DO 170 K1=1,NZ
  K=NZ+1-K1
  TT(I,J,K)=P(K)*TT(I,J,K+1)+Q(K)
170 CONTINUE
160 CONTINUE
180 CONTINUE

```

```

      IF (NDT.EQ.1) GO TO 182

      AEVAP=NEVAP*DZ*(2.0*3.1416*RO)
      ACOND=(NZ-NADIA)*DZ*(2.0*3.1416*RO)
      TCAVG=0.0

      DO 110 K=NADIA+1,NZ
      DO 115 J=1,NTHETA
        TCAVG=TCAVG+TW(J,K)/(NTHETA*(NZ-NADIA))
115    CONTINUE
110    CONTINUE

      QWTES=0.0
      DO 187 K=1,NZ
        QWTES=QWTES+QVTES(K)
187    CONTINUE

      XXX=AEVAP*QEVAP*PULSE
      QETTTL=QETTTL+AEVAP*QEVAP*PULSE*DT
      QCTTTL=QCTTTL+ACOND*EMISS*SIGMA*(TCAVG**4.0-TAMB**4.0)*DT
      QTES=QTES-QWTES*DT

182 DO 193 K=1,NZ
      DO 194 J=1,NTHEP1
      DO 195 I=1,NR
        T(I,J,K)=TT(I,J,K)
195    CONTINUE
194    CONTINUE
193    CONTINUE

C
C  ~~~~~
C  ~~~~~ COMPUTATION FOR THE SECOND ONE-THIRD TIME STEP ~~~~~

      NADI=123

      DO 280 I=1,NR
      DO 260 K=1,NZ
      DO 200 J=1,NTHEP1

      NGORD=(J-1)/NTHEPG+1
      JING=J-(NGORD-1)*NTHEPG

      IF (K.LE.KBURN) THEN

```

```

    CKL=0.0000001
ELSE
    CKL=75.7
ENDIF

```

```

IF (I.LE.NRS) THEN
    R=RO-(I-0.5)*DRS
    DR=DRS
    CKP=CKSS
    CKN=CKSS
    CKS=CKSS
    CKE=CKSS
    CKW=CKSS
    CKF=CKSS
    CKB=CKSS
    DENP=DENS
    CP=CS
    IF (I.EQ.NRS.AND.JING.GE.JING2.AND.JING.LE.JING3) CKS=
$      CKSS*CKL*(DRS+DRW)/(CKSS*DRW+CKL*DRS)
ENDIF

```

```

IF (I.GT.NRS) THEN
    R=RI-(I-NRS-0.5)*DRW
    DR=DRW
    IF (JING.LT.JING2.OR.JING.GT.JING3) THEN
        CKP=CKSS
        CKN=CKSS
        CKS=CKSS
        CKE=CKSS
        CKW=CKSS
        CKF=CKSS
        CKB=CKSS
        DENP=DENS
        CP=CS
        IF (JING.EQ.(JING2-1)) CKF=2.0*CKSS*CKL/(CKSS+CKL)
        IF (JING.EQ.(JING3+1)) CKB=2.0*CKSS*CKL/(CKSS+CKL)
    ENDIF

```

```

IF (JING.GE.JING2.AND.JING.LE.JING3) THEN
    CKP=CKL
    CKN=CKL
    CKS=CKL
    CKE=CKL
    CKW=CKL
    CKF=CKL
    CKB=CKL
    DENP=DENL
    CP=CL
    IF (I.EQ.(NRS+1)) CKN=CKSS*CKL*(DRS+DRW)/(CKSS*DRW+CKL*DRS)
    IF (JING.EQ.JING2) CKB=2.0*CKSS*CKL/(CKSS+CKL)
    IF (JING.EQ.JING3) CKF=2.0*CKSS*CKL/(CKSS+CKL)

```



```

ENDIF
ENDIF

```

```

IF (I.EQ.NR.AND.JING.NE.JING2.AND.JING.NE.JING3.AND.
$   DQDABAR(K).GT.0.0) CKS=0.0

```

```

C=-CKB*F1
A=3.0*DENP*CP*(R*DTHETA)**2.0/DT+(CKB+CKF)*F1
B=-CKF*F1
D2=(R*DTHETA**2.0*CKN*(R+DR/2.0)/DR**2.0)*F
D3=(R*DTHETA**2.0*CKS*(R-DR/2.0)/DR**2.0)*F
D4=((R*DTHETA)**2.0*CKW/DZ**2.0)*F
D5=((R*DTHETA)**2.0*CKE/DZ**2.0)*F
IF(K.EQ.1) D4=0.0
IF(K.EQ.NZ) D5=0.0
D1=3.0*DENP*CP*(R*DTHETA)**2.0/DT-D2-D3-D4-D5

```

```

IF (I.EQ.1.OR.I.EQ.NR.OR.K.EQ.1.OR.K.EQ.NZ) THEN

```

```

    D7=(2.0*R*DTHETA**2.0*CKS*(R-DR/4.0)/DR**2.0)*F

```

```

    IF (I.EQ.1.OR.I.EQ.NR) THEN

```

```

        IF (K.EQ.1.OR.K.EQ.NZ) THEN

```

```

            IF (I.EQ.1.AND.K.EQ.1) D=(D1+D2)*T(I,J,K)+D3*T(I+1,J,K)
$              +D5*T(I,J,K+1)+(QWALL(J,K)*RO*R*DTHETA**2.0/DR)*F
            IF (I.EQ.1.AND.K.EQ.NZ) D=(D1+D2)*T(I,J,K)+D3*T(I+1,J,K)
$              +D4*T(I,J,K-1)+(QWALL(J,K)*RO*R*DTHETA**2.0/DR)*F
            IF (I.EQ.NR.AND.K.EQ.1) D=(D1+D3-D7)*T(I,J,K)+D2*T(I-1,J,K)
$              +D7*TVOLD(K)+D5*T(I,J,K+1)
            IF (I.EQ.NR.AND.K.EQ.NZ) D=(D1+D3-D7)*T(I,J,K)+D2*T(I-1,J,K)
$              +D7*TVOLD(K)+D4*T(I,J,K-1)

```

```

        ELSE

```

```

            IF (I.EQ.1) D=(D1+D2)*T(I,J,K)+D3*T(I+1,J,K)+D4*T(I,J,K-1)
$              +D5*T(I,J,K+1)+(QWALL(J,K)*RO*R*DTHETA**2.0/DR)*F
            IF (I.EQ.NR) D=(D1+D3-D7)*T(I,J,K)+D2*T(I-1,J,K)
$              +D7*TVOLD(K)+D4*T(I,J,K-1)+D5*T(I,J,K+1)

```

```

        ENDIF

```

```

    ELSE

```

```

        IF (K.EQ.1) D=D1*T(I,J,K)+D2*T(I-1,J,K)+D3*T(I+1,J,K)
$              +D5*T(I,J,K+1)
        IF (K.EQ.NZ) D=D1*T(I,J,K)+D2*T(I-1,J,K)+D3*T(I+1,J,K)
$              +D4*T(I,J,K-1)

```

```

    ENDIF

```

```

ELSE

```

```

    D=D1*T(I,J,K)+D2*T(I-1,J,K)+D3*T(I+1,J,K)+D4*T(I,J,K-1)
$    +D5*T(I,J,K+1)

```

```

ENDIF

```



```

      QVOLD (K) =QV (K) +QVTES (K)
      TVOLD (K) =TV (K)
405 CONTINUE

      NQV0=NQV0+1
C1   IF (NQV0.GT. 1) GO TO 450

      DO 448 K=1,NZ
        IF (NQV0.GT.1) DQVDA (K) =DQVDA (K) +FRELAX* (DQVDAN (K) -DQVDA (K) )
        IF (NQV0.GT.1) DQDATE (K) =DQDATE (K) +FRELAX* (DQDATN (K) -DQDATE (K) )
448 CONTINUE

C
C   GUESS TV (KBURN+1) FOR THE NEXT TIME STEP

      TVEE1=0.0
      TVEE2=0.0
      NCALLV=0
400 NCALLV=NCALLV+1

      IF (NCALLV.GT. 200) THEN
        WRITE (6,*) 'NCALLV > 200'
        GO TO 1000
      ENDIF

      IF (NCALLV.EQ.1) TV (KBURN+1) =TV0 (KBURN+1) +DTV1
      IF (NCALLV.EQ.2) TV (KBURN+1) =TV0 (KBURN+1) -DTV1
      IF (NCALLV.GT.2) THEN
        IF ((TVEE1*TVEE2).EQ.0.0) THEN
          WRITE (6,*) 'TVEE1*TVEE2=0.0'
          GO TO 1000
        ELSE
          TV (KBURN+1) = (TVEE1+TVEE2) /2.0
        ENDIF
      ENDIF

C   IF ((NDT/XWRITE).EQ. (NDT/NWRITE)) THEN
C   WRITE (6,*) 'NCALLV=', NCALLV, 'TV0=', TV (KBURN+1)
C   ENDIF

C1  CALL BOWMAN
    CALL CHI

      DO 415 N= 1,NZ
C1  TV (N) =TV (KBURN+1)

```

```

                                TV(N)=TVREAL(N)
415  CONTINUE

DO 380 K=1,NZ
DO 360 J=1,NTHEP1
NGORD=(J-1)/NTHEPG+1
JING=J-(NGORD-1)*NTHEPG
DO 300 I=1,NR

IF(K.LE.KBURN) THEN
    CKL=0.0000001
ELSE
    CKL=75.7
ENDIF

IF(I.LE.NRS) THEN
    R=RO-(I-0.5)*DRS
    DR=DRS
    CKP=CKSS
    CKN=CKSS
    CKS=CKSS
    CKE=CKSS
    CKW=CKSS
    CKF=CKSS
    CKB=CKSS
    DENP=DENS
    CP=CS
    IF(I.EQ.NRS.AND.JING.GE.JING2.AND.JING.LE.JING3) CKS=
$      CKSS*CKL*(DRS+DRW)/(CKSS*DRW+CKL*DRS)
    ENDIF

IF(I.GT.NRS) THEN
    R=RI-(I-NRS-0.5)*DRW
    DR=DRW
    IF(JING.LT.JING2.OR.JING.GT.JING3) THEN
        CKP=CKSS
        CKN=CKSS
        CKS=CKSS
        CKE=CKSS
        CKW=CKSS
        CKF=CKSS
        CKB=CKSS
        DENP=DENS
        CP=CS
        IF(JING.EQ.(JING2-1)) CKF=2.0*CKSS*CKL/(CKSS+CKL)
        IF(JING.EQ.(JING3+1)) CKB=2.0*CKSS*CKL/(CKSS+CKL)
    ENDIF

```

```

IF (JING.GE.JING2.AND.JING.LE.JING3) THEN
  CKP=CKL
  CKN=CKL
  CKS=CKL
  CKE=CKL
  CKW=CKL
  CKF=CKL
  CKB=CKL
  DENP=DENL
  CP=CL
  IF (I.EQ.(NRS+1)) CKN=CKSS*CKL*(DRS+DRW)/(CKSS*DRW+CKL*DRS)
  IF (JING.EQ.JING2) CKB=2.0*CKSS*CKL/(CKSS+CKL)
  IF (JING.EQ.JING3) CKF=2.0*CKSS*CKL/(CKSS+CKL)
ENDIF
ENDIF

```

```

IF (I.EQ.NR.AND.JING.NE.JING2.AND.JING.NE.JING3.AND.
$   DQDABAR(K).GT.0.0) CKS=0.0

```

```

C=-CKN*(R+0.5*DR)*F1
A=3.0*DENP*CP*R*DR**2.0/DT+(CKN*(R+0.5*DR)
$+CKS*(R-0.5*DR))*F1
B=-CKS*(R-0.5*DR)*F1
D2=(DR**2.0*CKB/R/DTHETA**2.0)*F
D3=(DR**2.0*CKF/R/DTHETA**2.0)*F
D4=(R*DR**2.0*CKW/DZ**2.0)*F
D5=(R*DR**2.0*CKE/DZ**2.0)*F

```

```

IF (J.EQ.1) D2=0.0
IF (J.EQ.NTHETA) D3=0.0
IF (K.EQ.1) D4=0.0
IF (K.EQ.NZ) D5=0.0

```

```

D1=3.0*DENP*CP*R*DR**2.0/DT-D2-D3-D4-D5
IF (J.EQ.1.OR.J.EQ.NTHEP1.OR.K.EQ.1.OR.K.EQ.NZ) THEN
  IF (J.EQ.1.OR.J.EQ.NTHEP1) THEN
    IF (K.EQ.1.OR.K.EQ.NZ) THEN
      IF (J.EQ.1.AND.K.EQ.1) D=D1*T(I,J,K)
$      +D3*T(I,J+1,K)+D5*T(I,J,K+1)
      IF (J.EQ.1.AND.K.EQ.NZ) D=D1*T(I,J,K)
$      +D3*T(I,J+1,K)+D4*T(I,J,K-1)
      IF (J.EQ.NTHEP1.AND.K.EQ.1) D=D1*T(I,J,K)+D2*T(I,J-1,K)
$      +D5*T(I,J,K+1)
      IF (J.EQ.NTHEP1.AND.K.EQ.NZ) D=D1*T(I,J,K)+D2*T(I,J-1,K)
$      +D4*T(I,J,K-1)
    ELSE
      IF (J.EQ.1) D=D1*T(I,J,K) +D3*T(I,J+1,K)
$      +D4*T(I,J,K-1)+D5*T(I,J,K+1)
      IF (J.EQ.NTHEP1) D=D1*T(I,J,K)+D2*T(I,J-1,K)

```

```

$                                +D4*T(I,J,K-1)+D5*T(I,J,K+1)

    ENDIF
ELSE
    IF (K.EQ.1) D=D1*T(I,J,K)+D2*T(I,J-1,K)+D3*T(I,J+1,K)
$                                +D5*T(I,J,K+1)
    IF (K.EQ.NZ) D=D1*T(I,J,K)+D2*T(I,J-1,K)+D3*T(I,J+1,K)
$                                +D4*T(I,J,K-1)
    ENDIF
ELSE
    D=D1*T(I,J,K)+D2*T(I,J-1,K)+D3*T(I,J+1,K)+D4*T(I,J,K-1)
$    +D5*T(I,J,K+1)
ENDIF

IF (D1.LT.0.0) WRITE(6,328) I,J,K
328 FORMAT(1X,'D1=(-) IN ROOP1 I,J,K=',3(2X,I3))
IF (D1.LT.0.0) GO TO 1000

IF (I.EQ.1) THEN
    C=0.0
    A=A-CKN*(R+DR/2.0)*F1
    B=B
    D=D+(QWALL(J,K)*RO*DR)*F1
ENDIF
IF (I.EQ.NR) THEN
    C=C
    A=A+CKS*R*F1
    B=0.0
    D=D+2.0*CKS*(R-DR/4.0)*TV(K)*F1
ENDIF

C
C TDMA ALGORITHM
C
    P(I)=-B/(A+C*P(I-1))
    Q(I)=(D-C*Q(I-1))/(A+C*P(I-1))

300 CONTINUE

DO 370 I1=1,NR
    I=NR+1-I1
    TT(I,J,K)=P(I)*TT(I+1,J,K)+Q(I)
370 CONTINUE
360 CONTINUE
380 CONTINUE

IF (IPCM.EQ.2) THEN
    CALL TES
ENDIF

```

C

```

C   SEARCHING FOR TV(KBURN+1) FOR NEXT TIME STEP
C
      QIN=0.0
      SUMQVI=0.0
      SUMQVO=0.0
C
      DO 410 K=1,NZ
        QV(K)=0.0
      DO 420 J=1,NTHETA
        NGORD=(J-1)/NTHEPG+1
        JING=J-(NGORD-1)*NTHEPG

      DO 430 I=1,NR
        IF(I.EQ.NR) QVIN=CKNR(J,K)*(DTHETA*(RW+DRW/4.0)*DZ)*NGROV
        $          *(TT(NR,J,K)-TV(K))/(DRW/2.0)
430  CONTINUE
        QV(K)=QV(K)+QVIN
420  CONTINUE

      IF(QV(K).GT.0.0) QIN=QIN+QV(K)
      IF((QV(K)+QVTES(K)).GT.0.0) SUMQVI=SUMQVI+(QV(K)+QVTES(K))
      IF((QV(K)+QVTES(K)).LE.0.0) SUMQVO=SUMQVO-(QV(K)+QVTES(K))

410  CONTINUE
C
      SUMQV=SUMQVI-SUMQVO

      IF((NDT/XWRITE).EQ.(NDT/NWRITE)) THEN
C   WRITE(6,*) 'SUMQV=',SUMQV,'QVI=',SUMQVI,'QVO=',SUMQVO
      ENDIF

      IF((ABS(SUMQV)/ABS(SUMQVI+SUMQVO)).GT.EPSV) THEN
        IF(SUMQV.LE.0.0) TVEE1=TV(KBURN+1)
        IF(SUMQV.GT.0.0) TVEE2=TV(KBURN+1)
        GO TO 400
      ELSE
        GO TO 440
      ENDIF
C
C
440  IF((NDT/XWRITE).EQ.(NDT/NWRITE)) THEN
C   WRITE(6,*) 'NCALLV=',NCALLV
      ENDIF

C1  CALL BOWMAN
C1  CALL CHI

      PVMIN=PV(KBURN+1)

```

```

DO 465 N=KBURN+2,NZ
  IF (PV(N).LT.PVMIN) THEN
    PVMIN=PV(N)
    KPVMIN=N
  ENDIF
465 CONTINUE

CALL LIQUID

IF ((NDT/XWRITE).EQ.(NDT/NWRITE)) THEN
  WRITE(6,*) '      Z      PV      PL      DPV      DPL'
  DO 460 N=KBURN+1,NZ
    Z=(ZL/NZ)*(N-0.5)
    DPV(N)=PV(N)-PV(1)
    DPL(N)=PL(N)-PL(1)

    WRITE(6,462) Z,PV(N),PL(N),DPV(N),DPL(N)
462  FORMAT(2X,F8.4,4(2X,F8.1))
460  CONTINUE
  ENDIF

DPVMAX=PV(KBURN+1)-PVMIN
DPLMAX=PL(NADIA+1)-PL(KBURN+1)
PCMAX=2.0*TENLIQ/RC
C  IF ((NDT/NWRITE).EQ.(NDT/XWRITE)) WRITE(6,*) 'DPVMAX=',DPVMAX
C  $      , 'DPLMAX=',DPLMAX, 'PCMAX=',PCMAX

DO 442 K=1,NZ
  QVNEW(K)=QV(K)+QVTES(K)
  TVNEW(K)=TV(K)
  DQVDAN(K)=QV(K)/(2.0*3.1416*RW*DZ)
  IF(IPCM.EQ.1) GO TO 442
  DQDATN(K)=QVTES(K)/(NTESTU*2.0*3.1416*RTES*DZ)
442 CONTINUE

IF(METHOD.EQ.1) GO TO 450

C  DO 445 K=1,NZ
C  WRITE(6,906) K,QV(K),QVTES(K),QV(K)+QVTES(K)
C  IF(K.GT.1.AND.((QV(K)+QVTES(K))*(QV(K-1)+QVTES(K-1))).LT.0.0)
C  $PLM=K*DZ
C445 CONTINUE
C  IF ((NDT/XWRITE).EQ.(NDT/NWRITE)) THEN
C1  WRITE(6,*) 'PLM=',PLM

```



```

C1  WRITE(6,*) ' '
C1  WRITE(6,*) ' '
C1  WRITE(6,*) 'NQV0=',NQV0
C1  WRITE(6,*) 'QV0=',QV0(1), 'QV0OLD=',QVOLD(1), 'QV0NEW=',QVNEW(1)
C1  WRITE(6,*) 'TV0=',TV0(1), 'TV0OLD=',TVOLD(1), 'TV0NEW=',TVNEW(1)
C1  WRITE(6,*) ' '
C1  WRITE(6,*) ' '
C   ENDIF

C1  IF (ABS((TVNEW(1)-TVOLD(1))/(TVNEW(1)-TV0(1))).LE.EPSQVK) THEN
C1  WRITE(6,*) ' '
C1  WRITE(6,*) 'TV0 CONVERGE NOW!'
C1  WRITE(6,*) ' '
C1  ENDIF

      NWO0=0
      DO 452 K=1,NZ
      IF (ABS((TVNEW(K)-TVOLD(K))/(TVNEW(K)-TV0(K))).GT.EPSQVK)
$ NWO0=NWO0+1

      IF (NWO0.GE.30) GO TO 350

452  CONTINUE

450  DO 455 K=1,NZ
      DQVDA(K)=DQVDAN(K)
      DQDATE(K)=DQDATN(K)
455  CONTINUE

      NADI=6

      IF (IPCM.EQ.2) THEN
      CALL TES
      ENDIF

      THPTTL=0.0
      TVTTL=0.0
      DO 393 K=1,NZ
      DO 394 J=1,NTHEP1
      NGORD=(J-1)/NTHEPG+1
      JING=J-(NGORD-1)*NTHEPG
      DO 395 I=1,NR
      IF (I.GT.NRS.AND.JING.GE.JING2.AND.JING.LE.JING3.AND.K.LE.KBURN)
$ THEN
      T(I,J,K)=TV(K)
      ELSE
      T(I,J,K)=TT(I,J,K)

```

```

      ENDIF
      TOLD(I,J,K)=T(I,J,K)
      THPTTL=THPTTL+T(I,J,K)
395  CONTINUE
      TW(J,K)=T(1,J,K)+(DR1/2.0)*QWALL(J,K)*RO/CK1M/(R1M+DR1/4.0)
394  CONTINUE
      TVTTL=TVTTL+TV(K)
      DTV(K)=TV(K)-TVOLD(K)
393  CONTINUE

```

```

      THPAVG(NDT)=THPTTL/NZ/NTHEP1/NR
      TVAVG(NDT)=TVTTL/NZ
      CTIME(NDT)=TIME

```

```

      IF((NDT/XWRITE).EQ.(NDT/NWRITE)) THEN

```

```

        WRITE(6,910)
910  FORMAT(1X,//////)
        WRITE(6,920)TIME
920  FORMAT(28X,'TIME=',2X,F7.2,2X,'SECONDS',/)

```

```

        WRITE(6,*) ' '
        WRITE(6,*) ' '
        WRITE(6,*) ' '

```

```

        WRITE(6,940) (TW(2,K),K=1,NZ, 4)
940  FORMAT(1X,' WALL',10(1X,F6.1))

```

```

        DO 900 I=1,NR
        WRITE(6,950)I,(T(I,2,K),K=1,NZ, 4)
950  FORMAT(1X,'I=',I3,10(1X,F6.1))
900  CONTINUE
        WRITE(6,960) (TV(K),K=1,NZ, 4)
960  FORMAT(1X,'VAPOR',10(1X,F6.1)///)
        WRITE(6,970) THPAVG(NDT)
970  FORMAT(2X,'AVERAGE HEAT PIPE TEMPERATURE=',2X,F9.4)
        WRITE(6,980) TVAVG(NDT)
980  FORMAT(2X,'AVERAGE VAPOR TEMPERATURE=',2X,F9.4///)

```

```

      ENDIF

```

C
C
C

```

      IF((NDT/XWRITE).EQ.(NDT/NWRITE)) THEN
      IF(IPCM.EQ.2) THEN
      WRITE(6,*) '          TES          TEMPERATURE '
      WRITE(6,*) '

```

```

DO 990 I=1,NRTES,2
WRITE(6,930) I, (TE(I,K),K=1,NZ, 4)
930 FORMAT(1X,'IE=',I3,10(1X,F6.1))
990 CONTINUE
ENDIF
ENDIF

IF((NDT/NWRITE).EQ.(NDT/XWRITE)) THEN
PCTQWTES=(QWTES/QIN)*100.0
WRITE(6,*) 'SUMQVI=',SUMQVI,'SUMQVO=',SUMQVO
WRITE(6,*) 'QIN=',QIN,'QWTES=',QWTES,'%QWTES=',PCTQWTES,'% '
WRITE(6,*) 'QEVAP=',XXX
WRITE(6,*) ' '
WRITE(6,*) ' '

C ENERGY BALANCE CHECK
IF(NDT.GT.1.AND.((NDT/NWRITE).EQ.(NDT/XWRITE))) THEN
ERROR1=(QETTL-(QCTTL+QHP+QPCM))/QETTL*100.0
ERROR2=(QETTL-(QCTTL+QHP+QTES))/QETTL*100.0
IF(IPCM.EQ.2) ERROR3=(QTES-QPCM)/QTES*100.0
IF(IPCM.EQ.2) PCTMELT=QMELT/QPCMTTL*100.0

WRITE(6,902) QETTL,QCTTL,QHP,QPCM,QTES
902 FORMAT(1X,'QETTL=',F9.1,2X,'QCTTL=',F9.1,2X,'QHP=',F8.1,2X
$      , 'QPCM=',F8.1,2X,'QTES=',F8.1/)
WRITE(6,903) ERROR1,ERROR2,ERROR3,PCTMELT
903 FORMAT(1X,'ENERGY BALANCE ERROR=',2X,F6.2,' %',2X,F6.2,' %'
$      ,2X,F6.2,' %',2X,'%MELT=',F6.2,' %'///)
ENDIF

C DO 905 K=1,NZ
C WRITE(6,906) K,QV(K),QVTES(K),QV(K)+QVTES(K)
C 906 FORMAT(1X,I3,3X,'QV=',F10.5,5X,'QVTES=',F10.5,5X,'QVNET=',F10.5)
C 905 CONTINUE
C WRITE(6,*) 'PLM=',PLM
C WRITE(6,*) 'NQV0=',NQV0,'FRELAX=',FRELAX
DO 915 N=1,NZ
WRITE(6,916) N, PV(N),DPV(N),TVREAL(N),DENV(N)
916 FORMAT(1X,'N=',I3,2X,'PV(N)=' ,1X,F8.1,2X,'DPV(N)=' ,1X,F8.1,
$      2X,'TV(N)=' ,1X,F7.2,2X,'DENV(N)=' ,1X,F8.6)
915 CONTINUE

ENDIF

IF (NDT.EQ.NDTEND.OR.NQV0.GT.600) THEN

C DO 982 K=1,NZ
C WRITE(6,983) K,DQVDA(K)
C983 FORMAT(3X,'K=',I3,2X,'DQVDA=',F15.3)

```

C982 CONTINUE

GO TO 999
ENDIF

60 CONTINUE

999 IF(IPCM.EQ.1) WRITE(6,*)'C WITHOUT TES'
IF(IPCM.EQ.2) WRITE(6,*)'C WITH TES'
IF(METHOD.EQ.1) WRITE(6,*)'C EXPLICIT WITH VAPOR'
IF(METHOD.EQ.2) WRITE(6,*)'C IMPLICIT WITH VAPOR'

WRITE(6,*)'C','NTESTU=',NTESTU,'RTES=',RTES,'DT=',DT,'F=',F
WRITE(6,*)'C TIME -THP- -TV-'
DO 995 NDT=NWRITE,NDTEND,NWRITE
WRITE(6,996)CTIME(NDT),THPAVG(NDT),TVAVG(NDT)
996 FORMAT(1X,F7.2,2(2X,F8.2))
995 CONTINUE
1000 STOP
END

C
C
C
C
C
C
C
C
C
C
C

* SUBROUTINE BOWMAN *

C SUBROUTINE BOWMAN
C ONE DIMENSIONAL COMPRESSIBLE VAPOR FLOWFOR HEAT PIPE

REAL *8 TV(100)

COMMON /HPIPE/ TV,DQDATE(100),PL,DZ,NZ,NDT,QVTES(100),
\$NTESTU,TIME,KBURN,NWRITE,XWRITE,NGROV,RW,NADIA,PV(100)
COMMON /VCORE/ DQDA(100),DQDABAR(100),IPCM,PVTTL(100)
\$,TVREAL(100),PLM,DTES,DVAPOR,DWICK,DHYDRO,XMMAX,KPLM
\$,NEVAP,XTI,DENV(100)
IF(IPCM.EQ.1) THEN
DO 10 N=1,NZ
QVTES(N)=0.0
DQDATE(N)=0.0
10 CONTINUE
ENDIF

C GUESS THE VAPOR TEMPERATURE AT THE EVAPORATOR END TO
T0=TV(KBURN+1)

```

C      OMEGA=0.25
      R=361.5
C      WRITE(*,*) 'RCONST=',R
      LAMBDA=4636437.26-180.817*T0
      GAMMA=1.67
      GAMM1=GAMMA/(GAMMA-1.0)
C
C      INITIALIZE THE VARIABLES AT THE UPSTREAM PIPE END
C
      W=0.0
      Z=0.0
      RHO=6.335E08*10.0**(-5567.0/T0)/T0**1.5
      P0=RHO*R*T0
C
C      USE INCOMPRESSIBLE MODEL TO GET THE STARTING VALUES
C
      RHOV=-DQDABAR(KBURN+1)/LAMBDA
      RHOVTE=RHOV

      C2=GAMMA*P0/RHO
      XM22=(4.0*(RHOV*DWICK+NTESTU*RHOVTE*DTES)*DZ/RHO/DVAPOR**2.0)**2
$      /C2
      W2=W-RHOV*DZ*DWICK*3.1416-NTESTU*RHOVTE*DZ*DTES*3.1416
      Z2=Z+DZ/2.0
      P2=P0/(1.0+(GAMMA-1.0)/2.0*XM22)**GAMM1
      P02=P0
      RHO2=RHO
      TV(KBURN+1)=T0
      TVREAL(KBURN+1)=T0
      PV(KBURN+1)=P0
      PVTTL(KBURN+1)=P0
      DENV(KBURN+1)=RHO
C
C      MARCHING DOWN THE PIPE FINDING THE FLOW PROPERITIES ALONG THE WAY
C
      Z=Z2
C
C
C
CC      WRITE(6,*) '          Z/PL          P2/P0          T
CC      $          W2          XM22'

      XMMAX=0.0

      DO 5 N=KBURN+2,NZ
      XM2=XM22
      IF(XM2.GT.0.99) THEN
        WRITE(6,70) Z,XM2

```

```

70  FORMAT(3X,'Z=',F6.3,3X,'XM2=',F6.3)
    ENDIF

    P=P2
    P01=P02
    W=W2
    Z=Z+DZ
C
C  PREDICTOR AND CORRECTOR STEPS
C
C  CALCULATE THE INFLUENCE COEFFICIENTS
C
    XM2BAR=(XM2+XM22)/2.0
    CON1=1.0+(GAMMA-1.0)/2.0*XM2BAR
    CON2=1.0-XM2BAR
    CON3=1.0+GAMMA*XM2BAR
    CON4=GAMMA*XM2BAR
    FW=2.0*CON3*CON1/CON2
    FWP=CON4
C
C  FIND THE MASS ADDED THROUGH THE PIPE WALL
C
    RHOV=-DQDABAR(N)/LAMBDA
    RHOVTE=RHOV

    DELW=-RHOV*DZ*DWICK*3.1416-NTESTU*RHOVTE*DZ*DTES*3.1416
    W2=W+DELW
    IF(W2.LE.0.0) THEN
        XM22=0.0
        P02=P01
        T=T0
        GO TO 30
    ENDIF
C
C  FIND THE FRICTION FACTOR AND THE FRICTION INFLUENCE COEFFICIENT
C
    T=T0/CON1
    RMU=6.083E-09*T+1.2606E-05
    WBAR=(W+W2)/2.0

    IF(WBAR.LE.0.0) THEN
        XM22=0.0
        P02=P01
        T=T0
        GO TO 30
    ENDIF

    REY=(4.0*WBAR*DHYDRO)/(3.1416*DVAPOR**2.0*RMU)
    RER=-DELW/(3.1416*RMU*DZ)
    ZBAR=((Z-XTI)/OMEGA)**2

```

```

      IF ((NDT/NWRITE).EQ.(NDT/XWRITE)) THEN
C      WRITE(6,*) 'REY=',REY
      ENDIF
      IF (REY.GE.12000) WRITE(6,*) 'REY>12000'

      FL=16/REY*(1.2337-0.2337*EXP(-0.036*ABS(RER)))*EXP(1.20*XM2)
C      FL=24/REY

      BETA=ABS(RER/REY)
      FSTAR=0.046/REY**0.2

      FT=FSTAR*(1+55*REY**0.1*EXP(1.2*XM2)*BETA**0.9*(PL/DHYDRO)**0.1)

      IF (Z.LE.XTI) F=FL
      IF (Z.GT.XTI) F=FT-(FT-FL)*EXP(-0.412*ZBAR)

      FF=CON4*CON1/CON2*4.0*F/DHYDRO
      FFP=CON4/2.0*4.0*F/DHYDRO
C

      IF (W2.LE.0.0) WRITE(6,*) 'W2<0.0'
      XM22=EXP(ALOG(XM2)+FF*DZ+FW*ALOG(W2/W))
      IF (XMMAX.LT.(XM22**0.5)) XMMAX=XM22**0.5
      P02=EXP(ALOG(P01)-FFP*DZ-FWP*ALOG(W2/W))
30  P2=P02/(1.0+(GAMMA-1.0)/2*XM22)**GAMM1

      TX=T

      DO 80 NX=1,100
      T2=-5567.0/ALOG10(P2*TX**0.5/2.29E11)
      IF (ABS(T2-TX).LT.1.0) GO TO 90
      TX=T2
      IF (NX.EQ.100) WRITE(6,*) 'NX=100'
80  CONTINUE

90  TVREAL(N)=T2
      PV(N)=P2
      PVTTL(N)=P02
      DENV(N)=PV(N)/(R*TVREAL(N))
C
CC  WRITE(6,20) Z/PL,P2/P0,T,W2,XM22
CC 20  FORMAT(1X,5(3X,F15.10))
      5  CONTINUE
C
C
      DO 50 N=1,KBURN
      TVREAL(N)=TVREAL(KBURN+1)
      PV(N)=PV(KBURN+1)
      PVTTL(N)=PVTTL(KBURN+1)
50  CONTINUE
40  RETURN

```

```

END

C
C
C
C *****
C * SUBROUTINE CHI *
C *****
C
C
C SUBROUTINE CHI
C ONE DIMENSIONAL COMPRESSIBLE VAPOR FLOW FOR HEAT PIPE

REAL *8 TV(100),W(100)
REAL LAMBDA

COMMON /HPIPE/ TV,DQDATE(100),PL,DZ,NZ,NDT,QVTES(100),
$NTESTU,TIME,KBURN,NWRITE,XWRITE,NGROV,RW,NADIA,PV(100)
COMMON /VCORE/ DQDA(100),DQDABAR(100),IPCM,PVTTL(100)
$ ,TVREAL(100),PLM,DTES,DVAPOR,DWICK,DHYDRO,XMMAX,KPLM
$ ,NEVAP,XTI,DENV(100)
DIMENSION PP(100)

IF(IPCM.EQ.1) THEN
DO 10 N=1,NZ
QVTES(N)=0.0
DQDATE(N)=0.0
10 CONTINUE
ENDIF

AV=3.1416*DVAPOR**2.0/4.0

C GUESS THE VAPOR TEMPERATURE AT THE EVAPORATOR END T0
T0=TV(KBURN+1)
RHO=6.335E8*10.0**(-5567/T0)/T0**1.5
P0=RHO*R*T0

R=361.5
LAMBDA=4636437.26-180.817*T0
GAMMA=1.67
GAMM1=GAMMA/(GAMMA-1.0)
C2=GAMMA*P0/RHO

W(KBURN+1)=0.0
TVREAL(KBURN+1)=T0
PV(KBURN+1)=P0
PP(KBURN+1)=P0
DENV(KBURN+1)=RHO
XMMAX=0.0

```


DO 5 N=KBURN+2,NZ+1

RMU=6.083E-9*TVREAL(N-1)+1.2606E-5

RHO=6.335E8*10.0**(-5567/TVREAL(N-1))/TVREAL(N-1)**1.5

C

C FIND THE MASS ADDED THROUGH THE PIPE WALL

C

RHOV=-DQDABAR(N-1)/LAMBDA

RHOVTE=RHOV

DELW=-RHOV*DZ*DWICK*3.1416-NTESTU*RHOVTE*DZ*DTES*3.1416

W(N)=W(N-1)+DELW

IF(W(N).LE.0.0) THEN

PP(N)=PP(N-1)

PV(N)=PV(N-1)

TVREAL(N)=TVREAL(N-1)

GO TO 5

ENDIF

XM2=W(N)**2.0/(AV*RHO)**2.0/C2

IF(XMMAX.LT.(XM2**0.5)) XMMAX=XM2**0.5

REY=4.0*DHYDRO*W(N)/(3.1416*DVAPOR**2.0*RMU)

IF((NDT/NWRITE).EQ.(NDT/XWRITE)) THEN

C WRITE(6,*) 'REY=',REY

ENDIF

A=32.0*RMU/(DHYDRO**2.0*AV*RHO*LAMBDA)

B=0.076*RMU/(DHYDRO**2.0*AV*RHO*LAMBDA)

C=1.0+(GAMMA-1)/2*XM2

IF(REY.LE.2300.0.AND.XM2.LE.0.04) FV=A

IF(REY.LE.2300.0.AND.XM2.GT.0.04) FV=A*C**(-0.5)

IF(REY.GT.2300.0.AND.XM2.LE.0.04) FV=B*REY**0.75

IF(REY.GT.2300.0.AND.XM2.GT.0.04) FV=B*REY**0.75*C**(-0.75)

IF(REY.LE.2300.0) BETA=1.33

IF(REY.GT.2300.0) BETA=1.0

PP(N)=PP(N-1)-FV*W(N)*LAMBDA*DZ

PV(N)=PP(N)-BETA*W(N)**2.0/(AV**2.0*RHO)

PVTTL(N)=PV(N)*(1+(GAMMA-1)/2*XM2)**GAMM1

IF(XM2.GT.0.99) THEN

WRITE(6,70)N,XM2

70 FORMAT(3X,'N=',I4,3X,'XM2=',F6.3)

ENDIF

```

30 TX=TVREAL(N-1)

DO 80 NX=1,100
  T2=-5567.0/ALOG10(PV(N)*TX**0.5/2.29E11)
  IF(ABS(T2-TX).LT.1.0) GO TO 90
  TX=T2
  IF(NX.EQ.100) WRITE(6,*) 'NX=100'
80 CONTINUE

90 TVREAL(N)=T2
  DENV(N)=PV(N)/(R*TVREAL(N))
C
CC WRITE(6,20)Z/PL,P2/P0,T,WL, XM22
CC 20 FORMAT(1X,5(3X,F15.10))
  5 CONTINUE
C
DO 50 N=1,KBURN
  TVREAL(N)=TVREAL(KBURN+1)
  PV(N)=PV(KBURN+1)
  PVTTL(N)=PVTTL(KBURN+1)
50 CONTINUE
  RETURN
  END

C
C
C
C*****
C* SUBROUTINE TES *
C*****

      SUBROUTINE TES

C CKL -THERMAL CONDUCTIVITY OF LIQUID LIH (W/M-K)
C CKSS -THERMAL CONDUCTIVITY OF SOLID LIH (W/M-K)
C CKP -NODAL THERMAL CONDUCTIVITY (W/M-K)
C CL -HEAT CAPACITY OF LIQUID LIH (J/K-KG)
C CS -HEAT CAPACITY OF SOLID LIH (J/K-KG)
C CP -NODAL HEAT CAPACITY (J/K-KG)
C DENL -DENSITY OF LIQUID LIH (KG/M3)
C DENS -DENSITY OF SOLID LIH (KG/M3)
C DENP -NODAL DENSITY (KG/M3)
C DR -SPACE INCREMENT IN RADIAL DIRECTION IN TES (M)
C DT -TIME STEP (SEC)
C DTHETA -ANGULAR INCREMENT (RADIAN)
C DZ -SPACE INCREMENT IN AXIAL DIRECTION (M)
C HFUSE -FUSION HEAT OF LIH (J/KG)

```

```

C  RO      -OUTSIDE RADIUS OF HEAT PIPE WALL (M)
C  R        -NODAL RADIUS (M)
C  TMELT    -MELT TEMPERATURE OF LIH (K)
C  T(I,K)   -NODAL TEMPERATURE (K)
C  TV(K)    -VAPOR TEMPERATURE (K)
C  ~~~~~
REAL *8 T(40,100), TT(40,100), TOLD(40,100), TVOLD(100), TV(100)
REAL *8 TSTAR(40,100), TP, TW, TE, TS, TN, DTV(100)
REAL *8 DH(40,100), FH(40,100), FT(40,100), CSTAR(40,100)

REAL *8 P(100), Q(100), CKTES1(100), F, F1, T1, T2

COMMON /HPIPE/ TV, DQDATE(100), ZL, DZ, NZ, NDT, QVTES(100),
$          NTESTU, TIME, KBURN, NWRITE, XWRITE, NGROV, RW, NADIA, PV(100)
COMMON /PCM/ TVOLD, T, TT, DTV, DT, NADI, NR, DTHETA, RO,
$          TSTART, NTHETA, QPCM, QMELT, QPCMTTL

F= 0.01
F1=2.0-F

IF(NADI.EQ.4) GO TO 400
IF(NADI.EQ.6) GO TO 600

C  TES GEOMETRY
DR=RO/NR

C  THERMAL CONDUCTIVITY, HEAT CAPACITY AND DENSITY FOR TES

CKL=2.1
CKSS=4.2
CKM=2.0*(CKSS*CKL)/(CKSS+CKL)
CL=7370.0
CS=6280.0
CM=(CL+CS)/2.0
DENL=550.0
DENS=DENL
DENM=(DENL+DENS)/2.0
CSTEEL=500.0

C  MELTING TEMPERATURE AND HEAT FUSION
TMELT=956.0
HFUSE=2580000.0
QPCMTTL=3.1416*RO**2.0*ZL*DENM*HFUSE*NTESTU

T1=951.0
T2=961.0
H1=CS*T1
H2=CS*TMELT+CL*(T2-TMELT)+HFUSE

```

C TES STARTING TEMPERATURE

```
      IF (NDT.EQ.1) THEN
      DO 30 K=1,NZ
      DO 36 I=1,NR
      T(I,K)=TSTART
      TOLD(I,K)=TSTART
36  CONTINUE
30  CONTINUE
      ENDIF
```

```
      DO 50 I=1,NR
      DO 55 K=1,NZ
```

```
      R=RO-(I-0.5)*DR
```

C |||||

```
      TP=TOLD(I,K)
```

```
      IF (I.EQ.1) TN=TP+2*(TVOLD(K)-TP)*(1-DR/(4*RO))
      IF (I.EQ.NR) TS=TP
      IF (K.EQ.1) TW=TP
      IF (K.EQ.NZ) TE=TP
```

```
      IF (I.NE.1) TN=TOLD(I-1,K)
      IF (I.NE.NR) TS=TOLD(I+1,K)
      IF (K.NE.1) TW=TOLD(I,K-1)
      IF (K.NE.NZ) TE=TOLD(I,K+1)
```

```
      IF (TP.LE.TMELT) THEN
      IF (TN.LE.TMELT) CKN=CKSS
      IF (TS.LE.TMELT) CKS=CKSS
      IF (TW.LE.TMELT) CKW=CKSS
      IF (TE.LE.TMELT) CKE=CKSS
```

```
      IF (TN.GT.TMELT) CKN=CKM
      IF (TS.GT.TMELT) CKS=CKM
      IF (TW.GT.TMELT) CKW=CKM
      IF (TE.GT.TMELT) CKE=CKM
      ENDIF
```

```
      IF (TP.GT.TMELT) THEN
      IF (TN.LE.TMELT) CKN=CKM
      IF (TS.LE.TMELT) CKS=CKM
      IF (TW.LE.TMELT) CKW=CKM
      IF (TE.LE.TMELT) CKE=CKM
```

```
      IF (TN.GT.TMELT) CKN=CKL
```

```

      IF (TS.GT.TMELT) CKS=CKL
      IF (TW.GT.TMELT) CKW=CKL
      IF (TE.GT.TMELT) CKE=CKL
    ENDIF

```

```

      DH(I,K) = (DT / (DENM*R*DR**2.0)) * (CKN* (R+DR/2) * (TN-TP)
$              + CKS* (R-DR/2) * (TS-TP) )
$              + (DT / (DENM*DZ**2.0)) * (CKW* (TW-TP) + CKE* (TE-TP) )

```

C MELTING

```

      IF (DH(I,K).GE.0.0) THEN

        IF (TP.LT.T1) FH(I,K)=CS*TP
        IF (TP.GE.T1.AND.TP.LE.T2) FH(I,K) = (H2-H1) * (TP-T1) / (T2-T1) + H1
        IF (TP.GT.T2) FH(I,K) = (TP-T2) * CL + H2

        H = FH(I,K) + DH(I,K)

        IF (H.LT.H1) TSTAR(I,K) = H / CS
        IF (H.GE.H1.AND.H.LE.H2) TSTAR(I,K) = (H-H1) * (T2-T1) / (H2-H1) + T1
        IF (H.GT.H2) TSTAR(I,K) = (H-H2) / CL + T2

        IF (FH(I,K).LT.H1.AND.H.LT.H1) CSTAR(I,K) = CS
        IF (FH(I,K).GE.H1.AND.FH(I,K).LE.H2.AND.H.GE.H1.AND.H.LE.H2)
$      CSTAR(I,K) = (H2-H1) / (T2-T1)
        IF (FH(I,K).GT.H2.AND.H.GT.H2) CSTAR(I,K) = CL
        IF ((FH(I,K).LT.H1.AND.H.GT.H1).OR.(FH(I,K).LT.H2.AND.H.GT.H2))
$      CSTAR(I,K) = DH(I,K) / (TSTAR(I,K) - TP)
        ENDIF

```

C SOLIDIFICATION

```

      IF (DH(I,K).LT.0.0) THEN

        IF (TP.LT.T1) FH(I,K)=CS*TP
        IF (TP.GE.T1.AND.TP.LE.T2) FH(I,K) = (H2-H1) * (TP-T2) / (T2-T1) + H2
        IF (TP.GT.T2) FH(I,K) = (TP-T2) * CL + H2

        H = FH(I,K) + DH(I,K)

        IF (H.LT.H1) TSTAR(I,K) = H / CS
        IF (H.GE.H1.AND.H.LE.H2) TSTAR(I,K) = (H-H2) * (T2-T1) / (H2-H1) + T2
        IF (H.GT.H2) TSTAR(I,K) = (H-H2) / CL + T2

```

```

      IF (FH(I,K) .LT. H1 .AND. H .LT. H1) CSTAR(I,K)=CS
      IF (FH(I,K) .GE. H1 .AND. FH(I,K) .LE. H2 .AND. H .GE. H1 .AND. H .LE. H2)
$      CSTAR(I,K) = (H2-H1) / (T2-T1)
      IF (FH(I,K) .GT. H2 .AND. H .GT. H2) CSTAR(I,K)=CL
      IF ((FH(I,K) .GT. H1 .AND. H .LT. H1) .OR. (FH(I,K) .GT. H2 .AND. H .LT. H2))
$      CSTAR(I,K)=DH(I,K) / (TSTAR(I,K)-TP)
      ENDIF

```

```

55  CONTINUE

```

```

50  CONTINUE

```

```

C

```

```

C#####

```

```

C  ##### COMPUTATION FOR THE FIRST HALF TIME STEP #####

```

```

      QPCM=0.0

```

```

      QMELT=0.0

```

```

      DO 180 I=1,NR

```

```

      DO 160 K=1,NZ

```

```

      R=RO-(I-0.5)*DR

```

```

C |||||

```

```

      TP=TOLD(I,K)

```

```

      IF (I.EQ.1) TN=TP+2*(TVOLD(K)-TP)*(1-DR/(4*RO))

```

```

      IF (I.EQ.NR) TS=TP

```

```

      IF (K.EQ.1) TW=TP

```

```

      IF (K.EQ.NZ) TE=TP

```

```

      IF (I.NE.1) TN=TOLD(I-1,K)

```

```

      IF (I.NE.NR) TS=TOLD(I+1,K)

```

```

      IF (K.NE.1) TW=TOLD(I,K-1)

```

```

      IF (K.NE.NZ) TE=TOLD(I,K+1)

```

```

      IF (TP.LE.TMELT) THEN

```

```

        IF (TN.LE.TMELT) CKN=CKSS

```

```

        IF (TS.LE.TMELT) CKS=CKSS

```

```

        IF (TW.LE.TMELT) CKW=CKSS

```

```

        IF (TE.LE.TMELT) CKE=CKSS

```

```

        IF (TN.GT.TMELT) CKN=CKM

```

```

        IF (TS.GT.TMELT) CKS=CKM

```

```

        IF (TW.GT.TMELT) CKW=CKM

```

```

        IF (TE.GT.TMELT) CKE=CKM

```

```

      ENDIF

```

```

      IF (TP.GT.TMELT) THEN

```

```

      IF (TN.LE.TMELT) CKN=CKM
      IF (TS.LE.TMELT) CKS=CKM
      IF (TW.LE.TMELT) CKW=CKM
      IF (TE.LE.TMELT) CKE=CKM

      IF (TN.GT.TMELT) CKN=CKL
      IF (TS.GT.TMELT) CKS=CKL
      IF (TW.GT.TMELT) CKW=CKL
      IF (TE.GT.TMELT) CKE=CKL
    ENDIF

    DENP=DENM
    CP=CSTAR(I,K)

    IF (I.EQ.1) CKTES1(K)=CKN

    VOLP=((R+DR/2)**2.0-(R-DR/2)**2.0)*3.1416*DZ*NTESTU

    IF (T(I,K).LT.T1) THEN
      QPCM=QPCM+DENS*VOLP*CS*(T(I,K)-TSTART)
      QMELT=QMELT
    ENDIF
    IF (T(I,K).GE.T1.AND.T(I,K).LE.T2) THEN
      QPCM=QPCM+DENS*VOLP*CS*(T1-TSTART)+DENM*VOLP*(FH(I,K)-H1)
      QMELT=QMELT+DENM*VOLP*(FH(I,K)-H1)
    ENDIF
    IF (T(I,K).GT.T2) THEN
      QPCM=QPCM+ DENS*VOLP*CS*(TMELT-TSTART)+DENM*VOLP*HFUSE
      $      +DENL*VOLP*CL*(T(I,K)-TMELT)
      QMELT=QMELT+DENM*VOLP*HFUSE
    ENDIF

    C|||||F|||||||

    C=-CKW*F1
    A=2.0*DENP*CP*DZ**2.0/DT+(CKW+CKE)*F1
    B=-CKE*F1
    D2=(DZ**2.0*CKN*(R+DR/2.0)/R/DR**2.0)*F
    D3=(DZ**2.0*CKS*(R-DR/2.0)/R/DR**2.0)*F
    D1=2.0*DENP*CP*DZ**2.0/DT-D2-D3
    IF (I.EQ.1) D8=(2.0*DZ**2.0*CKN*(R+DR/4)/R/DR**2.0)*F

    IF (I.EQ.1.OR.I.EQ.NR) THEN
      IF (I.EQ.1) D=(D1+D2-D8)*T(I,K)+D3*T(I+1,K)+D8*TVOLD(K)
      IF (I.EQ.NR) D=(D1+D3)*T(I,K)+D2*T(I-1,K)
    ELSE
      D=D1*T(I,K)+D2*T(I-1,K)+D3*T(I+1,K)
    ENDIF

```

```

      IF(D1.LT.0.0) WRITE(6,128)I,K
128  FORMAT(1X,'D1=(-) IN ROOP3 I,K=',2(2X,I3))
      IF(D1.LT.0.0) GO TO 1000

```

```

      IF(K.EQ.1) THEN
        C=0.0
        A=A-CKW*F1
        B=B
        D=D
      ENDIF
      IF(K.EQ.NZ) THEN
        C=C
        A=A-CKE*F1
        B=0.0
        D=D
      ENDIF

```

```

C
C  TDMA ALGORITHM
C

```

```

      IF(K.EQ.1) THEN
        P(K)=-B/A
        Q(K)=D/A
      ELSE
        P(K)=-B/(A+C*P(K-1))
        Q(K)=(D-C*Q(K-1))/(A+C*P(K-1))
      ENDIF

```

```

      IF(NDT.EQ.1) THEN
        QVTES(K)=NTESTU*CKTES1(K)*(2.0*3.1416*(RO-DR/4)*DZ)
$      *(T(I,K)-TVOLD(K))/(DR/2)
        DQDATE(K)=QVTES(K)/(NTESTU*2.0*3.1416*RO*DZ)
      ENDIF

```

```

160  CONTINUE

```

```

      DO 170 K1=1,NZ
        K=NZ+1-K1
        IF(K.EQ.NZ) TT(I,K)=Q(K)
        IF(K.NE.NZ) TT(I,K)=P(K)*TT(I,K+1)+Q(K)
170  CONTINUE
180  CONTINUE

```

```

C
      DO 193 K=1,NZ
        DO 195 I=1,NR
          T(I,K)=TT(I,K)
195  CONTINUE
193  CONTINUE

```



```

      IF (NADI.EQ.123) GO TO 1000

C
C*****
C  ***** COMPUTATION FOR THE SECOND HALF TIME STEP *****
C
  400  DO 380 K=1,NZ
        DO 360 I=1,NR

          R=RO- (I-0.5) *DR

C  |||||
      TP=TOLD (I,K)

      IF (I.EQ.1) TN=TP+2* (TVOLD (K) -TP) * (1-DR/ (4*RO))
      IF (I.EQ.NR) TS=TP
      IF (K.EQ.1) TW=TP
      IF (K.EQ.NZ) TE=TP

      IF (I.NE.1) TN=TOLD (I-1,K)
      IF (I.NE.NR) TS=TOLD (I+1,K)
      IF (K.NE.1) TW=TOLD (I,K-1)
      IF (K.NE.NZ) TE=TOLD (I,K+1)

      IF (TP.LE.TMELT) THEN
        IF (TN.LE.TMELT) CKN=CKSS
        IF (TS.LE.TMELT) CKS=CKSS
        IF (TW.LE.TMELT) CKW=CKSS
        IF (TE.LE.TMELT) CKE=CKSS

        IF (TN.GT.TMELT) CKN=CKM
        IF (TS.GT.TMELT) CKS=CKM
        IF (TW.GT.TMELT) CKW=CKM
        IF (TE.GT.TMELT) CKE=CKM
      ENDIF

      IF (TP.GT.TMELT) THEN
        IF (TN.LE.TMELT) CKN=CKM
        IF (TS.LE.TMELT) CKS=CKM
        IF (TW.LE.TMELT) CKW=CKM
        IF (TE.LE.TMELT) CKE=CKM

        IF (TN.GT.TMELT) CKN=CKL
        IF (TS.GT.TMELT) CKS=CKL
        IF (TW.GT.TMELT) CKW=CKL
        IF (TE.GT.TMELT) CKE=CKL
      ENDIF

      DENP=DENM

```

CP=CSTAR(I,K)

C|||||||

C=-CKN*(R+0.5*DR)*F1
A=2.0*DENP*CP*R*DR**2.0/DT+(CKN*(R+0.5*DR)
\$+CKS*(R-0.5*DR))*F1
B=-CKS*(R-0.5*DR)*F1
D4=(R*DR**2.0*CKW/DZ**2.0)*F
D5=(R*DR**2.0*CKE/DZ**2.0)*F
IF(K.EQ.1) D4=0.0
IF(K.EQ.NZ) D5=0.0
D1=2.0*DENP*CP*R*DR**2.0/DT-D4-D5

IF(K.EQ.1.OR.K.EQ.NZ) THEN
IF(K.EQ.1) D=D1*T(I,K)+D5*T(I,K+1)
IF(K.EQ.NZ) D=D1*T(I,K)+D4*T(I,K-1)
ELSE
D=D1*T(I,K)+D4*T(I,K-1)+D5*T(I,K+1)
ENDIF

IF(D1.LT.0.0) WRITE(6,328) I,K
328 FORMAT(1X,'D1=(-) IN ROOP1 I,K=',2(2X,I3))
IF(D1.LT.0.0) GO TO 1000

IF(I.EQ.1) THEN
C=0.0
A=A+CKN*R*F1
B=B
D=D+2.0*CKN*(R+DR/4)*TV(K)*F1
C D=D+2.0*CKN*(R+DR/4)*(TVOLD(K)+DTV(K))*F1
ENDIF
IF(I.EQ.NR) THEN
C=C
A=A-CKS*(R-DR/2.0)*F1
B=0.0
D=D
ENDIF

C
C TDMA ALGORITHM
C

IF(I.EQ.1) THEN
P(I)=-B/A
Q(I)=D/A
ELSE
P(I)=-B/(A+C*P(I-1))
Q(I)=(D-C*Q(I-1))/(A+C*P(I-1))
ENDIF

360 CONTINUE

```

DO 370 I1=1,NR
  I=NR+1-I1
  IF (I.EQ.NR) TT(I,K)=Q(I)
  IF (I.NE.NR) TT(I,K)=P(I)*TT(I+1,K)+Q(I)
370 CONTINUE
380 CONTINUE

```

```

C
DO 310 K=1,NZ
  QVTES(K)=NTESTU*CKTES1(K)*(2.0*3.1416*(RO-DR/4)*DZ)*
$      (TT(1,K)-TV(K))/(DR/2.0)
310 CONTINUE

```

```

IF(NADI.EQ.4) GO TO 1000

```

```

600 DO 393 K=1,NZ
DO 395 I=1,NR
  T(I,K)=TT(I,K)
  TOLD(I,K)=TT(I,K)
395 CONTINUE
393 CONTINUE

```

```

1000 RETURN
END

```

```

C
C *****
C * SUBROUTINE HWANGBO *
C *****
C
C

```

```

SUBROUTINE HWANGBO

```

```

C ONE DIMENSIONAL CAPILLARY LIQUID FLOW

```

```

C QVL(K) - EVAPORATION (-) OR CONDENSATION (+) RATE PER UNIT HEAT
C PIPE LENGTH (W/M)
C VISLIQ - LIQUID DYNAMIC VISCOSITY (NS/M2)
C TENLIQ - LIQUID SURFACE TENSION (N/M)
C LAMBDA - LIQUID LATENT HEAT (J/KG)

```

```

REAL *8 TV(100)

```

```

DIMENSION MDOT(100)

```

```

DIMENSION ALPHA(101),ALPHAD(101),OMEGA(101),SAT(101)
DIMENSION WIDTH(101),DEPTH(101),A0(101),A1(101),QTERM(101)
DIMENSION VOLFLW(101),DVDALP(101),W(5),V(5),QVL(100)

```

```

COMMON /HPIPE/ TV,DQDATEE(100),ZL,DZ,NZ,NDT,QVTES(100),
$NTESTU,TIME,KBURN,NWRITE,XWRITE,NGROV,RW,NADIA,PV(100)
COMMON /LIQ/ QV(100),PL(100),SUMQVI
$          CL,NZP1,WIDBAR,DEPTHG,DENL,VISLIQ,TENLIQ,LAMBDA

```

```

C1    KBURN=0

```

```

      DO 3 K=1,NZ
        K1=NZ-K+1
        QVL(K1)=-1.0*QV(K)/NGROV/DZ
3     CONTINUE

```

```

C    ***** BOUNDARY AND INITIAL CONDITIONS *****

```

```

      DO 5 K=1,NZP1
        DEPTH(K)=DEPTHG
        WIDTH(K)=WIDBAR
5     CONTINUE

```

```

C    GUESS ALPHA(1), OMEGA(1)

```

```

      ALPHA(1)=3.1416/2.0
      OMEGA(1)=0.0

```

```

      DO 10 K=1,NZP1
        X=DEPTH(K)/WIDTH(K)/2.0
        A0(K)=-0.7058+0.8685*X+0.1646*X**2.0-0.0145*X**3.0
        A1(K)=0.1624+0.3167*X-0.1075*X**2.0+0.0073*X**3.0
        QTERM(K)=VISLIQ/(TENLIQ*DENL*WIDTH(K)**3.0)
        VOLFLW(K)=-(A0(K)+A1(K)*ALPHA(K))
        DVDALP(K)=-A1(K)

```

```

      IF (ALPHA(K).LT.(3.1416/180.0)) THEN
        KBURN=NZP1-K
        GO TO 30
      ENDIF

```

```

      IF (K.EQ.NZP1) GO TO 30

```

```

      VOLF=VOLFLW(K)
      DVDA=DVDALP(K)
      W(1)=0.0
      V(1)=0.0

```

```

      DO 20 N=1,4
        ALP=ALPHA(K)+0.5*DZ*W(N)
        OME=OMEGA(K)+0.5*DZ*V(N)
        W(N+1)=OMEGA(K)+0.5*DZ*V(N)
        V(N+1)=-(DVDA/VOLF+1.0/TAN(ALP))*(ABS(OME))**2.0

```

```

$          +QTERM(K) * (QVL(K) / LAMBDA) / (VOLF * SIN(ALP))
20  CONTINUE

      ALPHA(K+1) = ALPHA(K) + (DZ/6.0) * (W(2) + 2.0*W(3) + 2.0*W(4) + W(5))
      OMEGA(K+1) = OMEGA(K) + (DZ/6.0) * (V(2) + 2.0*V(3) + 2.0*V(4) + V(5))

10  CONTINUE

30  DO 50 K=1,NZP1-KBURN
      MDOT(K) = VOLFLW(K) * SIN(ALPHA(K)) * OMEGA(K) / QTERM(K)
50  CONTINUE

      IF ((NDT/NWRITE) .EQ. (NDT/XWRITE)) THEN
CC  WRITEE(6,*) '          '
CC  WRITEE(6,*) 'KBURN=', KBURN
CC  WRITEE(6,*) '          '
CC  WRITEE(6,*) '      K          ALPHAD          OMEGA          MDOT'

      DO 60 K=1,NZP1-KBURN
          ALPHAD(K) = (180.0/3.1416) * ALPHA(K)
CC  WRITEE(6,65) K, ALPHAD(K), OMEGA(K), MDOT(K)
CC65  FORMAT(1X,I4,2(2X,F10.5),2X,F11.6)
60  CONTINUE
      ENDIF
      RETURN
      END

C

C  *****
C  * SUBROUTINE LIQUID *
C  *****
C
C
C      SUBROUTINE LIQUID

C  ONE DIMENSIONAL CAPILLARY LIQUID FLOW

C  VISLIQ   - LIQUID DYNAMIC VISCOSITY (NS/M2)
C  TENLIQ   - LIQUID SURFACE TENSION (N/M)
C  LAMBDA    - LIQUID LATENT HEAT (J/KG)

      REAL *8 TV(100), KPERM

      DIMENSION QL(100), DELPL(100), DPVPL(100)

```

```

COMMON /HPIPE/ TV,DQDATE(100),ZL,DZ,NZ,NDT,QVTES(100),
$NTESTU,TIME,KBURN,NWRITE,XWRITE,NGROV,RW,NADIA,PV(100)
COMMON /LIQ/ QV(100),PL(100),SUMQVI,KPVMIN,PCMAX,DPVPLMAX,
$CL,NZP1,WIDBAR,DEPTHG,DENL,VISLIQ,TENLIQ,LAMBDA

```

```

FLREL=14.3
RM=RW+DEPTHG/2
AW=2.0*3.1416*RM*DEPTHG
EPS=NGROV*WIDBAR/(2.0*3.1416*RM)
RHL=2.0*WIDBAR*DEPTHG/(2.0*WIDBAR+2.0*DEPTHG)
KPERM=2.0*EPS*RHL**2.0/FLREL

```

```

FL=VISLIQ/(KPERM*AW*DENL*LAMBDA)

```

```

QL(KBURN+1)=QV(KBURN+1)

```

```

DO 10 K=KBURN+2,NADIA
  QL(K)=QL(K-1)+QV(K)
10 CONTINUE

```

```

DO 20 K= NZ, KBURN+1, -1

```

```

  IF(K.GT.NADIA) PL(K)=PV(K)
  IF(K.LE.NADIA) THEN
    DELPL(K)=-FL*QL(K)*DZ
    PL(K)=PL(K+1)+DELPL(K)
  ENDIF

```

```

20 CONTINUE

```

```

DO 30 K=KBURN+1,NADIA
  DPVPL(K)=PV(K)-PL(K)
30 CONTINUE

```

```

DPVPLMAX=DPVPL(KBURN+1)

```

```

C IF(DPVPL(KBURN+1).GE.PCMAX) THEN
C DO 60 K=KBURN+1,NADIA
C IF(DPVPL(K).GT.PCMAX) KBURNNEW=K-1
C 60 CONTINUE
C ENDIF

```

```

C IF(DPVPL(KBURN+1).LT.PCMAX.AND.KBURN.EQ.0) KBURNNEW=KBURN
C IF(DPVPL(KBURN+1).LT.PCMAX.AND.KBURN.NE.0) KBURNNEW=KBURN-1
C
C KBURN=KBURNNEW

```

KBURN=0

RETURN
END

REFERENCES

1. Mahefkey, E. T., "Military Spacecraft Thermal Management: The Evolving Requirements and Challenges," Progress in Astronautics and Aeronautics, Vol. 86, pp. 3-16, 1983.
2. Tilton, D.E., Chow, L.C., and Mahefkey, E.T., "Transient Response of a Liquid Metal Heat Pipe," Journal of Thermophysics and Heat Transfer, Vol. 2, No. 1, pp. 25-30, 1988.
3. El-Genk, M.S. and Seo, J.T., "An Analysis of the Effect of External Heating on The SP-100 System Radiator Heat Pipes," 23rd Intersociety Energy Conversion Engineering Conference, Denver, Colorado, July 1988.
4. Beam, J.E., Air Force Patent on Reservoir Heat Pipe, 1986.
5. Sheffield, J.W., Weight Characteristics of Future Spacecraft Thermal Management Systems, Air Force Technical Report No. AFVAL-TR-84-2005, February 1984.
6. Gauler, R.S., "Heat Transfer Devices," US Patent 2350348, December 1942.
7. Grover, G.M., "Evaporation - Condensation Heat Transfer Device," US Patent 3229759, December 1963.

8. Grover, G.M., Cotter, T.P., and Erickson, G.F., "Structures of Very High Thermal Conductance," J. Appl. Phys., Vol. 35, pp. 1990-1991, 1964.
9. Vinz, P. and Busse, C.A., "Axial Heat Transfer Limits of Cylindrical Sodium Heat Pipes Between 25 W/cm^2 and 15.5 kW/cm^2 ," Proceedings of the 1st International Heat Pipe Conference, Stuttgart, Germany, October 15-17, 1973.
10. Barantsevich, V.L., S.I. Opryshko and V.Y. Sasin, "Methods for Improving the Maximum Heat Transfer Capacity of Axially Grooved Heat Pipes," Heat Transfer-Soviet Research, Vol. 16, No. 4, pp. 92-98, 1984.
11. Chang, W.S. and Colwell, G.T., "Mathematical Modeling of the Transient Operating Characteristics of a Low-Temperature Heat Pipe," Numerical Heat Transfer, Vol. 8, pp. 169-186, 1985.
12. Kuramae, Masashi, "Transient Heat Transfer Characteristics of Heat Pipes," Proceedings of the 6th International Heat Pipe Conference, Grenoble, France, May 25-29, 1987.
13. Tilton, D.E., Chow, L.C., and Mahefkey, E.T., "A Two-Dimensional

Transient Liquid Metal Heat Pipe Model," AIAA Thermophysics, Plasmadynamics and Lasers Conference, San Antonio, Texas, June 1988.

14. Bowman, J. and Sweeten, R., "Numerical Heat-Pipe Modeling," AIAA 24th Thermophysics Conference, Buffalo, New York, June 1989.
15. Jang, J.H., Faghri A., Chang, W.S., and Mahefkey, E.T., "Mathematical Modeling and Analysis of Heat pipe Start-Up from the Frozen State," J. Heat Transfer, Vol. 112, pp. 586-594, August 1990.
16. Seo, J.T. and El-Genk, M.S., "A Transient Model for Liquid Metal Heat Pipes," 5th Symposium on Space Nuclear Power Systems, Albuquerque, New Mexico, January 11-14, 1988.
17. Thibault, J, "Comparison of Nine Three-Dimensional Numerical Methods for The Solution of The Heat Diffusion Equation", Numerical Heat Transfer, Vol. 8, pp. 281-298, 1985.
18. Chang, M.J., Chow, L.C., and Chang, W.S., "Improved Alternating-Direction-Implicit Method for Solving Transient Three-Dimensional Heat Diffusion Problems," Numerical Heat Transfer, Part B, Vol. 19, 1991, pp. 69-84.
19. Douglas, J., "Alternating Direction Methods for Three Space Variables," Numerische Mathematik, Vol. 4, pp. 41-63, 1962.

20. Brian, P.L.T., "A Finite-Difference Method of Higher-Order Accuracy for The Solution of Three-Dimensional Transient Heat Conduction Problems," A.I.Ch.E. Journal, Vol. 7, pp. 367-370, 1961.
21. Shamsundar, N. and Sparrow, E.M., "Analysis of Multidimensional Conduction Phase Change Via the Enthalpy Model," J. Heat Transfer, pp. 333-340, August 1975.
22. Shamsundar, N. and Sparrow, E.M., "Effect of Density Change on Multidimensional Conduction Phase Change," J. Heat Transfer, pp. 550-557, November 1976.
23. Hunter L.W. and Kuttler J.R., "The Enthalpy Method for Heat Conduction Problems with Moving Boundaries," J. Heat Transfer, Vol. 111, pp. 239-242, May 1989.
24. Cao, Y., Faghri, A., and Chang, W.S., "A Numerical Analysis of Stefan Problems for Generalized Multi-Dimensional Phase-Change Structure Using the Enthalpy Transforming Model," Int. J. Heat Mass Transfer, Vol. 32, No. 7, pp. 1289-1298, 1989.
25. Zhong, J., Chow, L., and Chang, W., "A Finite-Element Eigenvalue Method for Solving Phase Change Problems," 28th Aerospace Sciences Meeting, Reno, Nevada, January 1990.
26. Bonacina, C. and Comini, G., "Numerical Solution of Phase-Change

- Problems," Int. J. Heat Mass Transfer, Vol. 16, pp. 1825-1832, 1973.
27. Cleland, A.C. and Earle, R.L., "Prediction of Freezing Times for Foods in Rectangular Packages," J. Food Service, Vol. 44, pp. 964-970, 1979.
 28. Comini, G., Guidance, S.D., Lewis, R.W., and Zienkiewicz, O.C., "Finite Element Solution of Non-Linear Heat Conduction Problems with Special Reference to Phase Change," Int. J. Numer. Methods Engrg., Vol. 8, pp. 613-614, 1974.
 29. Comini, G. and Giudice, S.D., "Thermal Aspect of Cryosurgery," J. Heat Transfer, Vol. 98, pp. 543-549, 1976.
 30. Altgilbers, L.L., Wu, S.T., and Ruo, K.L., "On the ADI Scheme for a Two-Dimensional Transient Heat Conduction Problem with Phase Change," AIAA 22nd Aerospace Sciences Meeting, Reno, Nevada, January 1984.
 31. Hsiao, J.S., "An Efficient Algorithm for Finite Difference Analysis of Heat Transfer with Melting and Solidification," Numerical Heat Transfer, Vol. 8, pp. 653-666, 1985.
 32. Hsiao, J.S. and Chung B.T.F., "An Efficient Algorithm for Finite Element Solution to Two Dimensional Heat Transfer with Melting and Freezing," J. Heat Transfer, Vol. 108, pp. 462-464, May 1986.

33. Pham, Q.T., "A Fast, Unconditionally Stable Finite-Difference Scheme for Heat Conduction with Phase Change," Int. J. Heat Mass Transfer, Vol. 28, No. 11, pp. 2079-2084, 1985.
34. Pham, Q.T., "The Use of Lumped Capacitance in the Finite-Element Solution of Heat Conduction Problems with Phase Change," Int. J. Heat Mass Transfer, Vol. 29, No. 2, pp. 285-291, 1986.
35. Pham, Q.T., "A Note on Some Finite-Difference Methods for Heat Conduction with Phase Change," Numerical Heat Transfer, Vol. 11, pp. 353-359, 1987.
36. Busse, C.A. and Prenger, F.C., "Numerical Analysis of the Vapor Flow in Cylindrical Heat Pipes," Proceedings of the Fifth International Heat Pipe Conference, Tsukuba Science City, Japan, May 14-18, 1984.
37. Narayana, K.B., "Vapor Flow Characteristics of Slender Cylindrical Heat Pipes - A Numerical Approach," Numerical Heat Transfer, Vol. 10, pp. 79-93, 1986.
38. Faghri, A., "Vapor Flow Analysis in a Double-Walled Concentric Heat Pipe," Numerical Heat Transfer, Vol. 10, pp. 583-595, 1986.
39. Faghri, A. and Parvani, S., "Numerical Analysis of Laminar Flow in a Double-Walled Annular Heat Pipe," J. Thermophysics and Heat

Transfer," Vol. 2, No. 2, pp. 165-171, 1988.

40. Issacci, F., Catton, I., Heiss, A., and Ghoniem, N.M., "Analysis of Heat Pipe Vapor Dynamics," ASME National Heat Transfer Conference, Houston, Texas, July 1988.
41. Issacci, F., Catton, I., and Ghoniem, N.M., "Vapor Dynamics of Heat Pipe Startup," Proceedings of the 7th Symposium on Space Nuclear Power Systems, Albuquerque, New Mexico, January 1987.
42. Issacci, F., Catton, I., and Ghoniem, N.M., "Startup Transient Modelling of Vapor Flow in Heat Pipes," Proceedings of the 9th International Heat Transfer Conference, Jerusalem, Israel, August 19-24, 1990.
43. Hall, M.L. and Doster, J.M., "Transient Thermohydraulic Heat Pipe Modeling," 4th Symposium on Space Nuclear Power Systems, Albuquerque, New Mexico, January 1987.
44. Kelly, J.M. and Schor, A.L., "Heat Pipe Transient Analysis: Vapor Dynamics," 5th Symposium on Space Nuclear Power Systems, Albuquerque, New Mexico, January 1988.
45. Tien, C.L. and Rohani, A.R., "Analysis of the Effects of Vapor Pressure Drop on Heat Pipe Performance," Int. J. Heat Mass Transfer, Vol. 17, pp. 61-67, 1974.

46. Bowman, W.J., Simulated Heat Pipe Vapor Dynamics, Ph.D. Dissertation, Air Force Institute of Technology, 1987.
47. Beam, J.E., Unsteady Heat Transfer in Heat Pipes, Ph.D. Dissertation, School of Engineering, University of Dayton, 1985.
48. Ambrose, J.H., Chow, L.C., and Beam, J.E., "Transient Heat Pipe Response and Rewetting Behavior," J. Thermophysics and Heat Transfer, Vol. 1, No. 3, pp. 222-227, 1987.
49. Ambrose, J.H., Transient Liquid Movement in Heat Pipe Wicks, Ph.D. Dissertation, College of Engineering, University of Kentucky, 1989.
50. Kamotani, Y., "Thermal Analysis of Axially Grooved Heat Pipes," Proceedings of the 2nd International Heat Pipe Conference, Bologna, Italy, European Space Agency, pp. 83-91, 1976.
51. Hwangbo, H. and McEver, W. S., "Liquid Flow Analysis in the Evaporator Grooves of the Cold Plate," J. Thermophysics and Heat Transfer, Vol. 2, No. 2, pp. 172-179, 1988.
52. Ogushi, T. and Yamanaka, G., "Heat Transport Capability of Grooved Heat Pipes," Proceedings of the 5th International Heat Pipe Conference, Tsukuba Science City, Japan, May 14-18, 1984.
53. Kamotani, Y., "Analysis of Axially Grooved Heat Pipe Condensers," AIAA 14th Aerospace Sciences Meeting, Washington, D.C., January,

1976.

54. Peaceman, D.W. and Rachford, H.H., The Numerical Solution of Parabolic and Elliptic Differential Equations, J. Soc. Indust. Appl. Math., Vol. 3, pp. 28-41, 1955.
55. Carnahan, B., Luther, H.A., and Wilkes, J.A., Applied Numerical Methods, p. 453, Wiley, New York, 1969.
56. Pantankar, S.V., Numerical Heat Transfer and Fluid Flow, p. 37, McGraw Hill, New York, 1980.
57. Smith, G.D., Numerical Solution of Partial Differential Equations, 2nd ed., p. 92, Oxford University Press, New York, 1978.
58. Carslaw, H.S. and Jaeger, J.C., Conduction of Heat in Solids, 2nd ed., p. 112, Oxford University Press, New York, 1959.
59. Longworth, D., "A Numerical Method to Determine the Temperature Distribution Around a Moving Weld Pool," In Moving Boundary Problems in Heat Flow and Diffusion (Edited by Ockendon and Hodgkins), pp. 54-61, Clarendon Press, Oxford, 1975.
60. Furzeland, R.M., "A Comparative Study of Numerical Methods for Moving Boundary Problems," J. Inst. Maths Applies, Vol. 26, pp. 411-429, 1980.

61. Crowley, A.B., "Numerical Solutions of Phase Change Problems," Int. J. Heat Mass Transfer, Vol. 21, pp. 215-219, 1978.
62. Shapiro, A.H., The Dynamics and Thermodynamics of Compressible Fluid Flow, Vol.1, The Ronald Press Company, New York, 1953, pp. 238-241.
63. Chi, S.W., Heat Pipe Theory and Practice, pp 38-43, Hemisphere Publishing Corporation, Washington, D.C., 1976.